

# **Thermodynamic and environmental analysis of heat and power generation using renewable fuels**

Hadis Montazerinejad

A Thesis  
In  
the Department  
of Building, Civil and Environmental Engineering

Presented in Partial Fulfillment of the Requirements  
for the Degree of  
Doctor of Philosophy (Building Engineering) at  
Concordia University  
Montreal, Quebec, Canada

October 2024

© Hadis Montazerinejad, 2024

CONCORDIA UNIVERSITY  
School of Graduate Studies

This is to certify that the thesis was prepared

By: Hadis Montazerinejad

Entitled: Thermodynamic and environmental analysis of heat and power generation using renewable fuels

and submitted in partial fulfilment of the requirements for the degree of

DOCTOR OF PHILOSOPHY (Building Engineering)

complies with the regulations of the University and meets the accepted standards with respect to originality and quality.

Signed by the final examining committee:

_____	Chair
Dr. Andrea Schiffauerova	
_____	External examiner
Dr. Ahmad Arabkoohsar	
_____	External to Program
Dr. Mojtaba Kheiri	
_____	Examiner
Dr. Fuzhan Nasiri	
_____	Examiner
Dr. Zhi Chen	
_____	Supervisor
Dr. Ursula Eicker	

Approved by

\_\_\_\_\_

Dr. Mohamed Ouf, Graduate Program Director

October, 2024

\_\_\_\_\_

D. Mourad Debabbi, Dean

## **Abstract**

### **Thermodynamic and environmental analysis of heat and power generation using renewable fuels**

**Hadis Montazerinejad, PhD**

**Concordia University, 2024**

This study evaluates compact cogeneration technologies for urban areas with varying energy demands, focusing on renewable fuels such as hydrogen and biogas, compared to fossil fuels like methane. Among various options, proton exchange membrane fuel cells (PEM fuel cells) and recuperated micro-gas turbines (MGTs) are identified as the most promising technologies. Their performance under diverse scenarios, including control strategies, fuel choices, and operational conditions, is thoroughly modeled.

For PEM fuel cells, detailed electrochemical and thermal models simulate electricity and heat production, while for MGTs, a comprehensive model optimizes heat recovery and control strategies. The developed control strategy involves precise bypass valve adjustments to regulate mass flow distribution, improving efficiency. Heat management is further enhanced by coordinating bypass valve settings with storage tank cycles and auxiliary boiler transitions.

PEM fuel cells are shown to excel in high-efficiency cogeneration due to their direct conversion of chemical to electrical energy at low operational temperatures, minimizing heat loss and optimizing hydrogen utilization. MGT systems, on the other hand, benefit from hydrogen combustion's higher flame temperatures, boosting power generation. Parametric analysis reveals that increasing rotational speed, pressure ratios, and working parameters in MGTs enhances power output, while higher cell counts and ambient temperatures improve PEM fuel cell efficiency and hydrogen consumption.

To reduce emissions from MGTs, a dual axial swirler combustor is proposed, ensuring uniform temperature distribution, minimizing hot spots, and enhancing fuel-air mixing. These features improve combustion efficiency and stability under partial loads, effectively lowering NOX and CO emissions. The emission characteristics are assessed using CFD simulations, an Equivalent Chemical Reactor Network (ECRN) model, and a custom mathematical model. Hydrogen

combustion is associated with high NOX emissions due to its flame temperature, while methane and biogas show lower NOX concentrations. However, the inert CO2 in biogas presents challenges for efficiency.

In summary, this research provides a robust framework for evaluating renewable-fueled cogeneration systems, offering strategies to enhance efficiency and reduce emissions, supporting urban energy sustainability.

## **Acknowledgements**

During my educational journey, I experienced a severe tragedy in May 2022, which put me in an extremely stressful situation and prevented me from focusing on my PhD thesis for at least one year. The unexpected and tragic loss of my beloved sister in a terrible accident in Montreal, Canada, made me contemplate leaving the University and returning to my home country forever. It was the first time in my life that I felt such profound loneliness and despair because I had a very close relationship with my sister. I owe Professor Ursula Eicker, who gave me her full support during that challenging period, encouraged me to stay strong, and advised me to pursue my educational dreams in honor of my sister.

Although my emotional damage has stayed, I will not forget that Prof. Eicker prevented me from giving up and has greatly influenced my professional development through her mentorship. She broadened my horizons and increased my knowledge of technologies by supporting me in going to the Fraunhofer, the best research organization in Europe. With her exceptional supervision, encouragement, invaluable guidance, and technical and financial support throughout my PhD studies, I achieved numerous milestones and received several awards. It has been a great honor for me to work as her doctoral student all these years.

Also, I would like to express my gratitude to the academic staff at Next-Generation Cities Institute, who have supported me throughout my educational journey. This thesis was undertaken, in part, thanks to funding from the Canada Excellence Research Chairs Program.

## **Dedication**

This dissertation is dedicated to my dear husband, Emad Fakhimi, whose constant encouragement and love have been the foundation of my strength. His belief in me, even during the most challenging moments, inspired me to persevere. Emad, your unwavering patience, wisdom, and support have been the silent force behind this work. I owe this accomplishment to you, and I am forever grateful for having you by my side on this journey.

# Table of Contents

List of Figures .....	x
List of Tables .....	xiv
List of abbreviations .....	xv
Chapter 1: Introduction .....	1
1.1 Problem Statement .....	1
1.2 Objectives and Contributions.....	3
Chapter 2: Literature Review .....	6
2.1 CHP systems .....	12
2.2 Renewable fuels .....	17
2.2.1 Hydrogen.....	17
2.2.1.1 Methods for storing hydrogen.....	20
2.2.1.2 Methods for hydrogen production .....	21
2.2.2 Biogas and syngas.....	23
2.3 Gas turbines .....	26
2.3.1 Micro-Gas Turbines (MGTs).....	27
2.3.2 Pollutant emissions from MGTs .....	32
2.4 Internal combustion engine (ICE).....	35
2.5 Fuel cell.....	40
2.5.1 Proton Exchange Membrane Fuel Cell (PEMFC) .....	41
2.5.2 Alkaline and molten carbonate fuel cell (AFC and MCFC).....	44
2.5.3 Solid oxide fuel cell (SOFC).....	46
2.6 Organic and steam Rankine cycle.....	50
2.7 Stirling engine.....	56
2.7.1 Biomass-Stirling engines .....	59
2.7.2 Solar energy-Stirling engines.....	62
Chapter 3: Proposed Research Methodology .....	64
3.1 PEM Fuel Cell Cycle Description.....	64
3.2 Mathematical Modeling of PEM Fuel Cell.....	66
3.3 MGT Configuration Description.....	70
3.4 Combustor Geometric Design.....	71
3.5 Mathematical Modeling of MGT .....	72

3.5.1	Compressor .....	73
3.5.2	Recuperator .....	74
3.5.3	Combustion Chamber (CC) .....	75
3.5.4	Turbine .....	75
3.5.5	Heat Recovery Unit (HRU) .....	77
3.6	Model Implementation and Environment Analysis .....	77
3.6.1	Computational Mesh Generation .....	78
3.6.2	Emission Prediction Methods .....	80
3.6.3	Analytical Algorithm Flowchart .....	85
3.6.4	Heating Control Model Flowchart .....	88
3.6.5	Case study .....	91
Chapter 4: Results and discussion .....		96
4.1	Technological Analysis Results .....	96
4.1.1	Numerical and Thermodynamic Modeling Validation .....	96
4.1.2	Comparison scenarios .....	99
4.1.2.1	Technology scenario .....	99
4.1.2.2	Fuel scenario .....	101
4.1.2.3	Control scenario .....	105
4.1.2.4	Operating scenario .....	112
4.2	Environmental Analysis Results .....	118
4.2.1	NOX emission validation .....	118
4.2.2	CFD simulation results for various fuel scenarios .....	119
4.2.2.1	Temperature distribution .....	119
4.2.2.2	Pollutant emissions (NOX) distribution .....	121
4.2.2.3	Impact of PFP and fuel type on NOX emissions across operating loads .....	123
4.2.3	Effect of load on NOX emissions .....	126
4.2.4	ECRN model analysis of NOX emissions under off-design conditions .....	128
4.2.5	Mathematical and CFD-based CO prediction methodology .....	131
4.2.5.1	Validation and results of predictive models for CO emissions .....	132
4.2.5.2	Sensitivity analysis of CO emission characteristics using CFD .....	136
Chapter 5: Conclusion .....		143
Chapter 6: Future work .....		149

References ..... 152

## List of Figures

<b>Figure 1</b> -The classification of cogeneration systems based on their kinds of the cycle (modified from [2]).....	7
<b>Figure 2</b> -Capacity and efficiency of conversion devices [21]. .....	8
<b>Figure 3</b> -Prime movers' applications in various sectors [2]. .....	11
<b>Figure 4</b> -Functional comparison between prime movers shown by the radar chart [2]. .....	12
<b>Figure 5</b> -The configuration of decentralized hybrid CHP system [53]. .....	15
<b>Figure 6</b> -The procedure of generating hydrogen via single approaches, including (a) Electrolysis, (b) Gasification, (c) PV-electrolysis, (d) Dark fermentation [2,88,100].....	23
<b>Figure 7</b> -Schematic layout of the conventional (left) and the wet recuperated micro-gas turbines cycles [135]. .....	29
<b>Figure 8</b> - Schematic of the CHP system consisting of an MGT with the injection of hot water and steam [137]. .....	30
<b>Figure 9</b> -Schematic of a dual fluidized bed gasifier that runs a prime mover (micro-gas turbine) [142]. .....	31
<b>Figure 10</b> -EF7 as one type of ICE to meet demand loads [170]. .....	37
<b>Figure 11</b> -The results of the hybrid system at optimum design parameters [184]. .....	40
<b>Figure 12</b> -The schematic diagram of a hybrid power system, including ORC and PEM fuel cell [12]. .....	43
<b>Figure 13</b> -The block diagram of the ORC integrated with a PEM fuel cell [194]. .....	44
<b>Figure 14</b> - Schematic of the AFC-based CHP system [197]. .....	45
<b>Figure 15</b> - Schematic of a cogeneration system, with an MCFC [198]. .....	46
<b>Figure 16</b> -The cooperation between a micro-SOFC and other auxiliary equipment to meet load demands [202]. .....	47
<b>Figure 17</b> -The overview of the function of SOFC with (left part) and without (right part) CO <sub>2</sub> capture [209]. .....	49
<b>Figure 18</b> -The classification of power systems based on their working fluid [211]. .....	50
<b>Figure 19</b> -ORC's average size since 1984 until 2016 [216]. .....	51
<b>Figure 20</b> -The hybrid power system [222] was upgraded from the study proposed by [221]. .....	53
<b>Figure 21</b> -Different types of Stirling engine: (a) Alpha, (b) Beta, and (c) Gamma [233]. .....	56

<b>Figure 22-</b> The schematic of the micro-CHP system by using Stirling engine (SE) [64].....	57
<b>Figure 23-</b> The schematic diagram of coupling a SOFC with SE [235]. .....	58
<b>Figure 24-</b> The gasification energy system integrated with the SE to provide load demands for small buildings in Shanghai and Singapore [240]. .....	59
<b>Figure 25-</b> Three-dimensional model of the Stirling engine with components [242].....	60
<b>Figure 26-</b> Schematic of the wood pellets fired the Stirling engine system [245].....	61
<b>Figure 27-</b> Decentralized energy system, including a Stirling engine and a solar system [246]..	62
<b>Figure 28-</b> Schematic diagram of the insulated PEM fuel cell. ....	66
<b>Figure 29-</b> Schematic diagram of the recuperated MGT with a heat recovery unit.....	71
<b>Figure 30-</b> Schematic diagram of (a) MGT's combustor structure (b) CAD drawing. ....	72
<b>Figure 31-</b> Compressor map based on pressure ratio, corrected mass flow rate and rotational speed [13].....	73
<b>Figure 32-</b> Efficiency, and pressure drop of recuperator based on mass flow rate [13]. ....	74
<b>Figure 33-</b> Turbine map with efficiency as a function of WP and $\omega_{corr}$ [13].....	76
<b>Figure 34-</b> Turbine map with working parameter based on $m_{corr}$ and $\omega_{corr}$ [13].....	76
<b>Figure 35-</b> Mesh configuration for the swirler combustor. ....	79
<b>Figure 36-</b> ECRN model developed in Ansys Chemkin-Pro for analyzing NO <sub>x</sub> emissions. ....	85
<b>Figure 37-</b> Flow chart illustrating the numerical model and pollutant emissions analysis from a recuperated MGT. ....	87
<b>Figure 38-</b> Heating control strategy model flowchart of the recuperated MGT coupled with a heat recovery unit. ....	89
<b>Figure 39-</b> Various scenarios involved in modeling the heating control strategy for the CHP system comprised of MGT and HRU. ....	91
<b>Figure 40-</b> (a) Screenshot of five residential buildings in Karlsruhe, Germany, displaying house numbers, (b) Heating demand (kWh). ....	94
<b>Figure 41-</b> Validation results of the present modeling and the conducted work [12] regarding single-cell (a) Power output (b) Voltage against current density. ....	97
<b>Figure 42-</b> Validation results of the present numerical simulation and Rist's work [13] regarding (a) Electrical power (b) fuel mass flow and (c) electrical efficiency against shaft rotational speed. ....	99

Figure 43- Effect of the load on the overall efficiency for three fuels (a) hydrogen (b) methane (c) biogas .....	105
<b>Figure 44-</b> The response of the MGT to varying urban demands under the control scenario: (a) Comparison across distinct fuels, (b) Performance with methane combustion, (c) Temporal assessment of hydrogen-based MGT during the winter season, and (d) Hydrogen-based MGT performance during the fall season. ....	108
<b>Figure 45-</b> Analysis of Storage and Heating Performance with Seasonal Variation: (a), (b) and (c) Temporal variation in the state of the storage tank, illustrating charge and discharge profiles for three fuels; (d) Impact of hydrogen combustion on storage strategies and MGT heating performance during the winter season under hydrogen combustion; (e) A similar analysis for the fall season.....	111
<b>Figure 46-</b> Evaluation of system availability: (a) Comparison across three different fuel types; (b) Analysis using hydrogen over various time intervals. ....	112
<b>Figure 47-</b> Comparison of NO <sub>x</sub> pollutant level models with experimental results [157] in the context of methane utilization at full load operating condition and diverse PFP. ....	119
<b>Figure 48-</b> Temperature distribution contours in the dual-axial swirler combustor at baseload, and 9% PFP. From top to bottom: (a) Hydrogen, (b) Methane, (c) Biogas with 40% CO <sub>2</sub> . ....	121
<b>Figure 49-</b> Mole Fraction of NO <sub>x</sub> under different fuel types, including (a) Hydrogen, (b) Methane, and (c) Biogas. ....	123
<b>Figure 50-</b> Effects of PFP on NO <sub>x</sub> emissions (ppmv @15% O <sub>2</sub> ) at various operating loads based on CFD simulation for three fuel scenarios: (a) Hydrogen, (b) Methane, and (c) Biogas.....	125
Figure 51- The effect of the load on the NO <sub>x</sub> emission for three different fuels (a) hydrogen (b) methane (c) biogas. ....	127
<b>Figure 52-</b> Variation of NO <sub>x</sub> emissions (ppmv @15% O <sub>2</sub> ) versus equivalence ratio for three fuel scenarios.....	129
<b>Figure 53-</b> Impact of ambient temperature on NO <sub>x</sub> emissions (ppmv @15% O <sub>2</sub> ) for all presented fuels.....	130
<b>Figure 54-</b> Influence of CO <sub>2</sub> concentration on NO <sub>x</sub> emissions (ppmv @15% O <sub>2</sub> ) in biogas combustion.....	131
<b>Figure 55-</b> Comparative analysis of predicted vs. measured [157] CO emissions in the context of methane utilization at full load operating condition and varied PFP.....	133

<b>Figure 56-</b> Mole Fraction of CO emissions for (a) methane, and (b) biogas at the central plane of the combustor operated at 100% load condition, and 9% PFP. ....	135
<b>Figure 57-</b> Effect of PFP on CO emissions (ppmv @15% O <sub>2</sub> ) at multiple power settings based on CFD simulation for two fuels: (a) Methane, and (b) Biogas. ....	138
Figure 58- The effect of the load on the CO emission for different fuels (a) methane (b) biogas .....	140
<b>Figure 59-</b> Variation of CO emissions ((ppmv @15% O <sub>2</sub> ) with ER for methane, and biogas. ..	141
<b>Figure 60-</b> Effect of CO <sub>2</sub> concentration on CO emissions (ppmv @15% O <sub>2</sub> ) in biogas combustion. ....	142

## List of Tables

<b>Table 1</b> -The performance of four prime movers in the CHP system [21,27–29]. It is noted that some information is brought from manufacturer's datasheet. ....	9
<b>Table 2</b> -The impacts of critical parameters on exergy efficiency [193]. ....	42
<b>Table 3</b> -Required equations used for modeling the PEM fuel cell [11]. ....	67
<b>Table 4</b> - Design and operating parameters for PEM fuel cell simulation. ....	69
<b>Table 5</b> -Operating conditions for modeling the recuperated MGT and simulating the swirler combustor across all fuel types at full load. ....	79
<b>Table 6</b> -Mathematical modeling of adiabatic flame temperature, and CO emission for three distinct fuel types [9,257–259]. ....	82
<b>Table 7</b> -Constant values across various conditions [9,256,260]. ....	84
<b>Table 8</b> -The main characteristics of the commercial MGTs. ....	92
<b>Table 9</b> - Technical specifications for the mini Gas-Otto engine CHP system series 2726. ....	95
<b>Table 10</b> -The validation of the proposed study and the work of Zhao et al. [12] and Rist et al. [13]. ....	96
<b>Table 11</b> -Comparative Performance Analysis of MGT and PEM Fuel Cells in Cogeneration Systems based on their design operating points shown in <b>Table 4</b> and <b>Table 5</b> . ....	100
<b>Table 12</b> -Fuel scenario results for the recuperated MGT under two distinct control settings at a 40%-part load. ....	102
<b>Table 13</b> -Variability of key operating parameters across defined operating scenarios. ....	116
<b>Table 14</b> -Functional characteristics of the recuperated MGT coupled with HRU under the operational scenario. ....	116
<b>Table 15</b> -Analyzing PEM fuel cell Performance under diverse operational conditions. ....	117
<b>Table 16</b> - Numerical results of the MGT model for all fuels at full load, and 9% PFP. ....	120
<b>Table 17</b> -ECRN versus CFD simulation: A detailed comparison for accurate NO <sub>x</sub> emission (ppmv) prediction. ....	128
<b>Table 18</b> -Comparative analysis of CO emission levels (ppmv @15% O <sub>2</sub> ) for two fuel types under diverse load conditions, and 9% PFP using two prediction methods. ....	136

## List of abbreviations

$A_{cell}$	Area of active surface, $cm^2$	BPP	Bipolar Plate
GDL	Gas Diffusion Layer	ch	Chemical Heat
C	Number of carbon atoms	Comp	Compressor
$C_p$	Specific heat capacity, ( $kJ\ kg^{-1}k^{-1}$ )	Conc	Concentration
CH <sub>4</sub>	Methane	Cons	Consumption
CHP	Combined Heat and Power	Corr	Corrected
CO	Carbon Monoxide	FC	Fuel Cell
CO <sub>2</sub>	Carbon Dioxide	Gen	Generation
F	Faraday Constant, ( $C\ mol^{-1}$ )	H	Heating Demand
GT	Gas Turbine	H <sub>2</sub> O	Water
h	Specific Enthalpy, ( $kJ\ kg^{-1}$ )	N <sub>2</sub>	Nitrogen
H	Number of hydrogen atoms	Ohm	Ohmic
H <sub>2</sub>	Hydrogen	O <sub>2</sub>	Oxygen
HHV	Higher Heating Value ( $kJ\ kg^{-1}$ )	p	Combustion Products
HRU	Heat Recovery Unit	ST	Storage Tank
I	Stack Operating Current, (A)	S,l	Sensible/Latent Heat
MGT	Micro-Gas Turbine	Rec	Recuperator
$\dot{m}$	Mass Flow Rate, ( $kg\ s^{-1}$ )	turb	Turbine
$\dot{n}$	Molar Flow Rate, ( $mol\ s^{-1}$ )	<b><i>superscripts</i></b>	
$N_{cell}$	Number of Cell	Sat	Saturation
NO <sub>x</sub>	Nitrogen Oxides	<b><i>Greek letters</i></b>	
P	Pressure, (kPa)	$\eta$	Efficiency, (%)
PEM	Proton Exchange Membrane	$\lambda$	Stoichiometric Rate
$\dot{Q}$	Heat transfer rate, (kW)	$\kappa$	Isentropic Exponent
T	Temperature, (k)	$\pi$	Pressure Ratio
V	Voltage, (V)	$\gamma_c$	Heat Capacity Ratio - Air Flow

WP	Working Parameter	$\gamma_h$	Heat Capacity Ratio - Gas Flow
$\dot{W}$	Power, (kW)	$\beta$	Bypass Valve Position, (%)
X	Molar Fraction	$\omega$	Shaft Rotational Speed
<b><i>Subscript</i></b>		$\Delta$	Time Step
ab	Adiabatic	$\theta$	Dimensionless temperature
act	Activation	$\phi$	Fuel-air equivalence ratio
AUX	Auxiliary Boiler	$\psi$	H/C atomic ratio

# Chapter 1: Introduction

Combined heat and power (CHP) systems are designed for high energy efficiency and reduced greenhouse gas emissions when compared to separate generation of electricity and heat. However, conventional CHP systems primarily rely on fossil fuels, contributing to environmental pollution and resource depletion. The shift towards renewable fuels such as hydrogen, biogas, and syngas is increasingly important in mitigating these issues and achieving a sustainable energy future. Renewable fuels offer several advantages over traditional fossil fuels. For instance, hydrogen, when produced from renewable sources, is a carbon-free fuel that can significantly reduce CO<sub>2</sub> emissions when used in CHP systems. Biogas and syngas, derived from organic waste materials, provide a way to manage waste and contribute to a circular economy by transforming waste into valuable energy resources. Since using hydrogen in future cogeneration systems is beneficial, defining a comprehensive methodology, that indicates the best procedural choice with regards to life cycle assessment and cost, is important [1]. The growing demand for hydrogen CHP systems has led to the development of methods for detecting and analyzing the technology robustness, identifying malfunctions, and assessing the lifetime of CHPs. Implementing health monitoring will enhance the durability and reliability of these systems. According to the European Clean Hydrogen Alliance announcement, 40 GW of renewable technologies will be installed to generate the required hydrogen for operating cogeneration systems by 2030. The lifetime of fuel cell systems for mid-size cogeneration systems is around ten years with one stack replacement, and it is expected to double by 2030 [1].

## 1.1 Problem Statement

The rapid increase in urban energy demand has increased the need for sustainable and reliable energy sources. This poses significant economic, and environmental risks due to the depletion of finite fossil fuel reserves and the release of pollutants. To mitigate these challenges, there is a growing trend toward using alternative and renewable energy sources in cogeneration systems. Current research has extensively explored various technologies suitable for urban applications and their potential for integrating renewable fuels [2]. However, comprehensive evaluations comparing diverse technological options under real-world scenarios remain limited. Moreover, the evident growth over the years and the proportion of published studies on hydrogen cogeneration systems

indicate that researchers have more focused on performance (56%), than environmental analysis (20%), control (10%), and availability, and reliability (14%) [3]. The demand for research on detection, cognition, and malfunction control of CHPs has been responded to partly and should be addressed more. The current challenges that stop the penetration of hydrogen energy systems in the market are related to their operating efficiency, durability and cost. Cogeneration systems with fuel cells in micro-, mid-, and large sizes are today around 36%, 50%, and 55% for electrical efficiency, concurrently, while the desired aim is 67%-74% [2]. Finding the optimum load at which fuel cells operate and proposing control strategies for hydrogen integrated energy systems remains a subject of research.

Recent studies on gas turbines (GT) show that although the combustion temperature of hydrogen-based gas turbines has a uniform profile that prevents thermal fatigue, the dimension of combustion chambers is higher than for fossil fuels, because the combustion of hydrogen requires an extensive recirculation area. Working on optimum combustion structures can reduce the size of recirculation zones and improve performance [4]. Researchers have accurately predicted NO<sub>x</sub> emissions from GTs using various approaches, including reactor network modeling [5,6]. However, they have proved that this effective engineering method has limitations in predicting CO emissions in both large and small scales of combustors. Certain investigations [7,8] have highlighted inaccuracies in CO emission predictions by the Equivalent Chemical Reactor Network (ECRN) methodology, finding that this predictive method tends to overestimate CO concentrations during partial load conditions while underestimating them during scenarios of full operational capacity. The fundamental challenge in accurately predicting CO emissions lies in the complex dynamics of CO generation and breakdown processes. Several factors associated with the flow field profoundly affect these processes, including how gases mix, the stabilization of flames, and the cooling mechanisms. ECRN methodologies are inadequate in fully addressing these essential aspects. As a result, advanced approaches such as comprehensive mathematical models [9,10], or CFD simulations [10] are now regarded as the most effective means for estimating CO emissions within turbine combustors. The selection between these approaches depends on the specific aims and requirements of the research project.

Although hydrogen is expected to be more environmentally friendly than conventional fuels, it is considered an indirect greenhouse gas. The percentage of its unavoidable pollution from operating

energy systems, storage, and production is estimated to be almost 0.2 up to 10% [1]. When integrating renewable fuels, including hydrogen, into CHP systems, there is an opportunity to reduce dependence on fossil fuels, decrease greenhouse gas emissions, and improve the sustainability of urban energy systems. However, there are challenges to adopting renewable fuels in CHP systems, including variability in fuel composition, lower energy densities, and differences in combustion characteristics compared to conventional fuels. These factors can affect the efficiency, stability, and emissions of CHP systems. Therefore, it is essential to thoroughly evaluate different fuel options and their impact on system performance under various operating and control conditions.

## 1.2 Objectives and Contributions

The thesis aims to address the following research questions:

- Which cogeneration technologies are most suitable for renewable fuel applications in terms of efficiency, availability, and emissions across various power ranges?
- How do different renewable fuels impact the performance, efficiency, and emission characteristics of cogeneration systems under varied operational scenarios?
- What control strategies can be developed to enhance cogeneration efficiency and performance across different fuel types?
- How can advanced computational models improve the accuracy of predicting NO<sub>x</sub> and CO emissions in micro-gas turbines operating with different fuels and under varying load conditions?
- Which pollutant prediction methods provide the most accurate prediction of CO concentrations and simplify the complexities associated with CO formation under diverse fuel, operational, and control conditions?

In this study, a comprehensive numerical model for two cogeneration technology options, a PEM fuel cell [11] and a recuperated MGT [10], has been developed to analyze mass and energy balances. The modeling framework includes mathematical equations that are written by Fortran,

which is a programming language. The MGT model development involved considering equipment with variable efficiencies and a controllable bypass valve while integrating precise operational maps for the MGT components. The models' accuracy of PEM fuel cell, and MGT are validated against research conducted by Zhao et al. [12], and experimental data presented by Rist et al. [13] to ensure the reliability of the proposed models. This study aims to identify the most suitable compact-size technologies by analyzing their performance and availability under multiple scenarios, including technology, control, fuel selection, and operational considerations. Also, the proposed systems are studied under off-design conditions by varying their operating, and control parameters to achieve effective performance [10]. A state-of-the-art heating control process based on a demand response control strategy is introduced to assess the availability and efficiency of these technologies in meeting residential energy needs. The interaction among energy generation, utilization, and storage strategies is investigated under three fuel scenarios: methane, hydrogen, and biogas, containing 40% CO<sub>2</sub>, combusted in a swirl-stabilized combustion chamber. Moreover, an operational strategy involving functional trends and seasonal variations in the cogeneration systems' performance is applied to analyze their responsiveness to urban heating demands [10].

In the next step, an environmental analysis is conducted using three distinct predictive methods to assess pollutant emissions from a dual-axial swirler combustor operating under mentioned fuel scenarios. The proposed combustion chamber is simulated using Ansys Fluent utilizing the Eddy Dissipation Concept (EDC) and realizable k- $\epsilon$  turbulence model, suitable for swirling flow regimes. To evaluate NO<sub>x</sub> emission characteristics, two precise pollutant level prediction methods, including the CFD simulation, and the Equivalent Chemical Reactor Network (ECRN) model in Ansys Chemkin-Pro, are employed. In the former, a two-step global reaction mechanism developed by Polifke is applied, providing a streamlined approach to calculate emission levels effectively under diverse operating and control conditions. Accurate prediction of carbon monoxide (CO) emissions remains a significant challenge for combustion designers due to limitations in existing engineering approaches for all kinds of combustors. To address this issue, this research proposes a novel approach combining the CFD simulation model with a mathematical prediction method. Based on the proposed novel method in the CFD simulation model, regions near the cooling holes are treated differently from the rest of the combustor, leading to precise CO predictions in all zones. Additionally, the mathematical model simplifies the complex issues related to CO formation, making it more practical and understandable for combustion engineers

who often need quick estimates and insights into attainable emission levels based on available design variables. Moreover, this study investigates the dynamic behavior of the dual-axial swirler combustor under various operating conditions, including the engine loads, equivalence ratio, ambient temperature, and CO<sub>2</sub> concentrations, to develop analytical models, thereby enhancing the accuracy of pollutant emission predictions. The innovation of this research lies in integrating validated numerical simulation with the advanced CFD simulation, ECRN and mathematical modeling, which facilitates a comparative environmental analysis of three distinct fuels in the MGT. The proposed approach enables accurate prediction of emission levels and enhances the understanding of the ecological implications of alternative fuels. These insights contribute to the development of cleaner combustion technologies for MGTs, highlighting the potential for substantial advancements in the field.

In this thesis, Chapter 2 provides a comprehensive literature review and an overview of cogeneration technologies, detailing their applications, optimal operation strategies, and installation methodologies. This chapter also explores the most efficient configurations of cogeneration systems by considering material properties and operational conditions. In the context of renewable fuels, the focus is on hydrogen, biogas, and syngas, including their production methods, applications in sectors including buildings, thermodynamic considerations for storage, and environmental impacts. Chapter 3 investigates the core functions, capacities, and specifications of the technologies under study, outlining the methodologies for modeling these systems. It covers the necessary assumptions, design operating conditions, and detailed component behavior maps to simulate technologies accurately. This chapter also examines real-world scenarios and provides a comprehensive analysis of pollutant emissions from combusting various fuels under off-design conditions. Chapter 4 presents the validation of the models and discusses the technological and environmental analysis results, along with the performance trends of the selected systems under non-ideal conditions. Chapter 5 provides the conclusions of the thesis, summarizing the key findings. Finally, Chapter 6 concludes the thesis with an outlook on potential future research directions based on the findings of this study.

## Chapter 2: Literature Review

Many comprehensive studies have been carried out, and solutions have been proposed to fight global warming and reduce greenhouse gas (GHG) emissions. One of them is the deployment of combined heat and power (CHP) technologies, which present significant potential for ensuring robust availability, reliability, and adaptable power capabilities in forthcoming renewable energy frameworks. These devices offer a unique opportunity to improve the overall fuel-based engine conversion efficiency by using the engines' waste heat within the urban setting. Strategic selection of these technologies should be based on their applicability, power ranges, and performance objectives [2,11]. CHP systems can be run with natural gas or renewable sources such as biogas, biomass, wind, and solar. CHP systems consist of several components, such as conversion devices, generators, heat recovery systems, and electrical converters [2].

Local CHP systems, which are identified as decentralized energy generators, have various benefits compared to centralized systems. The first criterion to compare the aforesaid systems refers to the overall efficiency. Overall efficiency of 30-50% in central power stations without heat use can increase to almost 70-90% in decentral combined heat and power plants [14]. A considerable reduction of electrical transmission losses is used as an indicator against which to determine the decentralized systems' advantages. Consuming less fuel in local CHP systems causes the primary energy demand to be reduced, resulting in the decrease of CO<sub>2</sub> emissions and costs [15]. In residential CHP use, by consuming gas at low cost to generate electricity and heat, the energy bills can be reduced and consequently, it overcomes fuel poverty [16].

In terms of power capacities, there are three classifications for CHP systems: "micro-cogeneration" for capacities under 50 kW<sub>e</sub>, "small-scale cogeneration" for capacities between 50 kW<sub>e</sub> and 1 MWe, and "medium or large cogeneration" for capacities exceeding 1 MWe [2,17]. Considering the advantages offered by CHP systems (like their adaptability in using a wide range of energy sources and simultaneous production of electricity, heating, and storage of energy), they are already being used in a wide range of sectors such as residential sectors, healthcare, commercial sectors and also in remote locations with only intermittent access to the energy supplied by the grid. In these places, CHP units can offer great benefits in the form of improved reliability and resilience to the consumer in question. They are also able to provide much-needed stability and

flexibility when energy supply is not guaranteed, especially in locations where shutdowns can have grave consequences, like hospitals or data centers [2,18].

Also, CHP units can be classified based on the prime mover used, such as internal combustion engines (ICEs), Gas turbines (GTs), micro-gas turbines (MGTs), Stirling engines (SEs), fuel cells (FCs), organic Rankine cycles (ORCs), etc. They can be further categorized based on the energy source used to power the unit. The fuels used today are still mainly fossil fuels such as diesel and natural gas, but a shift to green fuels is ongoing using biogas, solid biomass, and hydrogen produced from renewable energies such as solar and wind. Furthermore, these systems can also be categorized based on whether they have a thermodynamic cycle or not (see **Figure 1**). Rankine cycles, including steam and organic Rankine cycles, belong to the first category. Other devices in the first group are ICEs, SEs, GTs, and MGTs. The second group contains fuel cells and solar thermal photovoltaic hybrid technologies (PV/T) that generate electricity and heat with no combustion process. FCs and external combustion engines are more compatible with fuel than GTs and ICEs [2,19,20].

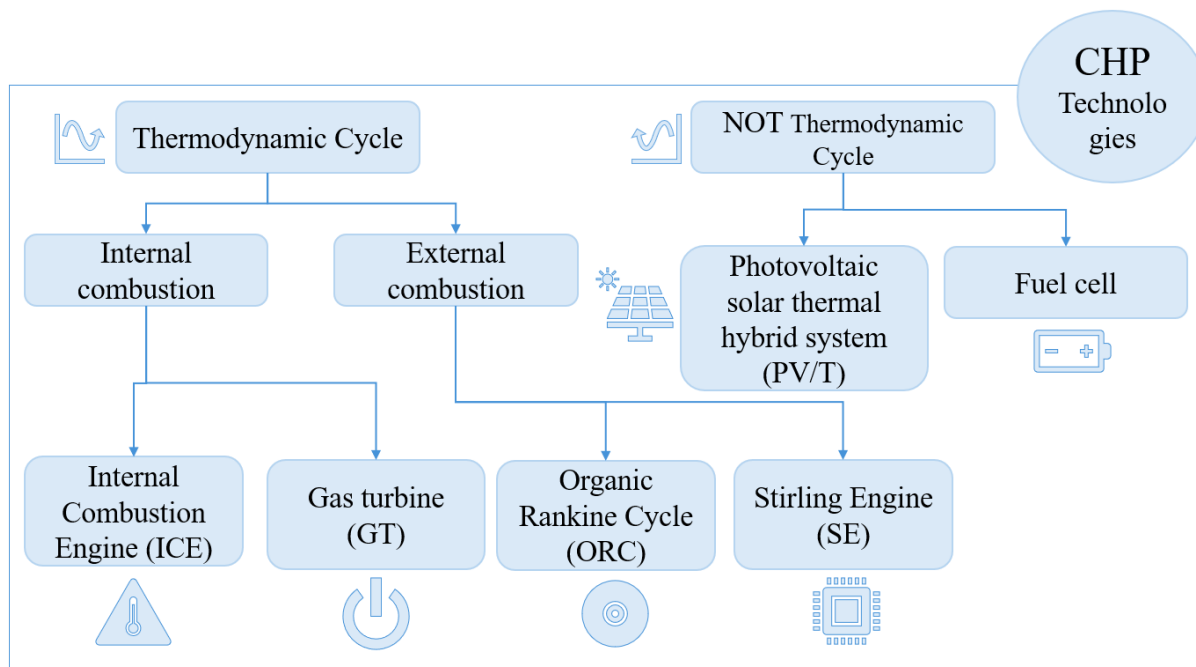


**Figure 1**-The classification of cogeneration systems based on their kinds of the cycle (modified from [2])

There are various conversion devices for small and micro-CHP applications such as internal combustion (ICE) and reciprocating engines, micro-gas turbines, Stirling engines, organic Rankine cycles, and fuel cells [20]. In **Figure 2**, the capacity and electrical efficiency of energy equipment

are shown. It shows that the highest electrical efficiency can be obtained by implementing fuel cells.

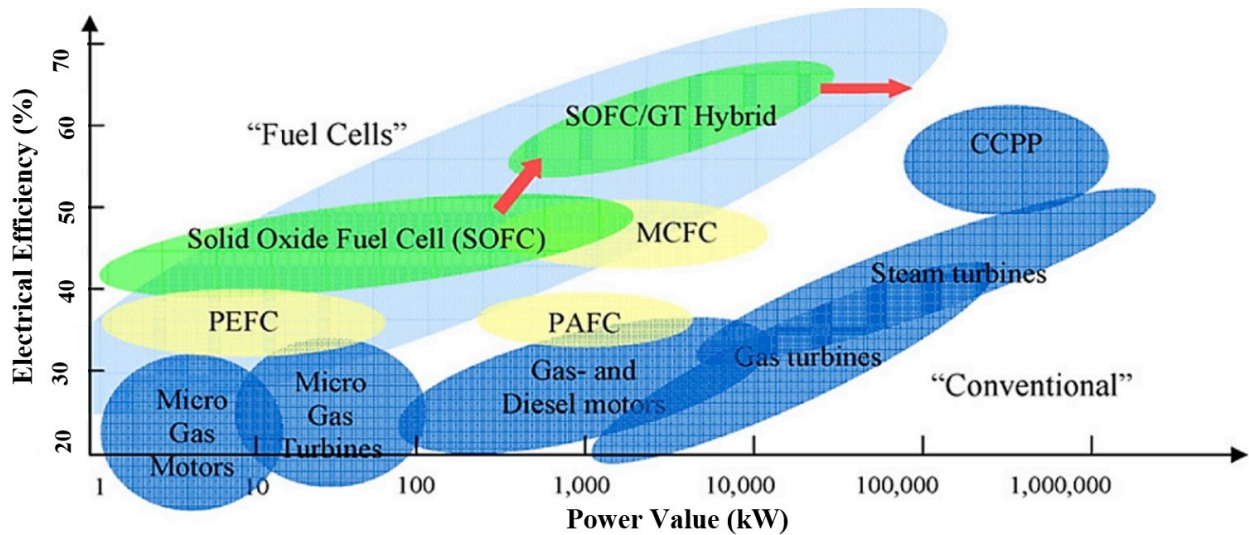


Figure 2-Capacity and efficiency of conversion devices [21].

By considering the rapid growth of urban areas that results in increasing district heating networks and heat demands, the investment in producing micro-CHP has been increasing because the production of electricity and heat locally leads to high efficiency [22,23]. As an example, Bianchi et al. proposed micro-CHP for the residential sector, and the studied components of the micro-CHP system were a CHP prime mover, an auxiliary boiler, and thermal storage. The generated power was used for domestic consumers or injected into the network [24]. Focusing on solar technologies should be prioritized because it can be used for domestic applications and is a great option for micro-CHP [25]. A review of the solar energy CHP technology with the production of electricity and heat/hot water for end-use was carried out by Modi et al. [26]. They considered a diversity of case studies in Denmark for evaluating the possibility of generating heat and power based on solar-CHP. After investigating some technologies, including solar photovoltaic modules, solar flat plate collectors, a ground source heat pump, a biomass burner, and an organic Rankine cycle, they found that using solar-biomass hybrid plants for CHP would be most economically and environmentally friendly. According to their results, using biomass instead of natural gas helped to reduce pollution, while the reduction of purchased fuel costs was highest for solar thermal systems [26].

The following table summarizes the comparison between CHP technologies based on their technical performance.

**Table 1**-The performance of four prime movers in the CHP system [21,27–29]. It is noted that some information is brought from manufacturer's datasheet.

Technical performance	Technology			
	Reciprocating engine	Gas turbine	Micro-gas turbines	Fuel cell
Size range	10 kW-10 MW	1 MW-300 MW	30 kW-330 kW	5 kW-2.8 MW
Electrical efficiency	30-42%	24-36%	25-29%	38-42%
Overall CHP efficiency	77-83%	65-71%	64-72%	62-75%
Power to heat ratio	0.6-1.2	0.6-1.0	0.5-0.8	1.3-1.6
Thermal output	16.7 kW-8.3 MW	1.7 MW-300	60 kW-412.5	3.8 kW-1.75
Net heat rate (BTU/kWh)	2,900-6,100	3,400-6,000	4,400-6,400	2,200-2,600
Fuel pressure (psig)	1-75	100-500	50-140	0.5-45
Part load efficiency	Good at both part and full load	Better at full load	Good at both part and full load	Best at both part and full load
Start-up time	10 s	10 min to 1 day	60 s	3 h to 2 days
Time to overhaul (hour)	30,000–60,000	25,000–50,000	40,000–80,000	32,000–64,000
Availability	96 – 98%	93 – 96%	98–99%	> 95%

Gaseous and liquid fuels can run reciprocating engine systems that provide excellent fuel conversion efficiency and high power to weight ratio [30]. Considerable fuel energy is wasted in ICEs. In recovering waste heat, organic Rankine cycles work well using especially medium-grade energy of the exhaust, and thermoelectric generators can be used [31], decreasing fuel consumption and CO<sub>2</sub> emissions [32]. The drawback of using ICE is low fuel adaptability. When it comes to reliability, gas turbines (GTs) perform well. Other advantages are high flexibility, low complexity, fast start, having a good function at full load, and low capital cost to power ratio [33]. According to power capacities, gas turbines can be classified into different parts, namely heavy-duty gas turbines whose power is higher than 500 MW, lightweight gas turbines whose power is lower than 60 MW, and micro-gas turbines with power less than 5 MW. The first category is used in central power generations, the second one supplies power for aircraft engines, and the last one (micro-gas turbines) is appropriate for distributed power generation [34]. Often the heat from GT is not used

and is released to the atmosphere. One solution to generate extra power from the waste heat would be Rankine cycles. Organic Rankine cycles have the ability to utilize low-grade heat, making them suitable for implementation in decentralized power plants with lower capacities. These power plants can then be utilized to generate both heat and power for a wide range of applications [35]. In combined heat and power systems, a heat recovery steam generator (HRSG) is applied between the gas turbine and Rankine cycle to recover high-temperature exhaust gases from the GT to generate the required steam for the Rankine cycle [36]. Recently for increasing the generated power and overall efficiency of gas turbines, the usage of flameless boilers has been proposed. A good case would be employing flameless duct burners before HRSG [37]. Another example is using a flameless boiler run by biogas and exhaust gases from GT to generate hydrogen through a solid oxide steam electrolyzer (SOSE). By using a flameless boiler, the amount of fuel to produce  $H_2$  is reduced significantly, and consequently, the  $NO_x$  and CO emissions are mitigated considerably [38].

Micro-gas turbines (MGTs) that can respond to lower power demands (less than 1000 kW<sub>el</sub>) are small-size gas turbines introduced in the 1990s for combined heat and power, and since 2000, they have been marketed on a larger scale [20]. A study on the characteristics of MGTs whose power is lower than 100 kW<sub>el</sub> was conducted by Backman et al. [39]. The authors represented some challenges related to the scale design of MGTs and investigated the effects of parameters on the CHP's function. The function of a typical micro-turbine with its simple open cycle are discussed in [40]. Air is sucked through the compressor and conveyed to the combustion housing where it combines with fuel; then combustion products leave the process by the compressor/diffuser. The above movements make the rotor rotate, leading to power generation through the alternator stator [40].

As a result of the presented classifications, technical compatibility, and definition of CHP systems, and research studies noted above, **Figure 3** has been drawn. The application of each component has been divided into three parts, including aerospace, aviation, and ground level [41].

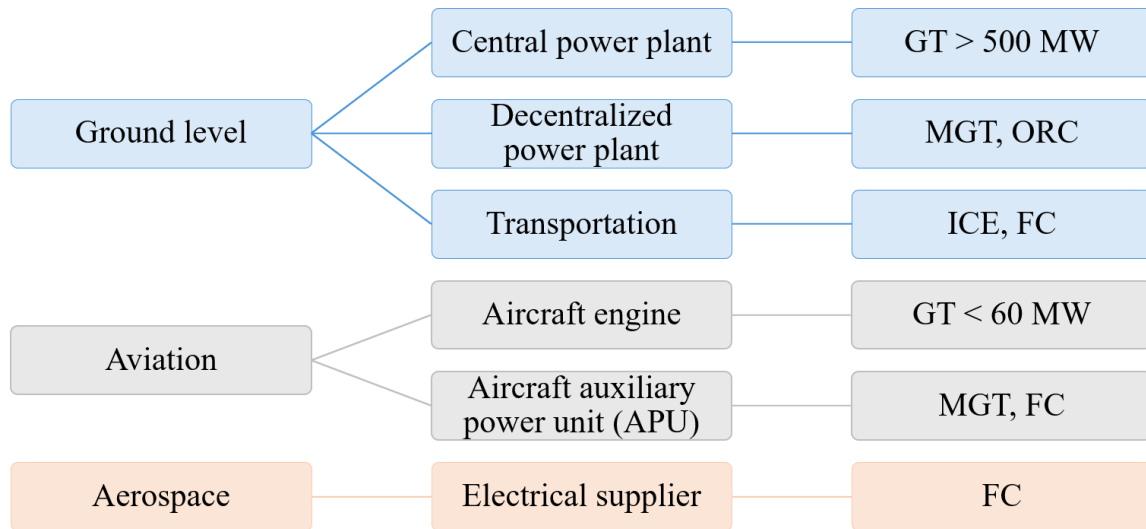


**Figure 3-**Prime movers' applications in various sectors [2].

Some cogeneration technologies, such as gas turbines, micro-gas turbines, or fuel cells, can use hydrogen, and the investigation of co-combustion of fuel blends in micro-gas turbines is a research priority [42]. Renewable electrical energy sources can be used to produce hydrogen, which has advantages, such as being a carbon-free energetic chemical, storage medium, and fuel [43]. A gas turbine can be run by the combination of H<sub>2</sub>/CH<sub>4</sub> fuel produced by a hybrid PV/hydrogen system. It proves that gas turbines are thus suitable for systems that generate sustainable power [44]. Recently, the need for sustainable and cleaner new technology has been increasing, so gas turbines with the usage of H<sub>2</sub> have become an important solution. Some crucial factors, such as fuel blending, combustion dynamics with H<sub>2</sub>, and associated combustor and turbine design strategies, are currently considered [45,46]. Reducing the amounts of hydrocarbons consumed and the related CO<sub>2</sub> emissions in the flue gas can be achieved by using the co-combustion of H<sub>2</sub> and CH<sub>4</sub> [47,48]. Also, H<sub>2</sub> burns fast, which results in improving flame stability, particularly at lean combustion [49]. Using pure H<sub>2</sub> causes some problems, including higher flame temperature, NO<sub>x</sub> emissions, flame speed, burning velocity, and flashback risk of H<sub>2</sub>. To reduce the flashback risk and constrain the combustion properties of the fuel, inserting CO<sub>2</sub> into the fuel was suggested [50]. If biogas is used in micro-gas turbines or gas turbines, it burns much slower than natural gas because of the CO<sub>2</sub>, which brings about a slowing combustion rate. Additionally, CO<sub>2</sub> with low specific heat diminishes heat transfer [51]. Investigations of micro-gas turbine performance and a wide range of biogas compositions were done, and it was shown that the electrical efficiency decreased with decreasing methane contents of the biogas [52]. **Figure 4** has been plotted based on multivariate

features to compare prime movers. Each prime mover is represented by a different colored polygon to highlight the differences in performance metrics across various parameters. The best performance of different technologies in various categories such as fuel consumption, ramp-up time or overall emissions is specified. This comparison gives a good overview which prime mover is the best depending on the criteria chosen [2].

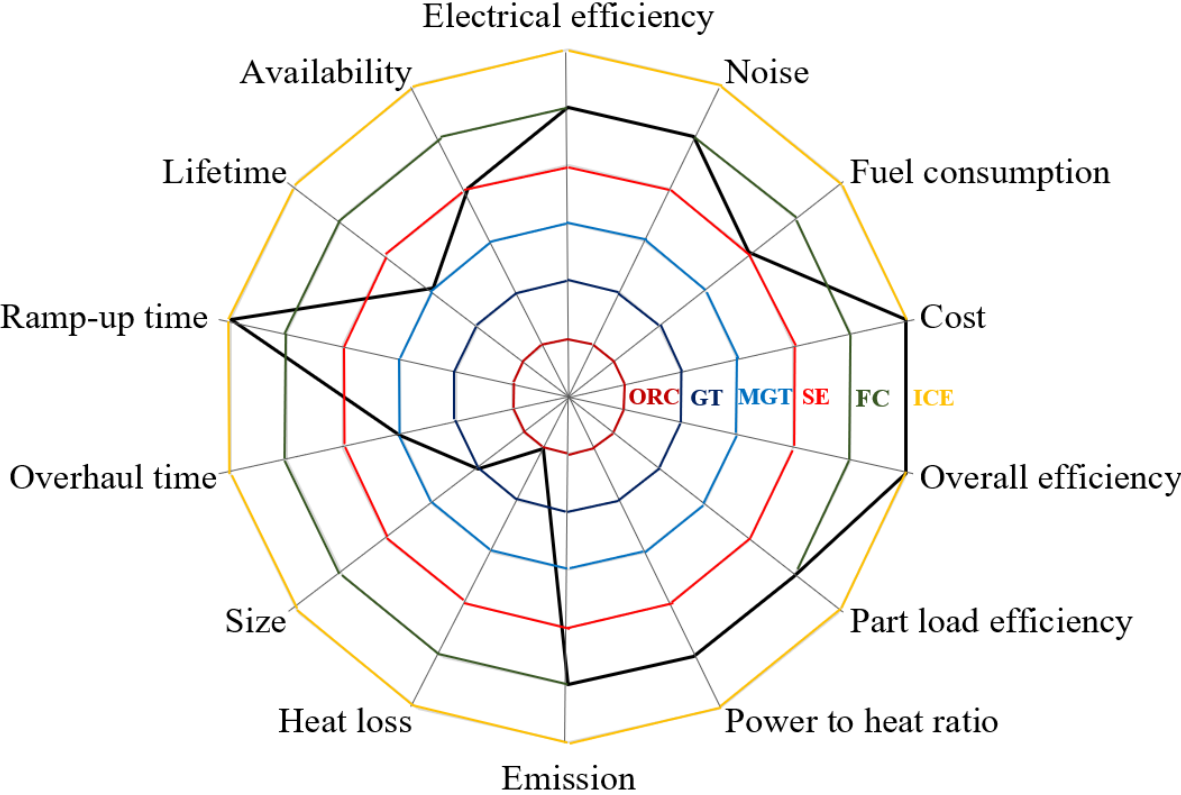


Figure 4-Functional comparison between prime movers shown by the radar chart [2].

### 2.1 CHP systems

CHP systems were introduced at the beginning of the 1880s when the only energy resource in industrial sectors was steam. The progress in their mechanisms was seen in the early 20<sup>th</sup> century when electricity was supplied by steam turbines, and coal-fired boilers provided steam. The growth of central power plants and electrical grids led to the decrement of electricity prices and the high preference of industries to buy electricity, resulting in cogeneration reduction. Since 1973, because of the significant increase in fuel costs, the attention to CHP systems has been raised [53]. They are run by fossil fuels or renewable energy, and their prime movers are gas turbines, micro-gas turbines, Stirling engines, fuel cells, and others. Their ability to operate independently of the grid leads to the highest reliability and resiliency in case of blackout events, provides considerable

energy saving and fewer greenhouse gas emissions, optimizes the consumption of rare fuels, and reaches the short payback period due to the reduction of consumed fuel costs. All the above points make them superior compared to the conventional separate energy technologies [54]. In the residential sector, the reduction of consumed primary energy and pollution is the main reason to use CHP in general and micro-CHP in particular [55].

To decarbonize the energy system, biomass can be used in CHP plants. Also, to improve the efficiency of biomass-CHPs, subcritical Rankin cycles can be transitioned to supercritical (SC) ones where steam operates at pressures and temperatures higher than the supercritical points (221.12 bar and 374.15°C). By using ultra-supercritical (USC) design, the CHPs can achieve the maximum performance because of the highest thermodynamic properties (pressure and temperature) of steam compared to SC. Better function of CHP plants at part loads regarding power and efficiency is at the root of operating SC and USC instead of using subcritical design [56]. By considering all the above-mentioned points [57], the performance of the CHP technology based on the USC model for supplying heat and power demands of aluminum and pulp and paper industries was analyzed. In some conditions, when heat demand was high, the CHP efficiency of the aluminum/pulp and paper was 92.50%/86.76%. The highest exergy destruction rate belonged to the combustion procedure because it had 67-70% of the total exergy destruction rate [57]. Since implementing the conventional and advanced exergy analyses gives detailed information about technologies and the effects of components on themselves, Caglayan and Caliskan [58] applied the mentioned methodology to analyze a CHP system comprised of a gas turbine. They revealed that at ambient temperature of 30 °C, the highest exergy efficiency (29.85%) and the lowest exergy destruction rates (17810.61 kW) were achieved. Amongst the different components, the combustion chamber had the highest exergy destruction rates of 10058.532 kW.

Patuzzi et al. [59] selected three small-scale CHP units based on biomass gasification and monitored them on-site in Italy. They recorded the value of mass and energy fluxes every 5 hours. An investigation on the gasification products and by-products was conducted. They concluded that the unit that consumed more pellets achieved higher electrical efficiency (25.3%) compared to others (18.3% and 16.8%) [59]. By applying Cycle Tempo software, Ahmadi et al. [60] simulated a CHP system based on various assessments, including the first and second thermodynamic laws. For achieving the highest performance and lowest emissions of a boiler, the authors equipped the

CHP system with an economizer that used the hot outlet gas from the boiler. After calculating the electric (8.22%), exergetic (7.87%), heat (48.92%), and overall (56.8%) efficiencies of the proposed CHP system, the researchers realized that the best solution for improving the overall efficiency was to connect the system with the main network. This process prevented operators from shutting down the system whenever they faced malfunctions and reduced heat waste by switching from a boiler, where the highest exergy destruction rate occurred (65571 kW), to an HRSG and a gas turbine [60].

A design and experimental strategy for a domestic micro-CHP system based on using ORC were conducted. The researchers selected R245fa as a working fluid. Based on the CHP efficiency profile they proved that all equipment of ORC was working not far from their nominal yields [61]. Dong et al. [62] studied the function of small- and micro-scale combined heat and power (CHP) systems run by biomass. Their investigation was based on using the organic Rankine cycle (ORC) in the mentioned power stations. They compared CHP systems based on available technologies such as ORC, micro-gas turbine, and biomass gasification. They concluded that ORC had a significant market potential in both the United Kingdom and the rest of the world [62]. A decentralized hybrid CHP system run by biogas was modeled and investigated [63]. The proposed system consisted of a pre-reformer, where a large amount of methane was converted to the required fuel for running a solid oxide fuel cell (SOFC), an afterburner whose high-temperature exhaust gas provided heat for the pre-reformer, a heat recovery boiler where a heating purpose was supplied, and a SOFC stack (see **Figure 5**). The electrical and CHP efficiency of the whole system were 55.6% and 85%, respectively [63].



An advanced review of domestic CHP systems was performed by focusing on fuel cells whose ability was transferring the generated energy from centralized to decentralized locals in an appropriate and efficient way. The researchers investigated the following steps [67]:

- The operational function of CHP systems based on applying fuel cells compared to conventional combustion systems.
- Addressing some problematic criteria such as energy security, cost, and decarbonization by using the fuel cell.
- Introducing the existing gaps, including fewer studies related to applying fuel cell-based systems in domestic applications and the methods for analyzing their environmental impacts.
- The necessity of reducing capital costs of fuel cells equipped with commercial, combustion-based, and trigeneration systems.

Finally, their future research would focus on fuel cell-based trigeneration systems, specifically for domestic purposes.

The environmentally friendly cogeneration system comprised of ORC, compressed air energy storage (CAES), and hybrid absorption-compression refrigeration cycle was assessed based on three important points of view namely, exergoeconomic, reliability, and availability [68]. To mitigate power shortages and generate chilled water at peak time, they bought extra and low-cost power from the network or applied renewable energy sources at off-peak times to stabilize the energy storage subsystem at critical times (high demand periods) [68]. For CHP and micro-CHP systems, an efficient energy management strategy to decrease the operation cost and increase reliability is essential [69]. Firouzmakan et al. [70] considered an intelligent energy management strategy (EMS) in microgrids (MG) for supplying electricity and heating demands. Electrical and heating loads were met with renewable energy resources (wind turbine (WT) and photovoltaic (PV)), micro-CHP systems (micro-gas turbine (MG) and fuel cell (FC)), energy storage systems (EES and TESS), and an auxiliary boiler. TESS played an important role in storing recovered heat at off-peak demands and using it at high heating demands. The results indicated that in the islanded (autonomous) mode of MG, operating micro-CHP units led to shutting down of auxiliary boiler, which resulted in decreasing natural gas consumption. The researchers used a demand response

program (DRP) based on working with users to reduce costs in grid-connected mode and increase islanding mode reliability.

## **2.2 Renewable fuels**

The ongoing crises resulting from the dependence on fossil fuels emphasize the need to change governments attitudes about the way of supplying energy and switching from fossil to renewable fuels and energy sources. Furthermore, global warming, caused by anthropogenic emissions such as CO<sub>2</sub>, methane, and other greenhouse gases, threatens to disrupt the ecosystems on which we all rely [71,72]. Therefore, being independent in producing energy, supplying energy for longer periods, and reducing carbon emissions in the energy sector requires some storable clean fuels that can compensate for the intermittency of many renewable electricity systems. Sustainable and clean hydrogen and alternative fuels, including biogas, are expected to play an essential role in the decarbonization of urban energy systems, from transportation to cogeneration systems [2].

### **2.2.1 Hydrogen**

Recent research has highlighted hydrogen as an appealing alternative due to its exceptional combustion properties and abundance. This enables hydrogen energy utilization in diverse technologies including gas turbines for on-demand energy production, significantly reducing pollutant emissions [2].

Hydrogen stands out as an efficient fuel, surpassing most hydrocarbons in combustion rate. This efficiency, paired with readily available sources such as water and surplus electricity, positions hydrogen as a cost-effective energy carrier. Hydrogen is notable for its relatively low volumetric energy content, which leads to a unique combustion requirement specifically, it requires significantly less oxygen for combustion, approximately half the volume needed for hydrogen, in contrast to the double volume required for methane combustion [73]. This distinction becomes clearer when examining the stoichiometric fuel-to-air volume ratio. In this context, hydrogen demonstrates a higher ratio in air (0.418) compared to methane (0.105), attributable to its lower density (0.089 kg m<sup>-3</sup> for hydrogen versus 0.656 kg m<sup>-3</sup> for methane). Consequently, to achieve stoichiometric combustion, a smaller mass of hydrogen (0.0292 kg) is required compared to methane (0.0581 kg), underscoring hydrogen's efficiency in terms of combustion properties

despite its lower energy density. Furthermore, hydrogen's application as a fuel enhancer is beneficial due to its superior heating value of  $141.8 \text{ kJ g}^{-1}$ , significantly surpassing that of biogas and methane, which are at  $23 \text{ kJ g}^{-1}$  and  $55.5 \text{ kJ g}^{-1}$ , respectively. Also, its lower heating value (LHV) is  $120 \text{ kJ g}^{-1}$ , which is higher than other fuels such as gasoline with LHV of  $44 \text{ kJ g}^{-1}$  [74]. Other properties, including critical temperature ( $-239.9 \text{ }^\circ\text{C}$ ), pressure ( $1296.212 \text{ kPa}$ ) with the values of specific heats  $C_p$  ( $14.34 \text{ kJ. (kg.K)}^{-1}$ ) and  $C_v$  ( $10.12 \text{ kJ. (kg.K)}^{-1}$ ) are given from the literature [75]. Despite this, hydrogen's lower density ( $0.089 \text{ kg m}^{-3}$ ) leads to a decreased volumetric heating value ( $10,766 \text{ kJ m}^{-3}$ ) compared to methane, which has a volumetric heating value of  $35,800 \text{ kJ m}^{-3}$  [76,77]. This aspect, coupled with hydrogen's extensive volumetric ratio in air, results in a diminished energy content ( $2,913 \text{ kJ m}^{-3}$ ) in the stoichiometric mix of air and hydrogen, in contrast to that of methane ( $3,088 \text{ kJ m}^{-3}$ ). Hydrogen combusts effectively at an equivalence ratio of around 0.5, which is markedly leaner compared to methane, which achieves optimal combustion at an equivalence ratio close to 1.0. These findings underscore hydrogen's capacity for combustion in significantly leaner mixtures, highlighting its advantageous combustion characteristics. This includes a lower ignition energy requirement, faster flame speed, and broader flammability limits than methane, making hydrogen a more reactive and efficiently utilized fuel [78,79]. Utilizing hydrogen ( $\text{H}_2$ ) as fuel in gas turbines presents an effective strategy for the prolonged storage and on-demand use of energy derived from variable renewable sources [80]. Hydrogen can be stored for long periods, making it a potential energy storage option for urban energy systems. Furthermore, hydrogen has a notably higher auto-ignition temperature than other fuels, making it an attractive option for urban energy systems. This characteristic effectively mitigates the risk of spontaneous ignition under standard operating conditions, thereby enhancing safety in industrial settings [81]. According to a study by Razaghi et al. [82], hydrogen production not only covers the annual capital investment, operating, and maintenance expenses but also generates a profit even during the worst-case scenarios for the energy system. The research showed that biofuel, solar-biofuel, and geothermal energy are three energy resources that can produce a significant amount of hydrogen income annually.

A pivotal concern, however, is the effect of hydrogen combustion in gas turbines on air quality, as described by the Zeldovich mechanism [83,84], which leads to nitrogen oxidation, producing nitric oxide (NO). The NO swiftly transforms into nitrogen dioxide ( $\text{NO}_2$ ), highlighting an environmental consideration in hydrogen's combustion process [85].  $\text{NO}_x$  emissions, known for

their harmful effects on respiratory health, smog formation, and acid rain, are different from other pollutants such as CO<sub>2</sub>, CO, particulates, and SO<sub>x</sub>. The latter originate from elements present in conventional fuels but absent in hydrogen. In contrast, NO<sub>x</sub> is primarily formed in gas-fueled systems by reacting nitrogen (N<sub>2</sub>) and oxygen (O<sub>2</sub>) in the atmosphere at high temperatures [86]. While transitioning to hydrogen fuels offers a cleaner alternative, reducing NO<sub>x</sub> emissions remains a critical challenge, similar to concerns faced in natural gas applications. Also, hydrogen burns at a much higher rate than methane, up to ten times faster at similar equivalence ratios, which poses significant challenges in hydrogen-fueled systems [87]. Despite the superior energy content of hydrogen and its ability to accelerate combustion, leading to better flame stability, especially in lean combustion environments, the usage of hydrogen presents operational complexities. These complexities are primarily due to the high flammability (1526.85°C), and low explosion temperature (400°C) of hydrogen, which poses significant safety risks [75]. Other challenges of utilizing hydrogen as a fuel include the high storage cost and the risks of leakage. In addition to various challenges, hydrogen exhibits a notably low electro-conductivity rating, which makes its usage complex. Both its liquid and gas states generate electrostatic charges that can trigger sparks. Therefore, all equipment in direct contact with hydrogen should be electrically grounded to prevent potential accidents [2,88]. Moreover, hydrogen is more prone to flame flashback due to its susceptibility to flame stretch and thermal-diffusive instabilities than natural gas. This requires a reassessment of traditional operational parameters used for natural gas systems to effectively accommodate hydrogen's unique combustion characteristics. As a result, there is a growing focus on research and the development of advanced burner technologies to address these challenges and improve combustion stability in hydrogen-based systems [89,90].

Chapman et al. [91] classified the application of hydrogen into four parts, the first one in industry as a heat source. It can be used in a variety of industrial applications, from powering manufacturing processes to providing heat for chemical reactions. The second group as a fuel for CHP systems to provide heating and cooling for buildings. The third category includes power systems such as internal combustion engines (ICEs), micro-gas turbines (MGTs), and gas turbines (GTs). Hydrogen fuel cells can be used to provide backup power in case of a power outage. This can be especially important in urban areas where power outages can significantly impact businesses and residents. The fourth group involves its storage and application in transportation via fuel cells. In fact, transportation alone accounted for over half of the world's oil consumption in 2019. Replacing

diesel buses with new technologies, that run by renewable fuels, is considered one of the most difficult aspects of the energy transition. However, the efforts to renew urban passenger transport fleets lead to decreased environmental and noise pollution in cities. Although internal combustion engine vehicles (ICEVs) still dominate the market, it is predicted that electric vehicles will comprise the majority of new vehicles by 2030. Hydrogen fuel cell electric vehicles are superior compared to other clean transportation technologies. These vehicles have made significant improvements towards commercialization and have already been deployed on a large scale in numerous countries because of their potential for long-range driving, the lowest pollution, and the highest performance [92,93].

Water vapor as the combustion product of hydrogen decreases the peak flame temperature and NO<sub>x</sub> formation compared to kerosene which leads to using hydrogen as aviation fuel, but the energy density of liquid hydrogen is four times less than kerosene. In the aviation sector, the aim is to improve the air quality and get a 50% decline in CO<sub>2</sub> emissions by 2050, so major alterations are required for engines to be fueled by liquid hydrogen, which should be kept at cryogenic temperatures and stored in highly insulating tanks. Since storing liquid hydrogen (LH<sub>2</sub>) needs enormous volume, wings are not suitable choices. Three areas with no space limitations, including the upper part of the fuselage in the short-to-medium aircraft, behind the cockpit, and at the end of fuselage next to the tail, in the long-range aircraft, are the best options. The performance of long-range aircraft fueled by LH<sub>2</sub> improves by 12%; however, the consumed energy (6-19%) and the weight of fuselage (6%) for short-range aircraft increase, leading to prohibiting it from using hydrogen. Although adapting conventional planes with LH<sub>2</sub> causes a 25% increment in costs, including making smaller wings and wider fuselage, they are lighter and more economical than kerosene-based planes [94].

### **2.2.1.1 Methods for storing hydrogen**

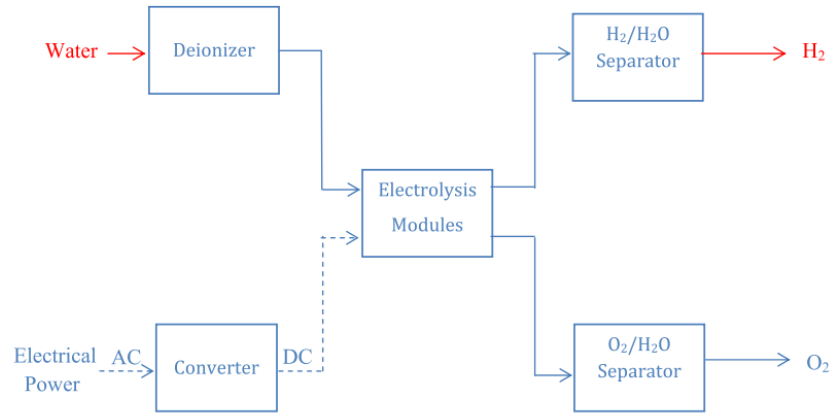
Hydrogen can be stored for long periods, making it a potential energy storage option for urban energy systems. Hydrogen can be stored in gaseous, liquid, or solid-phase containers, with the second being more economically viable due to its space efficiency. However, the design condition of liquefying hydrogen would be below  $-250^{\circ}\text{C}$ , identified as an energy-consuming process [95]. An evaluation is required to select suitable storage technologies based on reliability, efficiency,

cost-effectiveness, mass, and dimensions [96]. In the conventional gaseous storage systems, which are designed for high pressure, hydrogen leaks from the system requires upgrading the systems' material from steel and aluminum to Carbon Fiber Reinforced Polymer (CFRP) composite [97]. The advantages of composite storage tanks would be their versatility, rapid response, and modular design. Despite the fact that, the composite materials have strong resistance, they are very expensive, and salt caverns could be a cheaper option where compressed and massive hydrogen can be stored for an unlimited time without leakages and explosions. At standard cryogenic conditions, where hydrogen is maintained at very low temperatures close to its boiling point (-252.87°C), the density of hydrogen ( $70.85 \text{ kg m}^{-3}$ ) is higher than its gaseous state ( $0.089 \text{ kg m}^{-3}$ ), making it suitable to be stored in the shape of a cryogenic liquid. The required vessels for storing it need highly insulated walls [98]. The usage of this kind of vessel is limited to a system where hydrogen should be consumed during a short duration. Solid phase storage happens by absorbing and releasing hydrogen from solid materials through physisorption and chemisorption. In the former, the surface of solids is covered by hydrogen via van der Waals forces; then thermal processes release hydrogen. The disadvantage of this technique are its design conditions at ambient temperature with low storage capacity; only at a very low temperature its capacity increases. On the contrary, in the chemisorption scenario, the hydrides are produced by the chemical reaction that happens between atomic hydrogen and solids like  $\text{NaAlH}_4$ . Whenever hydrogen is needed by consuming heat, hydrides' bonds are broken, and hydrogen is generated [99].

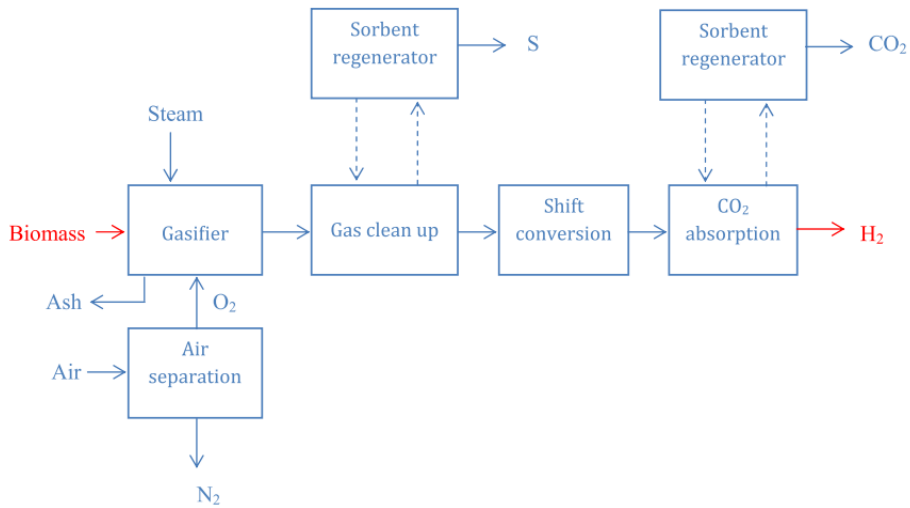
### **2.2.1.2 Methods for hydrogen production**

The production of hydrogen involves diverse pathways categorized based on their sources and applications. Hydrogen can be derived from sustainable feedstocks, which are further classified into single or hybrid methods. **Figure 6** illustrates single approaches, which encompass electrolysis, gasification, PV-electrolysis, and dark fermentation, exclusively depend on a specific energy carrier, be it electrical, thermal, photonic, or biochemical energy. Electrolysis is applied to split water into oxygen and hydrogen using electrical energy. Gasification is the thermochemical process where biomass is converted to syngas by absorbing thermal energy; then, syngas goes through a steam reformer to produce pure hydrogen. In PV-electrolysis, the required power for extracting hydrogen from water is delivered by PV panels that convert photonic energy. If the generated hydrogen from biomass occurs in dark and anaerobic conditions, the process is called

dark fermentation and is based on biochemical energy. In contrast, hybrid methods integrate two distinct types of energy, including the combination of electrical and thermal energy, electrical and photonic energy, biochemical and thermal energy, and photonic and biochemical energy [2,88,100].



(a)



(b)

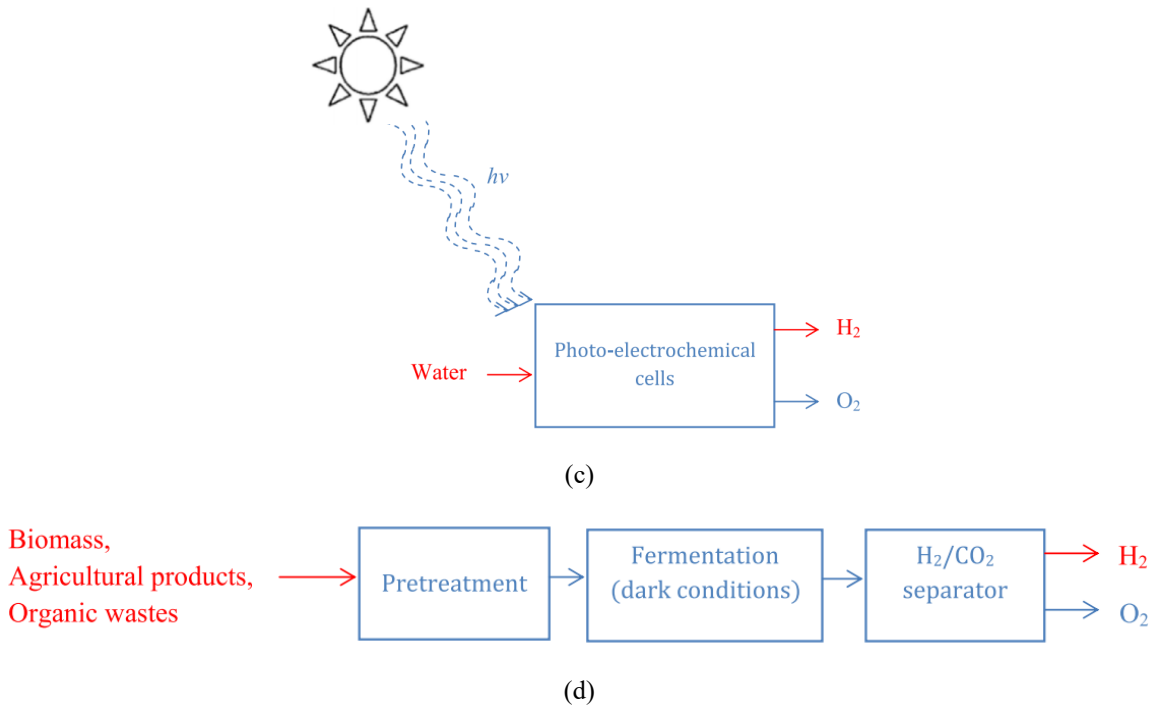


**Figure 6-**The procedure of generating hydrogen via single approaches, including (a) Electrolysis, (b) Gasification, (c) PV-electrolysis, (d) Dark fermentation [2,88,100].

### 2.2.2 Biogas and syngas

Decomposing biological waste, including sewage sludge, agro-industrial waste, and industrial animal waste provides biogas as a sustainable energy source. It is mainly composed of methane (50-70 vol%) with 30-50 vol%  $CO_2$ . At unsteady flame, the amount of  $CO_2$  emissions of biogas is lower than pure methane, proving its capability to conserve the environment. Fueling vehicles and producing heat and electricity through biogas are green energy options. To enrich biogas to biomethane, a cleaning approach can be used that eliminates  $H_2S$ ,  $NH_3$ , and hydrocarbons, and the second method removes  $CO_2$  to maintain the calorific value and relative density at an appropriate level. The later one, called an upgrading scenario, is commonly used for transportation and injection to the gas grid. Biomethane produced through upgrading biogas is more economical than renewable gas such as hydrogen. In Europe, the number of plants run by biogas and biomethane is estimated to be 17783 and 540, respectively, where 340 of 540 are injected into the network. Germany alone invested to install 195 energy systems fueled by biomethane [101,102].

Biogas can be generated by several processes, including anaerobic digestion (AD), anaerobic degradation in landfill sites (LFS), and new AD technologies. In AD, municipal solid waste

(MSW) and wastewater go through four levels, namely hydrolysis, acidogenesis, acetogenesis, and methanogenesis to transfer into biogas. Landfilling sites for solid wastes with gradual decomposition are economical, but the reactions are slow due to the lack of oxygen, which accelerates the decomposition procedure. High-rate anaerobic reactors or membrane bioreactors, or a combination of them are called new AD technologies [103]. Biogas can be used in a diversity of technologies such as gas turbines, micro-gas turbines, ICE, and combustion engines to generate heat and power. Because of its abundant quantities and wide distribution, the application of biogas in various scale distributed power generation (from small to medium) has been considered. For heating purposes, including domestic hot water and space heating, high-quality biomethane generated through upgrading biogas is used in boilers. Gas turbines and diesel engines convert approximately 30-40% of the biogas energy to produce power. In dual-fuel engines, biogas and diesel are burned to the extent that they keep the efficiency of the technology at its maximum. The application of biogas in the transportation sector is interesting, especially when the amounts of hydrogen in biogas increase. Biomethane can also be fed into gas networks and be mixed with natural gas. The upgraded biogas as a green gas drives power plants where green heating and power are generated [104,105]. The other form of biogas that is commonly applied in the urban transportation sector is compressed natural gas (CNG). Combustion of CNG produces lower amounts of pollutants compared to traditional fossil fuels, including gasoline and diesel. The high penetration of biogas in the agricultural sector supports sustainable rural growth, which leads to making profits for farmers and improving waste management [2].

The combination of hydrogen, carbon monoxide, and methane creates syngas whose auto-ignition temperature is high, and with the same percentage of hydrogen and carbon monoxide, its lower heating value is  $11.7 \text{ MJ (Nm}^3\text{)}^{-1}$ . The flame velocity and adiabatic temperature for its elements, including  $\text{H}_2$ ,  $\text{CO}$ , and  $\text{CH}_4$ , are  $2.7 \text{ m s}^{-1}$  at  $2210 \text{ }^\circ\text{C}$ ,  $0.19 \text{ m s}^{-1}$  at  $2121 \text{ }^\circ\text{C}$ , and  $0.37 \text{ m s}^{-1}$  at  $1963 \text{ }^\circ\text{C}$ , respectively. According to the process of syngas generation, there are two kinds with different volume concentrations of elements and heating values. Using steam or oxygen to produce syngas, its heating value is estimated to be  $10\text{-}28 \text{ MJ (Nm}^3\text{)}^{-1}$  with 25-30%  $\text{H}_2$ , while producer gas with 13-19%  $\text{H}_2$  is created based on air, resulting in the lower heating value of  $4\text{-}7 \text{ MJ (Nm}^3\text{)}^{-1}$ . During World War II, the demand for producer gas reached its peak, now India is the at the first place using syngas because of its bio-resources [106–108]. Syngas can also be produced from plasma gasification system whose feedstock is biomedical waste (BW). This system consumes high energy

leading to the reduction of energy efficiency of ICEs from 78.59% to 15.71% when they are integrated with plasma gasification to generate more power. The payback period for plasma gasification is in the range of 4 to 6 years, and it can supply 31% of its own required electricity. The volume percentage of elements in syngas generated by BW-based plasma gasification would be 26.5% for CO, 44.6% for H<sub>2</sub>, and 29.9% for N<sub>2</sub> [109,110]. Another way to produce a combustible gas (syngas) is pyrolysis, whose other products are biochar and bio-oil. It is a thermochemical technology where biomass is heated to more than 400 °C under anaerobic conditions [111].

In the transportation sector, heavy-duty trucks, buses, and other commercial vehicles can be equipped with dual-fuel engines and compression ignition (CI) engines as two types of internal combustion engines. In CI engines, the highest thermal efficiency is attained by injecting syngas and keeping compression ratios over 14:1. One of the drawbacks of using syngas is due to limitations to achieve its autoignition temperature. This can be addressed by a combination with diesel fuel as a transition concept. Dual-fuel engines are a good choice where a combination of diesel and syngas leads to lower emissions and good performance. Switching from gasoline to syngas for driving homogeneous charge spark ignition engines is possible, increases efficiency and diminishes the knocking tendency, which is due to the augmenting compression ratio [112]. Also, syngas can be used to generate synthetic fuels such as synthetic diesel and gasoline as a low-emission alternative to traditional fossil fuels. The best performance of engines will be provided if the flame velocity is laminar and high, which leads to the reduction of pollution. For achieving it, manufacturers focus on the interaction between CO and H<sub>2</sub> in syngas, operating conditions (pressure and temperature), and air to fuel ratio. Kishore [113] illustrated the relationship between the flame velocity at laminar mode with the ratio of H<sub>2</sub>/CO and the volume fractions of syngas composition. The results indicated that by increasing the fraction of H<sub>2</sub> from 12% to 48% without the existence of CH<sub>4</sub>, the laminar flame speed increased. He provided four scenarios that included different compositions of H<sub>2</sub> and CO and showed that the highest speed occurred in the range of 1.2 to 1.4 equivalence ratio. Also, by injecting methane (12%) into the mentioned mixtures, the flame velocity was not affected by the increase of hydrogen content [113]. A comparison between syngas and natural gas based on their extensive flammability range was conducted by Fossum and

Bayer [114]. They confirmed that the highest range of flammability belongs to syngas that depends entirely on factors such as fuel to air ratio (20-60%), pressure, and temperature [114].

In the power sector, syngas runs gas turbines, gas engines, and micro-CHP systems to supply energy demands. If syngas-based engines are equipped with cleaning technologies, the pollution is reduced and limits NO<sub>x</sub> and CO. [112,115]. To reduce the amounts of NO<sub>x</sub> emissions, the combustion products are recirculated to the combustion chamber's input and combined with fuel and inlet air, which results in a significant reduction of peak flame temperature [112,115]. Micro-CHP systems driven through syngas can be profitable if there are sufficient local solid and food wastes, which eliminates transportation expenses, and which can be used in gasification to generate syngas. The cost of generating syngas decreases (from 0.16 to 0.08 \$ (Nm<sup>3</sup>)<sup>-1</sup>) nonlinearly with power (from 100 to 1500 kW). The payback period for the systems that work 3000 hours per year was estimated to be 4-5 years [115,116].

### **2.3 Gas turbines**

Gas turbines (GTs) exhibit robust reliability and offer high operational flexibility, low complexity, swift start-up, efficient full-load operation, and a favorable capital cost-to-power ratio. A range of configurations and capacities of gas turbines are available from micro-scale to large-scale units. Based on power capacities, GTs are categorized into distinct segments: heavy-duty gas turbines (>500 MW), aeroderivative gas turbines (<60 MW), and micro-gas turbines (<5 MW). Heavy-duty turbines are employed in centralized power generation, aeroderivative models propel aircraft engines, while micro-gas turbines are suitable for decentralized power generation [34]. Researchers and manufacturers are currently focusing on achieving the ideal stoichiometric condition to increase the power and efficiency of gas turbines. The combustion performance with a high percentage volume of hydrogen is more significant than pure biogas. This improvement can be seen in flame structure, flame stability, and less gas turbines pollution. The optimum co-combustion of hydrogen and biogas occurs at the extra lean equivalence ratio of 0.2 with a 50% volume of hydrogen. It leads to reduced peak flame temperature and increased OH concentration. The former drops the creation of NO<sub>x</sub>, and the latter diminishes the amount of greenhouse gas emissions [117]. Controlling the flashback risk of hydrogen and reaching the highest safety with uniform and continuous combustion are at the root of injecting steam into combustion chambers. The maximum flow rate value of steam is 125% of fuel flow [118]. Gas turbines with the

combustion of hydrogen and ammonia have better performance and the lowest carbon emissions compared to conventional fuels. The best equivalence ratio for the proposed fuel blending is determined to be lower than 0.75 [119].

Some important subjects related to gas turbines' degradation, emission, operating cost, and their applications, such as transportation, have been studied recently. Chen et al. [120] proposed a novel methodology to diagnose the fault of a triple-shaft gas turbine. The chosen diagnostic method identified which components suffered from low reliability and availability with the highest accuracy and lowest set of measurements compared to the existing methods. They concluded that their proposed technique would assist an operator who wants to monitor gas turbines in distinguishing components' degradation, such as turbine erosion, sooner than before. This would result in increased reliability and efficiency. A few attempts have been made to replace new energy converters with internal combustion engines (ICE) to improve efficiency in the car manufacturing industry [121,122]. In 2020, Barakat et al. [123] analyzed the best configuration of gas turbines to replace conventional combustion engines in electric vehicles. The fuel saving values were between 8% and 23.6% compared to internal combustion engines [123]. Given the lack of information about biodiesel-based gas turbines, Rochelle and Najafi [124] researched cost of biodiesel, its thermophysical properties, combustion qualities, and applications in aviation and ground industries. They concluded that compared to gas turbines that worked with conventional fuels, biodiesel-fueled gas turbines at ground level had the lowest emissions, the same performance, and a little more consumed fuel. To increase the penetration of biodiesel-based gas turbines in overseas markets, some challenges, including the fuel cost, adapting gas turbines to biodiesel, and controlling engines at aviation conditions, should be addressed.

### **2.3.1 Micro-Gas Turbines (MGTs)**

Micro-gas turbines (MGTs) a class of small-scale gas turbines developed in the 1990s for combined heat and power applications, gained expanded commercialization after 2000 [125]. Their operational principles, design, and functionality are rooted in compact dimensions, minimal oscillation, and high combustion gas temperatures, making them particularly appealing for household-level applications [126]. Utilizing heat recovery boilers with micro-gas turbines facilitates the recovery of exhaust heat, enabling the generation of hot water for domestic use or heating purposes. Installing MGTs in a series configuration allows for the creation of larger

modular units with capacities surpassing 1,000 kW, making them suitable for meeting urban demands across [127]. The electrical and thermal efficiencies of micro-gas turbines range from 25-29% and 64-72%, respectively [128]. Another important factor that plays an important role in sizing CHP and micro-CHP sites is the power to heat ratio, which is between 0.5 and 0.8, depending on the size of the MGTs [129]. Implementing recuperators in conventional MGTs, a process involving preheating compressed air using turbine exhaust, decreases fuel consumption during combustion, resulting in heightened overall efficiency [130]. Round-trip efficiency is a criterion of merit to find the best integration of energy processes involving hydrogen generation, transportation, storage, and power production. Escamilla et al. [131] specifically investigated the optimal level of this efficiency to minimize energy losses. Their findings revealed that through the utilization of gaseous state hydrogen storage systems, along with various methods of hydrogen production, including solid oxide, alkaline, and proton exchange membrane electrolysis, the round-trip efficiency reached 29%, 22.2%, and 21.8%, respectively. On the other hand, employing systems for hydrogen storage in both liquid and solid states resulted in the lowest round-trip efficiency. Notably, the highest round-trip efficiency (42%) was achieved by utilizing hydrogen-based micro-gas turbines [131]. Hosseinimaab and Tousei [132] achieved the optimized configuration of a micro-gas turbine utilizing a scaled-down version of the NASA CC3 compressor, resulting in a power output of 150 kW. Their modification led to a significant improvement in the engine's efficiency and the generated power by 13.93% and 11.07%, correspondingly, along with a 12.15% reduction in fuel consumption [132]. Ayaz et al. [133] measured the emission levels of a 100 kW micro-gas turbine by co-combustion of fuel blends and investigated their impacts on thermal and exergy efficiencies. They concluded that the lowest CO<sub>2</sub> (48.9%) and CO (50.12%) emissions were achieved if a mixture of half ammonia and half of natural gas is combusted in the burner. However, higher NO<sub>x</sub> emission was reported compared to 100% natural gas fueling. Although co-combustion of methanol or ammonia led to the reduced exergy destruction rates, the thermal and exergy efficiencies decreased because of the increased power loss. Thu et al. [134] analyzed a Capstone C65 ICHP micro-gas turbine with an electrical capacity of 65 kW for micro/mini-Combined Heat and Power (CHP) applications. Their investigation was based on power demands covering from part-load to full-load operations. They developed comprehensive thermodynamic models to assess the efficiency and exergy destruction rates, which showed that the combustor is responsible for almost 70% of the total exergy

destruction. They also showed that the system's first law efficiency varies from 15.7% at a 25% load to 28.95% for full load operation. Stathopoulos et al. [135] performed an analysis of a micro-gas turbine operated with steam injection in the gas combustion chamber and considered a building as a case study in Berlin, Germany. The authors developed a thermodynamic model of the proposed system similar to the conventional micro-gas turbines, but they put a steam generator between the recuperator and the heat consumer of the CHP plant in order to study its adaptation for wet operation (see Figure 7). Finally, they realized that the retrofitted turbine has some advantages compared to the gas turbines such as having higher electricity production, better operational functions, and being profitable for the German CHP market.

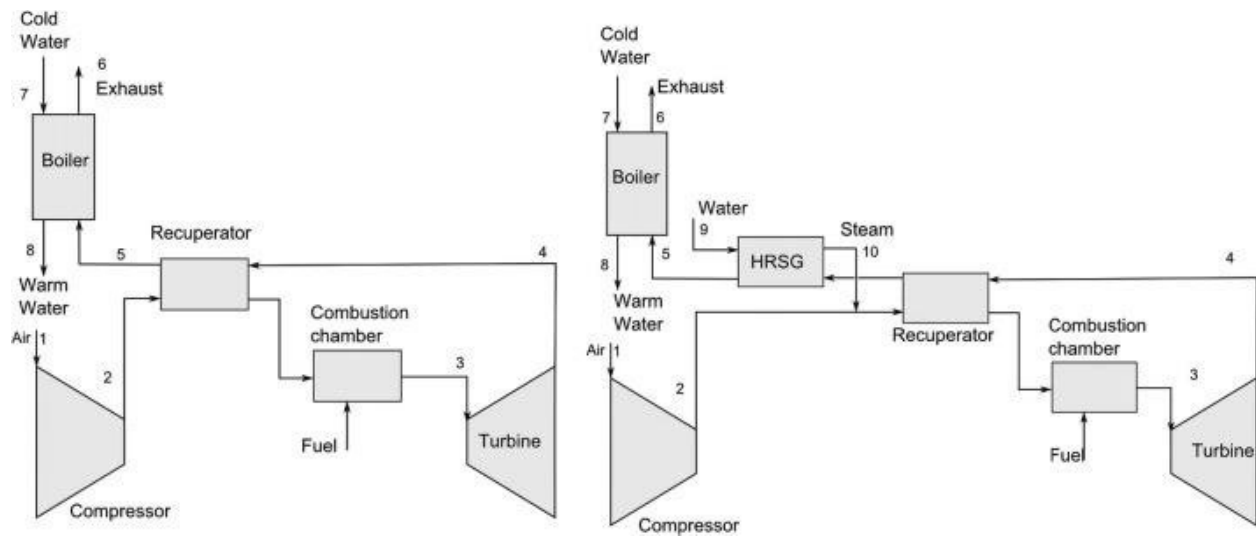


**Figure 7**-Schematic layout of the conventional (left) and the wet recuperated micro-gas turbines cycles [135].

For modeling micro-gas turbines, two important design parameters, namely atmospheric temperature and relative humidity, are needed. It can be shown that at the lowest ambient temperature and highest relative humidity, which is identified as the best condition, the generated power and electrical efficiency of micro-gas turbines reach their peak. This is due to the higher density of air that reduces power of the air compressor. Also the outlet enthalpy of incoming air to the recuperator increases with humidity, leading to the improvement of electricity and efficiency [136]. A novel prototype of a micro turbine system for domestic applications was experimented by Toit et al. [136] to calculate power output, electrical efficiency, and combustion emissions. The researchers analyzed three scenarios to evaluate the performance of the turbine. In the first one, they just considered 100% CH<sub>4</sub> (natural gas), while in the second scenario, they aimed to maintain

the outlet temperature (1050 K) the same as the first scenario while inserting 15% vol H<sub>2</sub>. In the third one, which was called as a biogas/H<sub>2</sub> scenario, they considered a fuel mixture of 20 vol% H<sub>2</sub>, 15 vol% CO<sub>2</sub>, and 65 vol% CH<sub>4</sub>. They found that in the second experiment, the CO emission was increased significantly due to the lowest combustion and turbine temperature. In contrast, NO<sub>x</sub> emission decreased because the main reason for its creation is high combustion and turbine temperature. As discussed earlier, increasing ambient temperature leads to the decrease in output power and the efficiency of MGTs. To overcome the mentioned problem, Lee et al. [137] studied the effects of injection water and steam into a micro-gas turbine on output power and efficiency (see **Figure 8**). Using hot water and steam generated in the same heat recovery unit produced more electricity, which was considered as a solution to minimize the performance penalty of the MGT at hot ambient conditions. They found that if water and steam were injected at the recuperator inlet, a higher efficiency and power generation were achieved compared to the injection both at the combustor. Also, using steam increased power and efficiency rather than using water in the same condition.

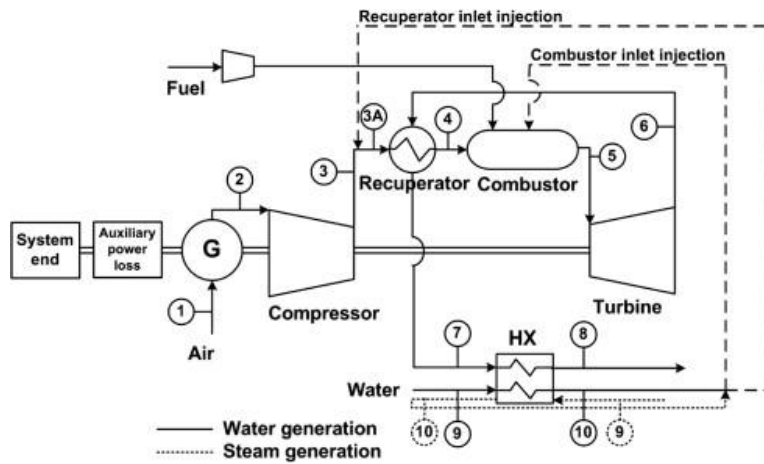


**Figure 8-** Schematic of the CHP system consisting of an MGT with the injection of hot water and steam [137].

Gimelli and Sannino [138] simulated a Capstone C30 as a micro-gas turbine combusted by biogas and used a multi-objective optimization to validate their results with experimental data. The selection of design parameters and objective functions were dependent on real data from the Capstone company. They showed that their dynamic model reproduced the data well despite some inconsistencies of the experimental results. A biogas-fueled cogeneration system, whose prime mover was a micro-gas turbine, was modeled based on an economic point of view [139]. The highest electrical efficiency was achieved based on the optimum combination of three kinds of

micro-gas turbines (MGT) with different power (30, 65,200 kW). The authors used the net present value (NPV) approach to distinguish which MGT was profitable, and they concluded that MGT-200 had the highest NPV because of the lowest investment cost and the highest power cost savings [139]. The function of two CHP systems whose aim was heating a biodigester was investigated at off-design conditions [140]. The first system comprised a series of commercial biogas-based MGT, and the second one included an ORC that used waste heat from the exhaust gas of MGT. The authors found that many parameters had effects on the economy of the system. If methane concentration in biogas and production changes take into consideration, 1200-kW class MGT has better performance although it has 2.3% less NPV instead of 1400-kW class MGT [140]. A Capstone C30 micro-gas turbine run by syngas was investigated experimentally and theoretically to improve the online identification approach from simple dynamic models [141]. They applied a second-order model that helped to have stable solutions and was able to reset parameters' values with changeable conditions [141]. The integration of a dual fluidized bed gasifier and a micro-gas turbine with 200 kW power was simulated (see **Figure 9**)[142].

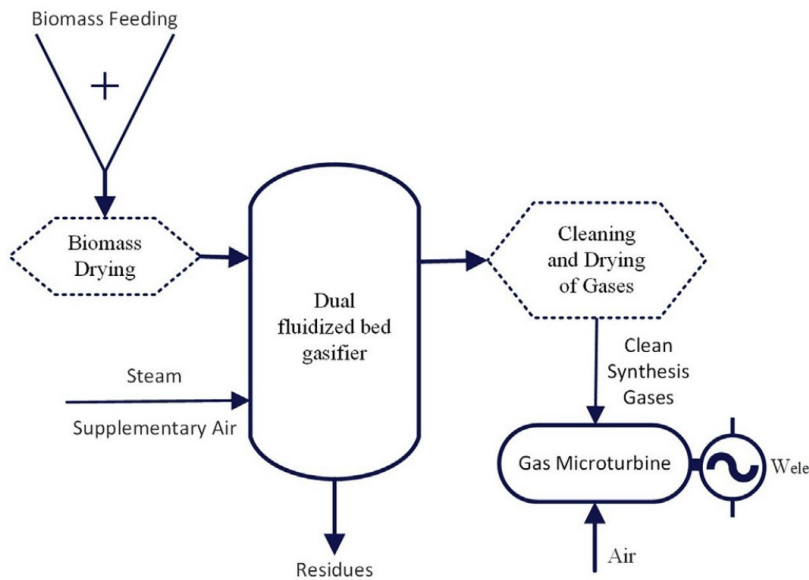


**Figure 9**-Schematic of a dual fluidized bed gasifier that runs a prime mover (micro-gas turbine) [142].

The generated power and overall efficiency were 44.85 kW and 13.42%, respectively. The outcomes indicated that the usage of solid biomass to generate gaseous fuels for feeding the MGT led to profitable operation, while being environmentally friendly, and achieving the highest resiliency [142]. Rasul et al. [143] analyzed the function of an anaerobic digester, where biogas

was produced, integrated with the micro-gas turbine. The authors illustrated that using micro-gas turbines with biogas instead of diesel generators was cost beneficial, and more environmentally friendly to meet power demand in agricultural applications [143]. When it comes to decentralized power stations or supplying electricity for remote areas, the usage of microgrids, that work at off-grid mode and islanding mode, is emphasized. A microgrid, whose prime mover is a micro-gas turbine with operation time above 25,000 h, shows high reliability. Because MGTs have high efficiency, stability, controllability, and low maintenance, they are suitable for microgrids, satisfying the demands, and increasing energy security [128,144].

### **2.3.2 Pollutant emissions from MGTs**

In the context of reducing pollutant emissions from micro-gas turbines, research efforts are directed toward controlling and reducing NO<sub>x</sub>, CO, and CO<sub>2</sub> concentrations. This is achieved by optimizing various intake conditions, including fuel-air ratio, flame temperature, intake humidity, combustion chamber temperature, and pressure [145]. Cong et al. [146] demonstrated that an increase in the intake aperture by 50% notably diminished NO<sub>x</sub> and CO concentrations to 9 ppm and 7 ppm, respectively. However, alterations in intake humidity appeared to exert a minimal impact on the levels of these pollutants. Additionally, research has demonstrated that incorporating hydrogen into the fuel mixture significantly reduces NO<sub>x</sub> emissions. This reduction is achieved through various methodologies, including lean-burn premixed combustion [147,148], optimized air distribution modes [149,150], and innovative designs in dilution holes [151,152]. These approaches contribute to a substantial decrease in gas temperatures and promote uniform distribution. Lu et al. [4] investigated the effect of air distribution on the reduction of pollutant emissions in a micro-gas turbine utilizing a blend of hydrogen and methane. The findings revealed that an increase in the proportion of premixed air enhances the extent of the recirculation zone and achieves a more homogeneous temperature distribution across the combustor. Remarkably, a premixed air ratio of 50% led to a significant decrease in NO<sub>x</sub> emissions, reaching 0.717 ppm, a substantial reduction from the peak of 23.46 ppm recorded at lower premixed air ratios (below 40%). Banihabib et al. [153] modified a 100-kW micro gas turbine to facilitate safe operation across a wide range of hydrogen concentrations (40% to 100%) while ensuring compliance with strict emission standards. The modifications included redesigning the combustor to handle hydrogen's high reactivity better, adjusting the fuel train to manage various hydrogen-methane

mixtures effectively, and enhancing the control system to maintain operational stability. These modifications resulted in a significant reduction in NO<sub>x</sub> emissions, as low as 22 ppm when operating on pure hydrogen, equivalent to 62 ppm at 15% O<sub>2</sub> in the exhaust, marking a substantial improvement in environmental performance. Xing et al. [154] proposed a novel modification of the micro-combustor design by integrating 40 jet-in-crossflow micro-mixing nozzles, each uniquely featuring tapered round outlets. This design aims to enhance the temperature distribution uniformity within the combustion field, mitigate NO<sub>x</sub> emissions, and effectively prevent hydrogen flashback occurrences. Through a comprehensive numerical analysis across a range of fuel temperatures, from 373 K to 573 K, the research revealed that lower fuel temperatures contribute to increased NO<sub>x</sub> emissions, a phenomenon attributed to the rise in local equivalence ratios. Dieter Bohn [155] examined the impact of burning biogas on the emissions of pollutants from a micro-gas turbine. The research investigated two control approaches, including keeping the turbine inlet temperature constant and maintaining a consistent energy input to the combustor. The study found that implementing a control system to stabilize the inlet temperature can effectively regulate NO<sub>x</sub> emissions for different biogas compositions. Additionally, modifying the air supply to maintain the optimal ratio of primary air to total air mass flow (31%) can prevent incomplete combustion and reduce the formation of NO<sub>x</sub> by avoiding excessively high local flame temperatures. Wang et al. [156] conducted a numerical analysis of a micro gas turbine swirl combustor to evaluate and compare the levels of NO<sub>x</sub> emissions produced by non-premixed flames when using two distinct fuels, including methane and ammonia, under a range of heat loads. Their findings revealed that despite methane having a higher flame temperature compared to NH<sub>3</sub>, the emissions of NO, N<sub>2</sub>O, and NO<sub>2</sub> from ammonia were significantly higher, with respective increases of 6.12, 161.05, and 2.89 times compared to those observed for methane under all tested conditions [156]. Zong et al. [157] reduced CO emissions to levels below the 40 ppmv threshold by an external combustion-air adjustment approach during partial load operations. However, this adjustment led to a significant increase in NO<sub>x</sub> emissions by 29.6% due to an extended combustion duration. To mitigate this issue, the researchers optimized the ratio of pilot fuel, reducing it from 9% to 8.2%. This adjustment significantly decreased NO<sub>x</sub> emissions, achieving a record low of 21.3 ppmv at a 50% load capacity. Micro-gas turbines fueled by biogas with high CO<sub>2</sub> content may encounter issues with flame stabilization, leading to increased CO emissions. Therefore, it is crucial to treat the biogas to ensure it contains sufficient methane for stable and clean combustion. Additionally,

preheating the biogas before it enters the combustor can improve the performance and efficiency of micro-gas turbines. This preheating compensates for the cooling effect of pressurized biogas, maintaining higher gas temperatures that enhance combustion efficiency and reduce CO emissions [155]. A comparison between the performance of simple and recuperative gas turbines (50 MW) run by two types of fuels, namely hydrogen and natural gas, was conducted [158]. The researchers found that CO<sub>2</sub> emission was 46.27 tones-CO<sub>2</sub> h<sup>-1</sup> for a simple unit and 71.15 tones-CO<sub>2</sub> h<sup>-1</sup> for a recuperative gas turbine system by using natural gas. On the contrary, by using hydrogen, the CO<sub>2</sub> emission tended to zero in the two kinds of turbines [158]. Using the optimal configurations of combustion chambers makes micro-gas turbines perform well and reach the lowest pollution. Adamou et al. [159] considered three essential criteria, including conical shape, swirling motion, and tubular configuration, to design a combustion chamber and reached a 20% improvement of fuel-air mixing and significant reductions of CO and NO<sub>x</sub> emissions by 40%, and 75%, respectively. They concluded that having a conical shape with a swirling pattern enhances the quality of fuel-air mixing, reduces the peak flame temperature, stabilizes flame, and develops combustion efficiency, even at various operating conditions and fuel blends. Also, the tubular combustor insulated thermally allowed the combustor walls to cool effectively [159].

Industrial gas turbine developers have invested heavily in dry low-emission (DLE) technologies to reduce NO<sub>x</sub> and CO emissions to comply with environmental regulations, which restrict such pollutants to 10 to 25 ppm. In the process of developing engines, it is traditionally necessary to conduct numerous tests on rigs and engines to ensure the emissions of pollutants stay within acceptable limits. These tests can often be complex and carry a high cost. Therefore, the development of dependable methods for predicting the levels of NO<sub>x</sub> and CO emissions in specific setups with a satisfactory degree of precision is a critical technical challenge within the field of gas turbine research [160]. Approaches to predicting pollutants from combustion processes can essentially be divided into three main categories: empirical (or semi-empirical) methods, physics-based frameworks, and high-fidelity simulations. In empirical strategies, correlations are initially suggested based on the operational conditions of the combustor. These correlations are later refined to suit specific combustion chamber designs through experimental research. A significant limitation of the empirical approach is its high dependency on specific problem contexts; the correlations yield accurate predictions for certain combustors under conditions but must be adjusted for application to different combustion systems [83]. A highly regarded substitute for

empirical methodologies is the Equivalent Chemical Reactor Network (ECRN) approach for modeling. This approach uses a conceptual framework of perfectly mixed chemical reactors to simulate the flow field within a combustor. To achieve this, the combustor is divided into numerous reactors based on the results from combustion analysis. The pathways connecting these reactors are then outlined, which helps to accurately analyze the generation of pollutants through comprehensive reaction kinetics [161]. CHEMKIN is a software tool that enhances the understanding of combustion mechanisms and pollutant formation by accurately computing the production rates of chemical species within computational cells defined by the ECRN approach. Its ability to visualize reaction mechanisms and examine the formation and destruction of pollutants, such as NO<sub>x</sub> emissions, is vital for investigating instantaneous chemical kinetics and comprehending the complex reactions of combustion phenomena. This, in turn, improves the accuracy of predictions related to combustion phasing control and emission reduction. Also, by allowing for a detailed analysis of key species destruction pathways, CHEMKIN provides insights into reaction dynamics that are difficult to achieve with conventional Computational Fluid Dynamics (CFD) models alone [162]. Mashruk et al. [163] conducted a detailed study on the effects of fuel blends and operational parameters on NO<sub>x</sub> emissions from premixed ammonia/hydrogen/air-swirling flames. Their innovative strategy involved modifying the burner geometry and optimizing fuel injection, utilizing both their ECRN model in Chemkin-Pro and experimental methods with a tangential swirl burner to improve mixing and stabilize the flame. The findings revealed a peak in NO emissions at an equivalence ratio of 0.8, while leaner conditions ( $\Phi \leq 0.65$ ) led to increased N<sub>2</sub>O emissions due to lower flame temperatures. Ultimately, the research highlighted an optimal equivalence ratio range between 1.05 and 1.2 for minimizing NO<sub>x</sub> emissions.

## **2.4 Internal combustion engine (ICE)**

High efficiency and flexibility can be achieved by cogeneration systems based on biomass gasification [164]. Conducting exergy analysis leads to identifying the benefit of a CHP installation and the produced energy quality, as Rovas et al. [165] pointed out. They considered a gasification-based small cogeneration system (SMART-CHP), coupled with the ICE system, and run by biomass fuels (olive oil, grape, and peach waste). Their aim was the evaluation of the whole system thermodynamically by using a tool for exergy efficiency that resulted in focusing on the

ICE where the highest exergy losses occurred [165]. The effects of using hydrogen as a fuel on the function of ICE have been studied recently. Applying renewable fuels, including hydrogen, and alcohol in dual injection engines, needs modern combustion systems that optimize the size of ICEs [166]. The maximum flammability, and flame velocity, with the minimum ignition energy of hydrogen increase the threshold of fuel to air ratio to avoid engine misfires. However, alcohol with the highest vapor enthalpy, and number of octanes causes fuel to burn steadily, and decreases the knock significantly. Also, direct injection of renewable fuels prevents the flashback risk and makes full use of the volume of cylinder resulting in improved power and torque [166]. In 2020, Jimenez et al. [167] considered two different scenarios based on various control strategies for monitoring the hydrogen inserted into ICE. The first one was based on applying the engine electronic control, and the last one corresponded to model predictive control. Both scenarios proved that by using the mentioned-control strategies, the combustion and thermal efficiencies were increased by 1.2%, and 18.1%, concurrently because of burning carbon-free burnable fuel ( $H_2$ ) compared to pure gasoline [167]. The use of alternative and environmentally friendly fuels such as alcohol reduces the  $CO_2$  emissions resulting from using gasoline [168]. To address pollution issues, a review of using fusel oil, which is popular in alcohol family, in ICE was conducted. Implementing fusel oil with a high-octane number in the spark ignition engine increases compression ratios, resulting in the reduction of emissions. Thanks to water as one of the fuel's substances, the reduction of  $NO_x$  and soot emissions are seen simultaneously [168]. Yildiz et al. [169] published the experimental and theoretical results of applying two fuels-based ICE manufactured in Mitsubishi Fuso with power 96 kW and rotational speed 3200 rpm. Their results demonstrated that the lowest and highest  $CO_2$  emissions were related to burning ICE with diesel, and biodiesel, respectively. They suggested that by integrating the biodiesel-based engine with diesel particle filter made by silicon carbide, the exhaust gas pollutions, and exergy destruction rates would be reduced. However, equipping the treatment system with the engine combusted by diesel led to the increment of exergy destruction rates, and  $CO_2$  emissions. Achieving the optimum configuration of ICE (EF7), whose duty was providing heating, cooling, and power with the lowest fuel consumption and emissions was investigated by Sheykhi et al. [170].

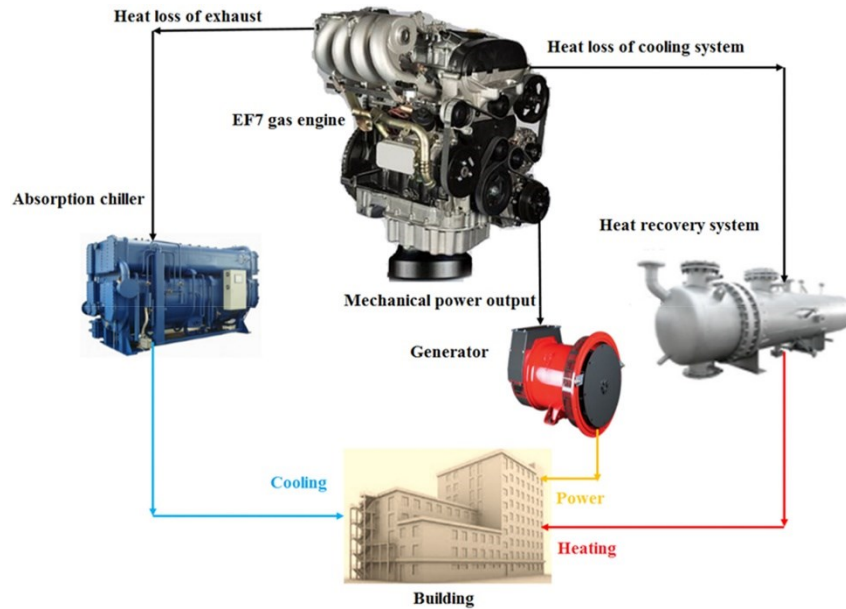


**Figure 10-**EF7 as one type of ICE to meet demand loads [170].

They considered some important parameters, including combustion start angle, combustion duration, compression ratio, and rotational speed, that had not been studied before. They found the location of the piston at its highest stroke as the top dead center (TDC) and concluded that for meeting power and heating demands, combustion occurred  $20^\circ$  and  $50^\circ$  before TDC, respectively, which led to consuming the lowest fuels [170]. Experiments on a  $20 \text{ kW}_{el}$  micro-cogeneration unit based on a wide-spread automotive gas ICE were conducted by Capaldi [171]. The author proposed a specific design, including small displacement and high boosted engine, which led to the improvement of engine efficiency, especially at part load, and finally, at full load, a global efficiency of 36.6% was achieved. Towoju and Ishola [172] compared electric and internal combustion engine cars run by gasoline and diesel based on the life cycle assessment. They proved that compared to ICE-based engines, electrical engines had negative effects on people's health because of battery disposal. Also, considering the emission of generated electricity puts electric vehicles in a worse place based on the  $\text{CO}_2$  emissions per kilometer. They suggested that by using synthetic fuels for running conventional internal combustion engines, the environmental impact of the transportation sector could diminish [172]. A Rankine cycle was proposed to recover waste heat from a turbocharged diesel engine of a combined cycle [173]. The results illustrated that using the heat recovery system improved the output power by 12% at  $80 \text{ kW}/2590 \text{ rpm}$  as the diesel engine's operational condition. Some numerical research has recently been conducted to improve

the efficiency of ICE despite it being a well-established technology. Experimental development of a 15 kW micro-CHP system with a reciprocating engine run by liquefied petroleum gas (LPG) was done by Muccillo et al. [174]. The authors also did a one-dimensional thermo-fluid dynamics model and an energetic analysis of the engine to understand the micro-CHP function entirely. As the recovered heat was completely dependent on thermal demand, different sectors were considered: residential, hospitals, offices, commercial and sports facilities, and hotels [174].

Having reliable, durable, and green ICE systems require upgrading the lubrication systems and the quality of fuels. Baskov et al. [175] found that if they used new approaches to improve the ICEs function, the thermophysical properties and the consumption of fuels would improve, resulting in higher power and efficiency [175]. As discussed earlier, reducing greenhouse gas emissions caused by using ICEs in the transportation sectors should be in the focus. According to research by Leach et al. [176], the best American spark ignition engines could mitigate fuel consumption by 14%, and by their developments, the value could go to 30%. Although some efforts have been made to eliminate ICE vehicles, the authors pointed out for long distance transport it would not be economical and feasible to apply electric engines. They recommended that if IC engines were run by renewable fuels and equipped with electrical storage where extra power was stored, the need to ban the sale of internal combustion engine vehicles (ICEV) would be decreased significantly [176]. Another solution to address pollutions is applying syngas for powering ICEs. A review of some experimental and theoretical studies related to using syngas in different kinds of ICEs such as dual-fuel compression ignition engines, homogeneous charge spark ignition engines, and direct injection spark ignition engines has been conducted [112]. In the review, the authors analyzed the function of the machinery mentioned above in detail and proved how sensitive they were when it came to changing syngas' thermophysical properties, including its density or the concentrations of hydrogen [112]. The performance of internal combustion engines, powered by pure hydrogen produced through dual-fired downdraft gasification, was investigated [177]. One of the key findings was a reduction in the engine's power output to 18% when using pure hydrogen instead of natural gas, which is a form of derating. The amount of CO emission from the hydrogen-fueled ICE was the same as natural gas engines, but the recorded value of NO<sub>x</sub> level (1.07 g kWh<sup>-1</sup>) proved that the hydrogen-based ICE was more environmentally friendly compared to diesel engines and those run by gas produced by air gasification [177]. A hybrid-CHP system consisting of an internal combustion engine (ICE) and a Stirling engine (SE) was modeled mathematically

and used for meeting the load demands of a building [178]. The authors studied two scenarios; the first one was based on considering just the main prime mover (ICE), and the second one corresponding to the combination of ICE and SE. The outcomes indicated that the second scenario had better performance from a thermodynamic, environmental, and economic point of view. They showed that at the maximum rotational speed of the hybrid system (3500 rpm), the thermal efficiency had its maximum value (38%), and the payback period was reduced from 10.5 to 7.5 years compared to the ICE alone [178]. For many years, engineers have used the diversity of mathematical models, experimental data, and optimization methods to investigate the function of ICEs and their behavior at off-design conditions. None of them has succeeded in finding a comprehensive mathematical model for ICE, which motivated Salam et al. [179] to write a review of different experimental, CFD, empirical, numerical, and optimization methods and the integration of all of them to achieve the unique algorithm.

Zheng et al. [180] simulated the micro-CHP system based on ICE and used TRNSYS, for which they developed a new modeling component. The model was validated by the experimental data at steady condition and start-up, cool-down, and overheat protection controls as dynamic processes. The validation results indicated that the dynamic model well predicted the output power and overall efficiency of the proposed system during dynamic processes. For modeling and choosing a CHP unit based on an internal combustion engine, a general method was proposed by Arbabi et al. [181]. After conducting a numerical analysis, they could calculate the generated power, recovered heat, and overall efficiency. Also, they showed that having some smaller engines in parallel has some advantages compared to a single large engine. Using the former led to a longer operation at full load and improved reliability. The integration of ICE with a Rankine cycle to generate the required power for running a desalination plant, where fresh water was produced, was studied based on thermodynamic points of view [182]. The authors compared two scenarios based on different fuels, including fossil diesel (D95B5) and biodiesel (B100). They concluded that if the former fuel ran an ICE, the exergy efficiency of the whole system was 6.9%, and the second scenario led to 6.7% exergy efficiency. Also, ICE was the worse component because of its highest exergy destruction rate that was 44.1% and 45.4% for the first and second scenarios, respectively [182]. Zhu et al. [183] simulated ICE fueled by hydrogen using a CFD model. They inserted extra hydrogen into the ICE and discovered that surplus hydrogen led to safe combustion, which resulted in more generated power [183]. A parametric study of the hybrid system, whose power was 5 kW

and components were solid oxide fuel cell (SOFC), homogeneous charge compression ignition (HCCI is one kind of ICEs), control systems, and other equipment was conducted [184]. The researchers used the available experimental data of HCCI and simulated the rest of the components through MATLAB to distinguish which design parameters fulfilled their requirements. The researchers adjusted three key control parameters, including the fuel utilization factor of the SOFC, the equivalence ratio of the ICE, and the ratio of bypassed gas to achieve the highest performance and reliability and the lowest emissions (<1 ppm). They found that keeping the bypassed gas ratio at its lowest (0.0) and the equivalence ratio at 0.75, with the optimum level of utilization factor at 0.7, resulted in a good balance between stability and efficiency, leading to the highest efficiency of 59.0% [184].

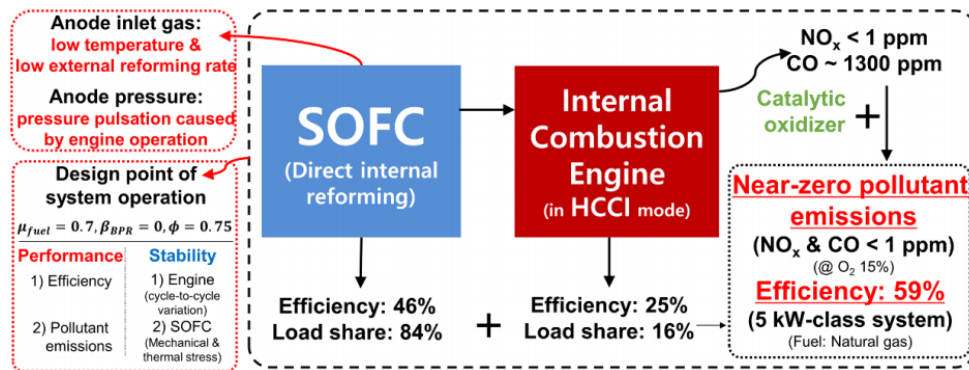


Figure 11-The results of the hybrid system at optimum design parameters [184].

## 2.5 Fuel cell

Fuel cells, as one of the most innovative technologies, provide the lowest environmental emissions, resulting in no regular carbon emission control. They have reliable functions against load fluctuations, start rapidly, and have compact sizes with low weight, making their installation easier [2]. Their exceptional electrical efficiency results in a notably low heat-to-power ratio, making them well-suited for domestic application. However, their penetration is restricted by substantial initial capital investment requirements [185,186]. They are noiseless due to the lack of moving parts, demonstrating a shorter lifespan compared to that of micro-gas turbines [2]. A diverse range of fuel cell types exists, categorized by electrolyte composition (polymer membrane, KOH, H<sub>3</sub>PO<sub>4</sub>), operating conditions, electrode materials (Carbon, graphite, ceramic, stainless steel), catalysts (Pt, Ni, CaTiO<sub>3</sub>), charge carriers, and fuels (H<sub>2</sub>, syngas, methane) [187]. Five kinds of fuel cells have been used for CHP applications, namely PEMFC (proton exchange membrane fuel

cells), SOFC (solid oxide fuel cells), MCFC (molten carbonate fuel cell), PAFC (phosphoric acid fuel cells), and AFC (alkaline fuel cells) [185]. In the aviation and aerospace segments, fuel cells are superior. Switching from MGTs to fuel cells in auxiliary power units (APU) decreases NO<sub>x</sub> emissions (80%) and the fuel consumption throughout both cruise (40%) and stationary (75%) and makes overhaul of aircraft engines easier. Amongst fuel cells, SOFC has the highest operating temperatures, leading to the highest performance of aircraft; however, it is extremely heavy. In addition, NASA proposed PEMFC, and AFC as electrical suppliers for space shuttles because they can meet peak demands without regular charging [94]

### **2.5.1 Proton Exchange Membrane Fuel Cell (PEMFC)**

Among the various fuel cell types utilized in CHP applications, proton exchange membrane (PEM) fuel cells stand out for their suitability in meeting urban energy demands. When using water or mineral acid electrolytes, these fuel cells exhibit remarkable operational efficiency, enabling them to perform optimally within the temperature range of 100 °C to 200 °C [188]. In 2018, 300,000 small cogeneration systems consisting of PEM fuel cells with a nominal capacity of 0.3 to 1 kW were installed in Japan to provide electricity, heat, and hot water for domestic demands. From 2016 to 2021, thermodynamic and environmental investigations on 2800 micro-CHP systems based on fuel cells were conducted by ten European countries. They showed that fuel cells with 95% overall efficiency were more effective and environmentally friendly than heat pumps and combustion engines [1].

As the degradation of components leads to fuel cell malfunction, consistent maintenance and periodic shutdowns become necessary. Consequently, this diminishes both reliability and lifespan while concurrently increasing operational expenses. Efforts to design the optimum stacks and cool them to reduce their voltage degradation have addressed the mentioned issues [1]. In 2021, Chen et al. [189] proposed a degradation model that could estimate the thermodynamic and economic performance of the PEM fuel cell stack. At off-designed conditions, when the increment of current density improved efficiency and power generation, a growth of degradation rate was observed, leading to a 25.9% reduction in the lifetime of the PEM fuel cell. Also, the degradation enhanced fuel and maintenance costs of the system (23%). The improved current density required more fuel to be burned in the system, acting as a catalyst. The procedure accelerated the chemical reactions and led to increased damages and decreased availability and reliability [189]. So, by designing

optimal fuel cell stacks and properly cooling them to reduce voltage degradation, these issues can be effectively addressed [11]. Chen et al. [190–192] optimized three critical parameters in a PEM fuel cell, including power density, thermal efficiency, and exergy efficiency, using a combination of response surface methodology (RSM) and non-dominated ranking genetic algorithm (NSGA-II). They also analyzed these parameters under various operating conditions to achieve the optimal PEM fuel cell design. The results indicate that membrane thickness and anode stoichiometry ratio significantly enhance functionality. Specifically, equipping the cathode channel design with gradient sinusoidal-wave fins and optimizing the fins' geometry results in higher power density and a more uniform membrane current density compared to conventional structures.

A review of exergy analysis of the PEM fuel cells and the effects of design parameters on improving exergy efficiency was conducted, whose results are summarized in the following table [193].

**Table 2-**The impacts of critical parameters on exergy efficiency [193].

<b>Parameter</b>	<b>Exergy efficiency</b>	<b>Explanation</b>
Developed operating temperature	Increased	The increase of operating temperature causes the improvement of irreversible losses (activation, ohmic, and concentration overvoltage), which results in the decrease of actual voltage.
Improved operating pressure	Increased	The growth of operating pressure leads to the increase of pressure drop between two electrodes that increases the movement of ions in the membrane.
Logical improvement of air stoichiometry	Increased	Putting this parameter between 2 and 4 changes the performance of the system for the better.
Augmented current density	Increased	The current density should be improved to a reasonable level; otherwise, the system experiences parasitic loads.
Higher relative humidity	Decreased	The creation of obstruction in the membrane.
Lower relative humidity	Decreased	Membrane experiences dehumidification.
Enhanced membrane thickness	Decreased	The increase of ohmic overpotential is predicted because of the growth of resistance in the fuel cell.

A hybrid energy system was proposed by Zhao et al. [12]; they combined the system with a proton exchange membrane fuel cell and an organic Rankine cycle to recover waste heat produced from the PEM fuel cell (see **Figure 12**). They evaluated the proposed system by mathematical models

based on thermodynamic laws. They showed that by using ORC and the mentioned fuel cell, the electrical efficiency of the hybrid system could be improved by 5% in comparison with the single PEM fuel cell stack without ORC. The PEM fuel cell electrical efficiency and overall electrical efficiency were also reduced at a high fuel flow rate [12].

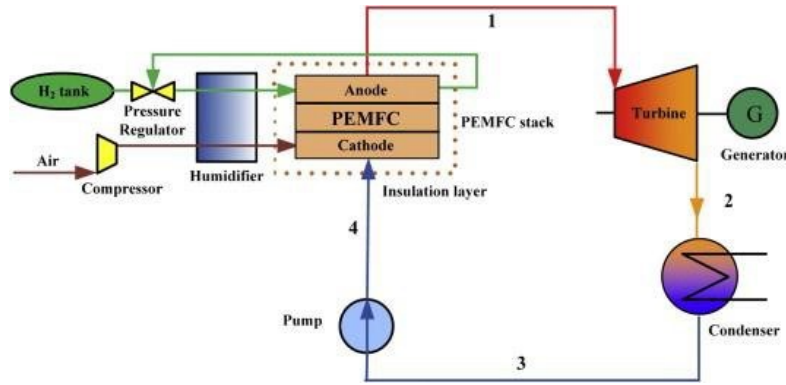


**Figure 12**-The schematic diagram of a hybrid power system, including ORC and PEM fuel cell [12].

Montazerinejad et al. [11] provided better insight into the performance of PEM fuel cells by applying advanced exergy analysis. They proved that the PEM fuel cell stack experienced the lowest exergy efficiency because of its highest irreversibility. Its highest endogenous (360.3 kW) made it more reliable even in the fluctuations, and it did not need regular maintenance or any improvements in its structure. Al-Nimr et al. [194] studied the behavior of the cogeneration system consisting of two subsystems; the first one was comprised of an ORC, whose main component was a concentrated photovoltaic/thermal (CPV/T) system, and the second one, which was called as a storage unit, included a PEMFC and an electrolyzer. The PEM fuel cell was run by hydrogen stored in a storage tank and generated from a water electrolyzer powered by output electricity from the ORC. Their parametric study concluded that improved overall efficiency was related to the increase of the turbine inlet temperature. The combination of PEM fuel cell and electrolyzer improved whole system's electrical efficiency (15.72%-17.78%). The block diagram of the consideration generated power technology is shown in **Figure 13** [194].

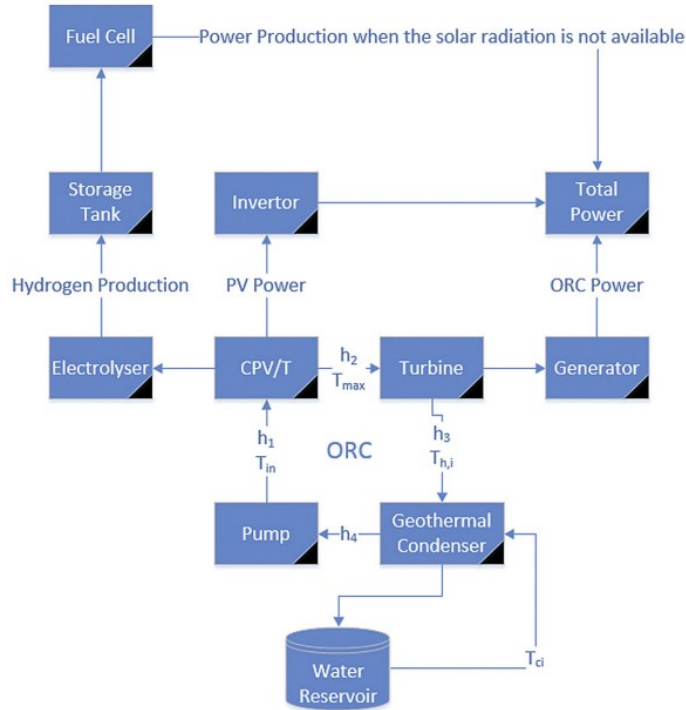


**Figure 13**-The block diagram of the ORC integrated with a PEM fuel cell [194].

Liu et al. [195] considered a novel proton exchange membrane fuel cell (PEMFC) system, and they studied the effect of inlet temperature of the PEMFC, saturation pressure, the current density, superheat temperature, and the ORC's working fluid on the performance of the system. Their results indicate that if the stack inlet temperature was 343.15 K, the optimum performance of the system indicators was reached. Among five organic working fluids investigated for the designed ORC system, R245fa had the best performance. From the exergy point of view, the PEMFC stack has the largest exergy loss in the system. Taner [196] presented the performance of a PEM fuel cell in terms of its voltage and pressure as important parameters. The author analyzed an open cathodic plate fuel cell and measured PEM fuel cell efficiency in terms of operating pressure and voltage parameters. They calculated 47.6% and 50.4% for the energy and exergy efficiencies of the PEM fuel cell, respectively.

### 2.5.2 Alkaline and molten carbonate fuel cell (AFC and MCFC)

Verhaert et al. [197] analyzed an alkaline fuel cell used for small-scale CHP, as illustrated in **Figure 14**, and did a sensitivity study on component performance. They found that the improvement of the inverter led to higher performance, and the reduction of cost resulted in choosing regular pumps and fans. The author optimized the water management and energy

performance of the proposed system based on a control strategy to compare its part load behavior to other micro-CHP technologies. According to the increase of electricity demand and decrease of heat demand, a fuel cell-based micro-CHP was the best option compared to other devices. AFC systems had better performance compared to the PEMFC system [197].

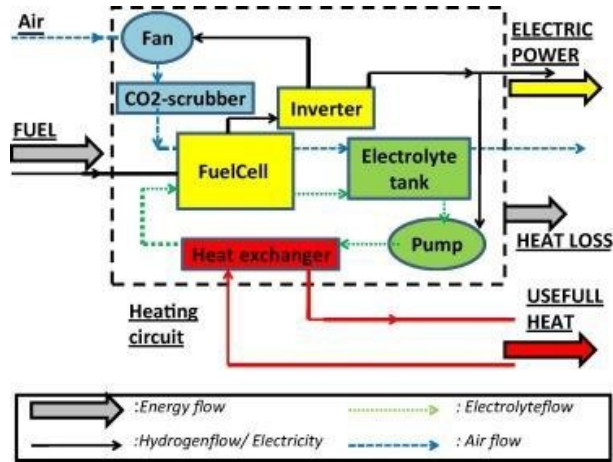


Figure 14- Schematic of the AFC-based CHP system [197].

A cogeneration system consisting of a molten carbonate fuel cell (MCFC) fed by a gasifier and other components was modeled based on the 3E evaluation comprising energy, exergy, and environment [198]. **Figure 15** depicts three sub-models in the cogeneration system, with an MCFC that meets energy needs and powers additional system components [198]. They used an exergy analysis to show that the gasifier (12.89%) and the fuel cell (7.61%) had the highest exergy destruction rates that were rooted in having considerable irreversibility. The authors accomplished a parametric study based on the variation of design parameters, i.e. augmenting the current density caused the decrease of energy and exergy for all categorized models. The output power of the fuel cell reached a maximum of 314.9 kW [198].

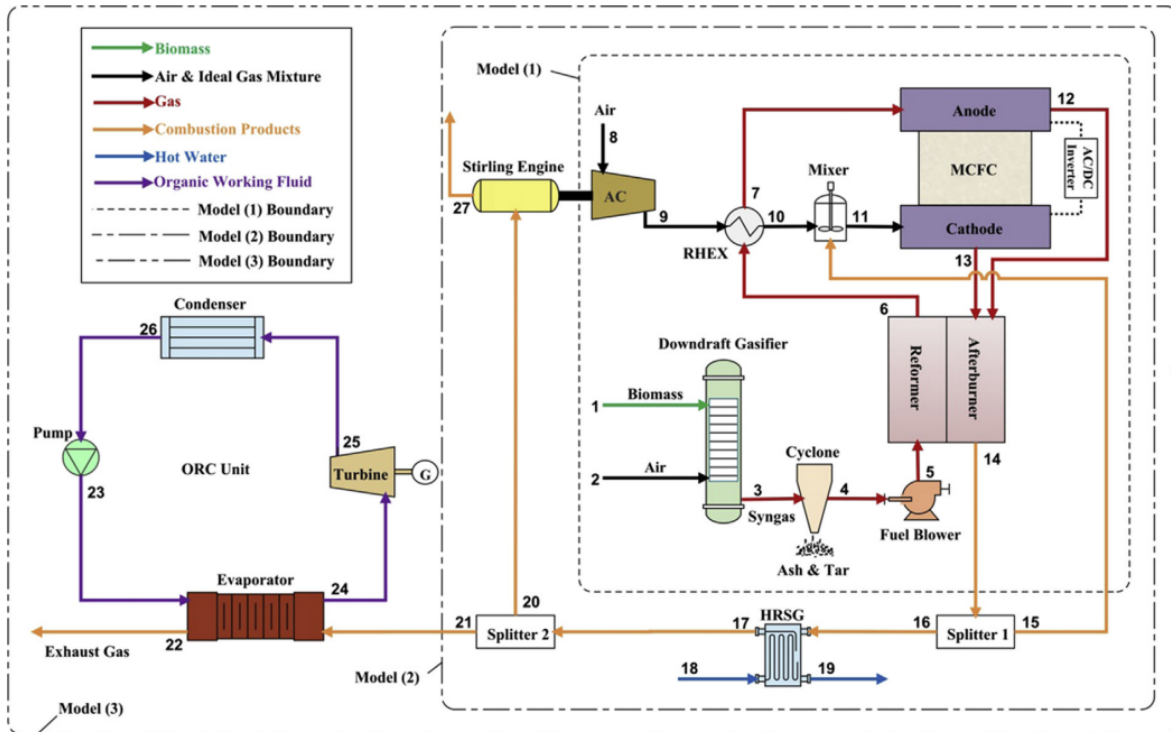


Figure 15- Schematic of a cogeneration system, with an MCFC [198].

Mamaghani et al. [199] carried out a 4E analysis, including comprehensive energetic, exergetic, economic, and environmental parts, by using mathematical models of a hybrid power system comprised of ORC and MCFC-GT (molten carbonate fuel cell-gas turbine). They considered total exergetic efficiency and total cost rate as objective functions for multi-objective optimization and tried to maintain the former one at high levels and minimize the latter one. By finding the Pareto front optimum solutions, they concluded that exergetic efficiency was 35.6%, 44.3%, and 54.9% for the fuel cell system, ORC cycle, and the combination of both. They performed a sensitivity analysis to see the effects of the fuel unit cost and the interest rate on the Pareto optimal solutions, which led to gaining two important results. The first one was increasing the total cost rate (3%) at the increase of fuel unit cost (25%), and the second one was moving the Pareto front curve to the zones with higher exergetic efficiency and total cost rate [199].

### 2.5.3 Solid oxide fuel cell (SOFC)

In reference [200], a new cogeneration system was proposed to meet urban energy needs. The system utilized a solid oxide fuel cell (SOFC), a GT, two organic Rankine cycle (ORC) turbines, and a liquefied natural gas (LNG) turbine to generate electrical power. Additionally, a LNG heat

exchanger was used to provide cooling. The system's design was based on powering the top ORC by recovering waste heat from SOFC-GT and operating the bottom ORC by conducting convection between organic fluid (Ethane) and the LNG stream. The highest exergy efficiency and lowest cost were achieved by applying multi-objective optimization, resulting in a total exergy efficiency of 51.6%, a cooling capacity of 567 kW, and a total generated electricity of 1040 kW. The authors pointed out that the proposed system was more economical than a sole SOFC because the Levelized cost of the former was 73.9% lower than that of the latter system [200]. Zeng et al. [201] proposed a micro-CHP system consisting of a flame fuel cell (FFC) whose advantages were the fast start, no sealing, and simple thermal management through a fuel-rich flame. In the biogas FFC reactor, a porous media burner with two layers and a micro-tubular SOFC were considered. The highest value of electricity was obtained for a single tubular fuel cell, and it was 1.4 W [201]. To meet the power and heating demands of domestic users, a small-scale SOFC whose electrical power was 5 kW integrated with a ZEBRA-type battery was considered (see **Figure 16**). In some circumstances where output heat from SOFC was sufficient, the extra heat was stored in the thermal energy storage (TES), and the auxiliary boiler (AUX) was shut down. The same logic control was used for a trade-off between the SOFC, ZEBRA system, and the external electric grid [202].

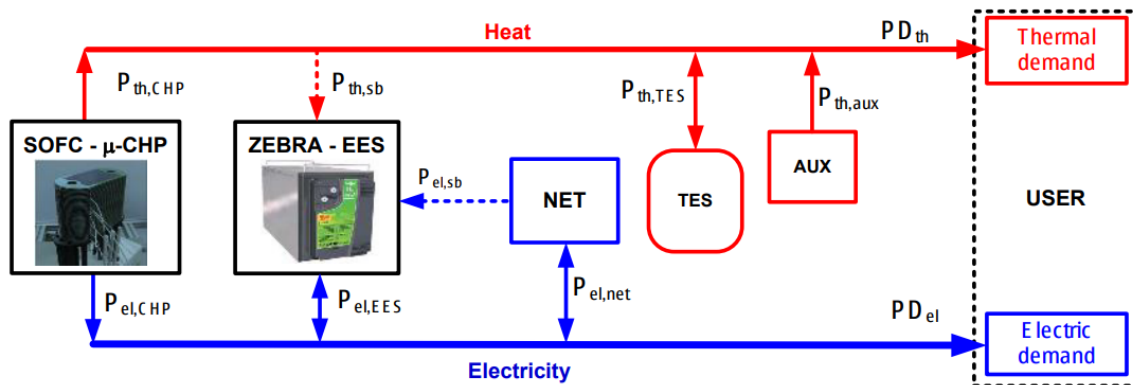


**Figure 16**-The cooperation between a micro-SOFC and other auxiliary equipment to meet load demands [202].

The above configuration helped the SOFC operate at a constant load, resulting in improved reliability and decreased operational costs. Some experimental test regarding the comparison between the mentioned prime mover with other available technologies was obtained which led to emphasizing the usage of micro-SOFC. The authors concluded that by keeping the considered micro-CHP system, the primary energy saving was around 1000 kWh/year per installed kW, and

it was profitable compared to non-CHP systems [202]. The integration of two 60-cell stacks of SOFC for the micro-CHP system was analyzed by Kupecki et al. [203] numerically and experimentally. The system was run by biogas. The authors validated their mathematical results by modeling all components with experimental ones, resulting in a reasonable agreement. Putting two fuel cells in series caused the increase of electrical efficiency, and the overall efficiency was obtained around 85% [203]. Ghorbani et al. [204] modeled a system comprised of a SOFC and a gas turbine through MATLAB to calculate some important parameters such as the electrical efficiency (61.4%) and generated power from the SOFC stack (1698 kW). To increase the overall efficiency, they used an ORC, where the waste gases of SOFC-GT were recovered by conducting heat transfer to R407C as a working fluid to produce more power. The system achieved its best function by implementing multi-objective optimization. This resulted in reaching maximum exergy efficiency and minimizing costs and pollution. As a result, the overall energy (electrical and thermal) and exergy efficiencies were 49.42% and 46.83%, respectively [204]. Mojaver et al. [205] identified a solid oxide fuel cell as the main part of the cogeneration system that supplied hot domestic water and electricity for consumers. The authors were concerned about the environmental issues of the cogeneration system, which motivated them to focus on current density, whose growth caused the reduction of CO<sub>2</sub> emission. Also, the highest electrical exergy efficiency (43.01%) and the lowest CO<sub>2</sub> emission (213.6 kg/MW.h) were obtained at desirable current density (0.78 A cm<sup>-2</sup>) by using multi-objective optimization [205]. Soleymani et al. [206] used the waste heat of cogeneration system consisting of gas turbine and solid oxide fuel cell (SOFC-GT) to produce hydrogen through the biogas reforming cycle. By conducting the thermodynamic simulation, the authors revealed that the net electricity, hydrogen rate, energetic, and exergetic efficiency were 2726 kW, 0.07453 kg s<sup>-1</sup>, 64.47%, and 64.65%, respectively [206]. In a study by Longo et al. [207], a detailed analysis was conducted on a micro-CHP system comprising two series of solid oxide fuel cells (SOFC). The anode and cathode materials used in the system were nickel and lanthanum, respectively, integrated with cold and hot boxes and casing. The researchers calculated the mass composition of each element used in the 2.5 kW micro-CHP system. They found that the highest percentage in each stack belonged to cells (34.13%), whose electrolyte (0.14%) and interconnect (82.49%) had the lowest and highest mass portions compared to other sections [207]. After comparing different prime movers such as micro-gas turbines, fuel cells, and combustion engines based on critical criteria such as reliability, sustainability, etc., Bia

and Jermittiparsert [208] selected an environmentally friendly fuel cell for supplying heat and electricity for residential buildings in Yazd, Iran. They proposed a new method called the Developed version of Pathfinder Optimizer (DPF) to achieve the most reliable and best design of the CHP system whose productivity was not affected by yearly cost-saving. They proved that the proposed algorithm could have a lower carbon footprint than the previous approaches [208]. Although most studies have been focused on fuel cells' function, a few attempts have been made to introduce new methods for CO<sub>2</sub> capture of the diversity of fuel cells such as SOFC and MCFC. In 2020, a comprehensive study based on introducing this technology, new approaches to gain CO<sub>2</sub>, and the comparison between all kinds of fuel cells from economic, technological, and environmental points of view, was conducted [209]. One of the promising results proved that the SOFC system equipped with CO<sub>2</sub> capture technology would have almost zero CO<sub>2</sub> emission. According to **Figure 17**, the left side indicated the general procedure inside the SOFC by following the combustion phenomena in the baffle board. On the contrary, by inserting steam that separated two outlet gas streams from the cathode and anode, the CO<sub>2</sub> capture happened even though the combustion occurred [209].

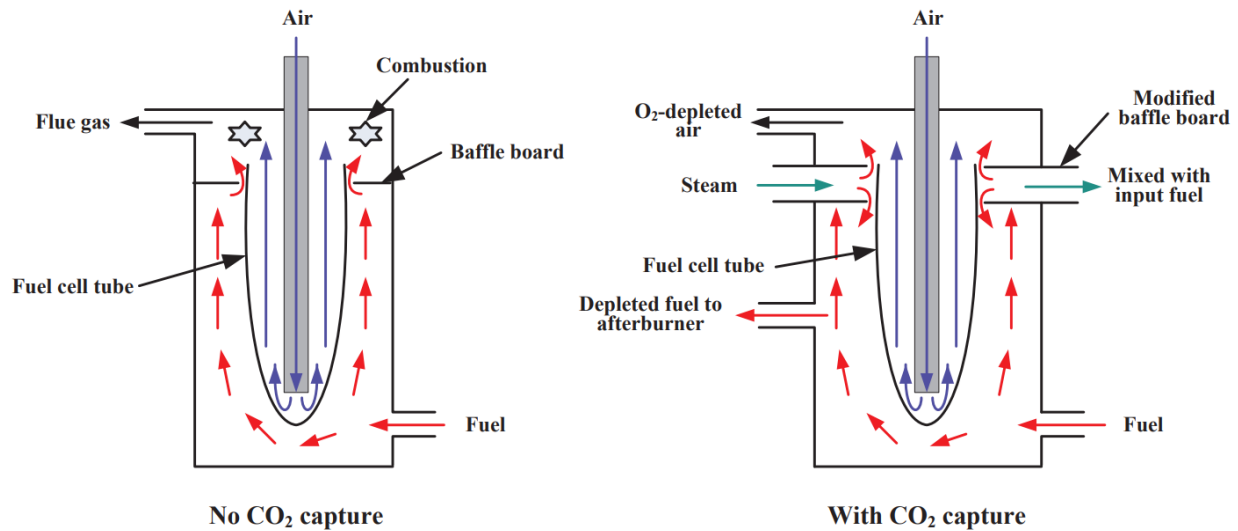


**Figure 17**-The overview of the function of SOFC with (left part) and without (right part) CO<sub>2</sub> capture [209].

## 2.6 Organic and steam Rankine cycle

Focusing on the decrement in burning fuels and increment of energy production has motivated scientists to upgrade the conventional energy systems or design novel structures that are more environmentally friendly [210]. For two centuries, steam Rankine cycles, where water as a working fluid has two states, saturated vapor, and saturated liquid through boiler and condenser, respectively, were used until Rankine cycles worked with renewable energy [211]. **Figure 18** indicates the category of the vapor power systems [211].

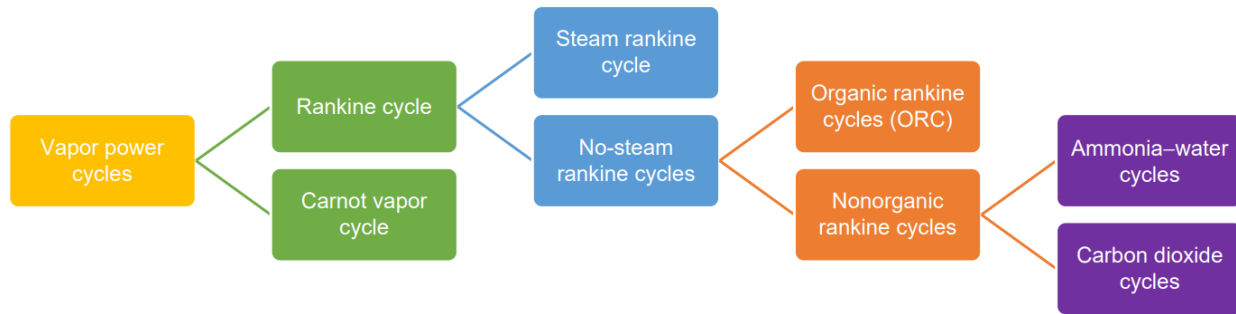


**Figure 18**-The classification of power systems based on their working fluid [211].

The ORC is a sustainable and clean system whose electrical power output ranges from 140 kW<sub>el</sub> to 2500 kW<sub>el</sub> and can be supplied through waste heat recovery. It works at low temperatures and can be integrated with diverse energy systems, namely solar energy [212], geothermal energy, biomass, and industrial waste heat [213]. Some benefits of the mentioned technology would be automatic operation, low maintenance, independent and low-risk operation, and flexibility [214]. The main reason that engineers switched from steam Rankine cycles (SRCs) to ORCs is the working conditions on which they operate. The first one operates at high temperatures, whereas the second technology has a good trade-off with low- and mid-temperature waste heat systems [215]. The trend of ORC's capacity from 1984 to 2016 is illustrated in **Figure 19**. At the beginning of the 21<sup>st</sup> century, the power capacity of ORC reached a peak of 30 MW, and in the next ten years, it went down almost by 83.33%, then it leveled off. During that same period, a total of 328 biomass-based ORCs were installed. Among them, 132 ORCs were powered by geothermal energy and had an electrical capacity of 2503 MW. Additionally, 170 ORCs were supplied by waste heat recovery with a capacity of 416 MW, and 8 ORCs were solar-powered with a capacity of 400 kW [216].

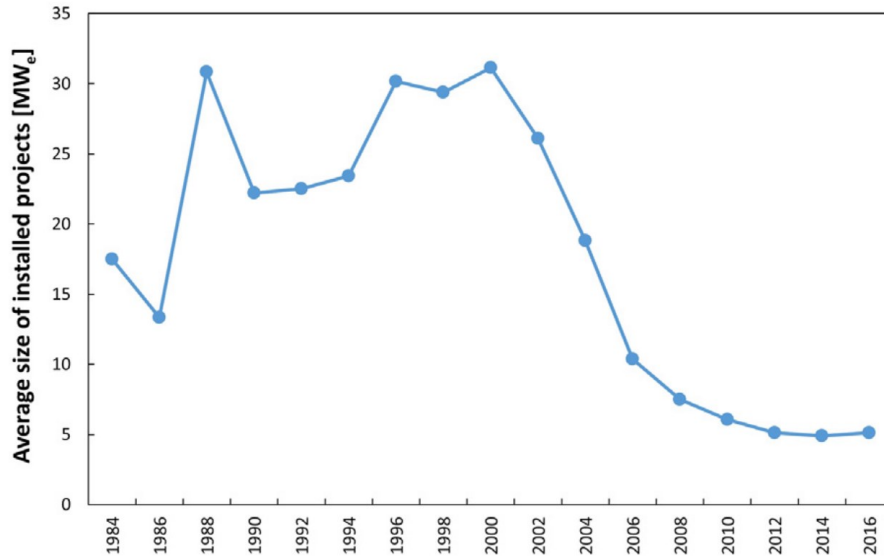


Figure 19-ORC's average size since 1984 until 2016 [216].

The significant difference between the ORC and the conventional Rankine cycle is using refrigerants or organic fluids as the working fluids instead of water. The performance of ORCs with the minimum costs depends on the working fluids, which was analyzed by Köse et al. [217]. Producing more power was possible using R141b, which was noncombustible but negatively affected the environment since it had a high GWP. On the contrary, acetone was an eco-friendly refrigerant with low GWP that made the system more efficient from an environmental point of view. Because the only drawback of acetone was related to its flammability, they increased the ORC safety by installing a ventilation system [217]. A major attempt has been made to demonstrate ORCs' abilities in responding to load demands in the diversity of sectors such as domestic applications. Pereira et al. [216] presented a solution that helped biomass-based ORC to respond fast to domestic demands, especially at peak load. They concluded that the conventional approach, including using plate heat exchangers for vaporizing organic working fluids, raised heat losses and thermal inertia. However, installing storage tanks met hot domestic water constantly and retrofitted the function of systems at off-design conditions resulting in reduced reaction time of the system against residential needs.

The waste heat from a marine engine was recovered through the combination of ORC and steam Rankine cycle (SRC), and its performance was compared with a sole SRC and a dual-pressure ORC [218]. The proposed technology proved that it performed better than the above-mentioned systems at full load because of increased thermal efficiency (4.42%). The decrease of burning fuel

(9322 tons year<sup>-1</sup>) was higher than that for the single SRC and DPORC [218]. ORC is identified as the best technology corresponding to exergy analysis because it has the lowest exergy destruction rates, as Salehi et al. [198] proved. They modified their model by adding ORC to recover waste heat from the MCFC and claimed that if they used ORC, the highest thermal (from 44.87% to 61.26%) and exergy (from 35.93% to 50.18%) efficiency and lowest pollutions based on CO<sub>2</sub> emission rates (from 0.422 to 0.289 t MWh<sup>-1</sup>) were achieved compared to the sole MCFC-SE fed by a gasifier [198]. An improvement of a solar energy system was made by ORC, which was cooled through a water reservoir located in the ground. The researchers found that the ORC helped the whole system have higher electrical efficiency (15.72-17.78%) than a single concentrated photovoltaic/ thermal device [194].

A thermodynamic and thermoeconomic analysis was conducted on a system comprised of steam and organic Rankine cycles and other components run by biomass to meet domestic consumers' load demands [219]. A logic control was implemented when biomass was not available, so the solar subsystem would be switched on to run the system. The Multi-production system proved that it could be a great investment, especially for domestic sectors, because it provided electricity (282.5 kW), heat (172.4 kW), cooling (77.4), and drinking water (0.4447 kg s<sup>-1</sup>) sufficiently [219]. The combination of ORC and SRC with a gas turbine (GT) was optimized based on monitoring the behavior of the system when various working fluids were used, and the input temperature and pressure of turbines were changed. Their approach helped the authors to distinguish which design conditions led to changing the system for the better [217]. They concluded that the highest exergy (67.35%) and thermal efficiency (47.65%) of the whole system were achieved if ORC operated at 40 bar and 225 °C by selecting R141b and SRC worked at 100 bar and 480 °C. The main advantage of using ORC and SRC in the proposed system was recovering the waste heat of the exhaust gas, which reduced CO<sub>2</sub> emissions by saving fuel during a year (2,168,538 \$ year<sup>-1</sup>) [217]. Modeling the coupling of a 100 kW<sub>el</sub>-class micro-gas turbine run by pure syngas produced through gasification and an ORC was implemented in Aspen Plus [220]. The novelty of the proposed system was injecting steam into the combustion chamber (CC) to increase relative humidity and decrease the air temperature, which resulted in improved net power. They proved that ORC satisfied domestic consumers who needed more heating at critical conditions and helped the micro-gas turbine produce more electricity. The more steam was injected into the CC (25 g s<sup>-1</sup>), the more electricity (127.6 kW<sub>el</sub>) and heat (78.7 kW<sub>th</sub>) were generated through the considered distributed

energy system [220]. Because of the fluctuations of renewable energy generation, the focus on storage systems has been increasing. One of the studies related to the abilities of heat storages was conducted in 2017 when the combination of a packed bed of rocks with a steam Rankine cycle (SRC) was analyzed [221]. Regarding the control strategy, during charging heat storage through an electrical coil, the steam Rankine cycle was shut down, and it was turned on when the discharged mode was on [221]. The generated heat from a condenser set at 100 °C was sufficient to meet heat demands and hot domestic water for local consumers [221]. After that, Arabkoohsar [222] promoted the previous system by equipping it with different organic Rankine cycles to distinguish which one was the best from the economic and environmental points of view. The researcher considered a real wind farm in Denmark, where a peak power demand was 5 MW, and modeled the energy system based on its electrical load curves. The maximum electrical efficiency (42.6%) was achieved in [222] by selecting R123, resulting in higher efficiency (24-35%) than the previous model [221]. A significant decrease in overall package size and costs was observed due to the ORC capturing waste heat from the condenser of the SRC and utilizing it to generate additional energy [222].

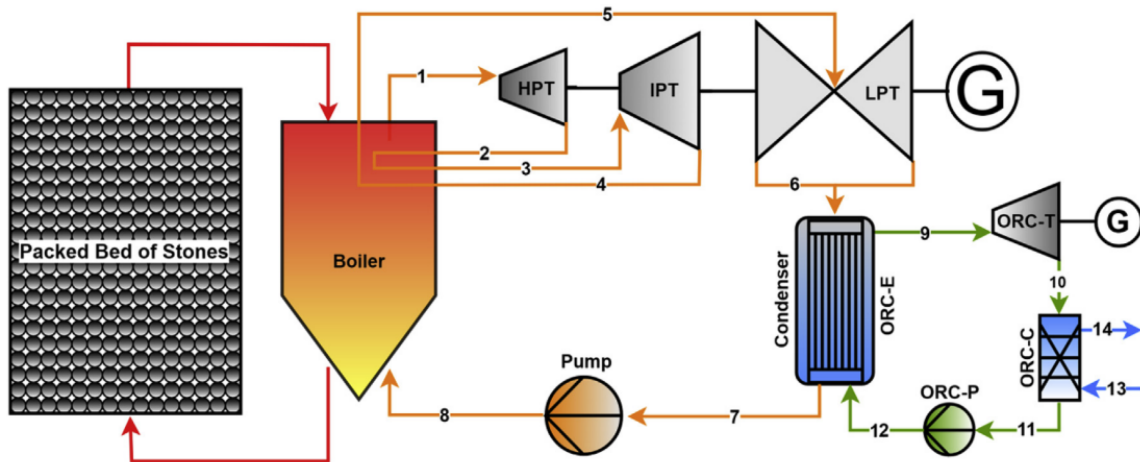


**Figure 20-**The hybrid power system [222] was upgraded from the study proposed by [221].

A hybrid cogeneration system comprised of two ORCs run by the exhaust gases from a SOFC connected to a gas turbine (GT) was optimized through the LINMAP method [200]. The proposed approach helped the authors to decide which working fluids kept ORCs at the highest exergy efficiency (33.0%) and the lowest costs (3.15 \$ hr<sup>-1</sup>), which resulted in selecting R601 and Ethane among 20 refrigerants. Two ORCs had a considerable portion (20.7%) of the total generated power

(1040 kW) and produced 564 kW of cooling for responding to local load demands [200]. Tchanche et al. [223] presented an ORC cycle run by solar collectors at low temperatures and assessed the functions of the proposed system from the thermodynamic and environmental points of view. They compared several organic fluids based on different factors such as efficiencies, volume flow rate, mass flow rate, pressure ratio, toxicity, flammability, ODP, and GWP, and they found out R134 was the best choice for small scale solar applications with a heat source below 90 °C. Farrokhi et al. [224] experimentally investigated a natural gas-fired micro-CHP system using an ORC cycle. Their research was based on residential buildings as a case study, and they chose Isopentane as a working fluid because of its environmentally friendly characteristics. They carried out their experiment according to various temperatures of the heat source and reached the maximum power output of 77.4 W and electrical efficiency of 1.66% at 84.1 °C inlet heating water temperature. Peris et al. [225] used a monitored test bench to describe an ORC module for small-scale CHP under operation conditions. During the test process, they considered a natural gas boiler as a heat source with a constant temperature of 165 °C. They realized that at higher pressure ratios, more thermal power output was achieved. Providing that the proposed system worked at the optimized pressure ratio, a suitable heat temperature for a CHP application was provided. The maximum output power and efficiency were obtained, and they were equal 5.6 kW<sub>el</sub> and 8.80%, respectively. Kaczmarczyk et al. [226] proved that the efficiency of the MGT affected the ORC performance since they modernized the first stator stage of a micro turbogenerator of the micro-CHP plant. They studied the impact of the mentioned upgrading on some key parameters such as exergetic efficiency, Carnot efficiency, microturbine internal efficiency, and ORC cycle efficiency. An improvement in electrical efficiency of 17% was reported. They recognized defects or malfunctions of the system by monitoring it at operation procedures. Experimental research on an ORC system that generated 3 kW power was done by Yang et al. [227]. They considered R245fa as a working fluid and investigated the effects of pressure drop, degree of superheating, and condenser temperature on the overall efficiency. Their findings showed that the condenser temperature had a negative impact on key performance metrics, including output power, thermal efficiency, and system generating efficiency. They reported that the maximum electrical power, thermal efficiency, and system generating efficiency were 1.89 kW, 5.92%, and 3.93%, respectively [227]. Algieri [228] compared subcritical and transcritical organic Rankine cycles for biomass micro-CHP systems and concluded that both of them saved energy considerably. The

author investigated the behavior of the system affected by internal regeneration. One of the important results was choosing the best working fluid that caused proper operations and optimized system behavior. The maximum electric performances were also obtained if the transcritical cycle was used and equipped with internal regeneration. On the contrary, the highest efficiency was calculated based on using the saturated cycle.

The simulation of a  $2 \text{ kW}_{\text{el}}$  biomass-fired CHP system consisted of an ORC was conducted by Liu et al. [229]. They modeled the proposed system through Engineering Equation Solver (EES) software to calculate the thermal efficiency of the whole system, and three refrigerants, namely HFE7000, HFE7100, and n-pentane, were selected as ORC fluids. The researchers concluded that the highest ORC efficiency reached 16.6% when n-pentane was chosen as a working fluid. Also, the overall CHP efficiency of the proposed system was about 80% for all the above-mentioned fluids, even though the selected fluids affect the quantity and quality of heating supplied by the CHP system [229]. An experimental study on a biomass-fired ORC-based micro-CHP for domestic applications was performed by Qiu et al. [230]. The proposed cycle consisted of a condenser where the outlet cooling water was heated to an appropriate temperature ( $46 \text{ }^\circ\text{C}$ ) for domestic washing and underfloor heating. Their results indicated that the biomass-ORC system produced 861 W power and  $47.26 \text{ kW}_{\text{th}}$  heat, based on electrical efficiency of 1.41% and CHP efficiency of 78.69% [230]. A micro-CHP system, including an ORC driven by solar energy, was modeled via EES software [212]. The authors chose three working fluids, including R123, R245fa, and R600a, to decide which one was suitable based on economic and thermodynamic points of view. The generated electricity and heating by using R123 ( $50.47 \text{ kW}_{\text{el}}/15.89 \text{ kW}_{\text{th}}$ ), R245fa ( $15.02 \text{ kW}_{\text{el}}/18.47 \text{ kW}_{\text{th}}$ ), and R600a ( $2.12 \text{ kW}_{\text{el}}/8.50 \text{ kW}_{\text{th}}$ ) were calculated. To achieve the maximum thermal and exergy efficiencies and the minimum costs and total heat exchanger areas, a multi-objective optimization through NSGA-II was implemented. The results proved the micro-CHP system was economical if R600a was selected, while by applying R123, the system experienced its maximum performance (36.81% for thermal efficiency and 17.03% for exergy efficiency) [212]. Montazerinejad et al. [231] used life cycle assessment (LCA) to simulate a solar-based cogeneration system that produced  $143.52 \text{ kW}_{\text{el}}$  power. The researchers performed an exergy analysis for each component, then by using LCA and Eco-indicator 99, they calculated the ecological index for all equipment related to their producing, movement, operating, maintenance, disposal, and installation. The results indicated that the vapor generator ( $231.2 \text{ kW}$ ) placed at the

second-highest exergy destruction rate after the storage tank, which led to a higher environmental impact rate ( $831.4 \text{ mPts h}^{-1}$ ). The authors suggested that the cogeneration system would become environmentally friendly if the exergetic efficiencies of the vapor generator (83.28%) and storage tank (79.71%) were improved [231].

## 2.7 Stirling engine

A promising conversion device for the micro-CHP system is the Stirling engine (SE), which is an external combustion engine. According to its characteristics, including low emissions, high efficiency, reliability, extended service intervals, low noise and vibration levels, it can meet the demands of local consumers. If the micro-CHP systems that are applied in the household sectors employ the Stirling engine as a prime mover, it provides substantial benefits such as multi-fuel capability and low-acoustic and pollutant emissions [232]. The general structure of the Stirling engine is made of different parts, namely, power piston whose duty is converting reciprocating movement to rotating movement, a cylinder that is divided into expansion and compression spaces, displacer that relocates gas between the mentioned spaces, regenerator, and mechanical links [233]. **Figure 21** illustrates the three kinds of configurations of the Stirling engine, including Alpha, Beta, and Gamma [233].

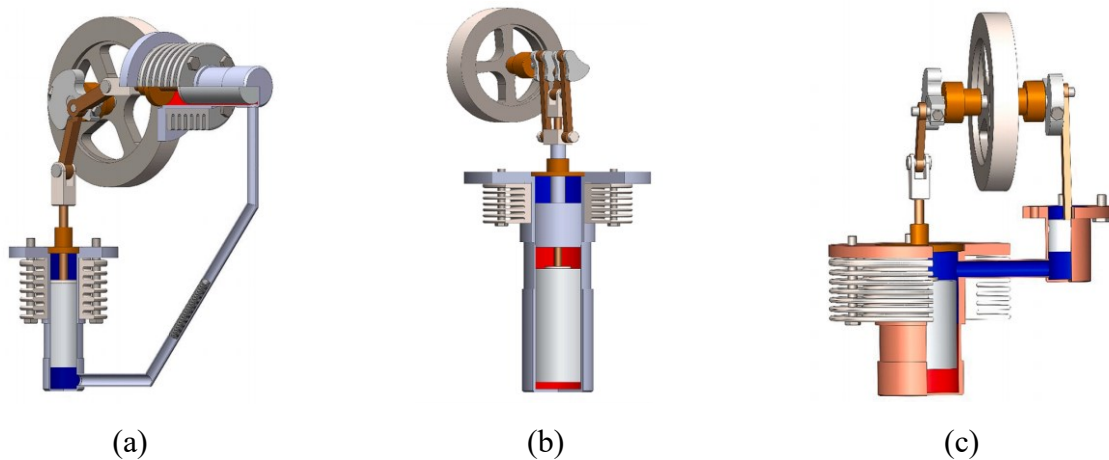


**Figure 21**-Different types of Stirling engine: (a) Alpha, (b) Beta, and (c) Gamma [233].

A micro-CHP system that uses the Stirling engine as a prime mover to generate energy for single-family or small multi-family houses is illustrated in **Figure 22**. SE drives a generator to produce the required power, and the heating purposes, including space heating and domestic hot water (DHW), are supplied through a heat exchanger where the waste heat from the engine casing and

the combustion exhaust gases is recovered and converted to heat. In some circumstances, the heating demand exceeds the main burner's capacity, the existence of an auxiliary burner (AB) installed on the heat exchanger is critical and necessary [64].

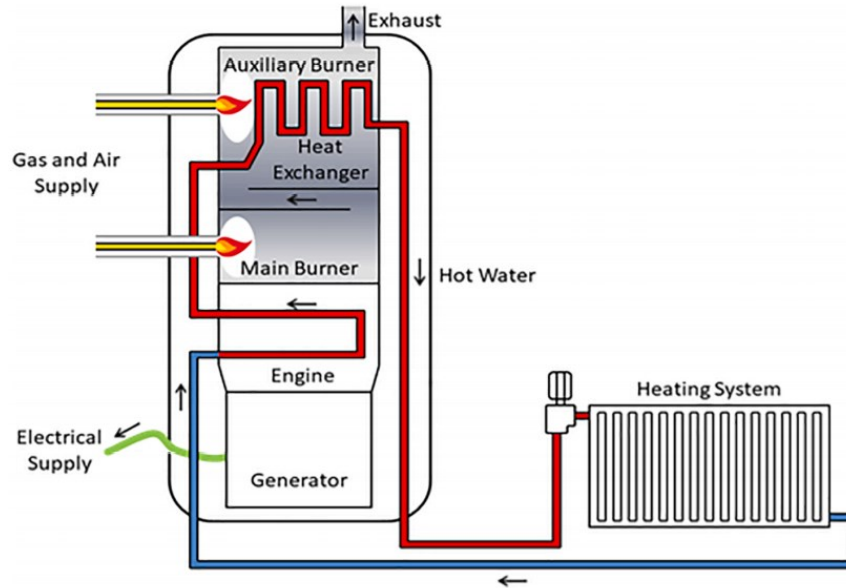


**Figure 22-** The schematic of the micro-CHP system by using Stirling engine (SE) [64].

A micro-power system, including an alpha-type Stirling engine was simulated, and the theoretical results were validated with the empirical data given from Solo V161 [234]. The research aimed to monitor the Stirling engine's function and its response to local load demands at different weather conditions. The SE was sized by following three scenarios: electrical load, thermal load, and overall efficiency. The researchers revealed that by using the first approach, the Stirling engine could meet electrical demand, but for supplying heat demand, the existence of an auxiliary boiler was highlighted. The Stirling engine designed through the second methodology was more economical than other approaches because it completely covered heating demands, and extra generated power was imported to the grid. The first and second scenarios helped the reduction of pollution such as CO<sub>2</sub> (40%). The Stirling engine experienced the highest overall efficiency when it was modeled corresponding to the last approach [234]. Hosseinpour et al. [235] claimed the best way to increase the performance of a SOFC would be to use its waste heat to run a SE where the required electricity and heating were generated (see **Figure 23**). They modeled the proposed cogeneration system at optimum conditions and obtained the maximum energy (73.32%) and exergy (56.44%) efficiencies. By increasing the compression ratio, the exergy efficiency of the

cogeneration system peaked at 54.27%. Also, the exergy destruction rate of the cogeneration system was 8.66 kW, where 1.71 kW belonged to SE [235].

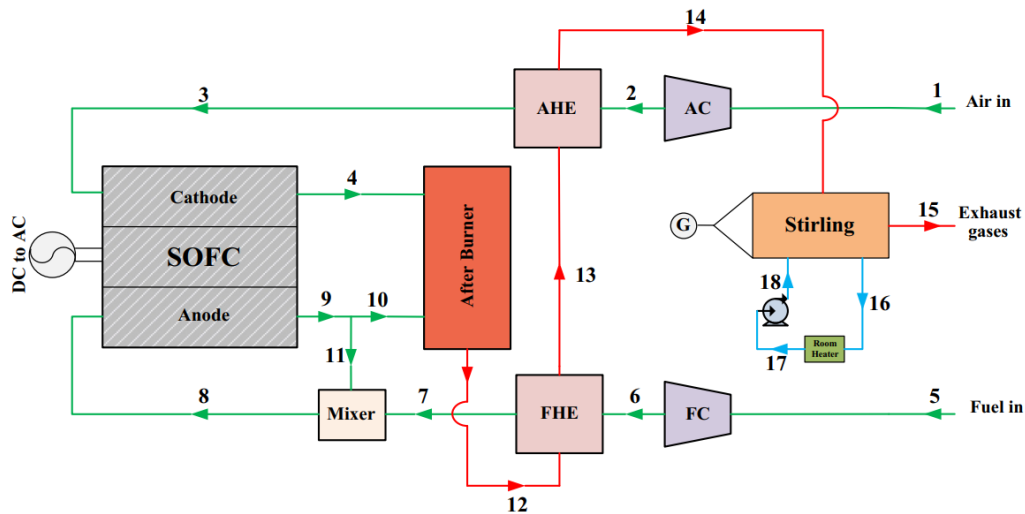


**Figure 23**-The schematic diagram of coupling a SOFC with SE [235].

Li et al. [236] used waste gases with an average temperature to drive a Stirling engine for the micro-CHP system. The authors used a thermodynamic design method and parallelly carried out experimental performance tests. During the test, they monitored the temperature of the heater head and the pressure of the working fluid helium in the Stirling engine through thermocouples and pressure sensors, respectively. The test results demonstrated that the technology generated 3476 W at a rotational speed of 1248 rpm, confirming its ability to meet the power requirements for engineering applications. González-Pino et al. [237] conducted an economic analysis on a 1 kW<sub>el</sub> SE for a micro-CHP residential plant in Spain. They used the TRNSYS 17 numerical platform to simulate and compare the dynamic model of a conventional boiler and the micro-CHP system. The results illustrated that the payback conditions of micro-CHP installations were hardly feasible in Spain, but in other, European countries such as Germany and the United Kingdom, the potential of this kind of technology was widely better due to feed-in tariffs and support policies [237].

If small-scale CHP systems use biomass fuel, Stirling engines are interesting with nominal electric capacities between 10 and 150 kW [238]. They can also easily convert concentrated solar energy into electricity [239]. A comparative analysis evaluated two Stirling engines (SEs) for small-scale residential use – one powered by solar energy and the other by biomass [232]. The receiver temperature of the boiler reached approximately 1288 K for the biomass-fueled SE, compared to

775 K for the solar-powered SE. This temperature difference led to an 87.5% increase in electricity generation in the biomass-fueled SE over the solar-powered counterpart. The overall efficiencies of the biomass and solar SEs were 46.67% and 31.33%, respectively. Additionally, the levelized cost of energy (LCOE) for the solar-powered SE was 52% higher than that of the biomass-powered SE, highlighting biomass as a more cost-effective heat source for Stirling engines [232].

### 2.7.1 Biomass-Stirling engines

Gasification processes can produce syngas to power internal combustion engines (ICEs); however, this technology requires pure syngas, necessitating the addition of auxiliary components. The installation of these supplementary devices significantly increases capital costs, prompting researchers in 2021 to explore the use of Stirling engines as an alternative to ICEs [240]. They proposed a configuration including a Stirling engine, a gasification system, and the absorption chiller to meet load demands for two case studies in Shanghai and Singapore [240].

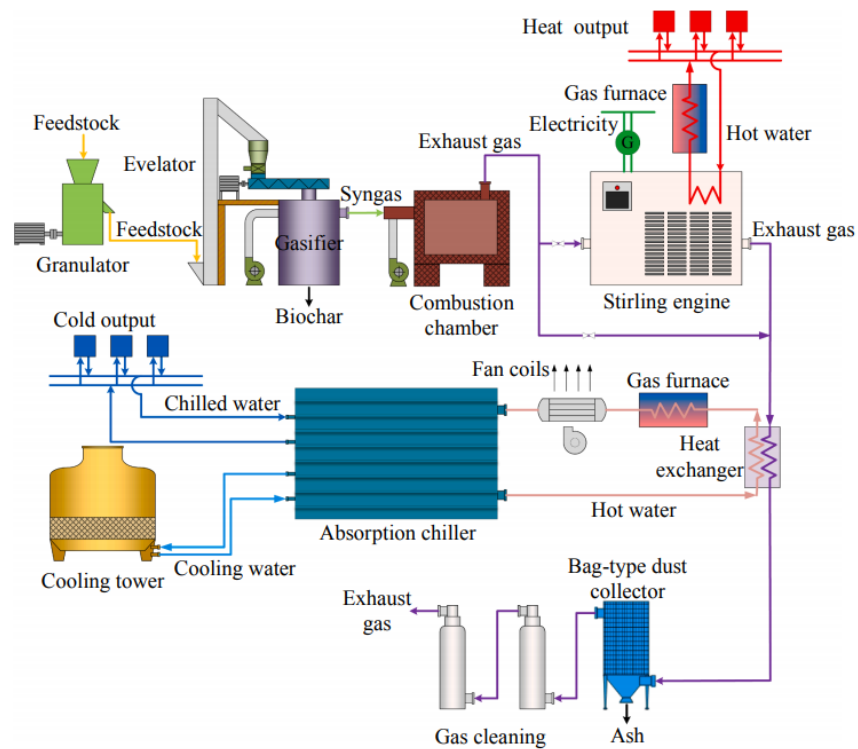


**Figure 24**-The gasification energy system integrated with the SE to provide load demands for small buildings in Shanghai and Singapore [240].

In Shanghai, a Stirling engine with a power output of 324 kW was installed, while in Singapore, a 383 kW Stirling engine was deployed. Compared to conventional gasification systems, these

energy systems in Shanghai and Singapore achieved significant cost savings, reducing the levelized cost of energy by 75.9% and 70.5%, respectively. Both Stirling engine-based gasification systems also demonstrated an identical CO<sub>2</sub> reduction ratio of 0.71, confirming their eco-friendliness [240]. Salehi et al. [198] modeled a cogeneration system, including an alpha-configuration SE that produced 32.3 kW electricity. The considered SE was powered through a portion of the generated electricity from MCFC, whose power was 161.7 kW. The authors monitored the system's function at off-design conditions and proved that the ratio of the low-temperature heat source to the high one played an important role in calculating the engine's electrical output. If the aforesaid factor was improved (0.4-0.6), the input heat of SE had to be enhanced to the level at which the air compressor operates at constant power [198]. A micro-energy system comprised of a Stirling engine (SE) whose exhaust gases were recovered through an ORC and a boiler to generate more power and heating was simulated in MATLAB and Aspen plus [241]. By increasing the rotational speed of SE, the heat source temperature increased, which resulted in the growth of power generated from ORC. Providing that the hybrid power system worked at 2500 rpm, an increase of thermal efficiency (by 63.4%) and a growth of the generated electricity (by 66%) were reported compared to a sole SE. Consuming biomass with 10% humidity led to the increase of primary energy saving by 55%, while the CO<sub>2</sub> emission was reduced to 43% [241]. Damirchi et al. [242] designed and optimized a micro-CHP system that consisted of a Stirling engine run by biomass to produce heat and electrical power. They calculated the heat transfer area for both the heater and cooler of the Stirling engine, which was 307 and 243 cm<sup>2</sup>, respectively (see **Figure 25**).

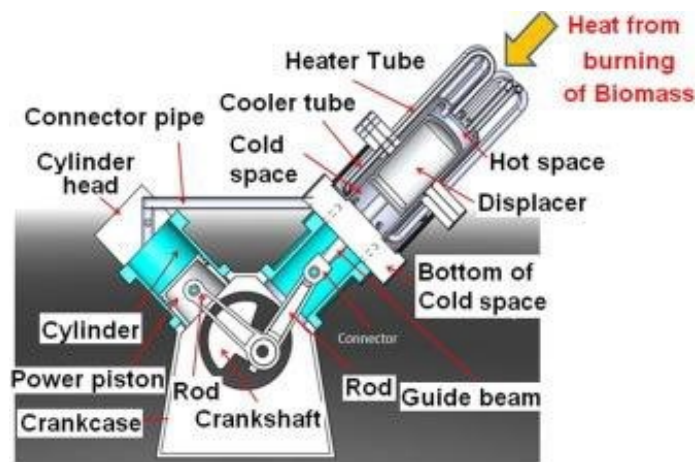


**Figure 25**-Three-dimensional model of the Stirling engine with components [242].

The authors used CFD simulation to analyze the fluid flow, and during the test of engines with helium, they monitored the temperature and pressure of helium by using thermocouples and pressure sensors. The researchers used biomass and flammable agricultural wastes (biomass sources) to produce electricity, and they found that by burning the sawdust, the maximum power was achieved (46 W). At that point, the internal efficiency of the engines was calculated, which was 16% [242]. A micro-CHP system, including a gamma type Stirling engine run by biomass to supply heating and power demands was modeled [243]. The highest thermal efficiency was achieved through burning sawdust compared to other biomass resources. On the contrary, by consuming more sawdust, the increase of pollutants such as CO (164 vol%) and NO<sub>x</sub> (by 24 ppm) was reported [243]. Arashnia et al. [244] modeled and optimized a micro-CHP system with an electrical power of 100 W that consisted of a Stirling engine fed with biomass fuels. The authors considered some design parameters such as the speed values of SE, temperature, and the kinds of biomass to assess the efficiency and generated power. They concluded that at an average speed of the SE (500-600 rpm), the highest efficiency was achieved. Among various types of fuels, by selecting sawdust whose minimum ignition time was 4 min, the most power was obtained (46 W), which led to having 16% of internal thermal efficiency. Cardozo et al. [245] integrated a Stirling engine (1 kW<sub>el</sub>) with a pellet burner (20 kW<sub>el</sub>) to generate heat, hot water, and power for domestic applications, which resulted in reaching 72% of overall efficiency (see **Figure 26**). The authors focused on the Stirling engine position because it played an important role in achieving more radiative heat from the burner. A 5 cm distance change between two devices increased temperature levels by 100 °C in the hot side of the engine. Also, they found that if Ø8 mm wood pellets were used, the amount of heat delivered to the engine was increased [245].

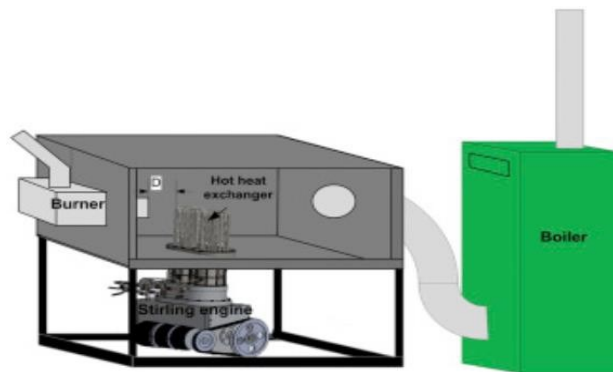


**Figure 26**-Schematic of the wood pellets fired the Stirling engine system [245].

### 2.7.2 Solar energy-Stirling engines

A micro-CHP system, including a Stirling engine with solar systems to provide electricity and heating purposes (i.e., hot domestic water) was analyzed experimentally [246]. The daily heating and electrical demands for the considered case study, which was completely independent of the electrical grid, were 6.8 kWh and 17.9 kWh, respectively. Two auxiliary devices, namely battery storage and heat storage tank, were installed to increase the resiliency and reliability of the energy system. The Stirling engine supplied 20.7% electrical demands. To increase the load covering, the battery capacity was increased (20 kWh). The whole system then not only wholly met the heating demands thanks to the Stirling engine, but also allowed to export 31.8% generated electricity to the grid, which led to making a profit. The authors estimated that the decentralized energy system could reduce the CO emission (36.2%) compared to a system where the electricity was bought from the grid and heat was generated from the diesel boiler [246].

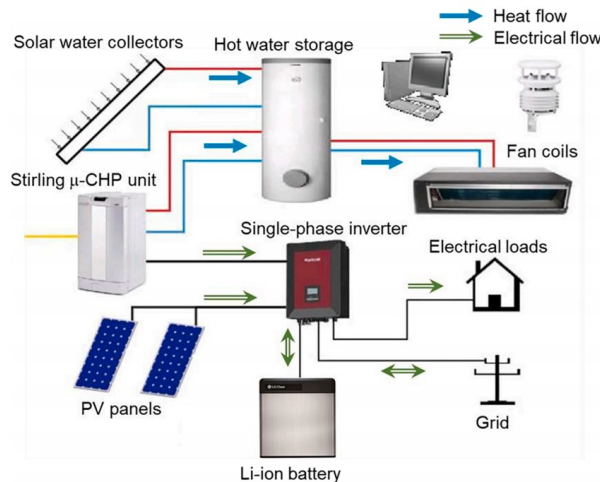


**Figure 27-**Decentralized energy system, including a Stirling engine and a solar system [246].

A micro-gas turbine, including a solar heliostat was considered a heat source of a Stirling engine and was modeled by Babaelahi and Jafari [247]. The exergy efficiency of the proposed system was 41.93%, which proved a 7% increase compared to a Capstone C200 micro-gas turbine. A parametric study to assess the performance of the system was conducted, which indicated that by increasing the compression ratio of the MGT (from 2.5 to 5), the pressure of SE was increased (from 2.75 to 5.5 MPa), which led to the improvement of generated electricity (0.8 to 1.7 kW) and the considerable reduction of electricity price. The Pareto front results of multi-objective optimization confirmed the increase of thermal (6.525%) and exergy efficiencies (8.842%) [247].

Moghadam et al. [248] considered a solar dish Stirling cogeneration technology to meet residential demands. They analyzed the whole system based on 3E sectors, including energy, environmental, and economic analysis. Three scenarios were chosen to assess and size the proposed system; in the first and second scenarios, the authors sized the system according to the lowest and highest annual electric power demands, respectively. On the contrary, the last procedure was done based on constant output capacity. They used the TOPSIS decision-making method to identify the best scenario with minimum values of the payback period (PBP) and maximum values for the carbon dioxide emission reduction and primary energy saving (CDER and PES) [248].

In summary, the comprehensive literature review [2] on a wide range of cogeneration technologies based on their application, efficiency priorities, power range, lifetime, and maintenance performance for new fuels, provide detailed insight into us to recognize which features of cogeneration systems stand out, leading to selecting the best technologies in future urban energy systems. If the electrical load demands are in the range of 1 to 20 MW<sub>el</sub>, the best options for meeting urban demands would be GTs and ICEs. Micro-gas turbines (MGTs), Stirling engines (SEs), and proton exchange membrane fuel cell (PEM fuel cells) can respond to lower power demands (less than 1500 kW<sub>el</sub>) [2]. The mechanism, design, and function of MGTs are based on low vibration, compact size, and hot exhaust gas temperature, which is interesting for domestic process use. The high power to heat ratios of fuel cells (FCs) make them particularly suitable for buildings. One of the drawbacks of the FC technologies is their higher cost. Compared to FCs, SEs and MGTs have lower electrical efficiency (15% and 30% vs. 50% for 100 KW), less power density (by a factor of 3-4), and less pure hydrogen is required for combustors. Stirling engines (SEs) suffer from low electrical efficiency when driven by biomass because the temperatures of combustion products are lower than when they are powered by natural gas (electrical efficiencies of 25-30%). The part-load efficiency of SEs, and MGTs is lower than for FCs. The lifetime of SEs and FCs are similar and low compared to MGTs.

## Chapter 3: Proposed Research Methodology

To address the research questions, mathematical models and simulations are developed for two cogeneration technologies to analyze their performance and assess pollutant emissions. For the PEM fuel cell, thermal and electrochemical models are developed. The governing mathematical equations are implemented in Fortran, a programming language, while thermodynamic properties for the models are obtained through the Engineering Equation Solver (EES). For the recuperated micro-gas turbine (MGT), a comprehensive analytical algorithm is developed, and a converged steady-state solution is achieved by applying the Newton-Raphson (N-R) method, also coded in Fortran.

This study proposes several emission models to simulate the dual-axial swirler combustor with distinct combustion zones. The emissions analysis includes Computational Fluid Dynamics (CFD) simulations, an Equivalent Chemical Reactor Network (ECRN) model using Ansys Chemkin-Pro, and mathematical modeling. These approaches account for complex flow behaviors and include kinetic mechanisms for the key chemical reactions occurring in the combustor. The CFD simulations employ the Eddy Dissipation Concept (EDC) model alongside the realizable  $k-\epsilon$  turbulence model, both effective in predicting pollutant emissions within swirling flows and widely recognized in Reynolds-Averaged Navier-Stokes (RANS) frameworks.

For  $\text{NO}_x$  emissions, an ECRN model is made in CHEMKIN, which enhances the understanding of combustion mechanisms by accurately calculating chemical species' production rates within computational cells. Additionally, a detailed analysis of key species destruction pathways is performed in CHEMKIN, offering insights into reaction dynamics that are challenging to capture with traditional CFD models alone. However, due to the limitations of the ECRN methodology in predicting CO emissions, a mathematical model is applied. This model simplifies the complexities of CO formation, making it more accessible for combustion engineers who require quick and practical estimates of attainable emission levels based on available design parameters.

### 3.1 PEM Fuel Cell Cycle Description

**Figure 28** shows the schematic of the insulated PEM fuel cell with an air compressor, a valve to regulate pressure, a humidifier, and a heat recovery unit (HRU). PEM fuel cell consists of main

sections, including bipolar plates (BPPs), gas diffusion layers (GDLs), catalyst layers (CLs), where electrochemical energy conversion takes place, and gaskets. BPPs protect the whole system from erosion and provide electrical conduction between cells as well as physical strength to the stack. GDL facilitates homogenous diffusion of reactants to the catalyst layered membranes. Gaskets between BPPs and CLs, prevent gases and liquids from leaking, avoid gas combining, and create thermal and chemical equilibrium. A humidifier plays a crucial role in controlling the moisture level within the fuel cell, protecting the membrane from drying out by providing the necessary humidity to the intake gases. By preventing the dehydration of the electrolyte membrane, the humidifier helps to enhance the efficiency and longevity of the fuel cell stack.

The compressed air (2) attains the required operational pressure for the fuel cell, subsequently crossing the cathode (3). Integrating a high-pressure storage cylinder for hydrogen necessitates the installing a pressure-regulating valve to modulate the pressure, effectively reducing it from storage pressure (4) to operational pressure (5). Consequently, the anode chamber within the FC stack is supplied with hydrogen regulated to the specified pressure (6). A direct current is generated based on electrochemical reactions, which are assumed to reach equilibrium states, and concurrently, substantial thermal energy is released. The HRU integrated into the system captures considerable thermal energy, utilized for domestic water and space heating, thereby minimizing heat loss to the environment, with only a small portion dissipating. Finally, any unused hydrogen (7) is recirculated to ensure efficient resource utilization and maintain continuous operation.

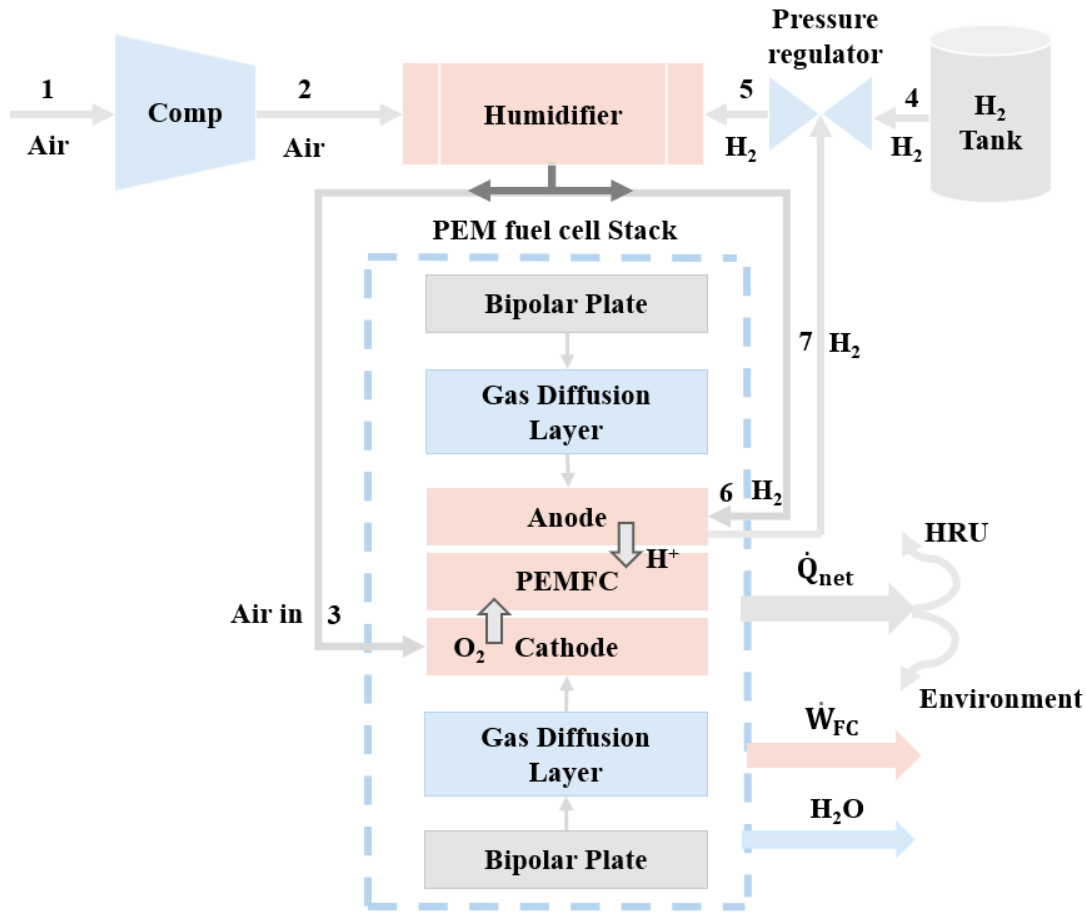


Figure 28-Schematic diagram of the insulated PEM fuel cell.

### 3.2 Mathematical Modeling of PEM Fuel Cell

The simulation approach is based on applying mass and energy conservations [249,250], along with some specific assumptions necessary for modeling the electrochemical and thermal aspects of the PEM fuel cell, derived from [11]. To calculate the generated power of the stack ( $\dot{W}_{FC}$ ), the PEM fuel cell model is developed based on the electrochemical reactions (see **Table 3**). Eq. (5) shows that the actual voltage ( $V_{FC}$ ) is less than the reversible one ( $E_{Nernst}$ ) because of some irreversibility, such as the activation ( $V_{act}$ ), ohmic ( $V_{ohm}$ ), and concentration ( $V_{conc}$ ) [11]. For achieving all terms in Eq. (5), some factors, including Gibbs free energy ( $\Delta G^0$ ), the operative temperature ( $T_{FC}$ ), fractional pressure of hydrogen ( $P_{H_2}$ ), oxygen ( $P_{O_2}$ ), the molar portion of nitrogen ( $X_{N_2}^{Channel}$ ), water vapor ( $X_{H_2O}^{sat}$ ), the concentration of oxygen ( $C_{O_2,conc}$ ), and hydrogen ( $C_{H_2,conc}$ ) at the common area of the cathode and anode with membrane, respectively, are required, in parallel with implementing some design parameters detailed in **Table 4** [11,249,250]. In the

next stage, the thermal modeling of the PEM fuel cell is conducted to obtain the net heat energy ( $\dot{Q}_{\text{net}}$ ) (Eq. (10)) by subtracting the actual work of stack ( $\dot{W}_{\text{FC}}$ ) and sensible/latent heat ( $\dot{Q}_{\text{s,I}}$ ) from chemical one ( $\dot{Q}_{\text{ch}}$ ). The electrochemical reaction causes  $\dot{Q}_{\text{ch}}$  that is determined directly by the consumption amount of hydrogen ( $\dot{n}_{\text{H}_2,\text{cons}}$ ). Its value with the consumed amounts of oxygen ( $\dot{n}_{\text{O}_2,\text{cons}}$ ), and water generation ( $\dot{n}_{\text{H}_2\text{O,gen}}$ ) are obtained based on the stack current (I) and cell numbers ( $N_{\text{cell}}$ ). To avoid the membrane degradation and failure in the fuel cell, the stoichiometric rate ( $\lambda$ ) is applied. This parameter is used to evaluate reactant flow rates and calculate  $\dot{Q}_{\text{s,I}}$ . Finally, Eq. (13) indicates the consumed power in the compressor computed ( $\dot{W}_{\text{comp}}$ ) based on pressure ratio ( $\pi$ ), the mass flow rate of air ( $\dot{m}_{\text{air}}$ ), the isentropic efficiency ( $\eta_{\text{comp}}$ ), outlet temperature ( $T_{\text{out,s}}$ ), and exponent ( $\kappa$ ) [11].

**Table 3-**Required equations used for modeling the PEM fuel cell [11].

Eq.	Equations	Auxiliary equations
<b>PEM fuel cell electrochemical model</b>		
		Saturation Pressure of Water Vapor,
	Nernst Equation,	$\log_{10}^{(\text{p}_{\text{H}_2\text{O}}^{\text{sat}})} = -2.1794 + 0.02953t$
(1)	$E_{\text{Nernst}} = \frac{-\Delta G^0}{n_e F} + \frac{RT_{\text{FC}}}{n_e F} \ln \left( \frac{P_{\text{H}_2} \sqrt{P_{\text{O}_2}}}{P_{\text{H}_2\text{O}}^{\text{sat}}} \right)$	$- 9.1837 \times 10^{-5}t^2$ $+ 1.4454 \times 10^{-7}t^3$
		$t = T_{\text{FC}} - 273.15$
	Molar Fraction of Nitrogen,	$X_{\text{N}_2,\text{in}} = 0.79(1 - X_{\text{H}_2\text{O}}^{\text{sat}})$
(2)	$X_{\text{N}_2}^{\text{Channel}} = \frac{X_{\text{N}_2,\text{in}} - X_{\text{N}_2,\text{out}}}{\ln(X_{\text{N}_2,\text{in}}/X_{\text{N}_2,\text{out}})}$	$X_{\text{N}_2,\text{out}} = \frac{1 - X_{\text{H}_2\text{O}}^{\text{sat}}}{1 + (\lambda_{\text{air}} - 1/\lambda_{\text{air}})(\frac{0.21}{0.79})}$
	Effective Partial Pressure of Hydrogen at an Anode,	
(3)	$P_{\text{H}_2} = (0.5P_{\text{H}_2\text{O}}^{\text{sat}}) \left[ \frac{1}{\exp(1.653/T_{\text{FC}}^{1.334}) \times X_{\text{H}_2\text{O}}^{\text{sat}}} - 1 \right]$	Both are the same over the entire cell.
	Effective Partial Pressure of Oxygen at the Cathode,	$X_{\text{H}_2\text{O}}^{\text{sat}} = \frac{p_{\text{H}_2\text{O}}^{\text{sat}}}{P}$
(4)	$P_{\text{O}_2} = P \left[ 1 - X_{\text{H}_2\text{O}}^{\text{sat}} - X_{\text{N}_2}^{\text{Channel}} \exp \left( \frac{0.291i}{T_{\text{FC}}^{0.832}} \right) \right]$	
	Actual Voltage,	-
(5)	$V_{\text{FC}} = E_{\text{Nernst}} - V_{\text{act}} - V_{\text{ohm}} - V_{\text{conc}}$	
	Activation Voltage,	
(6)	$V_{\text{act}} = \xi_1 + \xi_2 T_{\text{FC}} + \xi_3 T_{\text{FC}} \ln C_{\text{O}_2,\text{conc}} + \xi_4 T_{\text{FC}} \ln (I)$	$\xi_1 = 0.948$

$$\xi_2 = - \left( 0.00286 + 0.0002 \ln(A_{\text{cell}}) \right. \\ \left. + 0.000043 \ln(C_{\text{H}_2, \text{conc}}) \right)$$

$$\xi_3 = -0.000076$$

$$\xi_4 = 0.000193$$

$$C_{\text{O}_2, \text{conc}} = 1.97 \times 10^{-7} P_{\text{O}_2} \exp\left(\frac{498}{T_{\text{FC}}}\right)$$

$$C_{\text{H}_2, \text{conc}} = 9.174 \times 10^{-7} P_{\text{H}_2} \exp\left(\frac{-77}{T_{\text{FC}}}\right)$$

Nafion Membrane Specific Resistivity,

$r_{\text{mem}}$

(7) Ohmic Voltage,  
 $V_{\text{ohm}} = IR_{\text{int}}$

$$= \frac{181.6 \left[ 1 + 0.03i + 0.062 \left( \frac{T_{\text{FC}}}{303} \right)^2 i^{2.5} \right]}{[\zeta - 0.634 - 3i] \exp[4.18(T_{\text{FC}} - 303/T_{\text{FC}})]}$$

$$R_{\text{int}} = \frac{r_{\text{mem}} L}{A_{\text{cell}}}$$

(8) Concentration Voltage,  
 $V_{\text{conc}} = \frac{RT_{\text{FC}}}{n_e F} \ln\left(\frac{i_L}{i_L - i}\right)$

(9) Output power of the PEMFC stack,  
 $\dot{W}_{\text{FC}} = N_{\text{cell}} V_{\text{fc}} I$

---

### PEM fuel cell thermal model

---

(10) Net Heat Energy,  
 $\dot{Q}_{\text{net}} = \dot{Q}_{\text{ch}} - \dot{W}_{\text{FC}} - \dot{Q}_{\text{s,l}}$

(11) Chemical Heat  
 $\dot{Q}_{\text{ch}} = \dot{n}_{\text{H}_2, \text{cons}} \text{HHV}$

$$\dot{n}_{\text{H}_2, \text{cons}} = N_{\text{cell}} \frac{I}{2F}, \dot{n}_{\text{O}_2, \text{cons}} = N_{\text{cell}} \frac{I}{4F}, \\ \dot{n}_{\text{H}_2, \text{O}, \text{gen}} = N_{\text{cell}} \frac{I}{2F}$$

(12) Sensible and Latent Heat,  
 $\dot{Q}_{\text{s,l}} = C_{\text{H}_2} (\dot{n}_{\text{H}_2, \text{Out}} T_{\text{FC}} - \dot{n}_{\text{H}_2, \text{in}} T_{\text{amb}}) \\ + C_{\text{O}_2} (\dot{n}_{\text{O}_2, \text{Out}} T_{\text{FC}} \\ - \dot{n}_{\text{O}_2, \text{in}} T_{\text{out, comp}}) \\ + C_{\text{N}_2} (\dot{n}_{\text{N}_2, \text{Out}} T_{\text{FC}} \\ - \dot{n}_{\text{N}_2, \text{in}} T_{\text{out, comp}}) \\ + \dot{n}_{\text{H}_2, \text{O}, \text{gen}} (T_{\text{FC}} - T_{\text{amb}}) C_{\text{H}_2\text{O}} \\ + \dot{n}_{\text{H}_2, \text{O}, \text{gen}} H_v$

Inlet and Consumed Reactants Flow Rates,

$$\dot{n}_{\text{H}_2, \text{in}} = \lambda_{\text{H}_2} \dot{n}_{\text{H}_2, \text{cons}} = \lambda_{\text{H}_2} N_{\text{cell}} \frac{I}{2F}$$

$$\dot{n}_{\text{O}_2, \text{in}} = \lambda_{\text{O}_2} \dot{n}_{\text{O}_2, \text{cons}} = \lambda_{\text{O}_2} N_{\text{cell}} \frac{I}{4F}$$

---

### Compressor thermal model

---

(13) Actual Power of the Compressor

$$\frac{T_{\text{out, s}}}{T_{\text{amb}}} = \pi^{(\kappa-1/\kappa)}$$


---

$$\dot{W}_{\text{comp}} = \frac{\dot{m}_{\text{air}}(\kappa/\kappa - 1)RT_{\text{amb}}(\pi^{((\kappa-1))/\kappa})}{\eta_{\text{comp}}} \quad \eta_{\text{comp}} = \frac{T_{\text{out,s}} - T_{\text{amb}}}{T_{\text{out,comp}} - T_{\text{amb}}}$$

The performance of PEM fuel cell can be evaluated by the electrical efficiency as follows [11]:

$$\eta_{\text{PEM}} = \frac{\dot{W}_{\text{FC}} - \dot{W}_{\text{comp}}}{\dot{n}_{\text{H}_2, \text{cons}} \cdot \text{HHV}} \quad (14)$$

The operating parameters utilized in developing the PEM fuel cell model at design conditions, and all required data for estimating Gibbs function are outlined in **Table 4**.

**Table 4-** Design and operating parameters for PEM fuel cell simulation.

Operating parameters	Value [11]
Operating pressure, $P_{\text{FC}}$ (kPa)	303.96
Operational temperature, $T_{\text{FC}}$ (°C)	85
Cell operating voltage, $V$ (V)	0.68
Limiting current density, $i_L$ (A cm <sup>-2</sup> )	1.5
Stack operating current density, $i$ (A cm <sup>-2</sup> )	0.6
Number of Cell, $N_{\text{cell}}$	13,000
Electrons number, $n_e$	2
Faraday constant, $F$ (C mol <sup>-1</sup> )	96,485
Gas constant, $R$ (J mol <sup>-1</sup> K <sup>-1</sup> )	8.314
Stoichiometric rate of air, $\lambda_{\text{air}}$	2
Stoichiometric rate of hydrogen, $\lambda_{\text{H}_2}$	1.2
Active service area, $A_{\text{cell}}$ (cm <sup>2</sup> )	232
Membrane thickness, $L$ (cm)	0.00254
Vaporization heat of water, $H_v$ (J mol <sup>-1</sup> )	40,644
Higher heating value of hydrogen, HHV (kJ mol <sup>-1</sup> )	285.55
Properties at the standard condition	Value [249,250]
Enthalpy of water (Liquid), $h_0$ (J mol <sup>-1</sup> )	-285830.0
Enthalpy of water (Gas), $h_0$ (J mol <sup>-1</sup> )	-241826.0
Entropy of water (Liquid), $s_0$ (J mol <sup>-1</sup> K <sup>-1</sup> )	69.950
Entropy of water (Gas), $s_0$ (J mol <sup>-1</sup> K <sup>-1</sup> )	188.834
Entropy of hydrogen, $s_0$ (J mol <sup>-1</sup> K <sup>-1</sup> )	130.678
Entropy of oxygen, $s_0$ (J mol <sup>-1</sup> K <sup>-1</sup> )	205.148
Specific heat capacity of hydrogen, $C_{\text{H}_2}$ (J mol <sup>-1</sup> K <sup>-1</sup> )	28.86

Specific heat capacity of oxygen, $C_{O_2}$ (J mol <sup>-1</sup> K <sup>-1</sup> )	29.72
Specific heat capacity of nitrogen, $C_{N_2}$ (J mol <sup>-1</sup> K <sup>-1</sup> )	28.39
Specific heat capacity of water, $C_{H_2O}$ (J mol <sup>-1</sup> K <sup>-1</sup> )	75.95

---

### 3.3 MGT Configuration Description

The proposed MGT comprises a single-stage centrifugal compressor, a dual-axial swirler combustor, a single-stage turbine, and an integrated recuperator. As illustrated in **Figure 29**, intake air (1) is drawn into the compressor and directed towards the recuperator. Within this unit, compressed air (2) undergoes preheating (3) using high-temperature exhaust gas from the turbine (5). This process aims to decrease fuel consumption during combustion, consequently enhancing overall efficiency. Subsequently, in the combustion chamber, the preheated air is combined with fuel and undergoes combustion, resulting in the exiting of combustion byproducts (4) from the system. These actions induce rotation in the rotor, facilitating power generation through the alternator stator. To adjust the generated heat and electricity within an urban setting, a controllable bypass valve is connected to the recuperator to modify the bypass exhaust gasses flow within a system. Furthermore, as depicted in **Figure 29**, the system is equipped with a heat recovery unit (HRU) designed to fulfill the necessary heat demand. The incoming gas into the HRU (7) is influenced by factors such as the outlet gas from the recuperator (6), turbine (5), and the position of the bypass valve ( $\beta$ ).

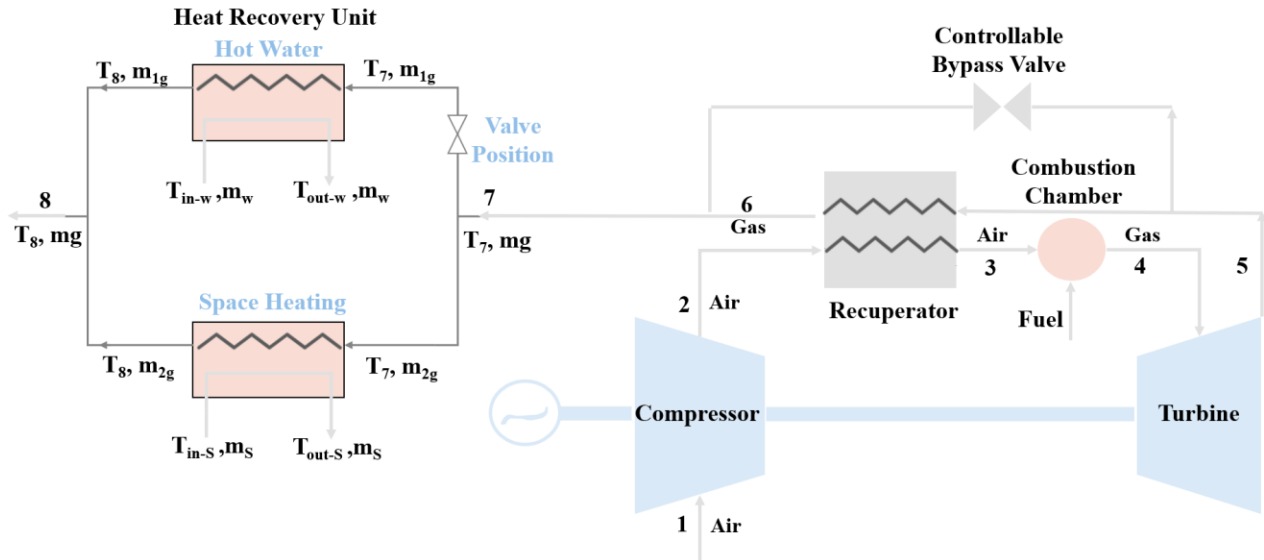
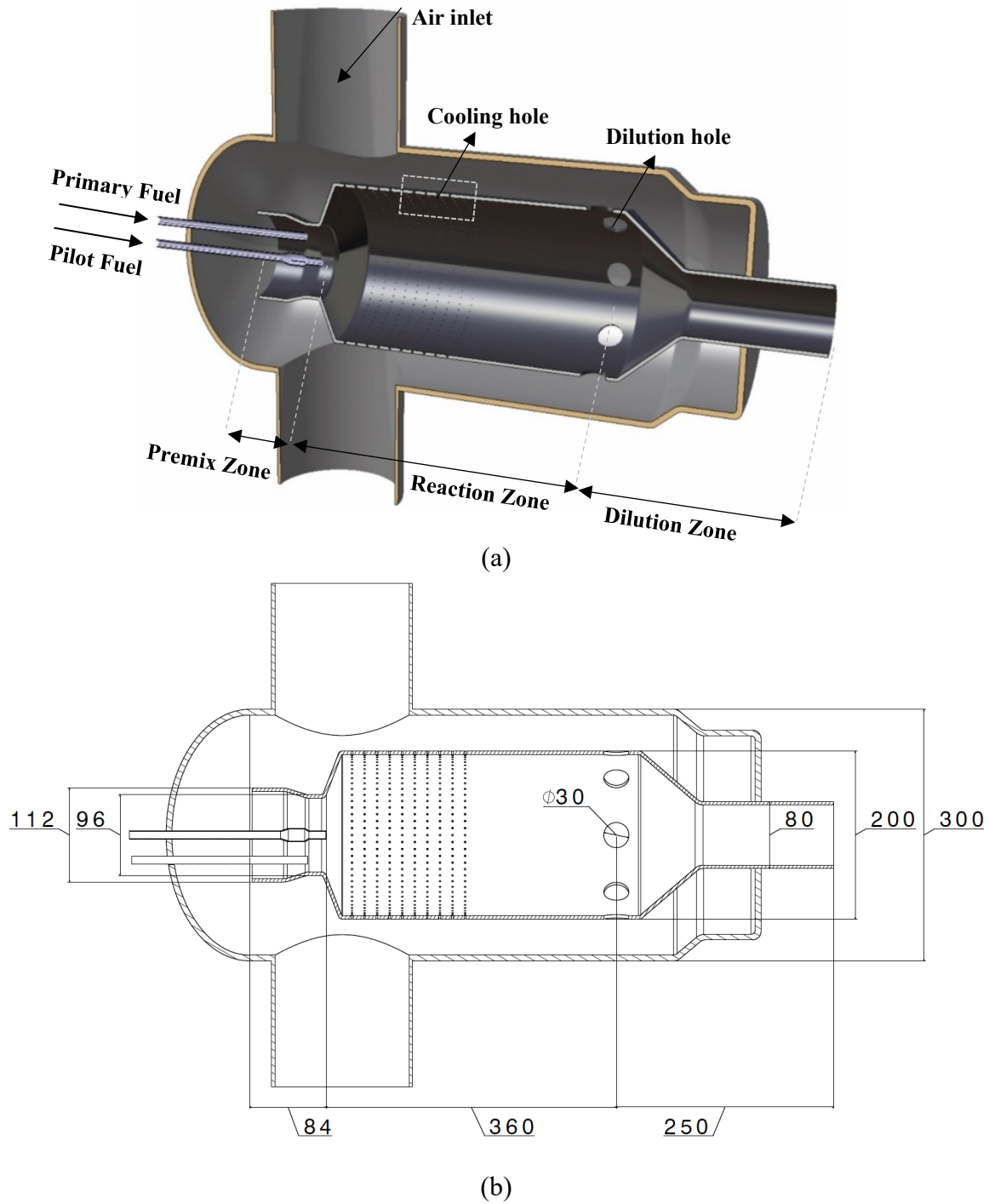


Figure 29-Schematic diagram of the recuperated MGT with a heat recovery unit.

### 3.4 Combustor Geometric Design

To evaluate the pollutant emissions from the combustor, this study employs a dual-axial swirler combustor. The combustor structure, and CAD drawing are illustrated in **Figure 30** (b) and (c), respectively. This combustor is divided into three distinct sections. At the combustor intake is the premixed zone, which serves as the combustion initiator, followed by the reaction zone, and finally, the dilution zone situated towards the end of the liner, surrounded by dilution holes. Air is channeled into the combustor via three distinct pathways: swirlers, cooling holes, and dilution orifices. The air directed through the swirlers is primarily tasked with supporting combustion in both the primary and the pilot phases, with a fraction reserved for cooling the pilot flame. Meanwhile, air passing through the cooling holes aids in reducing the temperature of the liner's walls, and the air that enters through the dilution holes is employed to lower the temperature of the exhaust gases, mitigating high-temperature emissions.



**Figure 30-**Schematic diagram of (a) MGT's combustor structure (b) CAD drawing.

### 3.5 Mathematical Modeling of MGT

All non-ideal components of MGT are evaluated based on applying mass and energy conservations along with the required design and off-design operating parameters, and some specific assumptions that are brought from [13,157,251,252].

### 3.5.1 Compressor

To achieve efficiency, outlet temperature, and the consumed power of the compressor, some crucial operational parameters are derived from a compressor map. **Figure 31** describes the pressure ratio and corrected mass flow rate ( $\dot{m}_{corr}$ ), with multiple curves that represent corrected rotational speed ( $\omega_{corr}$ ) and efficiency ( $\eta_{comp}$ ). Moving on the map at a specific pressure ratio generates numerous potential operating points based on non-dimensional parameters. To mitigate this ambiguity, an auxiliary line is introduced, facilitating the attainment of an optimal compressor function [13,249,252,253].

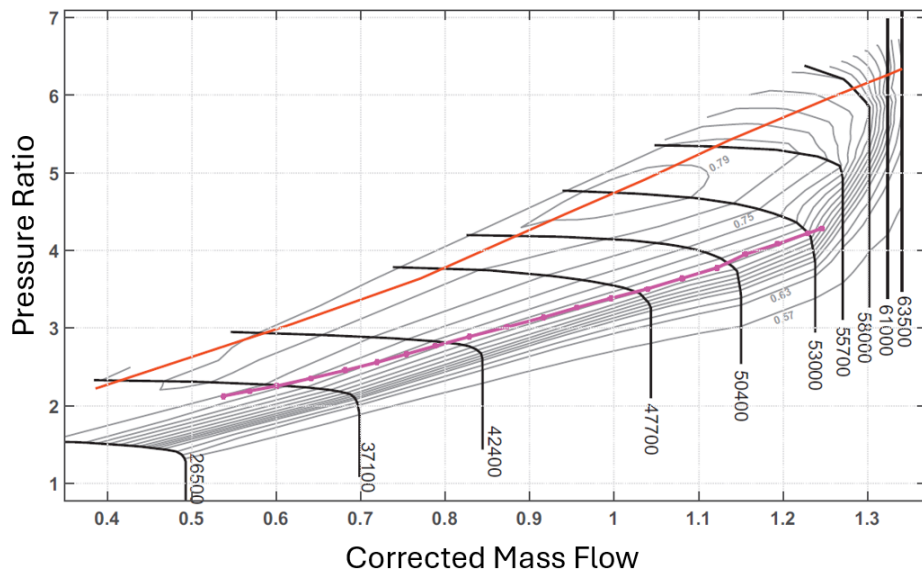


**Figure 31**-Compressor map based on pressure ratio, corrected mass flow rate and rotational speed [13].

$$\dot{m}_{corr} = \frac{\dot{m}\sqrt{T/T_{ref}}}{P/P_{ref}} \quad (15)$$

$$\omega_{corr} = \frac{\omega}{\sqrt{T/T_{ref}}} \quad (16)$$

Where  $P$ ,  $T$ ,  $P_{ref}$ ,  $T_{ref}$ ,  $\omega$ , and  $\dot{m}$  are inlet pressure, temperature, standard pressure, temperature, shaft rotational speed, and mass flow rate, respectively. The power consumption of the compressor, as determined in Eq. (19), is calculated by first deriving the optimal operating parameters from its performance map. These parameters are essential for accurately computing the compressor's

efficiency (Eq. (17)) and outlet temperature (Eq. (18)), which are critical to determining the overall power consumption [13,249,252].

$$\eta_{\text{comp}} = \frac{h_{03s} - h_{02}}{h_{03} - h_{02}} \quad (17)$$

$$T_2 = T_1 \left( \frac{1}{\eta_{\text{comp}}} \left( \left( \frac{P_2}{P_1} \right)^{\frac{\gamma_c - 1}{\gamma_c}} - 1 \right) + 1 \right) \quad (18)$$

$$\dot{W}_{\text{comp}} = \dot{m}_{\text{air}}(h_2 - h_1) \quad (19)$$

### 3.5.2 Recuperator

The output power of the MGT is highly affected by the consumed fuel, whose value is dependent on the recuperator performance. By extracting pressure drop, and efficiency data of the recuperator map (see **Figure 32**) [13], and using Eq. (20), the outlet recuperator temperature is characterized by [13,249,252,253].

$$\eta_{\text{Rec}} = \frac{q}{q_{\text{max}}} = \begin{cases} \frac{c_{P,5}\dot{m}_5(T_5 - T_6)}{c_{P,2}\dot{m}_2(T_5 - T_2)}, & c_{P,2}\dot{m}_2 < c_{P,5}\dot{m}_5 \\ \frac{(T_5 - T_6)}{(T_5 - T_2)}, & c_{P,5}\dot{m}_5 < c_{P,2}\dot{m}_2 \end{cases} \quad (20)$$

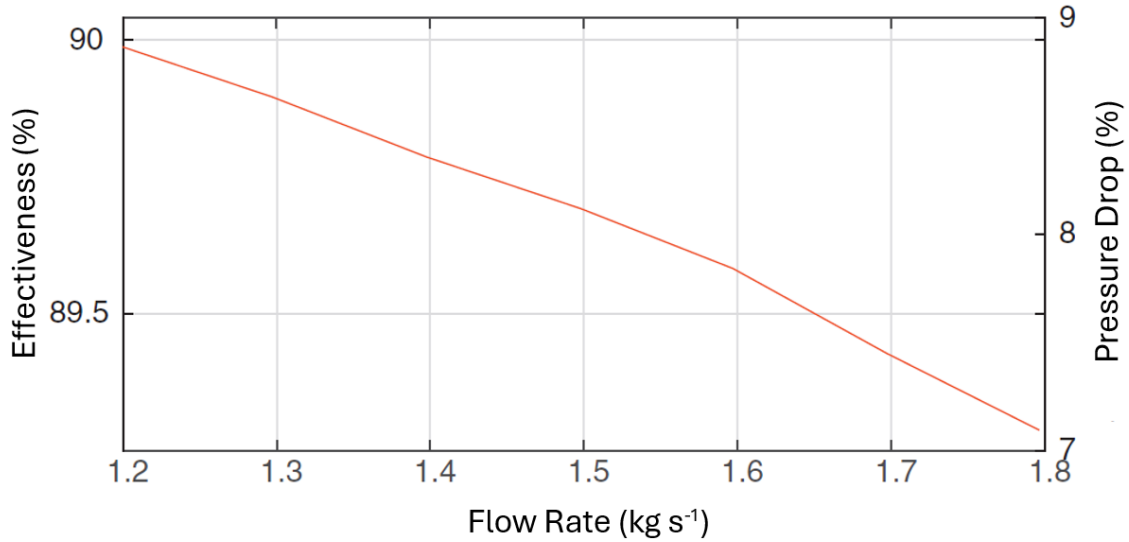


**Figure 32**-Efficiency, and pressure drop of recuperator based on mass flow rate [13].

### 3.5.3 Combustion Chamber (CC)

The thermal energy addition of the cycle takes place in the combustor, characterized by [13,249,252],

$$\dot{Q}_{cv} + \dot{n}_{fuel}h_{fuel} + \dot{n}_{air}h_{air} - \dot{n}_p h_p = 0 \quad (21)$$

By defining the fuel to air ratio on a molar basis ( $\bar{\lambda} = \frac{\dot{n}_{fuel}}{\dot{n}_{air}}$ ), applying chemical equations for three fuel scenarios with their lower heating values (kJ kg<sup>-1</sup>), including the combustion of methane, hydrogen, and biogas with 60 vol% CH<sub>4</sub>, and balancing nitrogen, carbon, oxygen, and hydrogen, the mole fractions of products elements ( $X_{N_2}$ ,  $X_{O_2}$ ,  $X_{CO_2}$ , and  $X_{H_2O}$ ) are calculated. They are used to determine the enthalpy ( $h_p$ ) of combustion products that are considered ideal gas mixtures. For combustion air mixture,  $X_{N_2} = 0.7748$ ,  $X_{O_2} = 0.2059$ ,  $X_{CO_2} = 0.0003$ ,  $X_{H_2O} = 0.019$  are considered to obtain the air enthalpy ( $h_{air}$ ). Finally, the flow rate of fuel is evaluated by Eq. (22) [13,249,252]:

$$\dot{m}_{fuel} = \bar{\lambda} \frac{M_{fuel}}{M_{air}} \dot{m}_{air} \quad (22)$$

Where  $M_{fuel}$ , and  $M_{air}$  are molecular weight of fuel and combustion air, concurrently.

### 3.5.4 Turbine

The conversion of thermal to mechanical energy happens in the turbine. Two maps for evaluating the turbine with non-constant efficiencies are considered. **Figure 33** indicates efficiency ( $\eta_{turb}$ ) as a function of working parameter (WP), and **Figure 34** shows working parameter versus mass flow rate ( $\dot{m}_{corr}$ ), and both maps are changed by corrected rotational speed ( $\omega_{corr}$ ) [13,249,252,253]. The definition of the working parameter is presented hereafter to enhance accessibility [13].

$$WP = 0.0239 \times \frac{T_4 - T_5}{T_4} C_p \times (T_4) \quad (23)$$

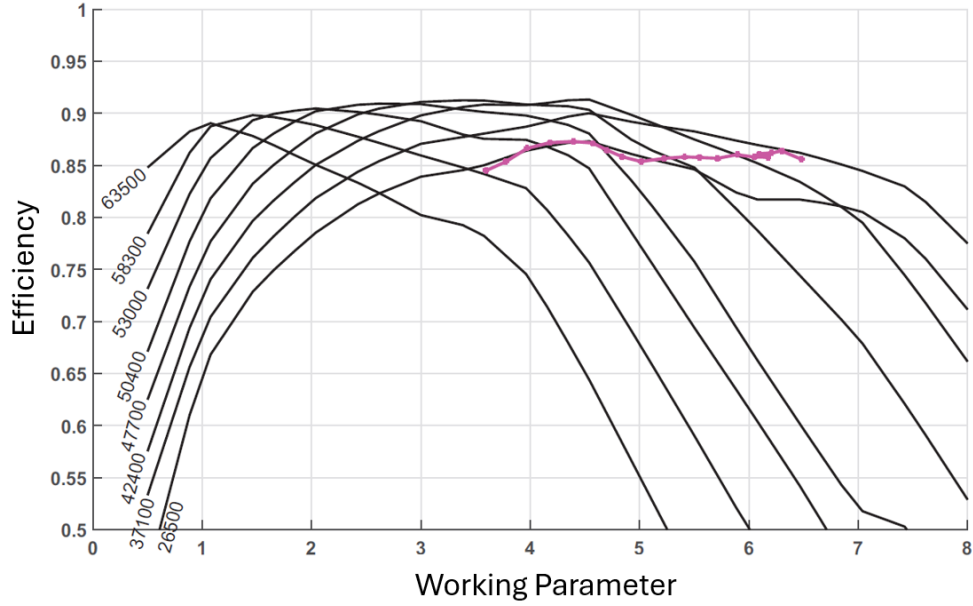


**Figure 33-**Turbine map with efficiency as a function of WP and  $\omega_{corr}$  [13].

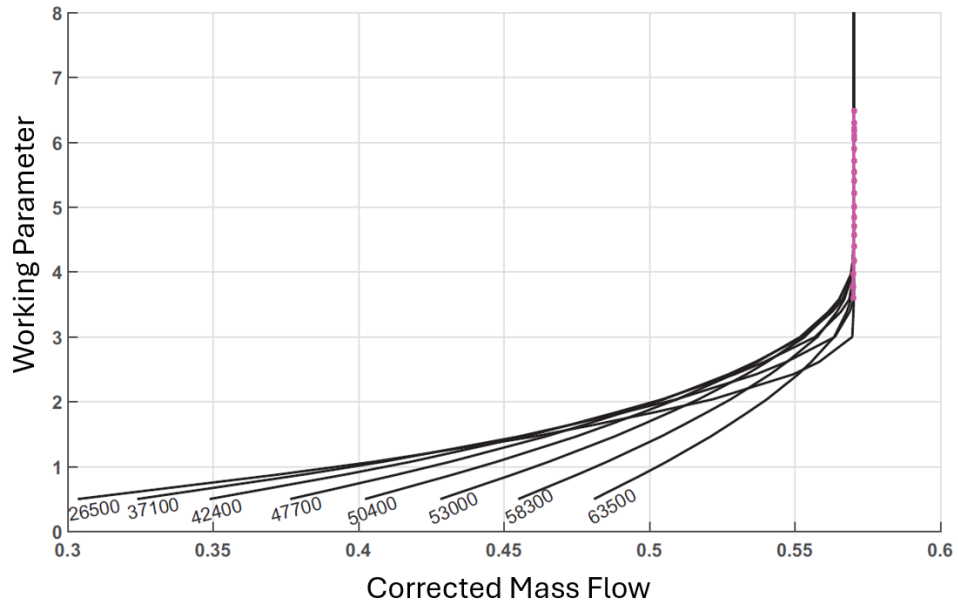


**Figure 34-**Turbine map with working parameter based on  $\dot{m}_{corr}$  and  $\omega_{corr}$  [13].

In the following, the efficiency ( $\eta_{turb}$ ), exhaust gas temperature ( $T_5$ ), and the generated electrical power ( $\dot{W}_{turb}$ ) of the turbine are achieved as [13,249,252],

$$\eta_{turb} = \frac{h_4 - h_5}{h_4 - h_{5s}} \quad (24)$$

$$\frac{T_4 - T_5}{T_4} = \eta_{\text{turb}} \left( 1 - \left( \frac{P_4}{P_5} \right)^{\frac{\gamma_h - 1}{\gamma_h}} \right) \quad (25)$$

$$\dot{W}_{\text{turb}} = \dot{m}_{\text{gas}}(h_4 - h_5) \quad (26)$$

### 3.5.5 Heat Recovery Unit (HRU)

The final component within this system comprises the Heat Recovery Unit (HRU), leveraging energy extracted from the exhaust gases of both the recuperator and turbine to serve as a vital heat source for end consumers. This study adopts a control strategy centered around meeting heating demands. The provision of required energy for heating and hot water production by the heat recovery unit relies on a complex interaction of factors: the composition of burned fuel blends, shaft rotational speed ( $\omega$ ), compressor pressure ratio ( $\pi$ ), and the position of the bypass valve ( $\beta$ ). Exhaust gases from the micro-turbine serve this purpose, with the bypass valve controlling the flow rate of these gases. To meet heating requirements, the valve adjusts from 0% to 100%. At these settings, a part of the turbine's exhaust gas passes through the recuperator, preheating incoming gas in the combustion section, while the remainder satisfies the heating needs. Notably, when the bypass valve is fully closed (0%), the heating demand is entirely met by the recuperator, where hot turbine exhaust gases preheat the incoming gas before it enters the combustion chamber. Conversely, with the bypass valve fully open (100%), heating is exclusively provided by the turbine exhaust gases, bypassing the recuperator and preventing any preheating of the gas in the combustion chamber. The inlet enthalpy of the HRU, defined as a function of the bypass valve position ( $\beta$ ), is detailed below [13,249,252].

$$h_7 = h_6(1 - \beta) + h_5\beta \quad (27)$$

### 3.6 Model Implementation and Environment Analysis

In this study, Fortran, a high-performance programming language, is employed to implement the proposed micro-gas turbine model. The program integrates comprehensive subroutines containing inputs, all data from the components' maps, nonlinear and linear equations, and complicated analytical algorithms to ensure an accurate system representation. To find the precise solution with fast convergence rates, the Newton-Raphson (N-R) method is performed. Also, the Engineering

Equation Solver (EES) is employed to access the thermodynamic properties necessary for the models. To compare and evaluate two cogeneration system options, multiple scenarios involving technological characteristics, control mechanisms, fuel types, and operational strategies are analyzed.

To analyze the combustion dynamics, and pollutant emissions of the dual-axial swirler combustor, a numerical simulation is carried out in Ansys Fluent. The governing equations for turbulence and combustion simulations are based on the steady-state conditions and the conservations of continuity, momentum, energy, and species which are derived from Ref. [254]. The simulation includes the Eddy Dissipation Concept (EDC) model to address the complex interactions between turbulence and chemical reactions. According to the EDC model, chemical reactions occur at a minor turbulent level, known as the fine scale. The simulation framework examines three fuel scenarios, including hydrogen, methane, and biogas to clarify the mechanisms of combustion reactions.

### **3.6.1 Computational Mesh Generation**

This study investigates the combustion dynamics within the dual-axial swirler combustor, focusing on three primary zones: premixing, reacting, and dilution. Air enters the combustor through the swirler inlets, cooling, and dilution holes. All combustor walls are modeled as adiabatic in this simulation. The mesh configuration for the swirler combustor, depicted in **Figure 35**, consists of 4.5 million elements, ensuring detailed resolution of the flow and combustion phenomena.

In the present work, the computational model simulates a non-reactive flow field under full-load conditions with a 9% pilot fuel proportion (PFP). The realizable k- $\epsilon$  turbulence model is employed for its effectiveness in predicting pollutant emissions within swirling flow regimes, making it a robust choice among RANS approaches. This configuration achieves a converged steady-state solution, effectively capturing critical aspects such as pollutant formation, temperature distribution, pressure, velocity, and flow patterns within the chamber. All design operating points, control states, and PFP, outlined in **Table 5**, along with validated results obtained from the MGT numerical model, are utilized in the CFD simulation. These parameters are critical to evaluate their impacts on pollutant emissions and overall combustor performance.

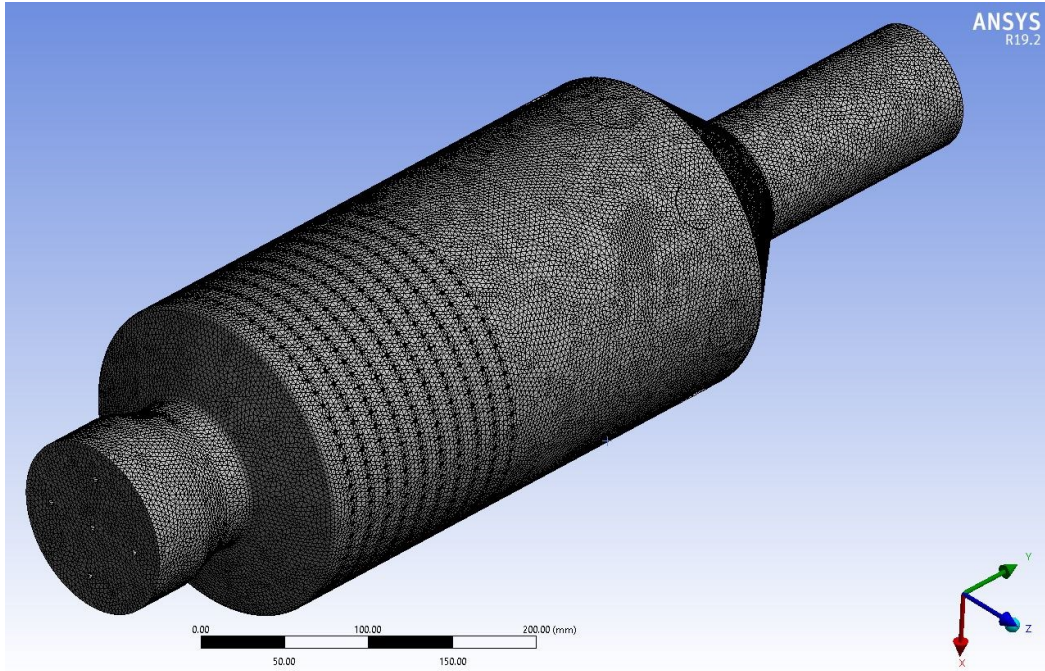


**Figure 35**-Mesh configuration for the swirler combustor.

**Table 5**-Operating conditions for modeling the recuperated MGT and simulating the swirler combustor across all fuel types at full load.

Operating parameters	Value [13,254,255]		
Shaft rotational speed, $\omega$ (rpm)	51,000		
Pressure ratio, $\pi$	4.1		
Working parameter, WP	8.9		
Turbine efficiency, $\eta_{\text{turb}}$ (%)	71		
Compressor efficiency, $\eta_{\text{comp}}$ (%)	77		
Cooling and Dilution air mass flow rate ( $\text{kg s}^{-1}$ )	Usually between 20 and 40% of $\dot{m}_{\text{air}}$		
Fuel inlet temperature ( $^{\circ}\text{C}$ )	25		
Fuel operating pressure (kPa)	86		
Pressure drops of combustor, $\Delta P$ (kPa)	0.95		
Pilot fuel proportion, PFP (%)	9		
Lower heating value of hydrogen, LHV ( $\text{kJ kg}^{-1}$ )	H <sub>2</sub> 119986.0	Biogas 30,000	CH <sub>4</sub> 50,000
Control states	Mode		
Binary '0'	System availability		
Binary '1'	System unavailability		
Bypass valve, $\beta=0$	AUX Standby	PEM fuel cell Standby	Storage tank Charge

Bypass valve, $\beta=1$	AUX Active under condition	PEM fuel cell Active under condition	Storage tank Discharge
<b>MGT's combustor structure</b>	<b>Value [157]</b>		
Dilution hole, diameter (mm)	30		
Cooling hole, diameter (mm)	3		
Premix zone (mm)	84		
Reaction zone (mm)	360		
Dilution zone (mm)	250		
Exhaust of chamber	80		
Diameter of chamber	200		

### 3.6.2 Emission Prediction Methods

The emission characteristics of the proposed micro-gas turbine, when utilizing three distinct fuels, including hydrogen, methane, and biogas, are investigated in this research study. The CFD simulation is utilized for environmental analysis, along with two precise pollutant level models. These comprehensive environmental analyses provide insights into the dynamics of CO and NO<sub>x</sub> emissions, which are critical pollutants resulting from fuels combustion. Two predicted approaches are performed on two separate platforms, including Ansys Chemkin-Pro, and Microsoft Visual Studio with Fortran 90. In the former as a chemical kinetics simulator, an equivalent chemical reactor network (ECRN) model (**Figure 36**) is created to predict NO<sub>x</sub> emissions, while in the latter the mathematical methodology (**Table 6**) is employed to measure CO emissions from the combustion of three fuel scenarios. Both mentioned prediction methods are validated against experimental data and compare with the CFD simulation. **Table 6** displays the mathematical relationship between the adiabatic flame temperature ( $TF_{ab}$ ) and CO emission formation model, incorporating a set of constants (**Table 7**) for precise emission formulation. The adiabatic flame temperature resulting from the combustion of different fuels can be estimated using thermochemical data. This calculation assumes no heat loss due to radiation, thermal conduction, or diffusion to the system's surfaces. Additionally, it assumes that the combusted gases reach a state of chemical equilibrium. The formation of CO emissions is intricately linked to the adiabatic flame temperature [9,256], a parameter influenced by various factors such as fuel composition,

C/H ratio, heat of dissociation, calorific value, and air-fuel ratio. **Table 6** provides a comparative overview of flame temperatures for hydrogen [257–259], biogas [257–259], and methane [9]. Also, Eq. (31)-(34) represent the mathematical modeling of CO emissions across various primary zones within the combustor. To ascertain the total CO emissions, the contributions from these different zones are integrated, considering the respective residence times and local conditions. This predictive method highlights the pivotal influence of flame temperature on CO emission dynamics, facilitating more precise predictions of CO emissions for a specific combustor, surpassing the accuracy of previously discussed general analytical models.

**Table 6**-Mathematical modeling of adiabatic flame temperature, and CO emission for three distinct fuel types [9,257–259].

Flame temperature	Definition of variable	Auxiliary equation	Eq.
Hydrogen			
$TF_{ab} = 2343.238 - 2.134 d_1$ $- 2.788 d_2$ $+ 2.177\phi$ $+ 0.003 d_1 d_2$ $+ 0.04 d_2 \phi$ $+ 0.063 d_1 \phi$	$d_1 = \text{Heat of dissociation (kJ mol}^{-1}\text{)}$ $d_2 = \text{Calorific value (MJ m}^{-3}\text{)} \times \text{C/H ratio (F/A)}$	-	(28)
Biogas			
$TF_{ab} = 2146.662 - 9.48 d_3$ $+ 46.804 d_4$ $- 16.173 d_5$ $+ 0.438 d_3 d_4$ $+ 3.616 d_4 d_5$ $- 0.201 d_3 d_5$	$d_3 = \text{Heat of dissociation ratio of F/A}$ $d_4 = \text{Calorific value ratio of F/A}$ $d_5 = \text{C/H ratio of F/A}$	-	(29)
Methane			
$TF_{ab}$ $= A\sigma^\alpha \exp(\xi(\sigma + \lambda)^2) \pi^B \theta^C \psi^D$	$\psi = \text{H/C atomic ratio}$ $\pi = P_{CC}/P_{Ref}$ $\theta = T_{CC}/T_{Ref}$ $\sigma = \phi (\phi \leq 1)$	$\sigma = \phi - 0.7 (\phi > 1)$ $B = a_1 + b_1\sigma + c_1\sigma^2$ $C = a_2 + b_2\sigma + c_2\sigma^2$ $D = a_3 + b_3\sigma + c_3\sigma^2$	(30)
Zone	Carbon monoxide formation	Auxiliary equation	Eq.
Premixing	If $TF_{ab} > 2000 \text{ K}$		
	$CO = 2.52 \text{Exp}(5000/TF_{ab})(0.00017 \text{Exp}(\phi/0.126)$ $+ 0.5)(P_{CC} \times 10^{-2}/1.4 \times 10^6)^{A_1} \tau^{A_2}$	$A_1 = 3.79 \text{Exp}(-1.56/\phi) - 0.8$ $A_2 = 0.875 \phi^{0.94} - 1.0$	(31)

If $TF_{ab} < 2000$ K		
	$CO = 0.122TF_{ab}^{-0.2}\phi^{-2.45}(P_{CC} \times 10^{-2}/4.34 \times 10^5)^{A_1}\tau^{A_2}$	
Reacting		$CE = 6.23 \times 10^4 \phi^{3.8}\text{Exp}(-\phi/0.56)^{1.75}$
	$CO = \text{Exp}(-CE/TF_{ab})C_{ph}(P_{CC} \times 10^{-2}/1.4 \times 10^6)^{A_3}(2 \times \tau)^{A_4}$	$C_{ph} = 4.54 \times 10^3 \phi^4\text{Exp}(-\phi/1.02)^{2.23}$
		$A_3 = -0.447\phi^{-1.87} + 0.2$
		$A_4 = -0.362\phi^{-1.9} + 0.2$
Dilution	$CO = 0.122TF_{ab}^{-0.2}\phi^{-2.45}(P_{CC} \times 10^{-2}/4.34 \times 10^5)^{-0.16}\tau^{A_2}$	- (33)
Near the Combustor Wall	$CO = (7 \times 10^{-15}\text{Exp}(TF_{ab}\tau^{0.57}/36.1)$	
	$+ 140)(P_{CC} \times 10^{-2}/4.34 \times 10^5)^{-0.62}$	- (34)

**Table 7**-Constant values across various conditions [9,256,260].

A	$\alpha$	$\xi$	$\lambda$	$a_1$	$a_2$	$a_3$	$b_1$	$b_2$	$b_3$	$c_1$	$c_2$	$c_3$
$0.3 \leq \phi \leq 1$ and $0.92 \leq \theta < 2$												
2361.76	0.12	-0.95	-1.09	0.01	0.4	0.01	-0.06	-0.44	-0.13	0.05	0.14	0.08
$0.3 \leq \phi \leq 1$ and $2 \leq \theta \leq 3.2$												
2315.75	-0.05	-1.11	-1.18	0.01	0.57	0.01	-0.05	-0.55	-0.13	0.05	0.13	0.08
$1 < \phi \leq 1.6$ and $0.92 \leq \theta < 2$												
916.83	0.29	0.15	-3.28	0.03	0.03	0	-0.08	0.26	-0.18	0.05	-0.13	0.1
$1 < \phi \leq 1.6$ and $2 \leq \theta \leq 3.2$												
1246.18	0.38	0.35	-2.04	0.04	0.01	0.02	-0.09	0.5	-0.19	0.05	-0.25	0.1

**Figure 36** represents the constructed network, wherein the flame zone is divided into 100 adiabatic perfectly stirred reactors (PSR) for the primary combustion zone. The energy equation for all PSR reactors has been solved by considering the equal input temperatures and operating pressures extracted from the numerical simulation of the MGT. However, the equivalence ratio distribution in this set of reactors has been accurately determined based on the results of previous researchers' numerical simulations [261–266] and implemented on the flame front position. Also, the post-flame zone, including cooling, dilution, and bypass, is modeled by one plug flow reactor (PFR), and finally, the network is completed by other components, including inlets, splitters, mixers, and exhaust. After defining reactor geometry in Ansys Chemkin-Pro to set up the simulation, the initial and boundary conditions are specified by calling the design operating points (**Table 5**), the calculated data from the MGT model developed in Fortran and utilizing an appropriate comprehensive chemical kinetic mechanism. Finally, the simulation results are visualized, and the NO<sub>x</sub> pollutants are calculated accurately for three mentioned fuels, whose databases, including chemical kinetics mechanism, thermodynamics, and gas transport, are extracted from [267–269]. The operating conditions and control states required in modeling the recuperated MGT of all fuels at 100% load and 9% pilot fuel proportion (PFP), along with the combustor's geometry, are specified in **Table 5**. In finite-rate chemistry models, the species conservation equations for all reactants are solved directly throughout the simulation, a computationally intensive process due to the complexity of detailed kinetic mechanisms. To mitigate this computational expense, the present study employs reduced or global kinetic mechanisms during the Chemkin calculation

process. These mechanisms simplify the inclusion of kinetics in finite-rate combustion models, balancing accuracy with computational efficiency.

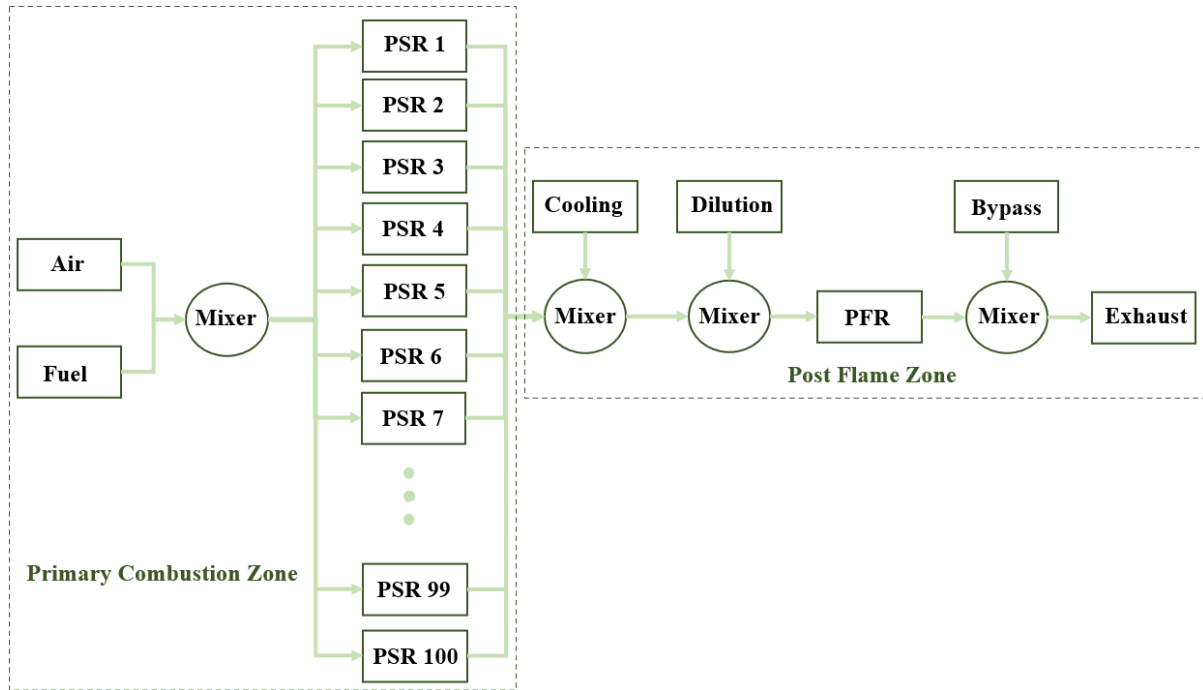


Figure 36-ECRN model developed in Ansys Chemkin-Pro for analyzing NO<sub>x</sub> emissions.

### 3.6.3 Analytical Algorithm Flowchart

Figure 37 indicates the workflow for the numerical model and environmental pollutant projection of the recuperated MGT. The algorithm illustrates the process of achieving a steady-state equilibrium among the MGT's components. It details the interactions among the MGT's shaft speed, the bypass valve's position, and the fuel consumption rate, ensuring efficient and effective operation under steady-state conditions. For a specified compressor pressure ratio and shaft rotational speed, two critical parameters—corrected mass flow rate and efficiency—are derived from the compressor's performance characteristics (Figure 31). This step enables the calculation of essential compressor outputs, including air mass flow rate, outlet temperature, and pressure, determining consumed power. Within this framework, three iterative loops are simultaneously resolved. The initial unknowns, the inlet temperatures at the combustion chamber ( $T_3$ ) and the turbine ( $T_4$ ) are essential for calculating the fuel mass flow rate across three fuel scenarios. Concurrently, the turbine's outlet temperature ( $T_5$ ) is estimated to ascertain the working parameter (WP) using Eq. (23). Two dimensionless quantities—corrected mass flow rate and efficiency—

are then extracted from the turbine performance maps as depicted in **Figure 33**, and **Figure 34**, based on the WP and specified shaft rotational speed, to determine the gas mass flow rate and generated power. Following this, the bypass valve position ( $\beta$ ) is obtained based on the heating control strategy model algorithm (see **Figure 38**). The specified  $\beta$  with the effectiveness extracted from the recuperator map (see **Figure 29**), the outlet temperature of the recuperator is calculated ( $T_6$ ) (Eq. (20)), updating the inlet temperature of the combustion chamber ( $T_3$ ) until convergence is achieved. The iterative refinement of the fuel mass flow rate leads to adjustments in the gas flow rate and a subsequent adjustment of  $T_{in,turb}$  based on precisely calculated values. A steady-state solution is reached upon full convergence of the algorithm, providing outputs such as fuel mass flow rate, electrical power, heat output, and electrical and heating efficiency. Subsequently, the validated results are leveraged to assess pollutant levels using three distinct predictive approaches: CFD simulations, the ECRN model in ANSYS Chemkin-Pro, and a mathematical methodology. Finally, a comparative analysis between these methods is conducted to evaluate  $NO_x$  and CO emission concentrations. This comprehensive evaluation offers critical insights into the environmental impact of the recuperated MGT, enhancing the understanding of its emission characteristics. The pollutant concentrations, which are measured by the mentioned predictive methods, are converted into the value of 15%  $O_2$  using Eqs. (35), and (36) [254,270].

$$NO_{ppmv,Normalized @ 15\% O_2} = NO_{ppmv,Measured} \times \frac{20.9 - O_{2Ref}}{20.9 - O_{2Measured}} \quad (35)$$

$$CO_{ppmv,Normalized @ 15\% O_2} = CO_{ppmv,Measured} \times \frac{20.9 - O_{2Ref}}{20.9 - O_{2Measured}} \quad (36)$$

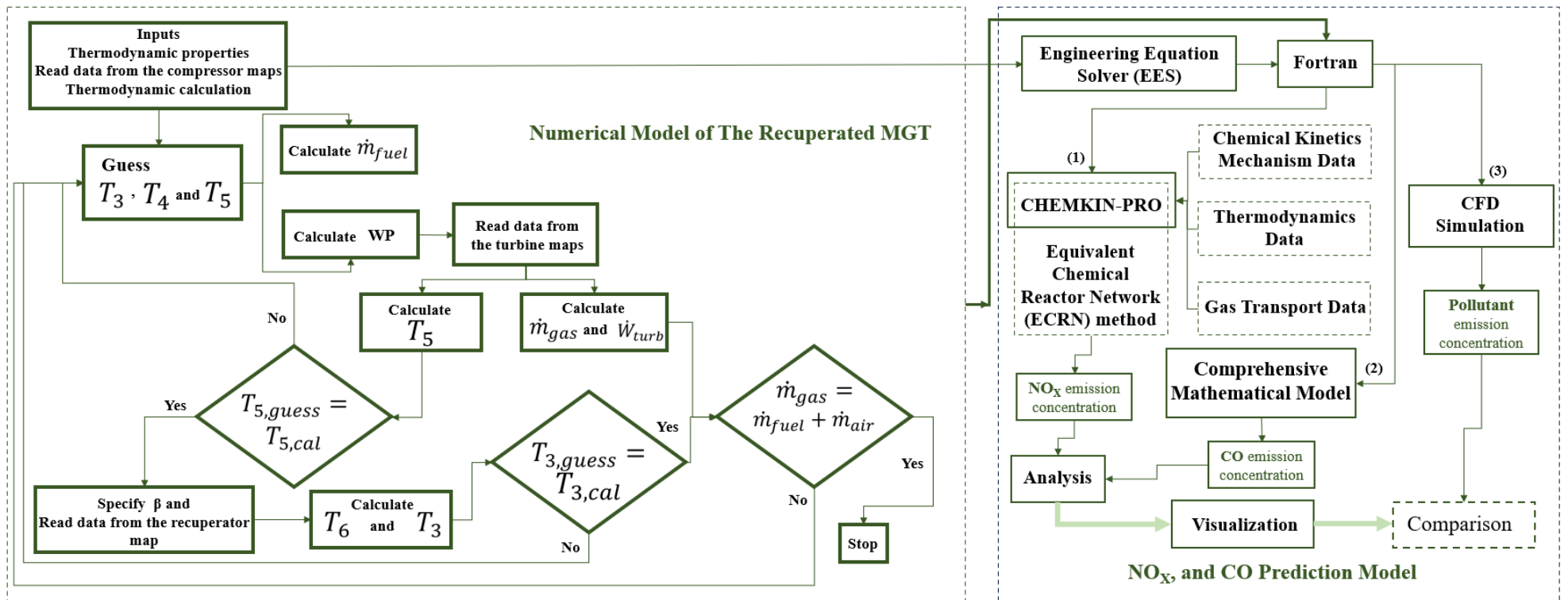
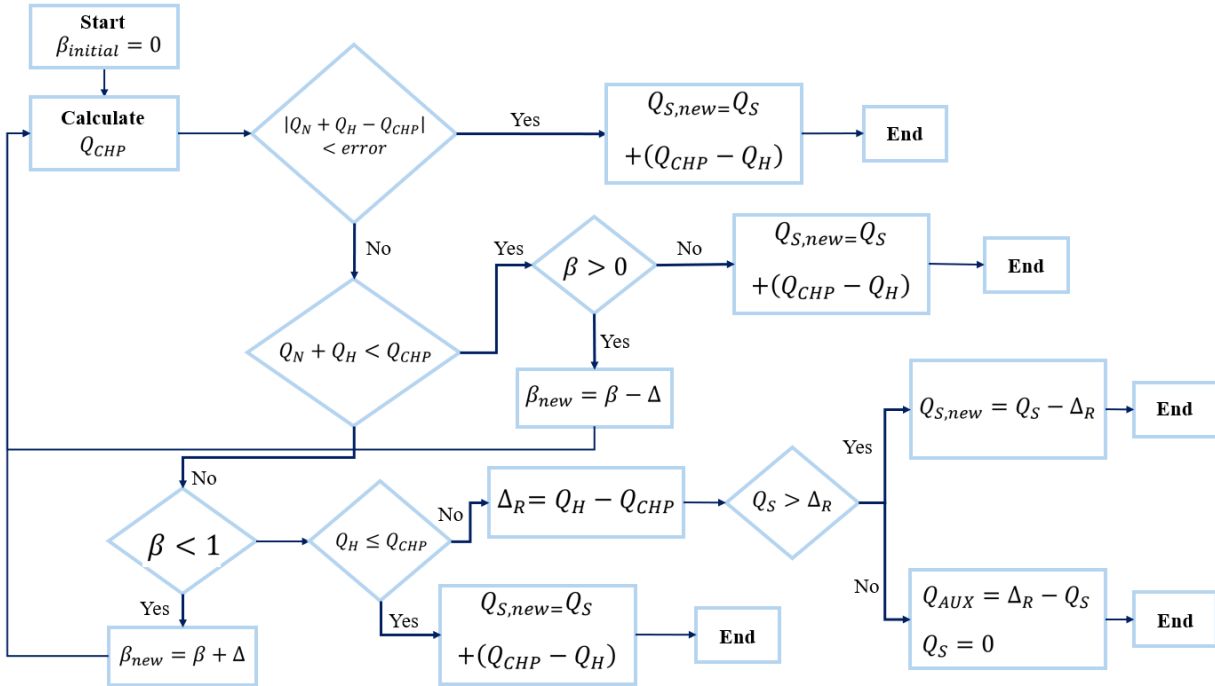


Figure 37-Flow chart illustrating the numerical model and pollutant emissions analysis from a recuperated MGT.

### 3.6.4 Heating Control Model Flowchart

The possibility of meeting heating demand through the proposed cogeneration systems is studied according to the demand response control. An algorithm flowchart depicting the heating control strategy for the MGT system is shown in **Figure 38**. It represents a dynamic model for the CHP system to display the accurate temporal aspects and include control components that allow for understanding the objects' behavior over time. The algorithm involves three critical considerations. The entire heating model entails a comparison between the heating demand ( $Q_H$ ), the generated heat from the CHP system ( $Q_{CHP}$ ), and the required heat to fill the storage tank ( $Q_N$ ). When the amount of  $Q_{CHP}$  exactly matches the sum of  $Q_H$  and  $Q_N$ , it becomes necessary to fill the storage tank. The valve can be adjusted from 0% to 100% based on the heating demand. If  $Q_{CHP}$  exceeds the sum of  $Q_H$  and  $Q_N$ , it demonstrates that the CHP system can meet the heating demands, and the bypass valve should be gradually closed. When fully closed, filling the storage tank becomes a requirement. In the final scenario, if  $Q_{CHP}$  is less than the sum of  $Q_H$  and  $Q_N$ , the bypass valve must be steadily opened until it reaches 100%. In this step, the heating demand and heat generated by the CHP system are compared. If the heating demand is lower than the generated heat, the model proceeds to fill the storage tank. Otherwise, to meet the heating demand, the storage tank must be utilized. In case  $Q_{CHP}$  and the storage tank are insufficient to meet the heating demand, the auxiliary boiler must be available as a backup for the system. In the final scenario, when the combined heat output from the CHP system, storage tank, and auxiliary boiler is insufficient to meet peak heating demands, the PEM fuel cell must be activated to compensate for the shortfall.



**Figure 38**-Heating control strategy model flowchart of the recuperated MGT coupled with a heat recovery unit.

**Figure 39** presents various scenarios considered in the design of a heating control strategy illustrated in **Figure 38** for the CHP system. A detailed explanation of each scenario is provided below.

In the first set of scenarios (1-3), the heating demand ( $Q_H$ ) is lower than the minimum generated heat ( $Q_{CHP}$ ) from the CHP system. In scenario 1, the sum of  $Q_H$  and the required heat to fill the storage tank ( $Q_N$ ) is less than the minimum value of  $Q_{CHP}$ , maintaining the bypass valve at 0%. In scenario 2, the sum of  $Q_H$  and  $Q_N$  is between the minimum and maximum heat generated by the CHP system, requiring the adjustment of the bypass valve position between 0% to 100% to meet heating demands and charge the storage tank. However, in scenario 3, the total  $Q_H$  and  $Q_N$  exceed the maximum  $Q_{CHP}$ , necessitating a fully open bypass valve (100%).

In the second set of scenarios (4–6), the heating requirement ( $Q_H$ ) is between the minimum and maximum heat outputs of the CHP system. Scenario 4 assumes a fully charged storage tank, allowing the bypass valve to modulate between 0% to 100% based on  $Q_H$ . In scenario 5, the recuperator bypass valve is adjusted between 0% to 100% to meet heating demands ( $Q_H$ ) and to fill the storage tank because the sum of  $Q_H$  and  $Q_N$  is within the CHP system’s capacity. Conversely, Scenario 6 requires the bypass valve to remain fully open (100%) to meet the heating

demand and charge the storage tank since the sum of  $Q_H$  and  $Q_N$  is more than maximum capacity of CHP system.

In the third set of scenarios (7–9), the heating demand ( $Q_H$ ) exceeds the maximum value of  $Q_{CHP}$ , leading to positioning the bypass valve to 100%. In Scenario 7, the storage tank is utilized to meet the heating demand. In scenario 8,  $Q_{CHP}$  and the storage tank are insufficient to meet the heating demand, necessitating the activation of the auxiliary boiler as a backup heat source. In Scenario 9, if the storage tank is depleted, the auxiliary boiler must be on standby to supply the required  $Q_H$ .

To make this model capable of meeting heating needs, particularly at peak load, an integrated strategy involving a 100% bypass valve position, utilization of the storage tank, and the availability of both the auxiliary boiler and PEM fuel cell as backup heat sources is imperative. In the final set of scenarios (10–12), the focus is on peak heating conditions where the bypass valve is fully open. In scenario 10, the heating demand is provided by the maximum  $Q_{CHP}$ , full utilization of the storage tank, and activation of the auxiliary boiler. However, in scenarios 11 and 12, neither of these solutions is able to meet peak heating demands, so the proton exchange membrane (PEM) fuel cell must be activated to compensate for the heating shortage.

	Scenario 1	Scenario 2	Scenario 3	Scenario 4	Scenario 5	Scenario 6
$Q_{Aux}$	$Q_H + Q_N < Q_{CHP, min}$ and $Q_H < Q_{CHP, min}$	$Q_H + Q_N = Q_{CHP}$ and $Q_H < Q_{CHP, min}$	$Q_H + Q_N > Q_{CHP, max}$ and $Q_H < Q_{CHP, min}$	$Q_H + Q_N = Q_{CHP}$ and $Q_{CHP, min} < Q_H < Q_{CHP, max}$	$Q_{CHP, min} < Q_H + Q_N < Q_{CHP, max}$ and $Q_{CHP, min} < Q_H < Q_{CHP, max}$	$Q_{CHP, max} < Q_H + Q_N$ and $Q_{CHP, min} < Q_H < Q_{CHP, max}$
$Q_{Storage}$						
$Q_{CHP, max}$			$Q_N$		$Q_N$	$Q_N$
$Q_{CHP, min}$		$Q_N$	$Q_N$		$Q_N$	$Q_N$
	$Q_N$			$Q_H$	$Q_H$	$Q_H$
	$Q_H$	$Q_H$	$Q_H$			

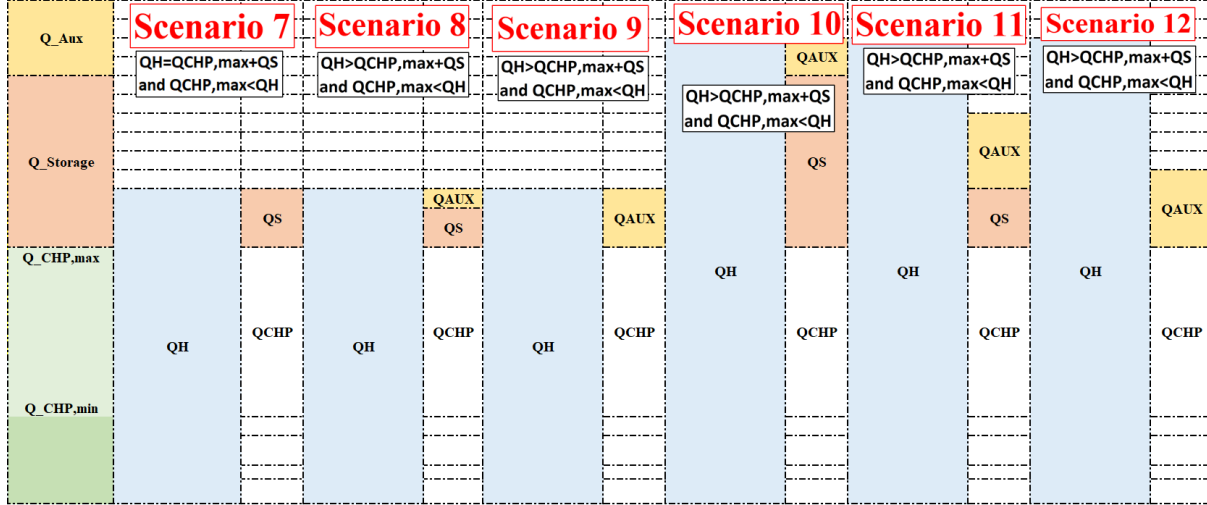


**Figure 39**-Various scenarios involved in modeling the heating control strategy for the CHP system comprised of MGT and HRU.

Based on the described numerical simulation and heating control strategy models, this section defines the valve position ( $\alpha$ ), as well as the heating ( $\eta_{th}$ ) and electrical ( $\eta_{el}$ ) efficiencies of the proposed CHP system. Determining the valve position enables operators to regulate the specific gas flow quantities required to deliver heating to designated spaces, distribute  $(1-\alpha)\%$ , and facilitate hot water provision with  $\alpha \%$  [13,249,252].

$$(\eta_{el})_{CHP} = \frac{\dot{W}_{turb} - \dot{W}_{comp}}{\dot{m}_{fuel} LHV_{fuel}} \quad (37)$$

$$Q_{CHP} = [(\alpha \dot{m}_{gas} + (1 - \alpha) \dot{m}_{gas})(h_7 - h_8)] \quad (38)$$

$$\alpha = (\dot{m}_w c_{p,w}(T_{out,w} - T_{in,w})) / (\dot{m}_{gas}(h_7 - h_8))$$

$$(\eta_{th})_{CHP} = \frac{Q_{CHP}}{\dot{m}_{fuel} LHV_{fuel}} \quad (39)$$

### 3.6.5 Case study

The present study analyzes various commercial micro-gas turbines (MGTs) using their specific design parameters, including pressure ratio, rotational speed, component efficiencies, and other critical specifications. The developed model in this thesis is capable of simulating different CHP gas turbine units under their designed operating conditions. The simulated outputs for nominal

power, electrical efficiency, and turbine inlet temperature are validated against actual data, presented in **Table 8**, demonstrating the model's accuracy. **Table 8** summarizes all MGT models evaluated in the proposed simulation framework.

**Table 8**-The main characteristics of the commercial MGTs.

Model [271]	Manufacturer	Electrical power (kW)	Pressure ratio, $\pi$	Shaft rotational speed, $\omega$ (rpm)	Inlet temperature of turbine (°C)	Recuperator	Electrical efficiency, $\eta$ (%)
C30	Capstone	30	3.2	96,000	840	Yes	26
AS75	AlliedSignal	75	3.7	72,000	900	Yes	28.5
TA45	Elliott	45	4.3	116,000	870	Yes	30
T100	Turbec (Ansaldo)	100	4.5	70,000	950	Yes	30
PW70	PowerWorks	70	3.3	60,000	870	Yes	33
TG80CG	Bowmen	80	4.3	68,000	680	Yes	25-28
Bladon12	Bladon	12	2.5	134,000	750	Yes	25
ET45	ETgroup	45	3.5	60,000	870	Yes	28
<b>GT333s</b>	<b>FlexTurbine</b>	<b>333</b>	<b>4.1</b>	<b>51,000</b>	<b>1300</b>	<b>Yes</b>	<b>37</b>
E100	ENN	100	4.2	51,000	927	Yes	26
T2-200	Wisdomturbine	240	7.5	54,000	1100	No	22.9

While many companies offer a range of CHP gas turbine units for consumers, as presented in **Table 8**, it is rare for customers to run these units exclusively at their designed operating point. Most users prefer the flexibility to adjust their usage according to specific demands. Consequently, the manufacturer-provided design point data is insufficient to accurately assess energy requirements across diverse scenarios, which are shown in **Figure 39**. Ideally, the product should perform effectively at the design point and under off-design (part-load) conditions. Therefore, a more comprehensive model of micro-gas turbines is essential to fully understand their performance across the entire operational spectrum. In this thesis, the model's innovation is not just theoretical, but also practical. It can dynamically adjust outputs based on specific energy demands throughout the entire operational range, making it effective for both design point and off-design (part-load) conditions.

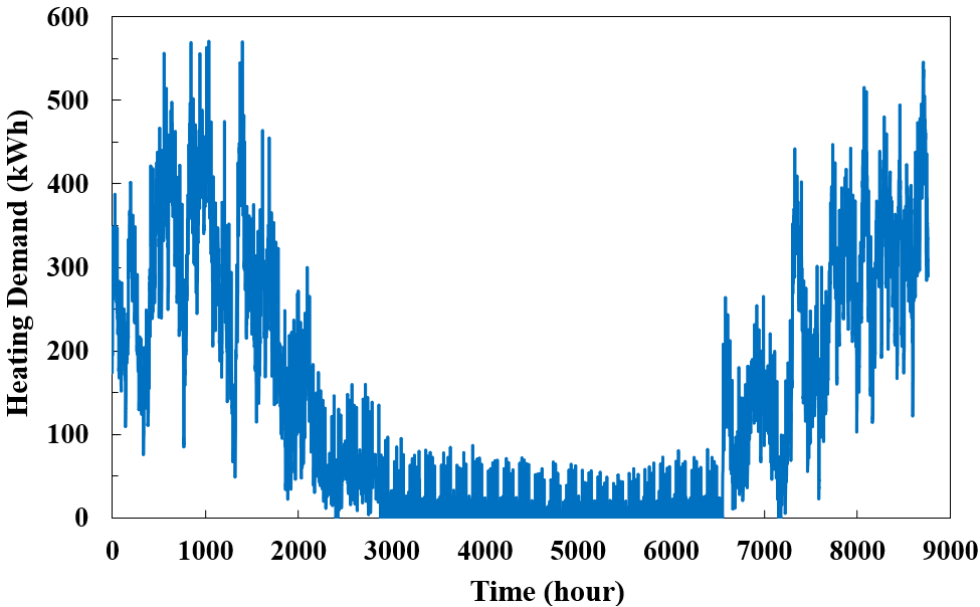
The implemented model for the CHP systems is analyzed through a case study of five residential buildings in Karlsruhe, Germany. These buildings are currently equipped with two mini gas-Otto engine CHP systems, supported by an auxiliary boiler and thermal storage tanks, to meet both electrical and heating demands. The project aims to replace the existing COMUNA cogeneration modules type 2726 with a micro-gas turbine and PEM fuel cell powered by renewable fuels. Information from P&ID files, heating, and electrical demand profiles, and the capacities of the storage tank and auxiliary boiler are integrated into the model. The building schematic and the time-dependent heating demands of the case study are depicted in **Figure 40** (a) and (b), respectively. The peak electrical demand for the five residential buildings is reported to be 120 kWh. Also, the technical specifications of the 2726 series are detailed in **Table 9**.

Based on the available MGTs in the market, as shown in **Table 8**, the GT333s model from FlexTurbine, which provides 333 kW of nominal electrical power, is selected for the simulation. Then, a comprehensive evaluation and comparison of the proposed cogeneration systems, including the micro-gas turbine and PEM fuel cell is conducted across various scenarios. These scenarios encompass different technological, fuel, control, and operational conditions, providing a thorough understanding of the systems' performance and supporting informed decision-making in selecting technology options for cogeneration systems. The technological scenario focuses on meeting the electrical demands of the case study, involving a detailed assessment of system performance for various options, particularly the proposed recuperated MGT and PEM fuel cell. The objective is to identify the most efficient cogeneration technology to produce the highest electrical output from a given fuel input. In the fuel scenario, different fuel types are evaluated to identify the optimal source for the cogeneration system, considering parameters such as heating, electrical output, and overall efficiency. This study performs a comparative analysis of renewable fuels, including hydrogen and biogas, against conventional fossil fuels, including methane, under various operational conditions to assess the performance of the MGT. Additionally, the analysis focuses on the MGT's function at part-load conditions (i.e., 40% electrical production) to determine the fuel consumption required to meet specific electrical demands. Additionally, a demand response control strategy is proposed to enhance the availability and efficiency of cogeneration systems in response to fluctuating heating demands. This control scenario incorporates a dynamic heating management system that modulates heating output according to real-time demand variations, thereby optimizing energy consumption and meeting specific thermal

requirements. Lastly, the operational scenario aims to assess the performance of cogeneration technologies by adjusting key operating parameters. This evaluation will inform future research on optimizing the size and function of the proposed system, making it suitable for urban applications.



(a)



(b)

**Figure 40-** (a) Screenshot of five residential buildings in Karlsruhe, Germany, displaying house numbers, (b) Heating demand (kWh).

**Table 9-** Technical specifications for the mini Gas-Otto engine CHP system series 2726.

<b>Model</b>	<b>Fuel</b>	<b>Electrical power</b>	<b>Thermal power</b>	<b>Electrical efficiency</b>	<b>Thermal efficiency</b>	<b>Overall efficiency</b>
COMUNA METALL CHP module 2726-02	Natural gas	50 kW	92 kW	32.0 %	59.0 %	91.0 %

## Chapter 4: Results and discussion

### 4.1 Technological Analysis Results

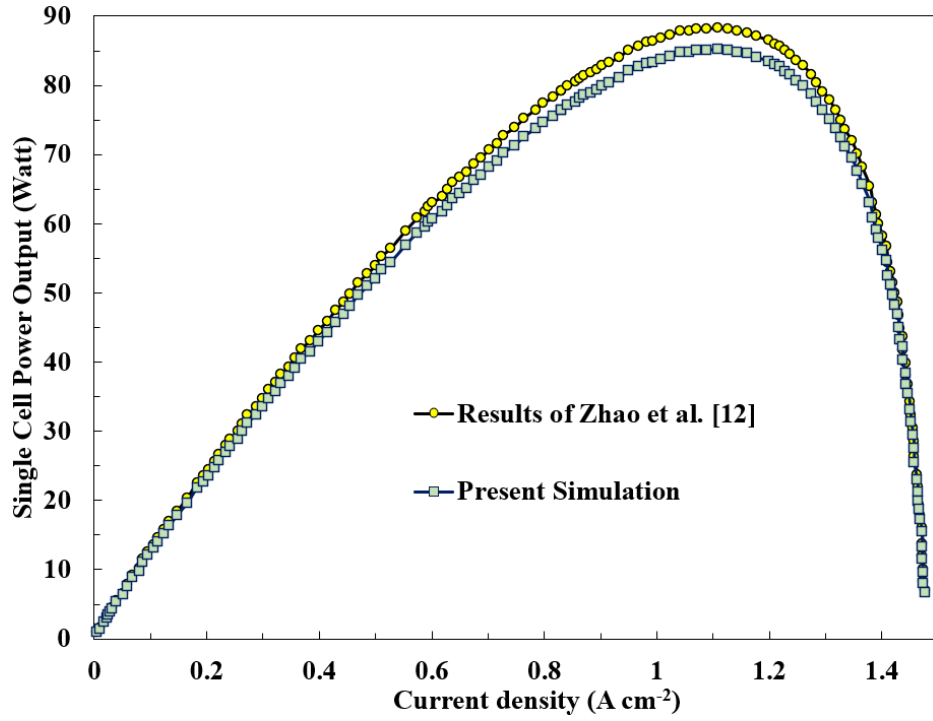
#### 4.1.1 Numerical and Thermodynamic Modeling Validation

The validation of the thermodynamic results of the PEM fuel cell and the numerical simulation for the recuperated MGT fueled by methane at design operating points with the previous modeling analyses are presented in **Table 10**. The former is compared with the research conducted by Zhao et al. [12], and the latter is validated with experimental data presented by Rist et al. [13]. This comparison underscores the study's accuracy, highlighted by minimal discrepancy.

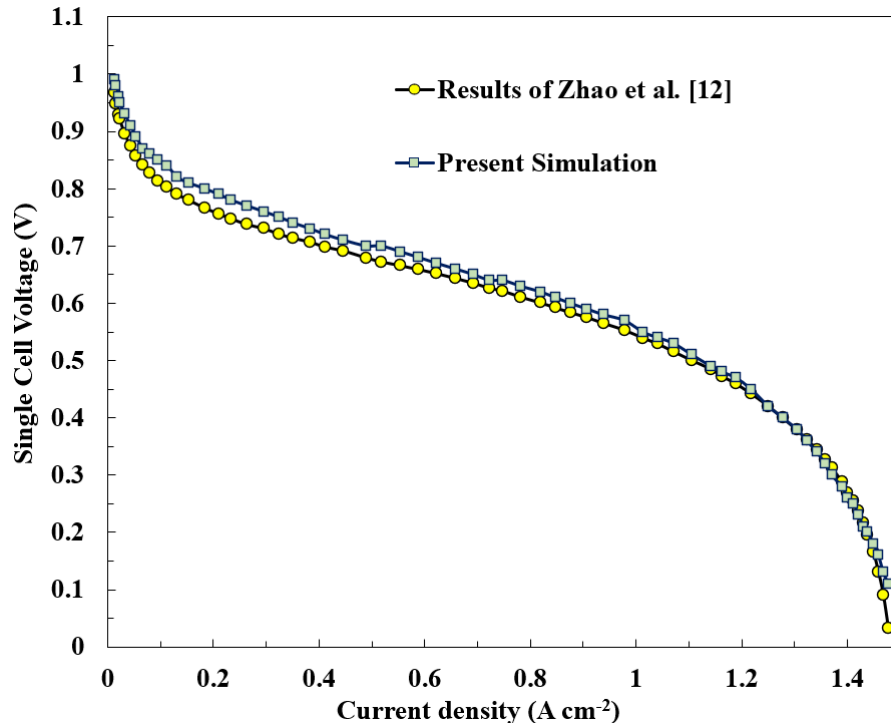
**Table 10**-The validation of the proposed study and the work of Zhao et al. [12] and Rist et al. [13].

Technology	Parameter	Mean Absolute Error (%)
Fuel Cell	Voltage, V, (V)	7.62
	Power output (Watt)	3.5
MGT (The first scenario)	Fuel mass flow rate, $\dot{m}_{\text{fuel}}$ ( $\text{kg s}^{-1}$ )	1.28
	Electrical power, $\dot{W}_{\text{NET}}$ (kW)	1.08
	Electrical efficiency, $\eta_{\text{el}}$ (%)	0.4

**Figure 41** (a) and (b) illustrate the validation of single-cell power (Watt) and voltage (V) variations based on current density ( $\text{A cm}^{-2}$ ), respectively. The figure demonstrates minor discrepancies between the presented simulations and the study by Zhao et al. [12] for the PEM fuel cell modeling, confirming the high precision of the results.



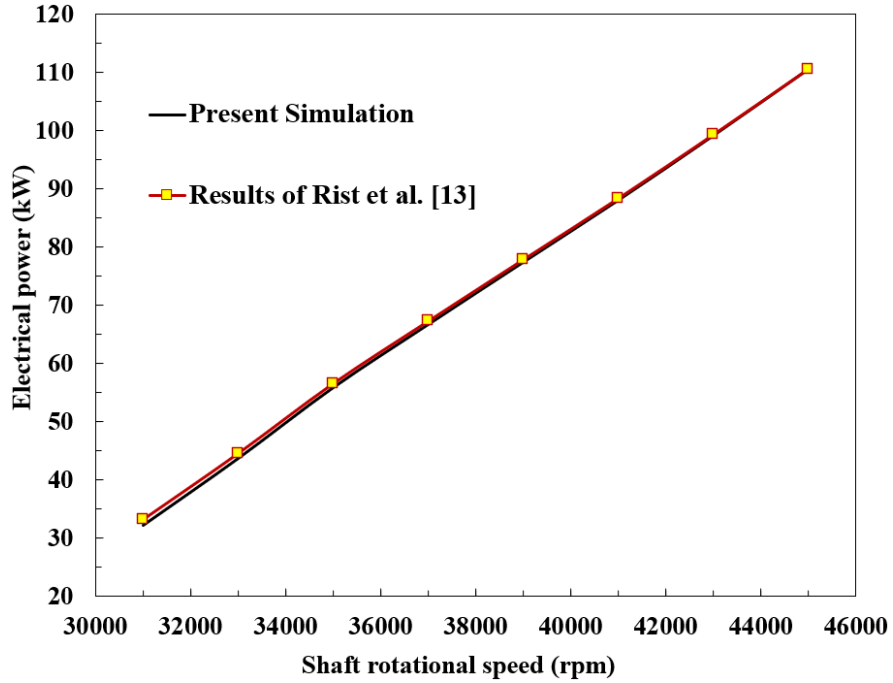
(a)



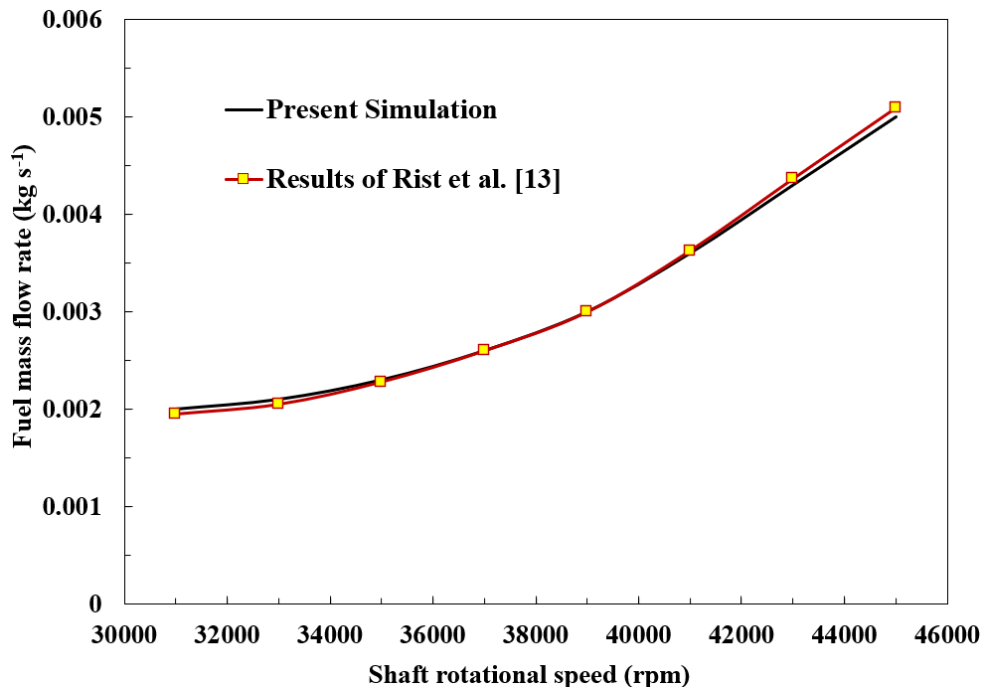
(b)

**Figure 41-**Validation results of the present modeling and the conducted work [12] regarding single-cell (a) Power output (b) Voltage against current density.

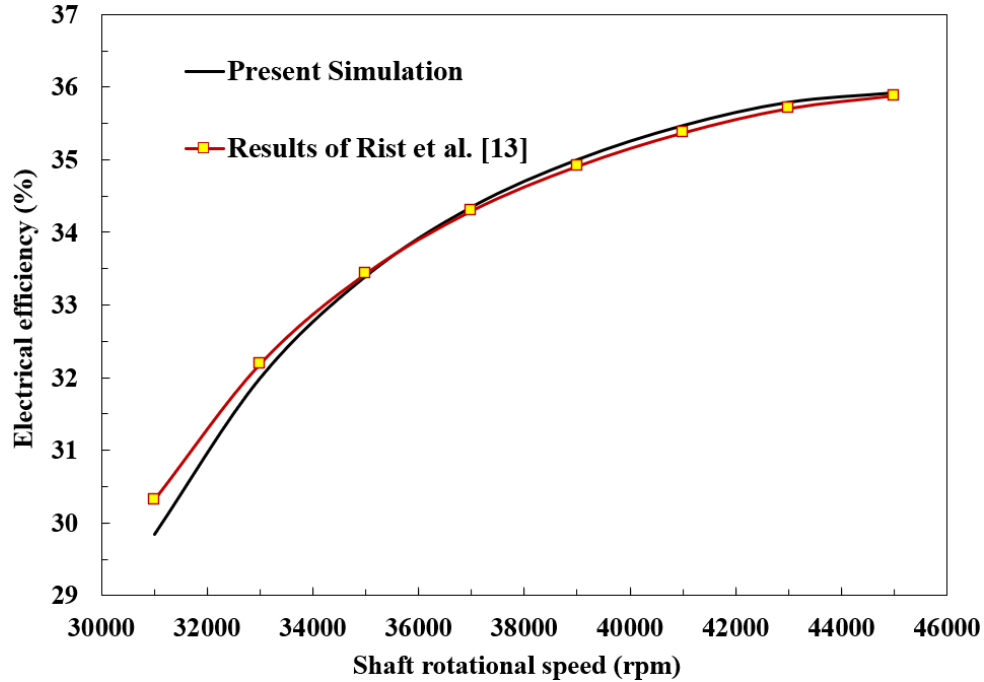
Additionally, **Figure 42** (a), (b), and (c) display the electrical power (kW), fuel mass flow rate ( $\text{kg s}^{-1}$ ), and electrical efficiency (%) versus shaft rotational speed (rpm) for both the numerical simulation and the experimental work by Rist et al. [13].



(a)



(b)



(c)

**Figure 42-**Validation results of the present numerical simulation and Rist's work [13] regarding (a) Electrical power (b) fuel mass flow and (c) electrical efficiency against shaft rotational speed.

#### 4.1.2 Comparison scenarios

In evaluating and comparing cogeneration technologies, it is essential to consider a range of scenarios containing different technological, fuel, control, and operational conditions. This study systematically analyzes these scenarios to provide a comprehensive understanding of the performance and to support informed decision-making in selecting technology options for cogeneration systems.

##### 4.1.2.1 Technology scenario

The technological scenario includes assessing system functionality across various options, specifically the proposed recuperated MGT and PEM fuel cell, aiming to determine the most efficient cogeneration system technology at the same amount of burned fuel. **Table 11** illustrates a comparative assessment of MGT (GT333s model from FlexTurbine) and PEM fuel cell performance at their design operational states that are specified in **Table 5**, and **Table 4**, respectively. Considering specific parameters, the air consumption rates for the MGT ( $0.949 \text{ kg s}^{-1}$ ) and PEM ( $0.89 \text{ kg s}^{-1}$ ) systems are determined when the same amount of  $\text{H}_2$  ( $0.018 \text{ kg s}^{-1}$ ) is

combusted. The data exhibits a notably higher power generation for a singular unit of PEM (1221.9 kW) compared to the MGT unit (627.11 kW). Furthermore, the compressor power consumption is lower for the PEM fuel cell (114.78 kW) than the second technology option (293.44 kW). Consequently, the net electrical power output from the MGT (333.67 kW) necessitates the installation of one MGT unit to meet the electrical requirements of the mentioned case study. Calculations based on Eq. (14) and (37) demonstrate electrical efficiencies of 41.34% for PEM fuel cells and 37.13% for MGT. The higher electrical efficiency of the PEM fuel cell can be attributed to its lower irreversible losses and higher operational efficiency of the electrochemical reactions compared to the mechanical processes in the MGT.

The net heat energy ( $\dot{Q}_{net}$ ) from the PEM fuel cell is derived from chemical energy (2677.60 kW), decreased by sensible and latent heat losses (65.39 kW) and the PEM stack's power output. The technological scenario proves that the PEM displays higher net heat energy (1390.5 kW), contributing to an overall efficiency of 93.27%, significantly reducing thermal dissipation, and surpassing the heating output (430.07 kW) and thermal efficiency (84.99%) compared to the MGT. The MGT, with its low heat-to-power ratio (0.69) despite the same hydrogen combustion rate ( $0.018 \text{ kg s}^{-1}$ ), presents a clear limitation in this comparison. The PEM fuel cell demonstrates superior overall efficiency primarily due to its direct conversion of chemical energy into electrical energy through electrochemical reactions, thereby circumventing the inefficiencies associated with combustion and mechanical energy conversion typical of MGTs. The high efficiency of the PEM fuel cell is further enhanced by its low operational temperature, which significantly reduces thermal dissipation and optimizes fuel utilization. In contrast, the MGT operates at higher temperatures, leading to greater thermal losses and necessitating additional energy for air compression, which diminishes its overall efficiency. Consequently, the PEM fuel cell emerges as a more viable option for high-efficiency cogeneration systems.

**Table 11**-Comparative Performance Analysis of MGT and PEM Fuel Cells in Cogeneration Systems based on their design operating points shown in **Table 4** and **Table 5**.

Parameter	Technology options	
	Micro-gas turbine	PEM fuel cell
Electrical power, $\dot{W}$ (kW)	627.11	1221.9
Consumed power of air compressor, $\dot{W}_{comp}$ (kW)	293.44	114.78
Net Electrical power, $\dot{W}_{NET}$ (kW)	333.67	1107.12

Heating output, $\dot{Q}$ (kW)	430.07	1390.5
Electrical efficiency, $\eta$ (%)	37.13	41.34
Overall efficiency, $\eta$ (%)	84.99	93.27
Consumed rate of air, $\dot{m}_{\text{Air}}$ (kg s <sup>-1</sup> )	0.949	0.89
Mass flow rate of hydrogen, $\dot{m}_{\text{H}_2}$ (kg s <sup>-1</sup> )	0.018	0.018

#### 4.1.2.2 Fuel scenario

Evaluating different fuel types is essential to identify the optimal energy source for a cogeneration system, considering its thermal output, electrical generation, and overall efficiency. This study provides a detailed assessment of three distinct fuel scenarios under varying operational conditions to evaluate the performance of the MGT. The analysis focuses on system performance under two separate control strategies, specifically at a 40% part-load electrical production of the GT333s model, to gain insights into the operational efficiency and adaptability of the system. At 100% bypass valve position, the objective is to determine the most effective fuel that yields maximum heat generation and efficiency. In the second condition, the system's operation is investigated by keeping the same heating output for all fuels to find the percentage of the bypass valve that should be opened to meet heating demands. The fuels considered are methane, hydrogen, and biogas, which contains 60% CH<sub>4</sub>. Providing heating demands depends on several factors, including the kinds of fuels, turbine shaft speed, compressor pressure ratio, and the position of the bypass valve. Both scenarios are evaluated at specified off-design points, maintaining a pressure ratio of 4.3 and a shaft speed of 53,000 rpm.

The results from 40% part-load electrical production indicate that at the initial operating condition, the hydrogen-based gas turbine provides a substantial electricity output of 137.08 kW at an inlet turbine temperature of 1610.84 K. However, the maximum quantity of biogas with 60% CH<sub>4</sub> (0.049 kg s<sup>-1</sup>) is combusted to provide less power (103.68 kW) at an inlet turbine temperature of 1440.43 K. When methane becomes the fuel source, power outputs of 118.76 kW are observed at an inlet turbine temperature of 1564.94 K. Although hydrogen has a higher energy generation potential due to its superior lower heating value (LHV), its electrical efficiency (14.28%) is slightly lower than that of natural gas (15.51%). This difference arises because hydrogen's higher energy content and lower volumetric energy density pose specific challenges in efficiently converting

energy into useful work in micro-gas turbines (MGTs). Furthermore, MGTs originally designed for natural gas may only partially adapt to hydrogen combustion due to its distinct thermophysical and combustion characteristics, resulting in reduced overall energy conversion efficiency. The combustion of biogas at its maximum rate ( $0.049 \text{ kg s}^{-1}$ ) yields the lowest electrical efficiency of 6.93%. The combustion of hydrogen facilitates elevated heat production (635.07 kW) with reduced fuel consumption ( $0.009 \text{ kg s}^{-1}$  compared to methane (591.8 kW and  $0.019 \text{ kg s}^{-1}$ ). However, burning biogas in the proposed cogeneration system diminishes the heating output to 540.36 kW under similar operational settings. Findings highlight that the micro-turbine system achieves peak heating and electricity generation when fueled by hydrogen, concurrently demanding less fuel for combustion. Moreover, the system attains its highest overall efficiency (80.42%) with  $\text{H}_2$  while operating at its lowest efficiency (43.07%) with biogas.

Under the secondary operational condition, when the cogeneration system is required to deliver 402.6 kW of thermal energy to meet the heating demand of the case study, the control system adjusts the bypass valve positions to 60%, 56%, and 66% for  $\text{CH}_4$ ,  $\text{H}_2$ , and biogas, respectively. Notably, it is discerned that alterations in the bypass valve positions exert minimal influence on electrical outputs. However, a marked enhancement in electrical efficiency is observed, which includes 29.99% for  $\text{CH}_4$ , 38.59% for  $\text{H}_2$ , and 30.01% for biogas. This improvement is related to the significant reduction in fuel consumption observed during the second operational condition. According to the numerical simulation model depicted in **Figure 37**, the inlet temperature of the combustion chamber is determined by the positioning of the bypass valve. Under these conditions, a portion of the gas flow meets the heating requirements, while the remainder raises the inlet combustion temperature above the initial setup, leading to a significant increase in the inlet turbine temperature for all fuels. **Table 12** demonstrates that under the condition of constant heating output, the system achieves its maximum performance when the bypass valve is set at 56% and the minimum quantity of hydrogen ( $0.006 \text{ kg s}^{-1}$ ) is combusted.

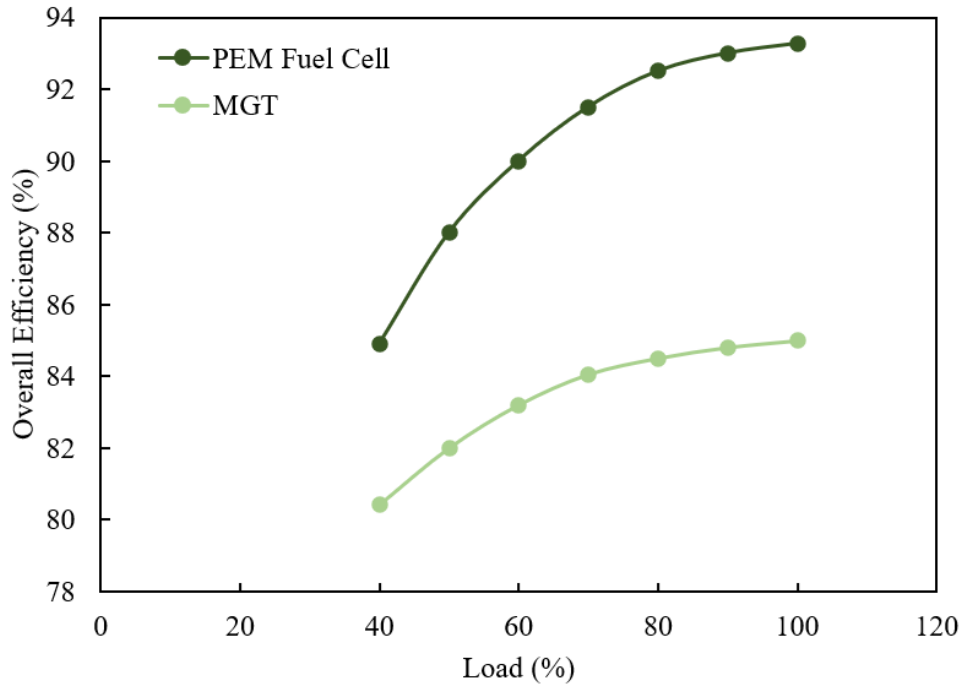
**Table 12**-Fuel scenario results for the recuperated MGT under two distinct control settings at a 40%-part load.

Parameter	Types of fuels		
	Methane	Hydrogen	Biogas
	First condition with $\pi=4.3$ , $\omega=53,000$ , $\beta=100\%$ for all fuels		
$\dot{W}_{\text{NET}}$ (kW)	118.76	137.08	103.68
$\dot{Q}_{\text{CHP}}$ (kW)	591.8	635.07	540.36

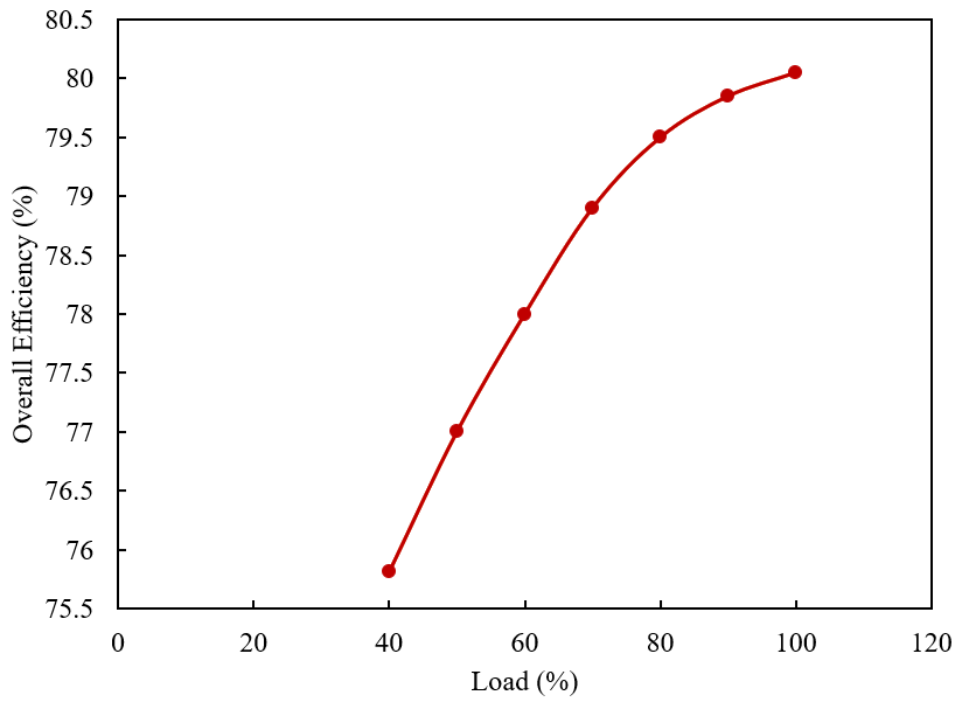
$\eta_{el}$ (%)	15.51	14.28	6.93
$\eta_{overall}$ (%)	75.81	80.42	43.07
$T_{in,comb}$ (k)	502.18	502.18	502.18
$T_{in,turb}$ (k)	1564.94	1610.84	1440.43
$T_{out,turb}$ (k)	1279.29	1316.19	1177.56
$T_{out,Rec}$ (k)	580.01	583.7	569.82
$\dot{m}_{fuel}$ (kg s <sup>-1</sup> )	0.019	0.009	0.049
<b>Parameter</b>	<b>Second condition with <math>\pi=4.3</math>, <math>\omega=53,000</math></b>		
$\beta$ (%)	60	56	66
$\dot{W}_{NET}$ (kW)	118.74	131.49	106.67
$\dot{Q}_{CHP}$ (kW)	402.64	402.64	402.64
$\eta_{thm}$ (%)	66.99	60.56	34.02
$\eta_{overall}$ (%)	87.14	80.35	43.03
$T_{in,comb}$ (k)	823.03	873	755.65
$T_{in,turb}$ (k)	1586.91	1623.05	1480.96
$T_{out,turb}$ (k)	1294.35	1322.96	1208.67
$T_{out,Rec}$ (k)	581.51	584.38	572.93
$\dot{m}_{fuel}$ (kg s <sup>-1</sup> )	0.014	0.006	0.038

### The Effect of load on the overall efficiency

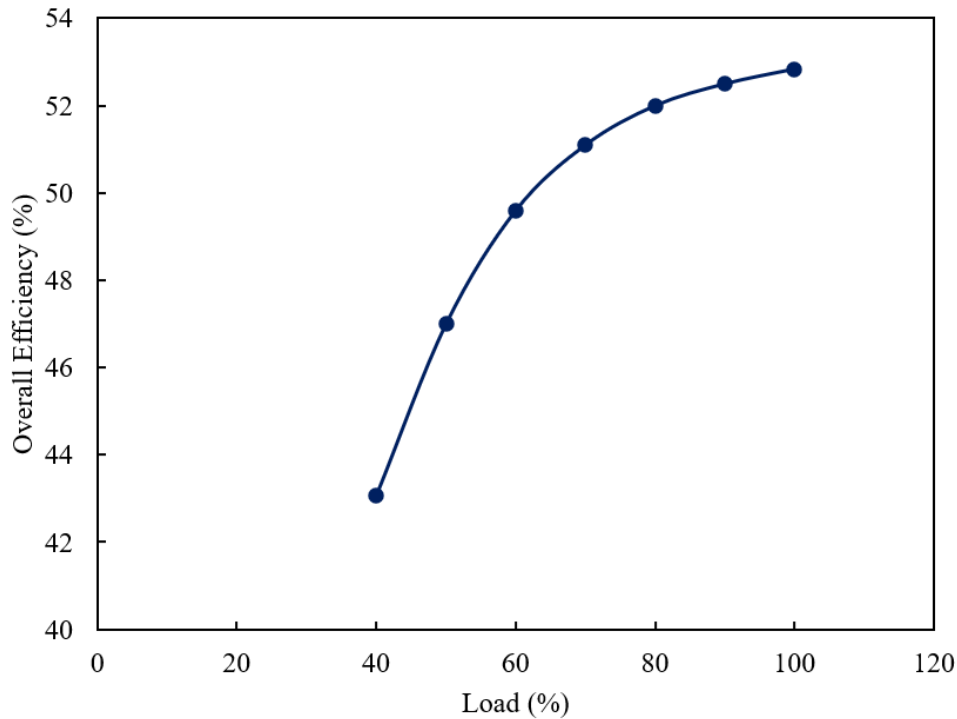
Figure 43 (a) shows the effect of the load on the overall efficiency of the systems for three different fuels including hydrogen, methene and biogas. As is can be seen the overall trend of all three figures are increasing by increasing the load percentage. The highest efficiency is for PEM fuel cell with 100% full-load which is 93.27% (Figure 43 (a)) while the lowest efficiency is for biogas in 40% part-load with 43.03% (Figure 43 (b)).



(a)



(b)



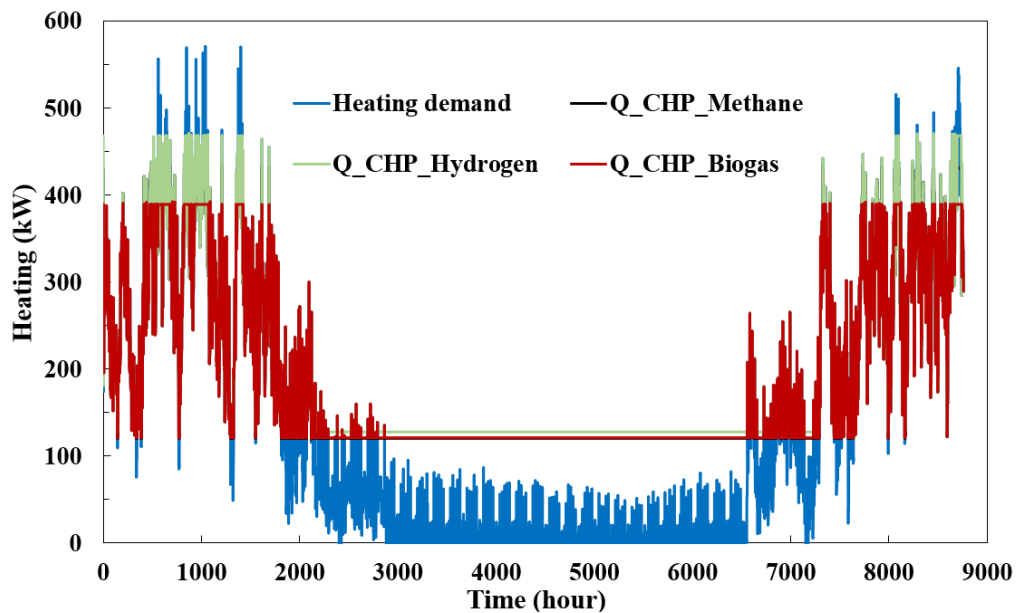
(c)

Figure 43- Effect of the load on the overall efficiency for three fuels (a) hydrogen (b) methene (c) biogas

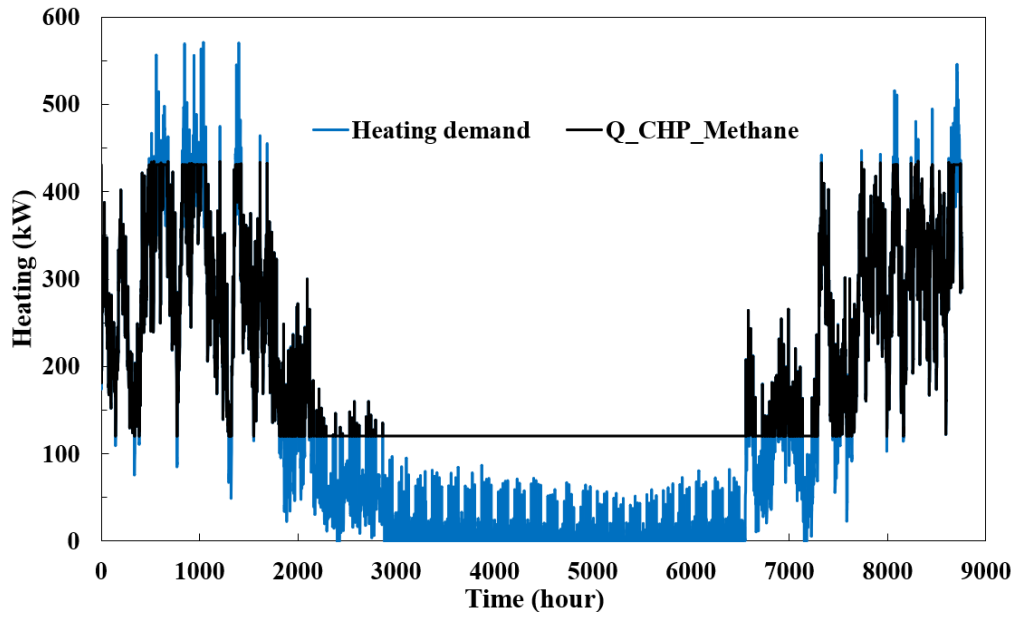
#### 4.1.2.3 Control scenario

In this study, a heating control algorithm has been developed and designed based on the interaction between the heat output ( $Q_{\text{CHP}}$ ) of the proposed CHP system, heating demands, bypass valve positions, operational modes, including charging and discharging of the thermal storage tank, and the standby mode or deactivation of the auxiliary boiler and PEM fuel cell as backup heat sources. The algorithm is structured to respond dynamically to all operational scenarios outlined in **Figure 39** and the heating control strategy illustrated in **Figure 38**. It effectively manages real-time demand fluctuations observed in five residential buildings in Karlsruhe, Germany. The control strategy aims to fulfill specific thermal requirements while enhancing the efficiency and availability of the cogeneration system by effectively controlling energy consumption. The novelty of this model lies in its flexibility and adaptability to different energy demands and MGT configurations, enabling precise adjustments of system outputs to optimize performance across diverse conditions and fuel types.

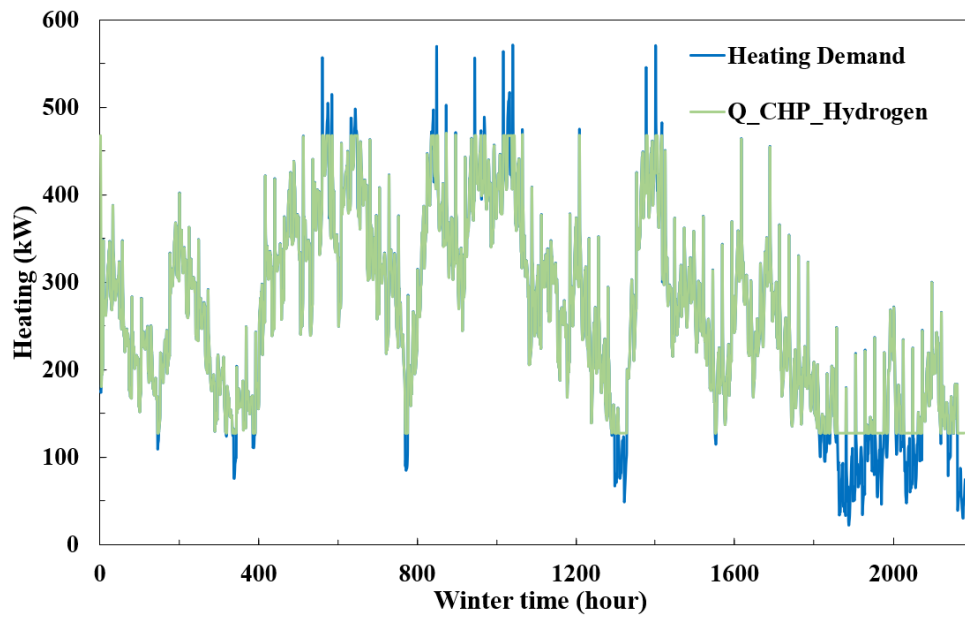
The time-dependent heating demands of the case study are illustrated in **Figure 44** (a). The interaction between heat generated from the recuperated MGT and the buildings' heating demands for all fuels is also indicated in **Figure 44** (a). To ensure clarity, the interplay between temporal analysis of the MGT heating performance when methane is utilized, and the buildings' energy needs is plotted in **Figure 44** (b). Specifically, the response of hydrogen-based MGT to urban demands during the winter and fall seasons is shown in **Figure 44** (c) and (d). The dynamic analysis of the MGT heating performance reveals notable trends within the control scenario. As illustrated in **Figure 44** (c) and (d), during winter (1 to 2180 hours) and fall (6580 to 8760 hours), the MGT coupled with the HRU effectively fulfills household heating requirements through combusting hydrogen, with occasional reliance on storage strategies to address peak demands. This performance is comparable to methane combustion in terms of efficiency. Subsequently, methane emerges as the next viable option after hydrogen. However, biogas combustion during these seasons presents limitations in meeting the CHP system's heating demands. Conversely, during spring and summer, similar performance patterns are observed across all three fuel types, revealing optimal system responsiveness to varying heating demands. This proficiency in meeting household heating needs underscores the system's flexibility when utilizing diverse fuels.



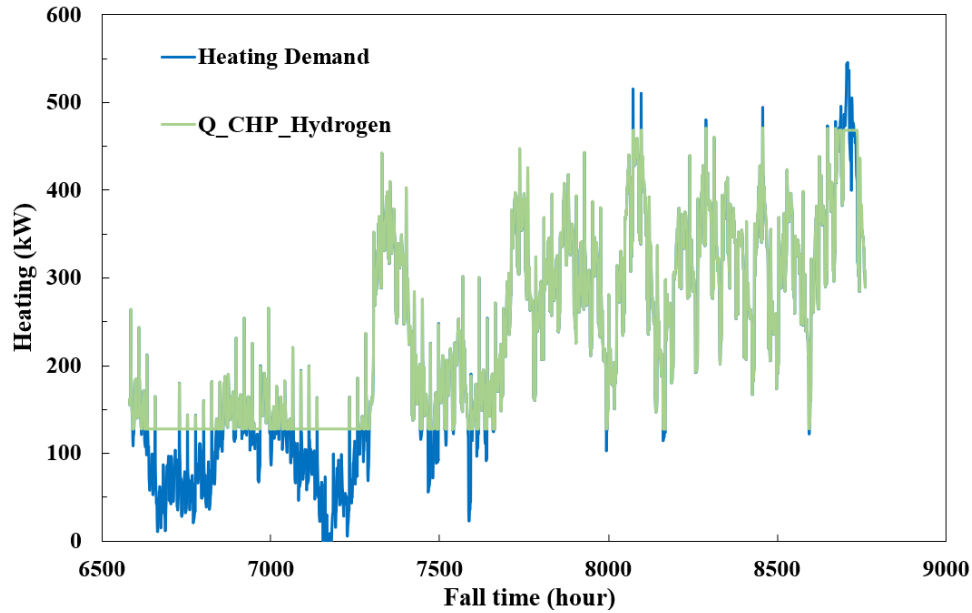
(a)



(b)



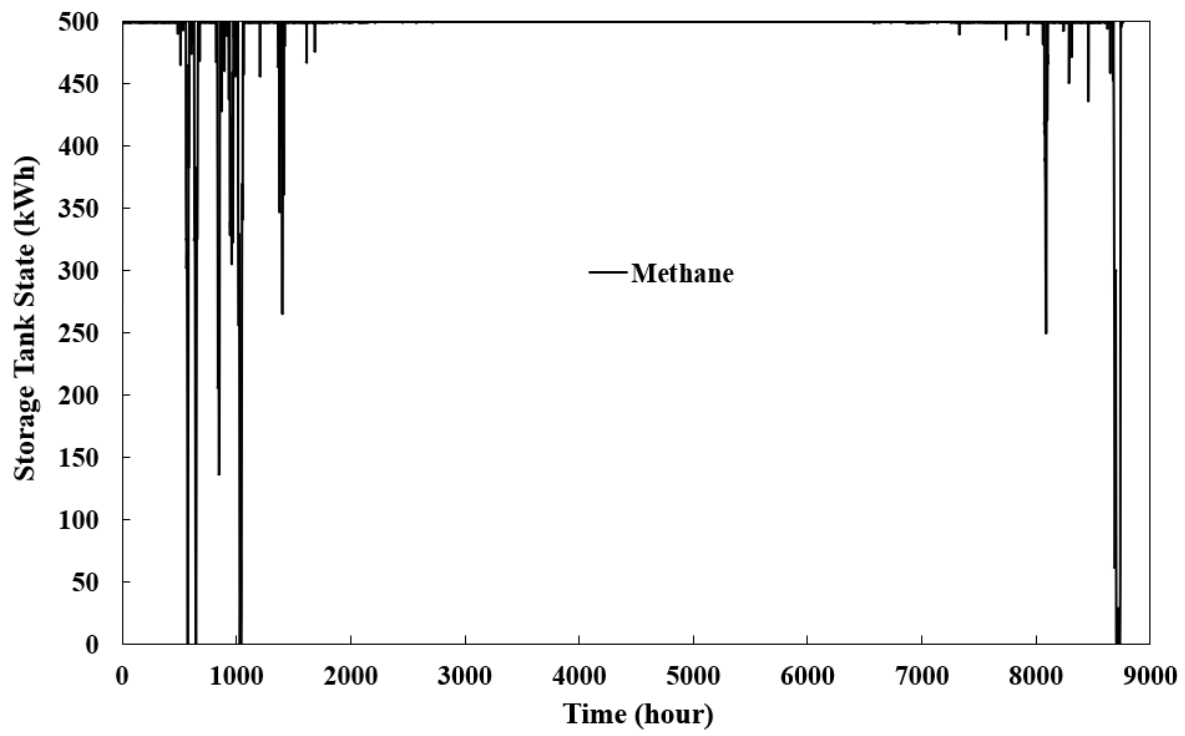
(c)



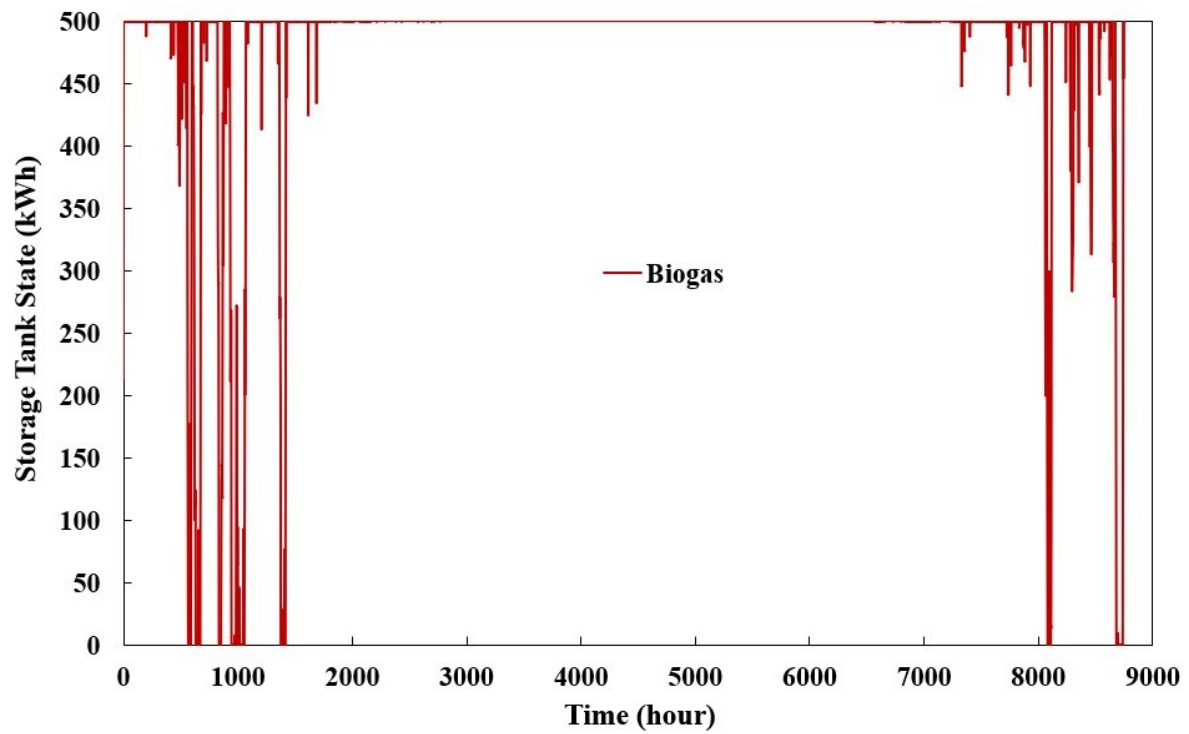
(d)

**Figure 44-** The response of the MGT to varying urban demands under the control scenario: (a) Comparison across distinct fuels, (b) Performance with methane combustion, (c) Temporal assessment of hydrogen-based MGT during the winter season, and (d) Hydrogen-based MGT performance during the fall season.

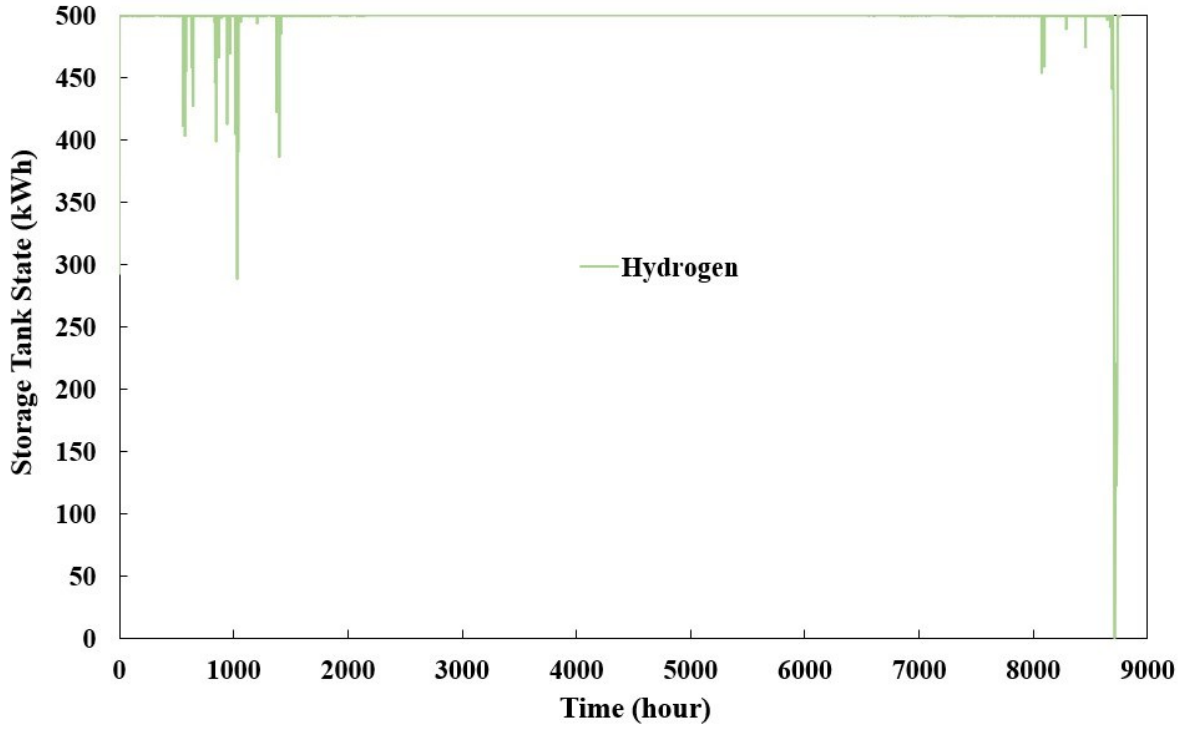
**Figure 45** (a), (b) and (c) developed from the scenario evaluations in **Figure 39**, illustrates the accumulation and depletion of stored energy with seasonal variation, clarifying the interaction between energy generation, utilization, and storage strategies for all fuel scenarios. The observed fluctuations in the storage tank state (kWh) emphasize the co-generation system's response to varying heating demands and fuel use. Additionally, the interaction of urban heating demands with storage tank operations, including charging and discharging during hydrogen combustion in the dual-axial swirler combustor, is depicted for the winter and fall seasons in **Figure 45** (b) and (c), respectively.



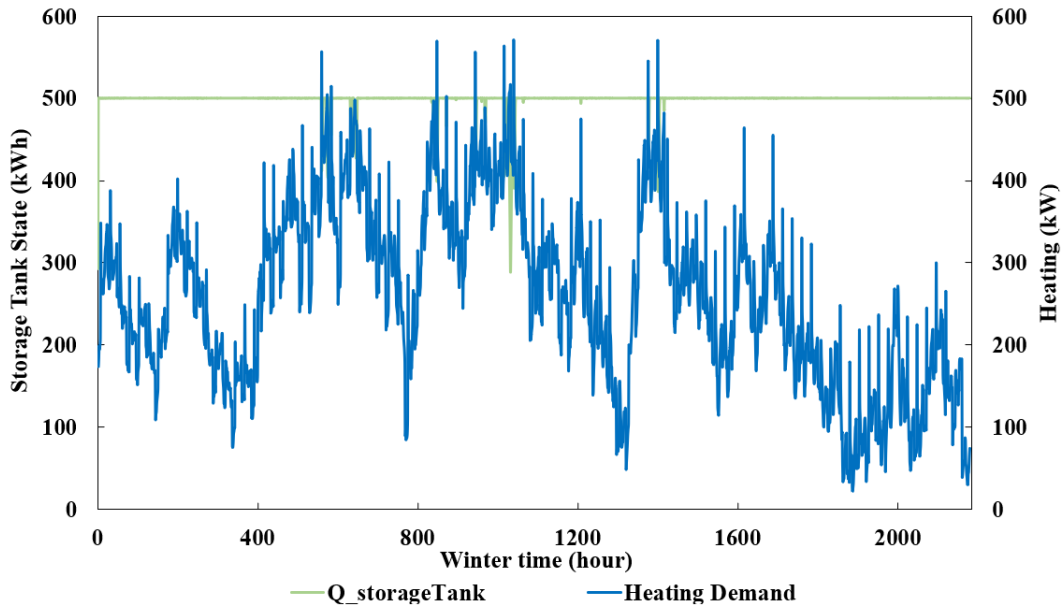
(a)



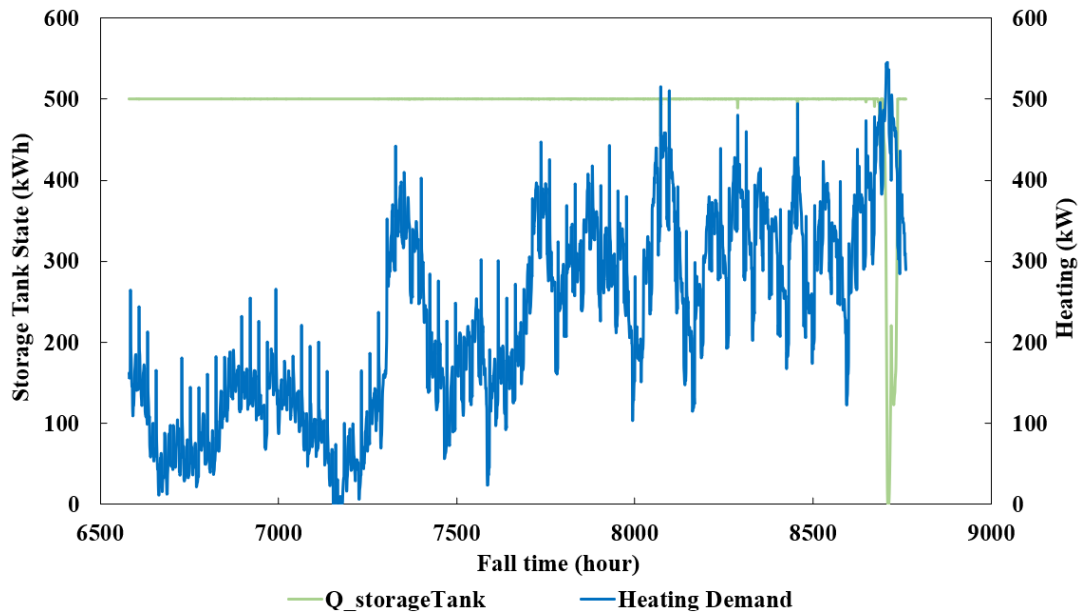
(b)



(c)



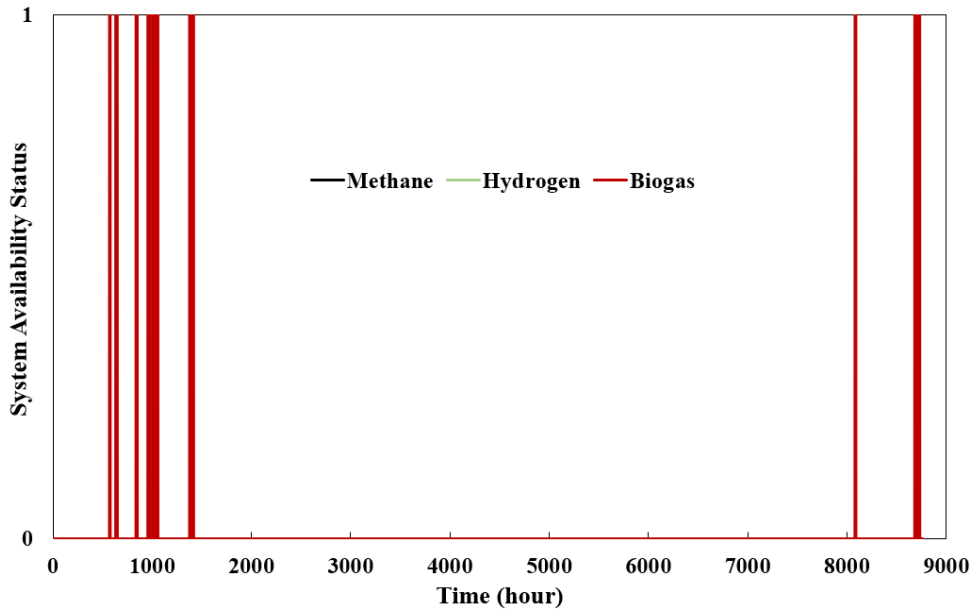
(d)



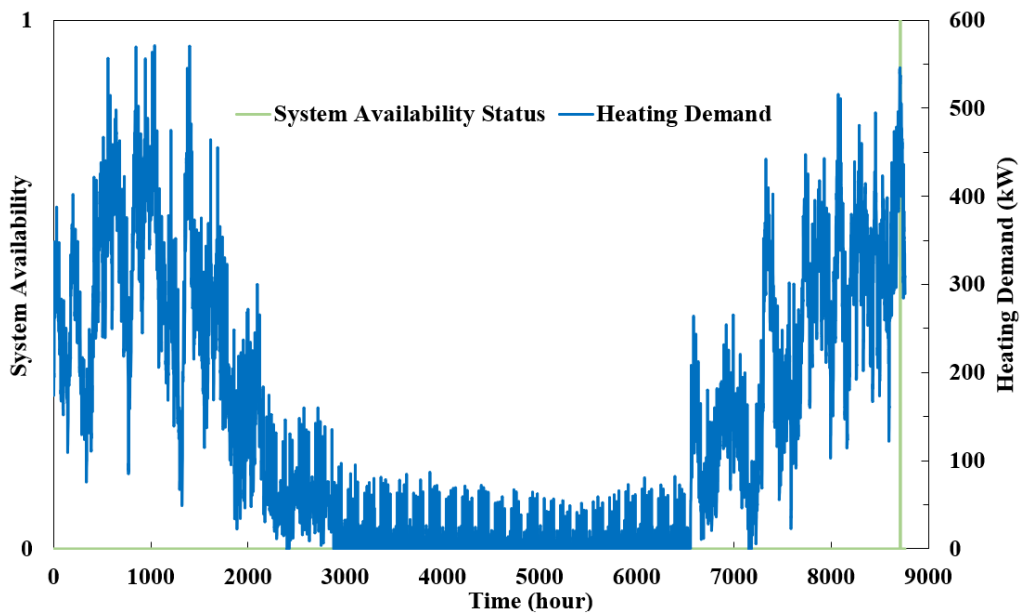
(e)

**Figure 45-** Analysis of Storage and Heating Performance with Seasonal Variation: (a), (b) and (c) Temporal variation in the state of the storage tank, illustrating charge and discharge profiles for three fuels; (d) Impact of hydrogen combustion on storage strategies and MGT heating performance during the winter season under hydrogen combustion; (e) A similar analysis for the fall season.

Assessing the 'System Availability Status' during the combustion of three different fuels across various time intervals in the micro-gas turbine is shown in **Figure 46** (a), which reveals valuable operational patterns. The metric employs a binary representation, '0' denoting system availability and '1' indicating unavailability to respond to heating demands. According to the implemented control strategy, the hydrogen-based system records just three instances of unavailability, as specified in **Figure 46** (b), which consistently facilitates its responsiveness to heating demands. On the other hand, in the methane combustion scenario, the system status indicates 14 instances of unavailability, which poses challenges and significantly affects the system's responsiveness to heating demands. In biogas combustion, the higher frequency of the system's unavailability (109 instances) indicates prolonged periods during which the system is unable to respond promptly to heating demands. This scenario highlights the operational interruptions among the fuel types and helps detect functional limitations, resulting in informed strategies to enhance system reliability. The percentage of the coverage of the demand on a whole year for hydrogen is 99.96% while this value for methene and biogas are 99.83 and 98.73% respectively.



(a)



(b)

**Figure 46**-Evaluation of system availability: (a) Comparison across three different fuel types; (b) Analysis using hydrogen over various time intervals.

#### 4.1.2.4 Operating scenario

The operational scenario is implemented to explore the interplay among the proposed technologies concerning net power output, heating capacity, fuel efficiency, overall performance, and system

control within future renewable energy frameworks. Key operating parameters, as shown in **Table 13**, are systematically adjusted along the beta line on the MGT's performance maps, including component Efficiency ( $\eta$ ), working parameter (WP), pressure ratio ( $\pi$ ), and shaft rotational speed ( $\omega$ ). This comprehensive exploration evaluates the behavior of the MGT coupled with the HRU under off-design conditions. **Table 14** presents the impact of key operating parameters on the CHP system's functionality. The overall performance trends, detailed below, remain consistent across the three distinct fuel types studied, though the specific values vary depending on the fuel utilized. Based on the results obtained from the operational scenario mentioned in **Table 14**, it is evident that increasing the rotational speed enhances the net power output of the CHP system, regardless of the type of fuel employed. As described in the compressor map (**Figure 31**) by moving on the axillary line, the rise of rotational speed ( $\omega$ ) and pressure ratio significantly improves compressor efficiency ( $\eta_{\text{comp}}$ ) and corrected mass flow rate ( $\dot{m}_{\text{corr}}$ ). Based on Eq. (15), and Eq. (19) these growths cause substantial increments in air flow rate ( $\dot{m}_{\text{air}}$ ), and work consumption by the compressor ( $\dot{W}_{\text{comp}}$ ). The high value of fuel flow rate ( $\dot{m}_{\text{fuel}}$ ) is also obtained accordingly based on Eq. (22).

On the other hand, two main operational phenomena happen which make the turbine generates more power. Based on Eq. (26), generated power is dependent on gas flow rate ( $\dot{m}_{\text{gas}}$ ), and the inlet, and outlet turbine temperatures. According to the turbine map (**Figure 33**), when moving along the beta line, the shaft rotation at the highest speed increases the working parameter (WP). This increase leads to an improved corrected gas flow rate along the auxiliary line, as shown in **Figure 34**, resulting in the highest value of  $\dot{m}_{\text{gas}}$ . Moreover, adjusting the operational points along the beta line in turbine maps allows the system to reach the optimal region where the highest values of working parameter (WP) and turbine efficiency are achieved. This optimization leads to an increase in both the inlet and outlet turbine gas temperatures. Consequently, the generated power peaks at the maximum values of gas mass flow rate and turbine temperatures. The observed growth in turbine power output surpasses the rise in compressor power consumption, signifying that higher rotational speeds tend to substantially enhance the overall net power of the system. This relationship underscores the critical impact of gradual increases in rotational speed on improving overall system performance.

Additionally, the observed fluctuations in the heat outputs depicted in **Table 14** illustrate the correlation among the bypass valve position ( $\beta$ ), charging and discharging of the storage tank, and the operational states of the auxiliary boiler, both standby and active modes, to fulfill heating needs. The valve position ( $\alpha$ ) is specified according to the heating control strategy, influencing its distribution across hot water and space heating. The dynamic trend of the valve's distribution adapts to the specific heating demands outlined by Eq. (38), enabling operators to switch the valve between on and off modes in response to these requirements. Concurrently, a detailed analysis investigates the various factors influencing PEM fuel cell performance, including cell count ( $N_{\text{cell}}$ ), ambient temperature ( $T_{\text{amb}}$ ), operational temperature ( $T_{\text{FC}}$ ), and the interaction of these operational parameters. **Table 15** provides an assessment of how each operational parameter impacts the function of the PEM fuel cell, along with the range of values provided in **Table 13**. Initially, variations in individual parameters are analyzed, followed by a comprehensive evaluation that considers all factors simultaneously. The results from the operational scenario, particularly the increase in generated heat and electricity due to the augmentation of cell numbers in the PEM fuel cell stack, align with expectations based on electrochemical kinetics. Increasing the cell count in PEM fuel cells leads to an enhanced reactive surface area, intensifying the electrochemical reactions and increasing the number of catalytic sites, thereby augmenting the overall energy output. This process is also associated with higher hydrogen consumption, a direct indicator of increased electrochemical activity within the fuel cell system. These observations highlight the positive correlation between cell count and system performance, demonstrating the potential for scalability in PEM fuel cell stacks to improve energy output significantly. Such scalability is essential for optimizing fuel cell technologies.

The conducted operational simulation signifies the sensitivity of the fuel cell's performance to ambient temperature variations. Elevating the ambient temperature within the considered range from 273.15 K to 303.15 K results in a noticeable rise in the fuel cell's overall efficiency, alongside increased heat and electricity generation. Remarkably, despite the varying ambient temperatures, the quantity of hydrogen consumption remains consistent, indicating a sustained reaction rate within the fuel cell system. Based on evaluating the collective impact of critical parameters on PEM fuel cell performance, the study reveals substantial increments in both generated heat and electricity. The rise in hydrogen consumption is also attributed to intensified reaction rates prompted by elevated temperatures and augmented cell counts. This increased activity within the

fuel cell system requires more hydrogen to sustain the electrochemical reactions that produce electricity and heat. However, the fuel cell exhibits robust stability in overall efficiency despite these multivariate enhancements, indicating a noteworthy inherent resilience in its performance under varied operating conditions.

**Table 13-**Variability of key operating parameters across defined operating scenarios.

Technology	Parameter item	Ranges
MGT	Shaft rotational speed, $\omega$ (rpm)	$30,000 \leq \omega \leq 65,000$
	Pressure ratio, $\pi$	$2 \leq \pi \leq 8$
	Working parameter, WP	$5 \leq WP \leq 16$
	Turbine efficiency, $\eta_{\text{turb}}$ (%)	$71 \leq \eta_{\text{turb}} \leq 86$
	Compressor efficiency, $\eta_{\text{comp}}$ (%)	$65 \leq \eta_{\text{comp}} \leq 77$
PEM fuel cell	Number of Cell, $N_{\text{cell}}$	$500 \leq N_{\text{cell}} \leq 22000$
	Ambient temperature, $T_{\text{amb}}$ (K)	$273.15 \leq T_{\text{amb}} \leq 313.15$
	Operational temperature, $T_{\text{FC}}$ (°C)	$30 \leq T_{\text{FC}} \leq 120$

**Table 14-**Functional characteristics of the recuperated MGT coupled with HRU under the operational scenario.

$\omega$ (rpm)	$\dot{W}_{\text{NET}}$ (kW)			$\dot{Q}_{\text{CHP}}$ (kW)			$\dot{m}_{\text{fuel}}$ (kg s <sup>-1</sup> )			$\beta$ (%)			$\alpha$ (%)		
	CH <sub>4</sub>	H <sub>2</sub>	Biogas	CH <sub>4</sub>	H <sub>2</sub>	Biogas	CH <sub>4</sub>	H <sub>2</sub>	Biogas	CH <sub>4</sub>	H <sub>2</sub>	Biogas	CH <sub>4</sub>	H <sub>2</sub>	Biogas
30,000	41.91	46.32	38.49	325.41	351.04	295.24	0.01	0.005	0.026	100	100	100	15.65	14.5	17.24
30,500	51.57	56.17	48.07	348.11	376.1	315.71	0.016	0.006	0.028	100	100	100	14.63	13.54	16.13
40,000	73.87	75.63	68.43	400.24	350.4	405.04	0.018	0.005	0.036	86	68	100	12.72	14.53	12.57
45,000	101.97	109.71	92.04	277.95	220.61	341.89	0.01	0.004	0.033	40	26	58	18.32	23.08	14.89
50,000	105.13	113.52	96.76	299.27	255.55	353.74	0.015	0.005	0.034	44	32	61	17.01	19.92	14.39
55,000	171.76	184.31	160.25	240.98	257.02	243.39	0.014	0.006	0.03	0	0	0	21.13	19.81	20.92
60,000	304.94	333.67	279.58	397.36	430.07	400.55	0.018	0.008	0.049	0	0	0	12.81	11.84	12.71

65,000    326.21   363.13   293.65    497.84   536.5   502.34    0.021   0.01   0.058    0   0   0    10.23   9.49   10.14

**Table 15-**Analyzing PEM fuel cell Performance under diverse operational conditions.

Operating parameters															
$T_{amb}$ (K)				$N_{cell}$				$T_{FC}$ (°C)				$T_{amb}, N_{cell}, \text{ and } T_{FC}$			
$\dot{W}_{NET}$ (kW)	$\dot{Q}_{CHP}$ (kW)	$\dot{m}_{fuel}$ (kg s <sup>-1</sup> )	$\eta_{overall}$	$\dot{W}_{NET}$ (kW)	$\dot{Q}_{CHP}$ (kW)	$\dot{m}_{fuel}$ (kg s <sup>-1</sup> )	$\eta_{overall}$	$\dot{W}_{NET}$ (kW)	$\dot{Q}_{CHP}$ (kW)	$\dot{m}_{fuel}$ (kg s <sup>-1</sup> )	$\eta_{overall}$	$\dot{W}_{NET}$ (kW)	$\dot{Q}_{CHP}$ (kW)	$\dot{m}_{fuel}$ (kg s <sup>-1</sup> )	$\eta_{overall}$
1114.88	1344.42	0.02	91.85	42.58	53.48	0.001	93.27	1079.43	1472.97	0.02	95.32	41.82	54.88	0.001	93.9
1112.93	1355.91	0.02	92.2	85.16	106.95	0.001	93.27	1093.09	1449.31	0.02	94.95	84.54	108.83	0.001	93.88
1110.97	1367.4	0.02	92.56	340.63	427.81	0.006	93.27	1102.87	1429.53	0.02	94.58	340.55	432.79	0.006	93.87
1109.01	1378.89	0.02	92.92	596.11	748.66	0.01	93.27	1109.06	1413.36	0.02	94.2	598.24	754.85	0.01	93.85
1108.23	1383.48	0.02	93.06	851.58	1069.52	0.015	93.27	1111.56	1400.86	0.02	93.83	855.95	1072.28	0.015	93.62
1107.05	1390.38	0.02	93.27	1107.05	1390.38	0.019	93.27	1107.05	1390.38	0.02	93.27	1107.05	1390.38	0.019	93.27
1103.14	1413.36	0.02	93.98	1362.53	1711.23	0.023	93.27	1102.69	1389.74	0.02	93.08	1352.34	1738.73	0.023	93.8
1101.18	1424.85	0.02	94.34	1618	2032.09	0.028	93.27	1087.73	1394.71	0.02	92.71	1581.18	2088.8	0.028	93.78
1099.22	1436.34	0.02	94.7	1873.48	2352.95	0.032	93.27	1005.11	1457.34	0.02	91.96	1687.71	2544.04	0.032	93.39

## 4.2 Environmental Analysis Results

### 4.2.1 NO<sub>x</sub> emission validation

**Figure 47** presents a detailed comparative analysis of nitrogen oxides (NO<sub>x</sub>) emission predictions from the combustion of methane, against empirical data referenced in [157] based on a range of pilot fuel proportions (PFP%). The NO<sub>x</sub> emissions are normalized to a dry basis with 15% oxygen content based on Eq. (35).

Pilot Fuel Proportion (PFP) is pivotal in studying combustion systems, signifying the fraction of pilot fuel to the total fuel mixture. In these systems, pilot fuel, characteristically more ignitable than the main fuel, plays a vital role in stabilizing the combustion process within the primary flame zone. Adjusting the PFP is a control strategy to stabilize combustion and control flame distribution within the combustion chamber. This regulation prevents blowout or inefficient burning and significantly affects the flame's shape, location, and temperature profile, which, in turn, critically influences the formation and emission of pollutants like nitrogen oxides (NO<sub>x</sub>) and carbon monoxide (CO). In practice, the PFP is adjusted based on load conditions, fuel type, and standard emission levels to maintain stable operation and compliance with environmental regulations. Properly managing PFP is essential for reducing the environmental impact of combustion processes while ensuring efficient energy conversion.

In this research study, the proposed NO<sub>x</sub> emission prediction approaches are the CFD simulation, and ECRN model within Ansys Chemkin-Pro. The former models the combustor's flow field using the realizable k- $\epsilon$  turbulence model, coupled with the Eddy Dissipation Concept (EDC) and a two-step global reaction mechanism as outlined by Polifke. According to **Figure 47**, there are minor variances between CFD-generated outcomes and the empirical data, so it proves that the CFD methodology reliably estimates NO<sub>x</sub> emissions within the proposed combustor for all fuel scenarios. Also, the algorithm implemented in Chemkin-Pro shows excellent agreement between the predicted NO<sub>x</sub> concentrations and the experimental results for methane at 9% PFP. Given the accuracy of the two proposed approaches in predicting NO<sub>x</sub> emissions for methane, it is concluded

that the generated datasets significantly improve the ability to extrapolate or interpolate NO<sub>x</sub> emissions across diverse operational conditions, as illustrated in **Figure 47**.

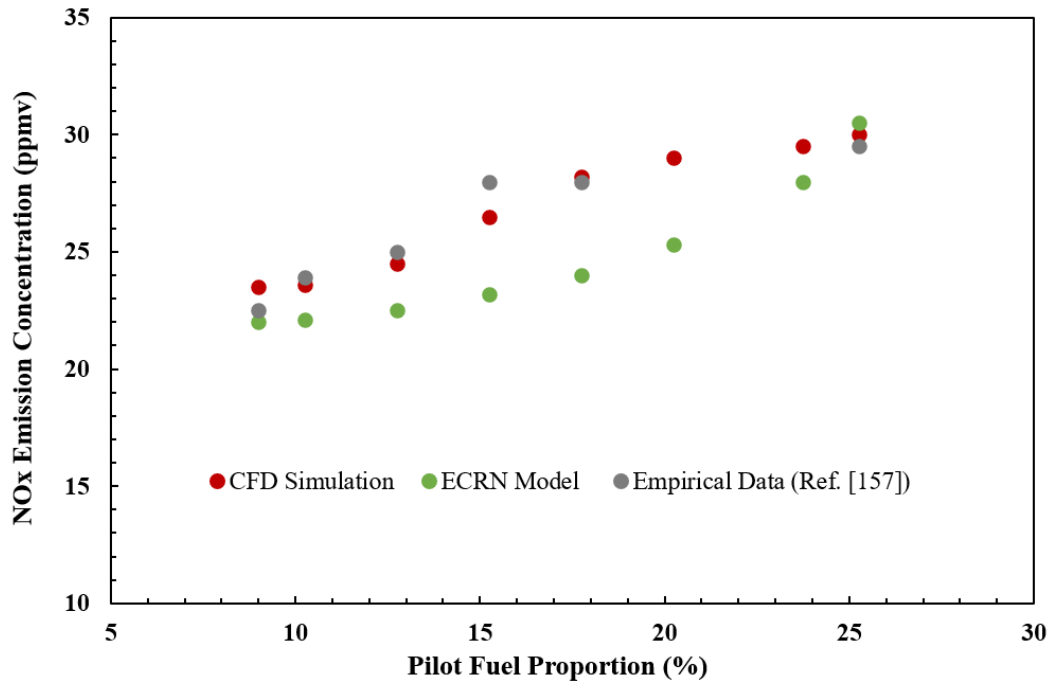


**Figure 47-** Comparison of NO<sub>x</sub> pollutant level models with experimental results [157] in the context of methane utilization at full load operating condition and diverse PFP.

## 4.2.2 CFD simulation results for various fuel scenarios

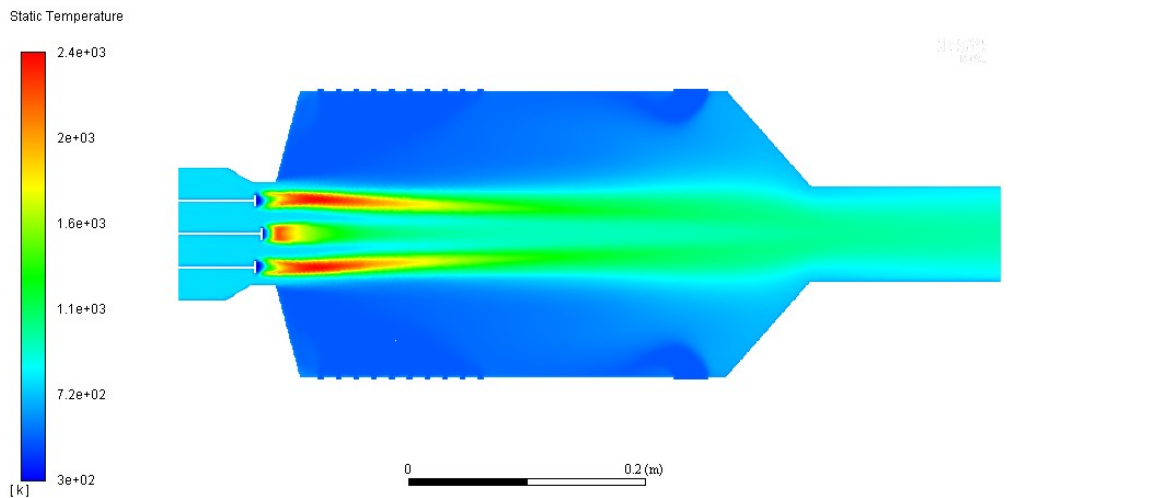
### 4.2.2.1 Temperature distribution

**Figure 48** shows the temperature distribution across the central plane of the combustor for three different fuel scenarios using all the design operating conditions listed in **Table 5** and the numerical results of the MGT model at 100% load and 9% pilot fuel proportion (PFP) specified in **Table 16**. All fuel types exhibit a consistent temperature distribution pattern, highlighting two distinct flame zones: a smaller, less intense pilot flame near the pilot cooling holes and a larger, more intense primary flame closer to the liner. Hydrogen combustion, with its high diffusivity, reaches the highest peak temperatures, leading to increased NO<sub>x</sub> emissions. On the other hand, biogas demonstrates a more uniform temperature distribution with lower peak values at baseload conditions because of the presence of CO<sub>2</sub>, which absorbs heat and reduces combustion intensity,

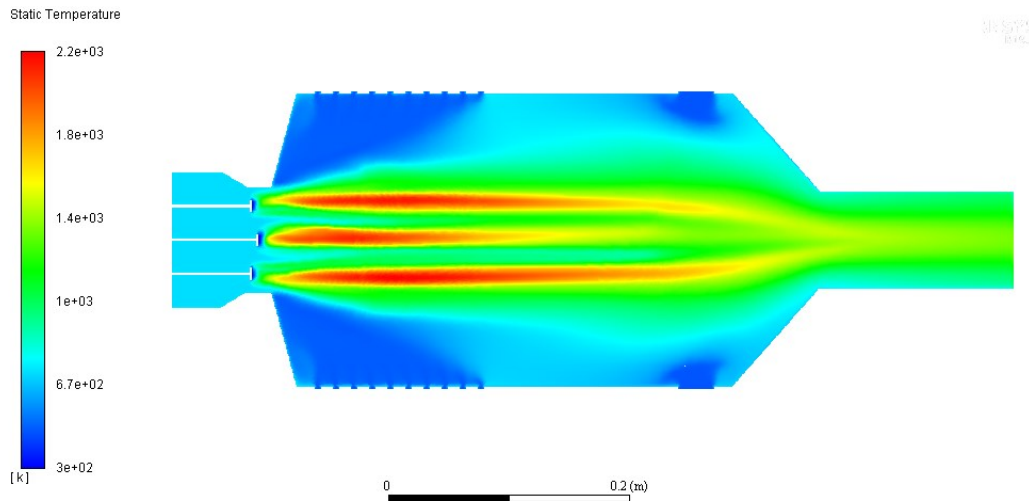
thereby lowering NO<sub>x</sub> emissions. Methane combustion reveals a balanced temperature profile, with peak temperatures lower than hydrogen but higher than biogas.

**Table 16-** Numerical results of the MGT model for all fuels at full load, and 9% PFP.

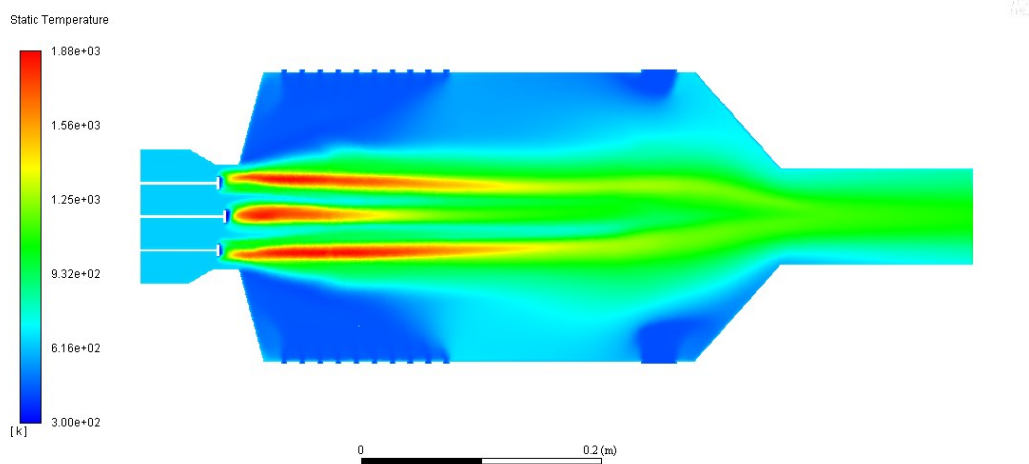
Numerical results the MGT model	Value		
Air mass flow rate, $\dot{m}_{\text{air}}$ (kg s <sup>-1</sup> )	0.949		
Cooling and Dilution air mass flow rate (kg s <sup>-1</sup> )	0.474		
Outlet pressure of compressor (kPa)	327.56		
Inlet pressure of combustion chamber (kPa)	311.18		
Inlet pressure of turbine (kPa)	295.62		
Outlet temperature of compressor, T <sub>2</sub> (°C)	207.72		
	H <sub>2</sub>	Biogas	CH <sub>4</sub>
Fuel mass flow rate, $\dot{m}_{\text{fuel}}$ (kg s <sup>-1</sup> )	0.008	0.048	0.018
Inlet temperature of combustion chamber, T <sub>3</sub> (°C)	826.52	527.65	704.21
Inlet temperature of turbine, T <sub>4</sub> (°C)	1409.47	1254.19	1373.33
Outlet temperature of turbine, T <sub>5</sub> (°C)	1123.94	995.64	1095.29
Outlet temperature of recuperator, T <sub>6</sub> (°C)	300.0	286.63	296.61



(a)



(b)



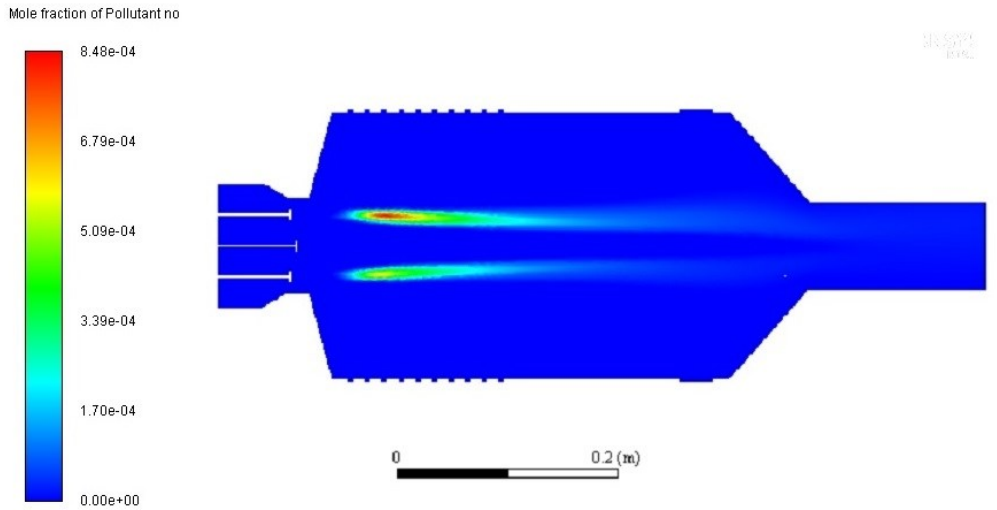
(c)

**Figure 48**-Temperature distribution contours in the dual-axial swirler combustor at baseload, and 9% PFP. From top to bottom: (a) Hydrogen, (b) Methane, (c) Biogas with 40% CO<sub>2</sub>.

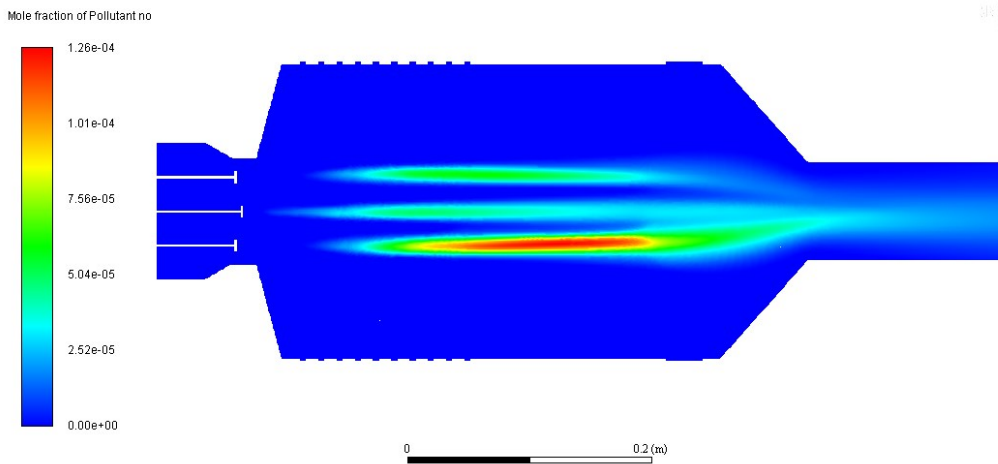
#### 4.2.2.2 Pollutant emissions (NO<sub>x</sub>) distribution

The distributions of NO<sub>x</sub> concentration levels from the combustion of hydrogen, biogas, and methane within the dual-axial swirler combustor are observed in **Figure 49**. The findings align with the results of Zong et al. [28], showing significant NO<sub>x</sub> production between primary and pilot flames. Hydrogen combustion exhibits the highest NO<sub>x</sub> emissions, primarily due to the Zeldovich

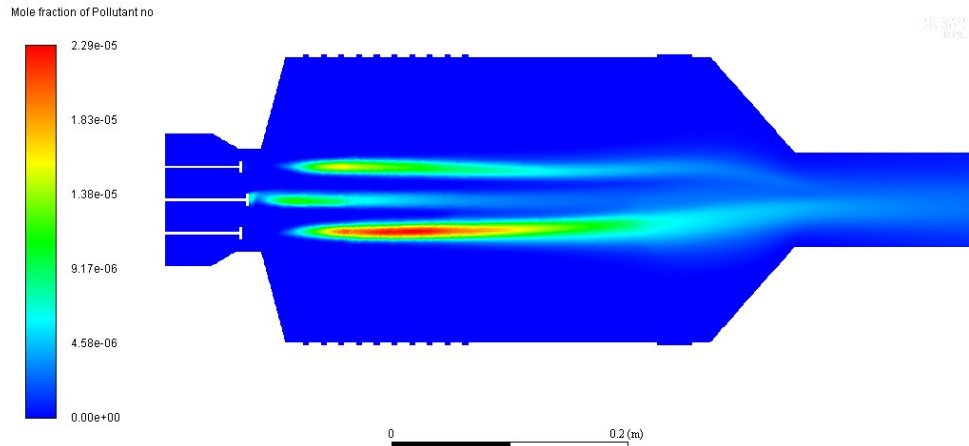
mechanism dominating thermal  $\text{NO}_x$  formation at high temperatures. This mechanism involves reactions between nitrogen ( $\text{N}_2$ ) and oxygen ( $\text{O}_2$ ) in high-temperature flame zones, thereby increasing  $\text{NO}_x$  formation. In contrast,  $\text{CO}_2$  in biogas has a cooling effect that restricts the formation of  $\text{NO}_x$ . Methane combustion results in intermediate  $\text{NO}_x$  emission levels compared to those produced by other fuels.



(a)



(b)



(c)

**Figure 49-**Mole Fraction of NO<sub>x</sub> under different fuel types, including (a) Hydrogen, (b) Methane, and (c) Biogas.

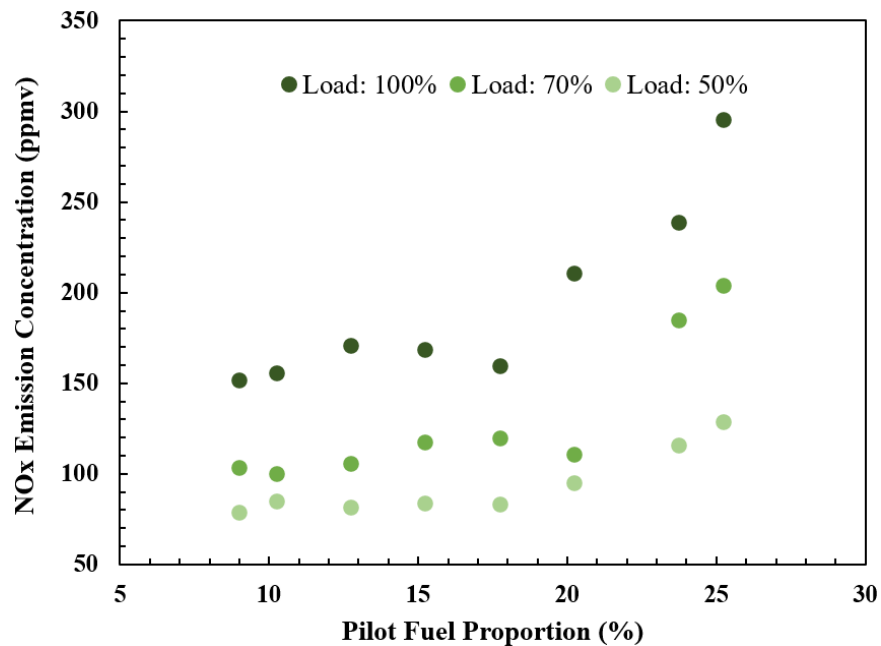
#### 4.2.2.3 Impact of PFP and fuel type on NO<sub>x</sub> emissions across operating loads

**Figure 50** illustrates the changes in NO<sub>x</sub> emissions for three different fuel types across various operating loads, as determined through the CFD simulation. The results reveal that decreasing operational load leads to a reduction in NO<sub>x</sub> emission levels (normalized to a dry basis at 15% O<sub>2</sub> [254]), a trend consistently observed for all three fuels studied in this research. At partial loads, lower flame temperatures reduce thermal gradients, and because NO<sub>x</sub> formation is highly temperature-dependent, the formation of thermal NO<sub>x</sub> is consequently diminished. According to the NO<sub>x</sub> formation trends shown in **Figure 50**, higher combustion temperatures at full load result in increased NO<sub>x</sub> concentrations. Additionally, turbulence and mixing in the combustion chamber are generally less active at partial loads. Inadequate mixing can cause uneven combustion, with some regions experiencing more fuel-rich conditions than others. This uneven combustion can produce hot spots, which generate more NO<sub>x</sub>, and cooler regions, which lead to higher CO production.

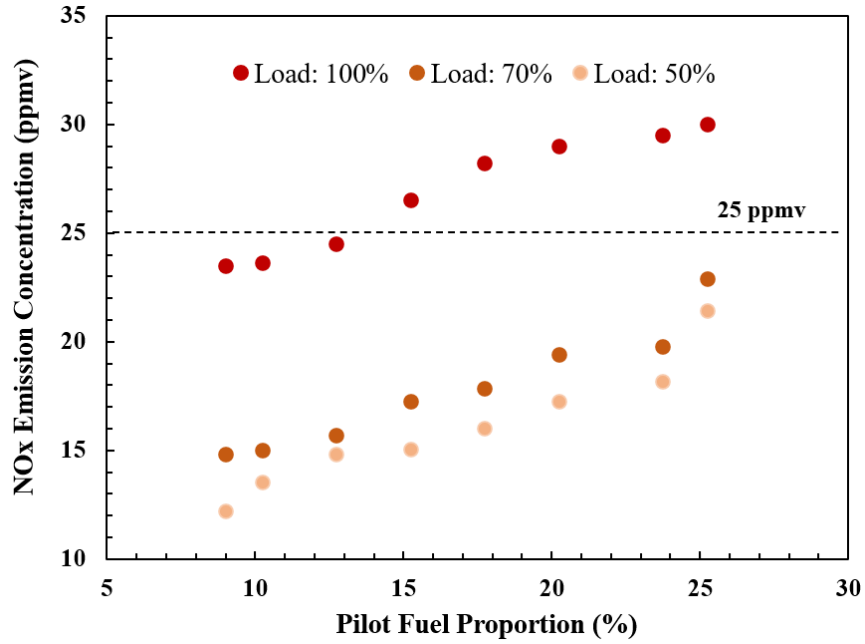
Also, based on the CFD simulation results indicated in **Figure 50**, it is evident that a reduction in PFP causes a significant decline in NO<sub>x</sub> emissions regardless of the type of fuel employed. As the PFP increases, the pilot flame often burns at a higher temperature due to the dense, rich mixture and intense localized combustion. Higher flame temperatures accelerate the thermal NO<sub>x</sub>

formation pathway, a mechanism by which atmospheric nitrogen ( $N_2$ ) and oxygen ( $O_2$ ) react under high temperatures to generate  $NO_x$ . The thermal  $NO_x$  mechanism is highly sensitive to temperature, so even small increases in flame temperature can lead to significant increases in  $NO_x$  emissions. Conversely, reducing the PFP can lower flame temperatures, thereby reducing  $NO_x$  emissions. Therefore, optimizing PFP is critical for balancing efficient combustion and minimizing harmful emissions.

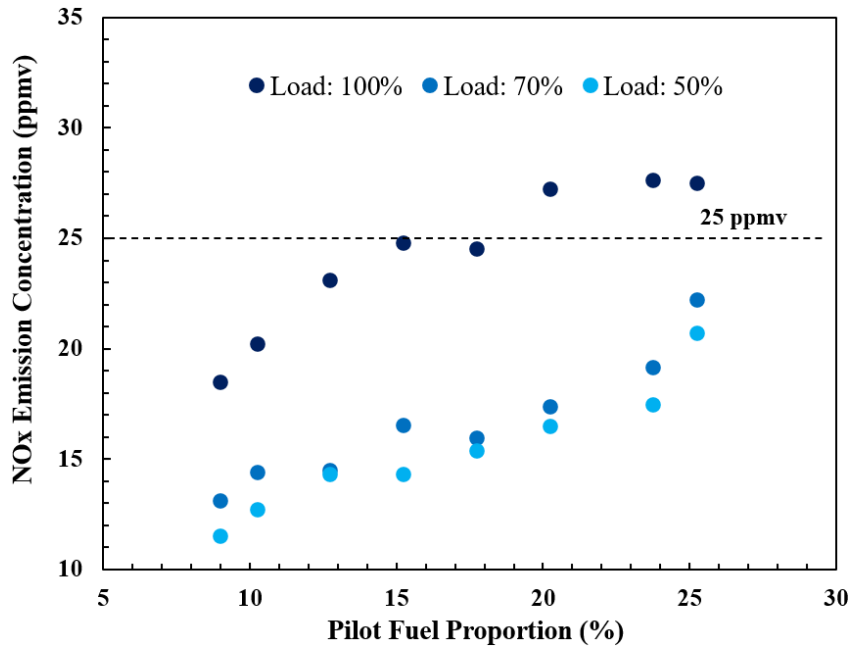
Specifically for methane and biogas at full load conditions,  $NO_x$  emissions surpass the regulatory limit of 25 ppmv when the PFP is above 13% and 18%, respectively. However, further reduction in PFP brings  $NO_x$  emissions below the specified threshold for these fuels. This trend is consistent at partial loads of 70% and 50%, where a lower PFP effectively mitigates  $NO_x$  emissions. Although reducing PFP causes a declining trend in  $NO_x$  emission, hydrogen fails to meet regulatory thresholds across both design and off-design conditions, as illustrated in **Figure 50** (a). These findings signify that the highest flame temperature of hydrogen prevents  $NO_x$  emissions from staying within regulatory limits, even with minimized PFP at all operational loads.



(a)



(b)

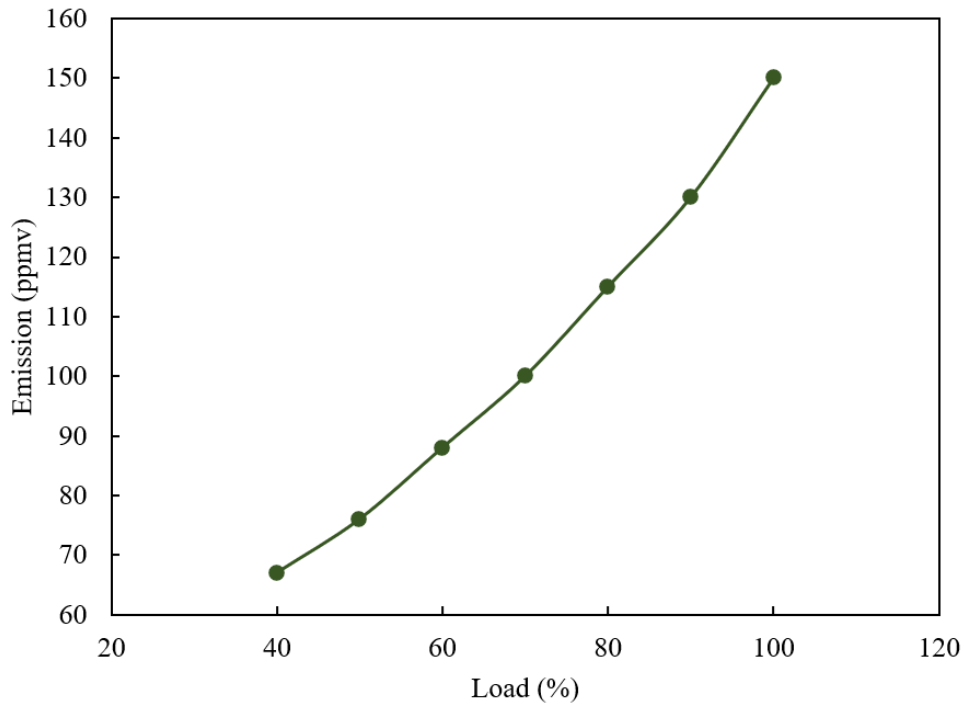


(c)

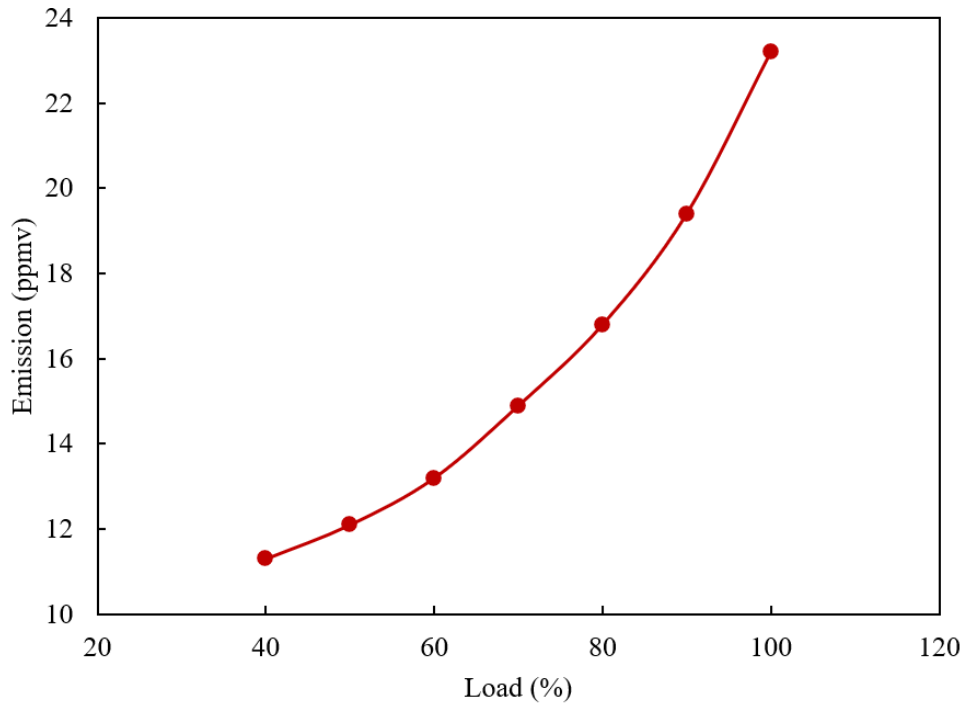
**Figure 50**-Effects of PFP on NO<sub>x</sub> emissions (ppmv @15% O<sub>2</sub>) at various operating loads based on CFD simulation for three fuel scenarios: (a) Hydrogen, (b) Methane, and (c) Biogas.

### 4.2.3 Effect of load on NO<sub>x</sub> emissions

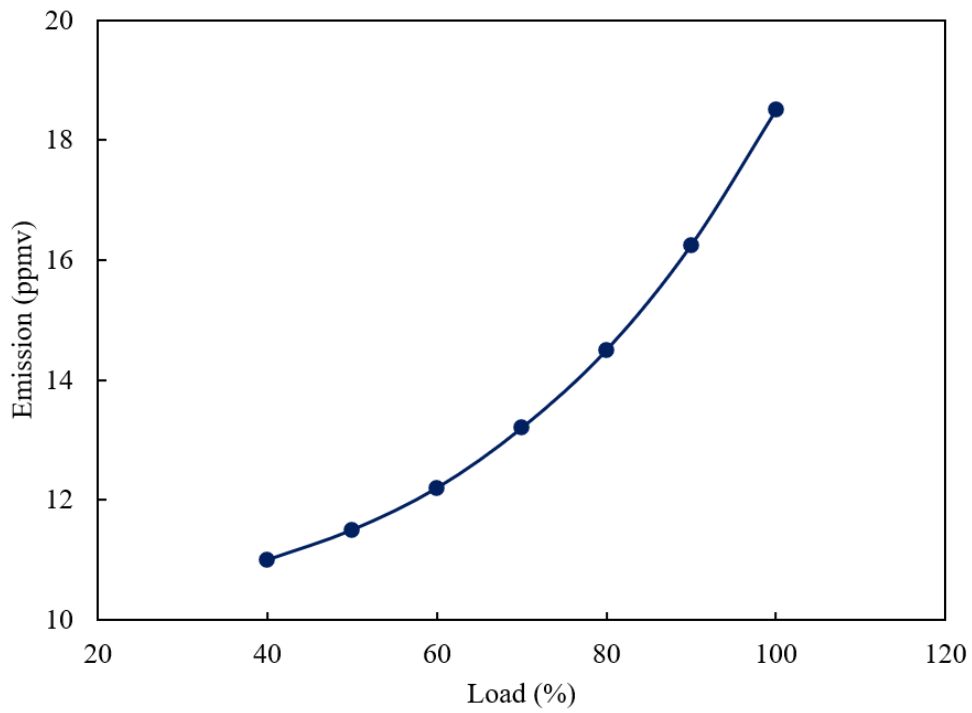
**Figure 51** shows the effect of the load on the NO<sub>x</sub> emission for three different fuels including hydrogen, methane and biogas at 9% PFP. As it can be seen as the percentage of the load increases the number of the emission increases in all cases. The highest increase can be seen in hydrogen where the NO<sub>x</sub> emission incline from around 64.2 in part load to more than 150 ppmv in 100% full load. Analysing the same scenarios for methane and biogas shows us although they follow the same trend as hydrogen even at 100% part load they NO<sub>x</sub> emission is blow the threshold of 25 ppmv.



(a)



(b)



(c)

Figure 51- The effect of the load on the NO<sub>x</sub> emission for three different fuels (a) hydrogen (b) methane (c) biogas.

#### 4.2.4 ECRN model analysis of NO<sub>x</sub> emissions under off-design conditions

**Table 17** displays the accuracy of the ECRN model in predicting NO<sub>x</sub> emissions under part-load conditions, as validated by comparison with CFD simulation results. The analysis reveals that the highest mean absolute error is 6.48% and the lowest is 1.64%, observed during the combustion of biogas and methane at 50% load, respectively.

**Table 17**-ECRN versus CFD simulation: A detailed comparison for accurate NO<sub>x</sub> emission (ppmv) prediction.

Fuel	Equivalent Chemical						Mean Absolute Error		
	CFD Simulation			Reactor Network (ECRN)			(%)		
	Model								
	Operational Load Conditions								
50%	70%	100%	50%	70%	100%	50%	70%	100%	
Hydrogen	78.5	103.25	151.8	74.9	100.5	148.4	4.59	2.66	2.24
Methane	12.2	14.8	23.5	12	14.5	22	1.64	2.03	6.38
Biogas	10.8	13.1	18.5	11.5	12.7	17.7	6.48	3.05	4.32

A sensitivity analysis of NO<sub>x</sub> emissions formation is conducted using the CFD simulation under off-design conditions, involving varying parameters such as ambient temperature, fuel composition, and air-fuel ratio. For the parametric analysis, the airflow rate is fixed at 0.949 kg s<sup>-1</sup>, while the fuel flow rate is adjusted according to the type of fuel used to simulate different equivalence ratio conditions. **Figure 52** presents the relationship between NO<sub>x</sub> emissions and the equivalence ratio (ER) for each fuel type studied. NO<sub>x</sub> formation is primarily affected by combustion temperature, flame speed, and fuel characteristics. Hydrogen, with its high flame speed and low ignition energy, tends to produce higher NO<sub>x</sub> emissions than methane and biogas, particularly at elevated ERs, due to its notably higher adiabatic flame temperature. Methane, characterized by moderate flame speed and ignition energy, yields NO<sub>x</sub> emissions that are intermediate between those of hydrogen and biogas. Its adiabatic flame temperature, lower than hydrogen's but higher than biogas's, results in balanced NO<sub>x</sub> production at similar ERs. Biogas, with a significant CO<sub>2</sub> content, lowers turbine outlet temperature and reduces combustion intensity. The inert CO<sub>2</sub> acts as a diluent, decreasing combustion temperatures and slowing

reaction kinetics. Consequently, under similar equivalence ratios, biogas combustion produces the lowest NO<sub>x</sub> emissions among the fuels studied.

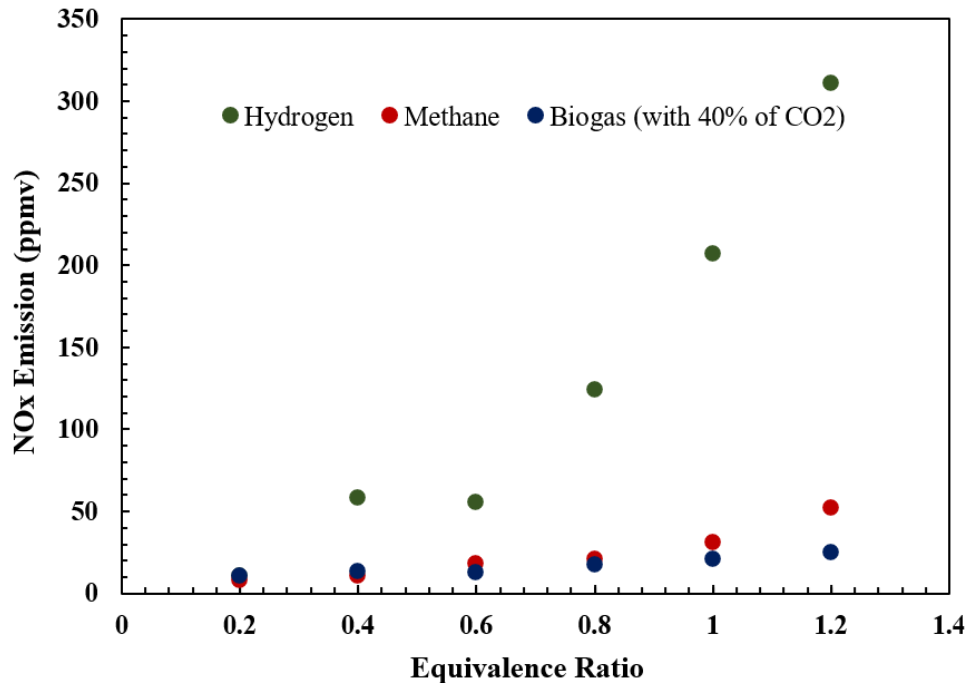
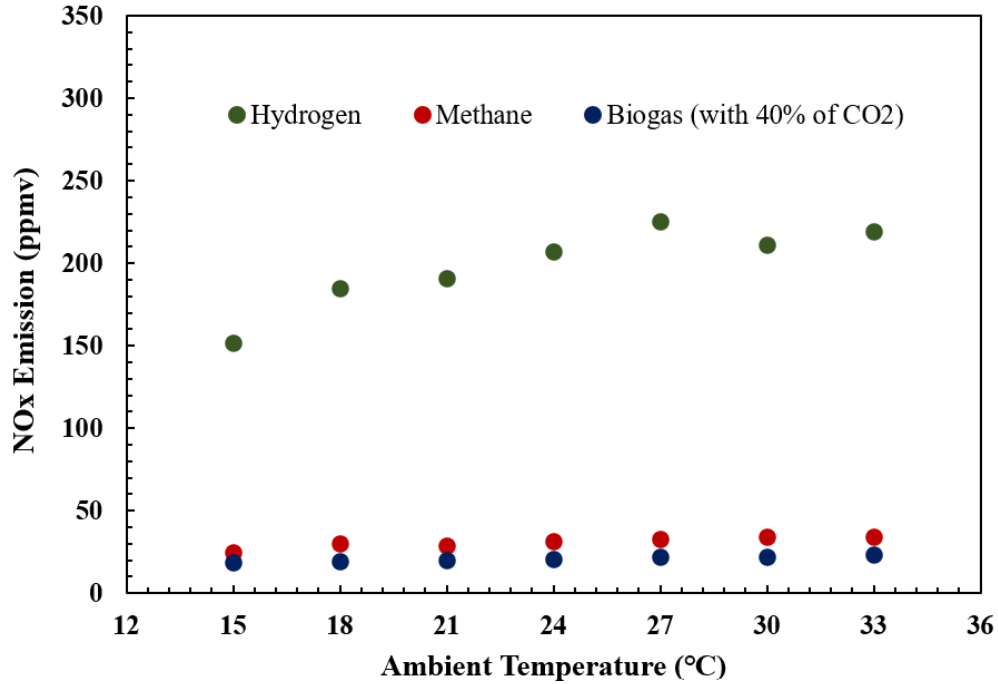


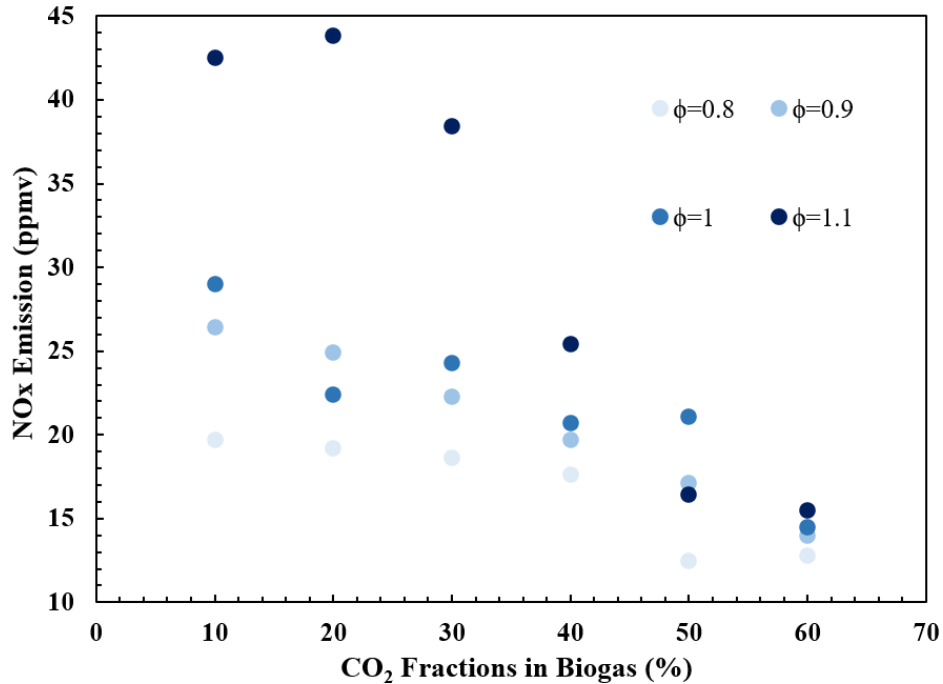
Figure 52- Variation of NO<sub>x</sub> emissions (ppmv @15% O<sub>2</sub>) versus equivalence ratio for three fuel scenarios.

Figure 53 demonstrates the variation of NO<sub>x</sub> emissions with ambient temperature for different fuel types. At lower ambient temperatures, NO<sub>x</sub> emissions decrease due to reduced combustion temperatures, which inhibit the oxidation of nitrogen in the air to form nitrogen oxides. Conversely, these conditions tend to increase CO formation, as the lower temperatures may lead to incomplete combustion. As ambient temperatures rise, NO<sub>x</sub> emissions increase, driven by higher flame and combustion temperatures that facilitate the oxidation of atmospheric nitrogen into NO<sub>x</sub>. At the highest ambient temperature of 33 °C, the peak NO<sub>x</sub> emissions are observed as 218.9 ppmv for hydrogen, 34.1 ppmv for methane, and 23 ppmv for biogas. This trend highlights the sensitivity of NO<sub>x</sub> production to variations in combustion and flame temperatures across different fuels.



**Figure 53-**Impact of ambient temperature on NO<sub>x</sub> emissions (ppmv @15% O<sub>2</sub>) for all presented fuels.

The impact of CO<sub>2</sub> fractions in biogas on NO<sub>x</sub> emissions trends is depicted in **Figure 54**. It is evident that under the same CO<sub>2</sub> concentration, transitioning from lean to rich combustion conditions causes a substantial rise in flame temperature, leading to increased NO<sub>x</sub> emissions. Conversely, in all tested scenarios, an increase in the CO<sub>2</sub> content in the biogas mixture results in a significant reduction in NO<sub>x</sub> emissions. This reduction is attributed to the crucial role of CO<sub>2</sub> concentration in mitigating thermal NO<sub>x</sub> formation, providing a practical approach to minimize pollution and enhance combustion efficiency.



**Figure 54**-Influence of CO<sub>2</sub> concentration on NO<sub>x</sub> emissions (ppmv @15% O<sub>2</sub>) in biogas combustion.

#### 4.2.5 Mathematical and CFD-based CO prediction methodology

Accurate prediction of carbon monoxide (CO) emissions remains a significant challenge for gas turbine designers, despite extensive efforts in the field. Previous studies have demonstrated that the ECRN model often fails to precisely predict CO emissions in gas turbine combustors. Although the ECRN method employs a comprehensive mechanism to capture chemical kinetics, discrepancies arise due to the simplifications in the flow field representation, resulting in notable differences between experimentally measured and modeled CO emissions. This paper addresses this gap by applying two distinct approaches, including a mathematical model and the Eddy-Dissipation combustion model for CO emission prediction for all utilized fuels.

Several mechanisms contribute to CO formation, including low burning rates due to suboptimal equivalence ratios or insufficient residence times, incomplete fuel-oxidizer mixing, and the development of localized low-temperature zones near cooling holes. In the current combustor configuration, the recirculation zones enhance both mixing and residence time of the combusted gases, thereby simplifying the problem by assuming that CO formation is predominantly influenced by the cooling effects near these regions. To develop a framework for the prediction of

CO emission, first, the adiabatic flame temperature for methane, hydrogen, and biogas, are calculated mathematically. Then, the total CO emissions for these fuels under full load operation are obtained and presented in **Table 18** to quantify the emissions.

Additionally, a new methodology, integrating a CFD simulation and a temperature-based criterion, is proposed to accurately predict CO emissions near cooling holes. In the present simulation, a three-step mechanism developed by Polifke is employed near the combustor wall, while a simpler two-step chemical mechanism is applied to the remaining areas within the combustor. This means the regions near the cooling holes are treated differently from the rest of the combustor. This differential treatment accounts for the distinct thermal and chemical dynamics near the cooling holes compared to the bulk flow regions. The critical temperature ( $T_{critical}$ ) is introduced as a threshold to delineate regions where cooling effects dominate, potentially leading to incomplete combustion and higher CO formation. The formula to define this threshold is:

$$\frac{T_{max} - T_{critical}}{T_{max} - T_{coolant}} = 0.99 \quad (40)$$

The ratio that is set to 0.99 signifies a very high temperature (near  $T_{max}$  of the burnt gases) where cooling effects start to impact. This criterion ensures that in the regions where  $T < T_{critical}$  the effects of cooling become dominant, and the combustion process might start to become less efficient, leading to higher CO emissions. Therefore, the chemical reaction is treated with the three-step mechanism developed by Polifke at regions with  $T < T_{critical}$ , while the two-step mechanism is used at regions with  $T > T_{critical}$ .

#### 4.2.5.1 Validation and results of predictive models for CO emissions

The numerical model's predictions of CO emissions are validated against experimental measurements from a swirl flame database [157], as depicted in **Figure 55**. The results demonstrate a strong correlation between predicted and observed CO levels (ppmv @15% O<sub>2</sub>) under baseload conditions with a 9% pilot fuel proportion (PFP). This high level of agreement can be attributed to the implementation of a comprehensive kinetic mechanism and an accurate turbulence model within the simulation. These advanced modeling techniques enable the effective capture of intermediate combustion products, contributing to the precise prediction of CO

formation in swirling flows. Also, the proposed mathematical methodology is developed by applying all the design operating conditions listed in **Table 5** and the numerical results of the MGT model at 100% load and 9% pilot fuel proportion (PFP) specified in **Table 16**. Then, its accuracy is validated against empirical data [157] when methane is combusted, confirming its precision and reliability are the same as the applied CFD simulation method. Consequently, this predictive approach is extended to evaluate CO emissions for hydrogen and biogas, with the results specified in **Table 18**.

Also, **Figure 55** provides a comparison between the measured CO emission levels at the burner outlet for methane and predictions obtained using the two proposed methods under various operating conditions. The aim is to assess the accuracy of the CFD simulation technique against empirical data and to highlight the potential alignments between the mathematical model predictions and observed outcomes under off-design conditions. As shown in **Figure 55**, the overall trend of CO emissions concentration with two predictive methods is consistent with the experimental data. As a result, these validated frameworks are subsequently extended to predict CO emissions for biogas at various operating states.

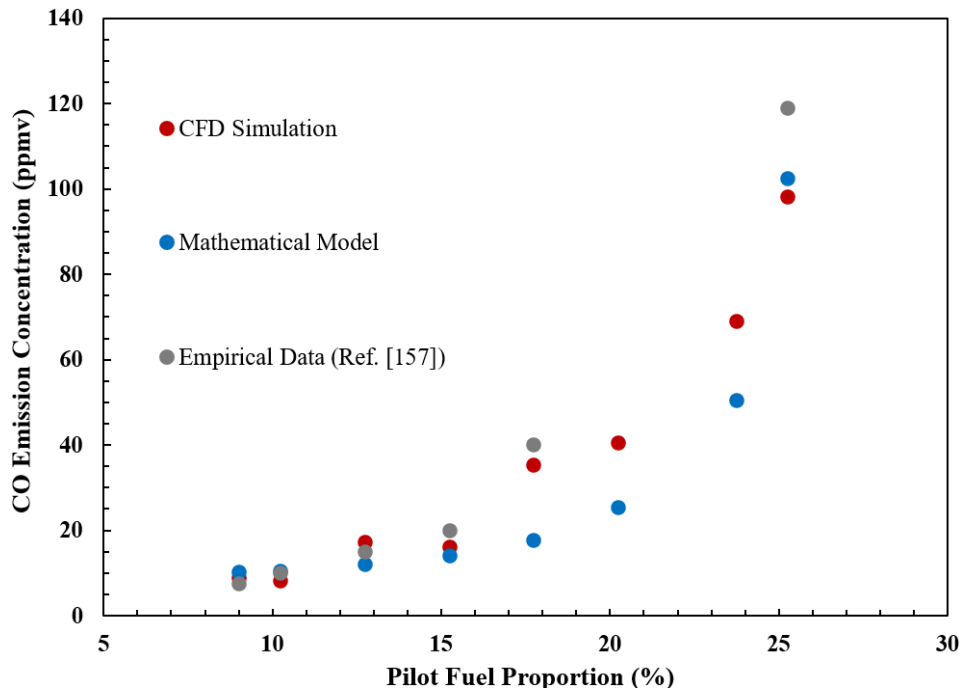
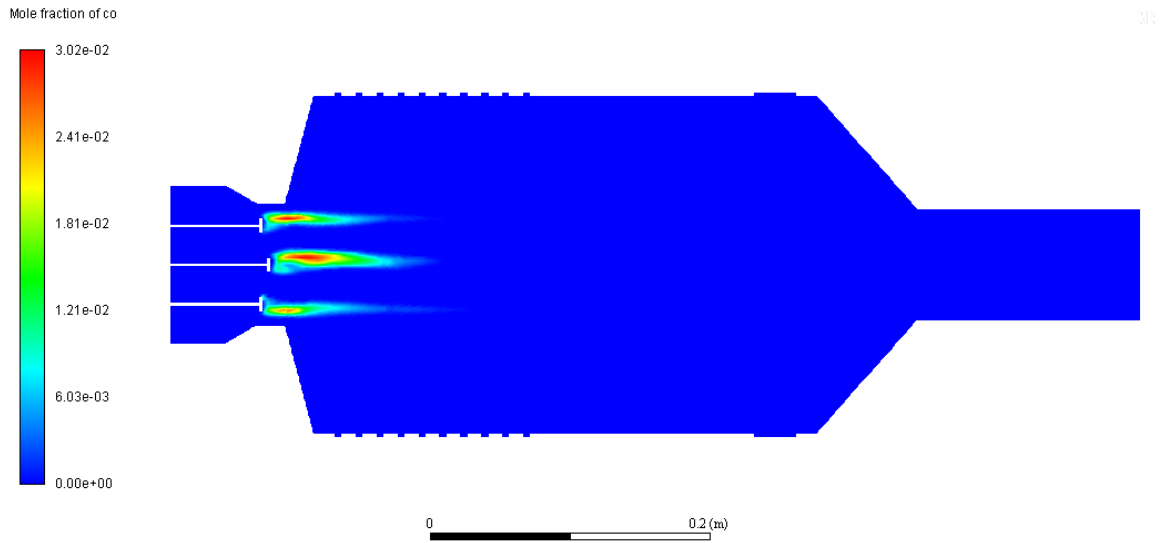


**Figure 55-** Comparative analysis of predicted vs. measured [157] CO emissions in the context of methane utilization at full load operating condition and varied PFP.

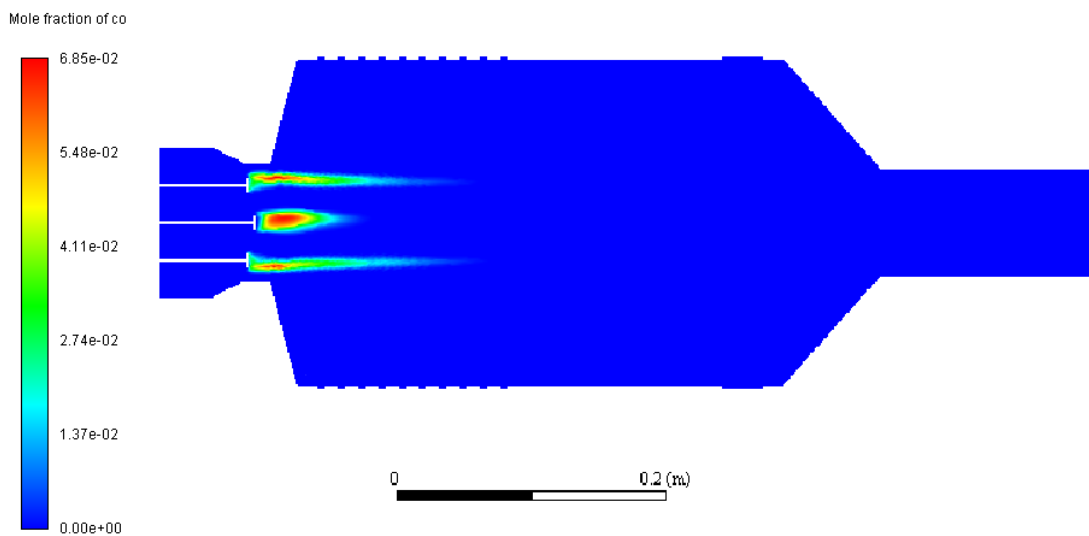
**Figure 56** (a), and (b) demonstrate the CO emission distributions in the dual-axial swirler combustor fueled by methane, and biogas at full load operation, respectively. The temperature analysis (see **Figure 48**) reveals that the upper part of the flame is extinguished, leading to unreacted fuel escaping from the combustor's reaction zone, resulting in incomplete combustion and elevated CO emissions. The CFD simulation utilizing the three-step Polifke mechanism, as shown in **Figure 56**, indicates significant CO production near the liner wall.

Reducing CO emissions is essential for improving combustion efficiency, which depends on oxygen availability and the fuel's chemical properties. Hydrogen, a carbon-neutral fuel, substantially reduces CO emissions due to its high flame velocity, low ignition energy, and superior diffusivity, which promote efficient fuel oxidation. Additionally, hydrogen combustion generates reactive radicals (H, O, OH), enhancing the conversion of CO to CO<sub>2</sub>.

While the CFD simulation results do not report CO emission levels for hydrogen combustion, it is evident that using hydrogen in the MGT significantly reduces CO emissions compared to methane and biogas under various operating conditions. However, the mathematical model, that considers some parameters (see **Table 6**), including fuel composition, C/H ratio, heat of dissociation, calorific value, and air-fuel ratio, can predict CO emission levels across different combustion zones for all fuel scenarios, as detailed in **Table 18**. Although hydrogen theoretically produces negligible CO emissions due to the lack of carbon, practical scenarios may involve trace CO formation due to impurities and organic compounds in the hydrogen or air supply. These low levels of pollutants can be further reduced using pure hydrogen, and clean air, or catalytic converters to convert CO to CO<sub>2</sub>.



(a)



(b)

**Figure 56**-Mole Fraction of CO emissions for (a) methane, and (b) biogas at the central plane of the combustor operated at 100% load condition, and 9% PFP.

**Table 18** provides accurate CO emission predictions from the proposed mathematical model at design conditions, listed in **Table 5**, for two fuel scenarios. It also includes a comparative analysis of two predictive approaches across different operating scenarios. The analytical approaches show

that the highest mean absolute error is 13.48%, observed under the baseload condition for methane combustion, while the lowest error of 2.4% occurs under partial load (70%) for biogas combustion.

**Table 18**-Comparative analysis of CO emission levels (ppmv @15% O<sub>2</sub>) for two fuel types under diverse load conditions, and 9% PFP using two prediction methods.

Fuel	CFD simulation			Mathematical model			Mean Absolute Error (%)		
	50%	70%	100%	50%	70%	100%	50%	70%	100%
Methane	540.9	212.68	8.9	519.7	206.3	10.1	3.92	3.0	13.48
Biogas	773.7	520	99.84	748.6	532.5	95.2	3.24	2.4	4.65

#### 4.2.5.2 Sensitivity analysis of CO emission characteristics using CFD

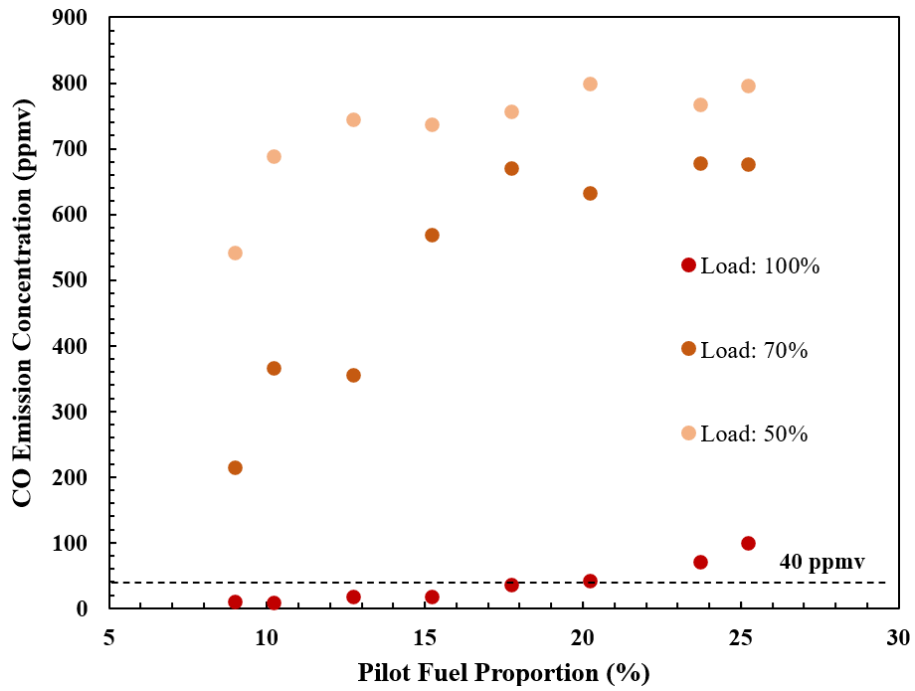
The impact of pilot fuel ratios on CO emissions is analyzed under varying load scenarios using the CFD simulation for methane and biogas. As depicted in **Figure 57**, a notable increase in CO emissions (measured in ppmv at 15% O<sub>2</sub>) occurs for both fuels as the power levels decrease, which contrasts with the trend observed for NO<sub>x</sub> emissions. Specifically, at a 50% load and a 25% PFP, CO emissions peak at 795.3 ppmv and 1049 ppmv for methane and biogas, respectively. At partial loads, combustion chambers often do not achieve optimal conditions for complete combustion. This suboptimal operation is primarily due to reduced fuel flow rates, resulting in lower flame temperatures and incomplete combustion, thereby increasing carbon monoxide (CO) emissions. Additionally, partial load conditions may necessitate a higher pilot fuel proportion (PFP) to maintain flame stability. This adjustment results in locally fuel-rich regions within the pilot flame, where the fuel concentration exceeds the available oxygen for complete combustion. While the overall oxygen level in the combustion chamber remains unchanged, the localized fuel-rich conditions lead to insufficient oxygen in those zones for complete combustion. Consequently, this oxygen deficiency in the localized regions promotes incomplete combustion, further contributing to elevated CO levels.

Conversely, the influence of PFP on CO emissions exhibits a similar pattern to that of NO<sub>x</sub> emissions; decreasing the PFP consistently leads to a decline in CO emission concentrations. For instance, when the engine operates at full load with methane, the combustor maintains CO

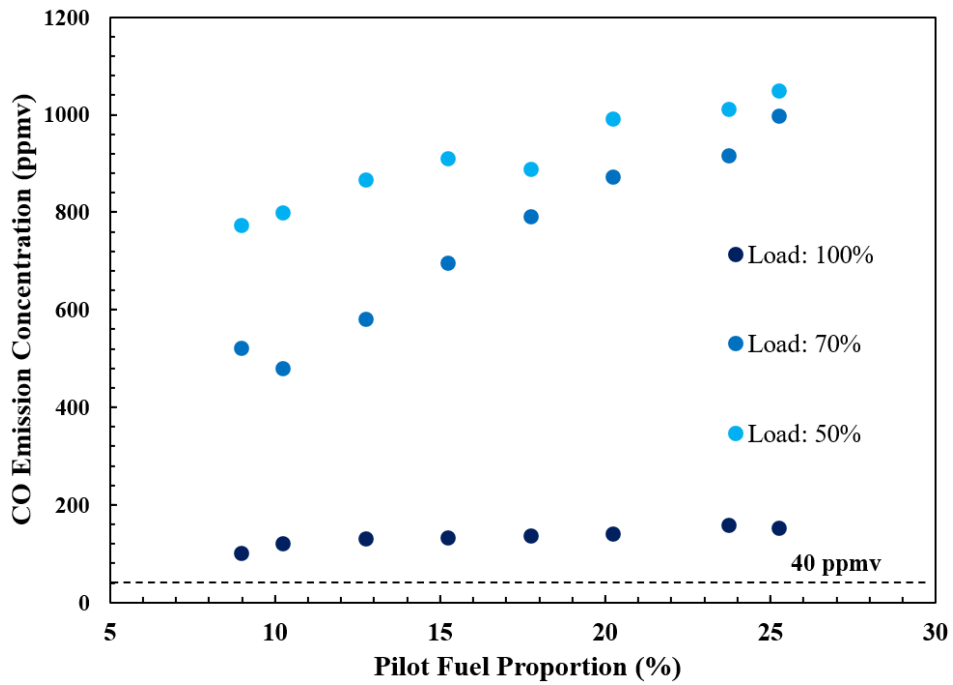
emissions below the regulatory threshold of approximately 40 ppmv when the PFP is kept below 20%. However, this limit is not met under partial loads of 75% or 50%, primarily due to a leaner fuel-air ratio in the reaction zone compared to the design conditions. While modifications in PFP can alter fuel distribution locally, they do not sufficiently improve the overall fuel-air ratio, hindering effective CO oxidation under these conditions.

When PFP is increased, a larger portion of the fuel is burned in the pilot flame, which typically has a richer fuel-to-air mixture compared to the main combustion zone. This creates locally fuel-rich conditions that may not have enough oxygen for complete combustion, leading to the formation of CO due to incomplete oxidation of the fuel. The primary role of the pilot flame is to stabilize the main flame, but an excessive PFP can disrupt this balance, causing uneven combustion and poor mixing of air and fuel, which further increases CO emissions. The PFP is critical in ensuring flame stability, particularly under varying operational conditions. However, increasing the PFP beyond an optimal level can adversely affect flame dynamics, creating overly rich zones near the pilot flame and resulting in less efficient combustion in the main flame zone. This can lead to localized areas of incomplete combustion, further elevating CO emissions. Additionally, the higher temperature and concentration of the pilot flame can increase NO<sub>x</sub> production due to enhanced thermal NO<sub>x</sub> formation mechanisms. Thus, optimizing the PFP is crucial in combustion design to balance flame stability and emission control. While a higher PFP can help maintain flame stability and prevent blowout or instability at low loads or when using lower-quality fuels, it also tends to increase CO and NO<sub>x</sub> emissions. Therefore, combustion engineers must carefully adjust the PFP to ensure stable operation while minimizing emissions to meet regulatory limits.

In addition, **Figure 57** (b) indicates that biogas fails to meet the compliance limit under different load capacities because of the presence of CO<sub>2</sub> in methane, which poses critical challenges. CO<sub>2</sub>, acting as an inert diluent, reduces flame stability and burning velocity, leading to a phenomenon known as 'flame out' if the combustor fails to maintain adequate fuel supply. This effect lowers the adiabatic flame temperature, hinders fuel oxidation, and inhibits CO-to-CO<sub>2</sub> conversion, resulting in higher CO emissions.



(a)

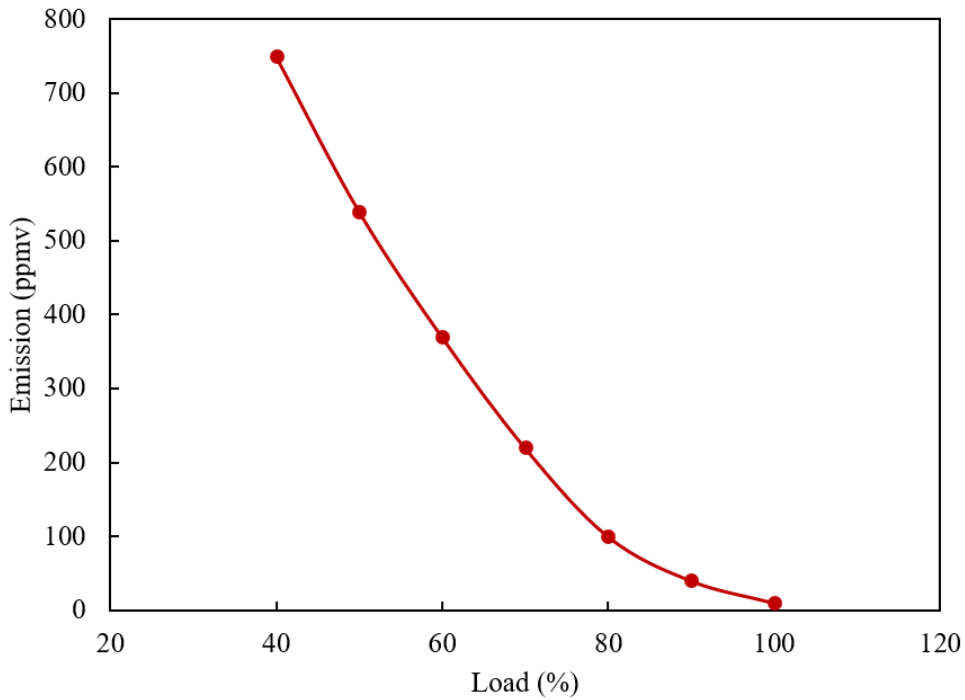


(b)

Figure 57- Effect of PFP on CO emissions (ppmv @15% O<sub>2</sub>) at multiple power settings based on CFD simulation for two fuels: (a) Methane, and (b) Biogas.

### Effect of Load on CO emission

**Figure 58** illustrates the effect of the load on the CO emission for two different fuels including methane and biogas. As it can be seen for both case scenarios the maximum amount of the emission is released when the system works at the part load and as the percentage of the load increases the amount of the emission decreases and reach its minimum at 100% full-load. Comparing these two fuels gives us the insight that in all similar work load the CO emission of the biogas is more than methane and this lays into two factors. First the existence of the CO<sub>2</sub> inside the biogas and second its lower flame temperature. The same conclusion can be generated for the higher CO emission in lower load percentage. Because when the percentage of the work is lower, we have lower flame temperature and in causes the increase in CO emissions.



(a)

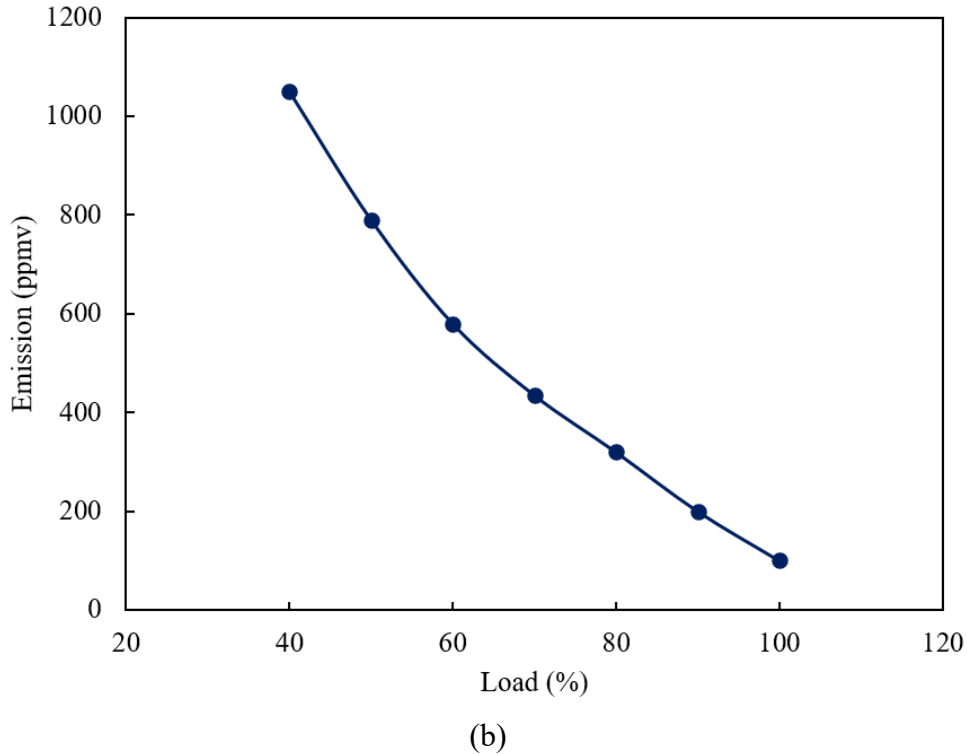
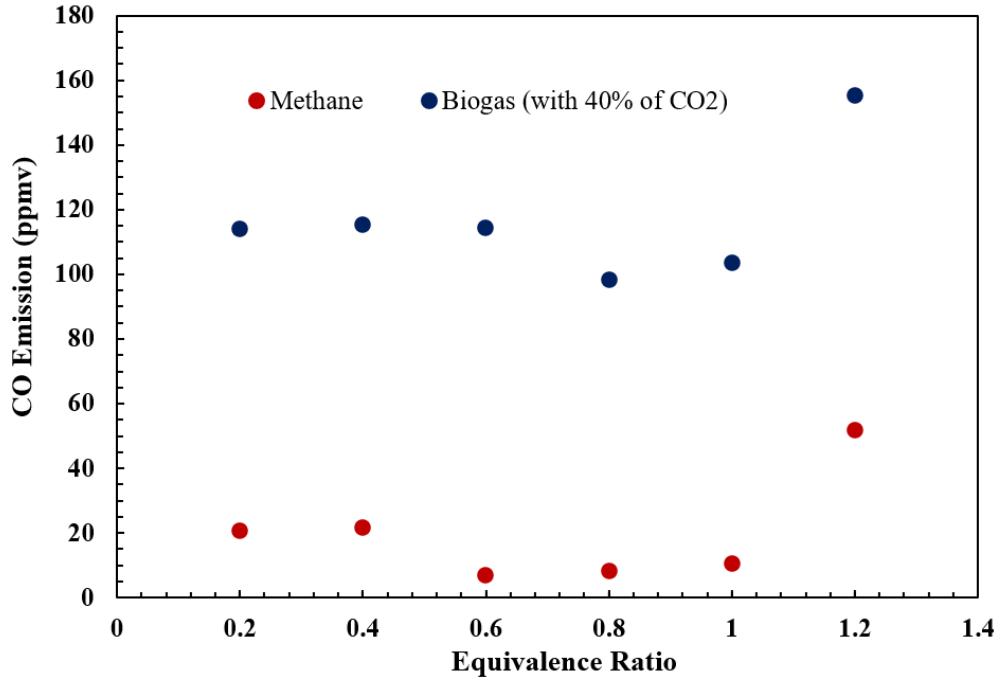


Figure 58- The effect of the load on the CO emission for different fuels (a) methane (b) biogas

**Figure 59** shows the impact of equivalence ratios (ER) on mitigating CO emission concentrations during the combustion of biogas and methane in the MGT, as analyzed through CFD simulations. According to the following scatter plot, methane generates lower CO emissions in comparison to biogas, presenting a trend where CO emissions decrease to a minimum of 7.1 ppmv at an ER of 0.6, followed by a slight increase at higher ERs. For biogas, CO emissions reach a minimum of about 98.4 ppmv at an ER of 0.8, thereafter experiencing rapid growth with increasing ERs. These observations underscore the importance of fuel composition and ER in CO emission profiles, emphasizing the advantage of hydrogen combustion, which inherently produces minimal CO emissions due to its carbon-free nature.



**Figure 59**-Variation of CO emissions ((ppmv @15% O<sub>2</sub>) with ER for methane, and biogas.

**Figure 60** illustrates the impact of varying CO<sub>2</sub> concentrations in biogas on CO emissions. At a constant CO<sub>2</sub> level, CO emissions are minimized under lean combustion conditions. Specifically, at the design condition with 40% CO<sub>2</sub>, CO emissions reach 98.4 ppmv at an equivalence ratio (ER) of 0.8 and then increase. Beyond this ER, a consistent trend is observed, with a relative rise in CO emissions due to oxygen depletion and resulting incomplete combustion. Under lean and stoichiometric conditions, CO emissions remain low and show minimal sensitivity to changes in CO<sub>2</sub> content in the biogas. In contrast, under rich combustion scenarios, CO emissions increase substantially, attributable to two main factors: first, CO<sub>2</sub> acts as a diluent, reducing flame speed and temperature; second, there is decreased oxygen availability in the combustion zone at high ER.

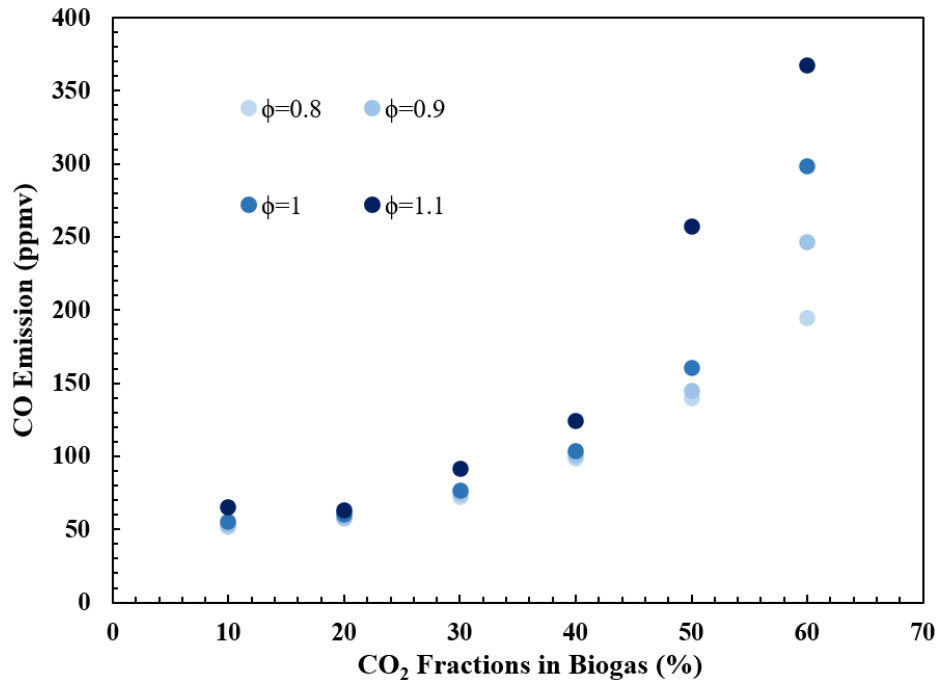


**Figure 60**-Effect of CO<sub>2</sub> concentration on CO emissions (ppmv @15% O<sub>2</sub>) in biogas combustion.

## Chapter 5: Conclusion

Urban areas are experiencing increasing energy demands, which significantly contribute to the rise in global emissions. Dependence on fossil fuels to satisfy this demand presents severe economic and environmental threats due to the depletion of these finite resources and the pollutants they emit. In response to these concerns, there is a growing shift towards integrating alternative and renewable energy sources into cogeneration systems for urban energy generation.

This thesis contributes to identifying the most suitable small-scale cogeneration systems for urban settings with varying energy demands. The study examines how renewable energy sources, notably hydrogen and biogas, influence the efficiency of such cogeneration systems in contrast to conventional methane-based fuels. This analysis underscores the importance of integrating renewable fuels for sustainable urban energy solutions. Based on the comprehensive literature review on a wide range of cogeneration technologies regarding their application, efficiency priorities, power range, lifetime, and maintenance performance for renewable fuels, the two most promising technology options for urban energy supply are selected for detailed analysis, including a proton exchange membrane fuel cell (PEM fuel cell) and a recuperated micro-gas turbine (MGT). The function and availability of proposed cogeneration systems under multiple scenarios, including technology, control, fuel selection, and operational considerations, are modeled. Additionally, their performance under off-design conditions, as well as various control strategies, are comprehensively evaluated.

To model the proposed technologies, the governing mathematical equations, are implemented in Fortran, a programming language, and thermodynamic data for the models are obtained through the Engineering Equation Solver (EES). Detailed electrochemical and thermal models are developed to simulate electricity and heat production from the PEM fuel cell. For the recuperated MGT integrated with a heat recovery unit (HRU), a comprehensive numerical algorithm is developed based on real maps and required assumptions. To achieve a converged steady-state solution the Newton-Raphson (N-R) method is applied, also coded in Fortran. The focus of this algorithm is to optimize heat recovery from exhaust gases and to find the best control strategy to meet the required heating demand. The developed control strategy involves the precise adjustment of the bypass valve position, which regulates the mass flow rate distribution between the heat

recovery unit and the recuperator, where the preheating of the combustion inlet air improves the system's overall efficiency. Additionally, to effectively meet the required heating demands, the positioning of the bypass valve must be carefully coordinated with the charging and discharging cycles of storage tanks, as well as the transition between standby and active modes of auxiliary boilers. The model developed in this thesis can simulate various CHP gas turbine units operating under both their designed and part-load conditions. For the simulation, the GT333s model from FlexTurbine, which can provide 333 kW of nominal electrical power, is chosen to meet the electrical and heating needs of five residential buildings in Karlsruhe, Germany.

Based on the technology scenario, the performance of the MGT and the PEM fuel cell is assessed under their respective design conditions. The results show that a PEM fuel cell is a more attractive option for high-efficiency cogeneration because it directly converts chemical energy into electrical energy at a low operational temperature. This eliminates the inefficiencies associated with combustion and mechanical energy conversion in the recuperated MGT. It also reduces thermal dissipation and optimizes hydrogen utilization compared to MGT systems that operate at higher temperatures. The developed model in this study is innovative in its practicality, as it can adjust outputs based on different energy demands across various operational ranges. For the case study, with specific data integrated into the model, the findings indicate that the net electrical power output from the MGT (GT333s model by FlexTurbine), which generates 333.67 kW from hydrogen combustion, necessitates the installation of a single MGT unit to meet the electrical demands.

Assessing various renewable fuels in a MGT is essential to specify the effective fuel source for this cogeneration system, considering its heating, electrical outputs, overall efficiency (both electrical and thermal), and availability across diverse operational and control scenarios. During partial load operations, particularly when the bypass valve is fully opened to accommodate peak thermal demands, hydrogen emerges as the optimal fuel, enhancing both thermal and electrical generation. Hydrogen combustion, noted for its high diffusivity, fast flame speed, and low ignition energy, achieves the highest gas temperatures, contributing to improved system performance. Secondly, methane combustion, with its stable combustion characteristics, favorable heat transfer properties, and compatibility with turbine operation at lower power levels, demonstrates the second most efficient efficiency. For example, in the proposed case study, when the turbine

operates at 40% part-load with a 100 % bypass valve position, the hydrogen-based gas turbine generates significant electrical and thermal outputs of 137.08 kW and 635.07 kW, respectively. In comparison, the methane-fueled turbine produces 118.76 kW of electricity and 591.8 kW of thermal energy, while the biogas-fueled turbine delivers 103.68 kW and 540.36 kW, respectively. To supply 402.6 kW of heating for the described buildings, the bypass valve is adjusted to 60% for methane, 56% for hydrogen, and 66% for biogas combustion to efficiently meet the required thermal demands. These bypass valve positions result in overall system efficiencies of 75.14% for CH<sub>4</sub>, 80.35% for H<sub>2</sub>, and 43.03% for biogas.

During winter and fall, hydrogen combustion within the MGT demonstrates the highest efficiency in meeting urban heating demands, achieving complete coverage without auxiliary boiler support. Methane combustion is the next viable option, requiring auxiliary boiler operation for 43 hours to supplement heating. In contrast, biogas combustion, due to its lower heating value, necessitates the longest auxiliary heating duration, amounting to 230 hours. Additionally, the parametric analysis shows that increasing rotational speed, pressure ratio, and working parameter enhances gas flow rates and gas temperatures, which causes the generated power to peak at the maximum values, regardless of the fuel type utilized. Moreover, the operating performance of the PEM fuel cell is assessed under the sensitive analysis. The results indicate that increasing the cell count and ambient temperature in PEM fuel cells leads to increased hydrogen consumption and enhanced reactive surface area, intensifying the electrochemical reactions and increasing the number of catalytic sites, thereby augmenting the overall efficiency and energy output.

Environmental considerations are critical in technological advancements, necessitating precise prediction and control of fuel combustion pollutants. The validated results from MGT's numerical model are utilized to assess pollutant levels through advanced strategies and innovative methodologies. Based on a comprehensive literature review and input from manufacturers, various combustor designs for micro-gas turbines are compared to identify the most effective technology for reducing emissions. A dual axial swirler combustor is selected because its design features ensure a uniform temperature distribution across the combustion chamber, minimize localized hot spots and significantly enhance fuel-air mixing. These characteristics contribute to improved combustion efficiency and flame stability, even at partial loads, making this type of combustor particularly effective in achieving low NO<sub>x</sub> and CO emissions. To analyze the combustion

dynamics of the dual-axial swirler combustor focusing on the premixing, reacting, and dilution zones, a numerical simulation is carried out in Ansys Fluent utilizing the Eddy Dissipation Concept (EDC), and realizable  $k-\epsilon$  turbulence model, suitable for swirling flow regimes. The emission characteristics of the proposed combustion chamber under distinct fuel and operational scenarios are studied using three pollutant level models, including CFD simulations, an Equivalent Chemical Reactor Network (ECRN) model in Ansys Chemkin-Pro, and the mathematical modeling.

To evaluate  $\text{NO}_x$  emissions, a two-step global reaction mechanism, as developed by Polifke, is implemented within the CFD simulations. Additionally,  $\text{NO}_x$  concentrations are quantified using an ECRN model in CHEMKIN, which facilitates a deeper understanding of combustion mechanisms by accurately calculating the production rates of chemical species within defined computational cells. Furthermore, a comprehensive analysis of key species destruction pathways is conducted in CHEMKIN, providing valuable insights into reaction dynamics that are difficult to capture using conventional CFD models alone.

Combustion analysis of methane under the baseload condition and a 9% pilot fuel ratio reveals a minor discrepancy between  $\text{NO}_x$  emissions from the CFD (23.5 ppmv), ECRN model (22 ppmv), and empirical data (22.5 ppmv). This alignment confirms the accuracy of  $\text{NO}_x$  formation predictions in swirling flows by the two proposed methods, validating their reliability in predicting emissions from other fuels, across various operating conditions. The temperature, and  $\text{NO}_x$  emissions distribution from the CFD simulation reveal that hydrogen combustion, due to its high diffusivity, and flame velocity, achieves peak temperatures around 2400 K, leading to the highest  $\text{NO}_x$  emissions compared to other fuel types.

Also, a parametric analysis is performed through the CFD simulation to assess the combustion chamber's performance for three fuel scenarios under various parameters, including power settings, pilot fuel proportion (PFP), ambient temperature, equivalence ratio (ER), and  $\text{CO}_2$  concentration. The numerical simulation shows a similar decrement pattern for  $\text{NO}_x$  and CO emission levels by decreasing the PFP under different load capacities, irrespective of the fuel type utilized. However, pollutant levels have different behaviors under varying load scenarios. Under parametric analysis, the findings reveal that  $\text{NO}_x$  emission levels from the combustion of methane and biogas comply with the regulatory limit (25 ppmv) at partial loads. However, under the base

load, the emission levels meet the regularity threshold when the PFP is below 13% and 18% for methane and biogas, respectively. Moreover, hydrogen fails to meet the emission limit at any operational loads because of the highest flame temperature, the highest flame velocity, and the lowest ignition energy demand of hydrogen, even with a minimized PFP. Notably, in two distinct control scenarios, including the enriched combustion (ER=1.2) and the highest ambient temperature (33°C), peak NO<sub>x</sub> emissions are observed during hydrogen combustion, while methane and biogas yield moderate and the lowest NO<sub>x</sub> concentrations, respectively.

Since an accurate prediction of carbon monoxide (CO) emissions remains a significant challenge for combustion designers, and due to the limitations of the ECRN methodology in predicting CO emissions, a three-step chemical mechanism developed by Polifke in the CFD simulation and a mathematical model are applied in this thesis to accurately predict CO emissions. The mathematical model simplifies the complexities of CO formation, making it more accessible for combustion engineers who require quick and practical estimates of attainable emission levels based on available design parameters.

The comparative analysis of CFD simulations (8.9 ppmv) and mathematical modeling (10.1 ppmv) for CO emission predictions, normalized to a dry basis with 15% oxygen content, demonstrates excellent agreement with experimental data (7.5 ppmv) from a swirl flame database in the context of methane combustion under design conditions. The CFD simulations also indicate that biogas fails to meet the CO emission limit (40 ppmv) across all operating conditions. This is primarily due to the dilution effect of CO<sub>2</sub> in biogas, which reduces the efficiency of the fuel-air mixture by not actively participating in the combustion process. As a result, combustion becomes even less efficient under partial load conditions and complicates emission control strategies.

The parametric analysis, conducted using CFD simulations, reveals that under 50% engine load and 25% PFP, CO emissions for both biogas and methane reach their peak values. This behavior is driven by suboptimal combustion conditions at partial loads, where reduced fuel flow rates lead to leaner fuel-air mixtures in the combustion zone. As a result, flame temperatures drop below optimal levels, causing incomplete combustion and elevated CO emissions. At the same PFP, the analysis confirms that as the engine transitions from baseload to partial load, CO emissions increase, while NO<sub>x</sub> emissions follow the opposite pattern. This inverse relationship is a direct

consequence of the combustion process: at higher temperatures, typical of full-load conditions, thermal NO<sub>x</sub> formation is dominant, while lower temperatures at partial loads hinder complete fuel oxidation, leading to increased CO production. Although PFP is critical for maintaining flame stability, especially under varying operational conditions, increasing PFP beyond its optimal range can negatively impact flame dynamics. Excessive PFP can create fuel-rich zones near the pilot flame, leading to less efficient combustion in the main flame zone. This results in localized regions of incomplete combustion, further elevating CO emissions. At the stoichiometric ratio, the CO emission concentrations from burning biogas are increased by the increment of CO<sub>2</sub> concentration from 20% to 60%.

## Chapter 6: Future work

This thesis has offered significant insights into compact-size technology options by conducting a comprehensive analysis of their functions, availability, control strategies, and operational patterns. Additionally, it has provided a comparative assessment of pollutant emissions from the swirler micro-gas turbine combustor across three different fuel scenarios, utilizing distinct predictive methods. However, there are several promising directions for future research and development. Below are some potential areas for further investigation.

**Working on BPP, and cooling stacks:** It is crucial to focus on future research for developing Bipolar Plates (BPPs) and cooling stacks to enhance the overall efficiency and longevity of PEM fuel cells. Bipolar plates are essential components that separate individual cells and guide the flow of reaction gases for the fuel cell stack while providing mechanical support. They are classified based on materials into non-metals, metals, and composites. BPPs have essential functions such as electrical conduction, gas distribution, gas sealing, and thermal management. Advanced materials and innovative designs in BPPs can significantly reduce weight, cost, and corrosion issues while improving electrical conductivity and mechanical strength. Optimizing the cooling stack is equally essential as it directly impacts the thermal management of the fuel cell, which is vital for maintaining performance and preventing degradation. Therefore, a strong focus on BPP and cooling stack advancements will benefit the industry by reducing manufacturing costs, improving fuel cell performance, and enhancing durability, making PEM fuel cells more viable for widespread adoption.

**Multi-objective Optimization:** Future research on recuperated MGTs should focus on multi-objective optimization frameworks to balance minimizing emissions and maximizing system performance. This approach requires a comprehensive evaluation of various parameters, including pilot fuel proportion (PFP), combustion chamber design, operating conditions, and control strategies. Optimizing the PFP can help stabilize the flame and reduce NO<sub>x</sub> emissions without compromising combustion efficiency. Additionally, adjusting design parameters like swirler geometry and cooling strategies can enhance mixing and temperature control, thereby decreasing pollutant formation. Identifying optimal operational conditions involves modifying variables such as recuperator efficiency, working parameters, and component efficiency. These modifications are

vital to optimizing the turbine inlet temperature, air-to-fuel ratio, and other crucial factors, thus enhancing the overall system efficiency while concurrently reducing CO<sub>2</sub> and NO<sub>x</sub> emissions. Moreover, applying advanced control mechanisms, including Model Predictive Control (MPC) and adaptive algorithms, enables dynamic adjustment of the MGT's functioning to ensure superior performance across a diverse range of loads and fuel types. By integrating these optimization strategies, researchers and engineers can develop advanced MGT systems that meet environmental regulations and contribute to sustainable energy solutions.

**Life cycle assessment (LCA):** Conducting a comprehensive Life Cycle Assessment (LCA) of PEM fuel cells and recuperated micro-gas turbine (MGT) systems is essential for evaluating their environmental impacts across all life cycle stages, from raw material extraction to disposal. LCA provides a detailed analysis of where CO<sub>2</sub> emissions and other ecological impacts occur, enabling the identification of critical areas for improvement to enhance the overall sustainability of these technologies. Among the various LCA methodologies, Consequential LCA (cLCA) is particularly relevant for assessing the broader environmental effects of changes in product systems, such as fluctuations in demand or shifts in production processes. By considering market responses and the potential shifts in production or consumption patterns, cLCA offers insights into the long-term environmental consequences of adopting these technologies. This future work is crucial for industry stakeholders and policymakers, as it supports the development of greener technologies and aids in compliance with increasingly stringent environmental regulations.

**Combustion Design and Characteristics:** Modifying current combustion chamber designs to optimize hydrogen combustion is a critical area of future research, particularly for reducing NO<sub>x</sub> emissions to comply with regulatory limits. Although hydrogen is a clean fuel that significantly reduces carbon emissions, its combustion at high temperatures results in the formation of NO<sub>x</sub>, a harmful pollutant. To mitigate NO<sub>x</sub> production while maintaining high combustion efficiency, innovative combustion chamber designs are needed. Key strategies include lean premixed combustion to lower flame temperatures, the use of cooling holes and angled injectors for effective cooling and fuel mixing, swirler modifications to enhance fuel-air mixing, flame stabilization techniques to maintain stable combustion under lean conditions, micro-mixing injectors for precise control of fuel distribution, advanced cooling methods like film cooling, and burner head modifications for optimal flame control. These advancements are essential for developing low-

emission hydrogen combustion technologies that align with environmental regulations and support a sustainable energy future.

## References

- [1] Yue M, Lambert H, Pahon E, Roche R, Jemei S. Hydrogen energy systems : A critical review of technologies , applications , trends and challenges. *Renew Sustain Energy Rev* 2021;146:111180. <https://doi.org/10.1016/j.rser.2021.111180>.
- [2] Montazerinejad H, Eicker U. Recent development of heat and power generation using renewable fuels: A comprehensive review. *Renew Sustain Energy Rev* 2022;165:112578.
- [3] Zakaria Z, Kamarudin SK, Abd Wahid KA, Hassan SHA. The progress of fuel cell for malaysian residential consumption: Energy status and prospects to introduction as a renewable power generation system. *Renew Sustain Energy Rev* 2021;144:110984.
- [4] Lu J, Fu Z, Liu J, Pan W. Influence of air distribution on combustion characteristics of a micro gas turbine fuelled by hydrogen-doped methane. *Energy Reports* 2022;8:207–16.
- [5] Gupta S, Malte P, Brunton SL, Novosselov I. Prevention of lean flame blowout using a predictive chemical reactor network control. *Fuel* 2019;236:583–8.
- [6] Kaluri A, Malte P, Novosselov I. Real-time prediction of lean blowout using chemical reactor network. *Fuel* 2018;234:797–808.
- [7] Bhargava A, Kendrick DW, Colket MB, Sowa WA, Casleton KH, Maloney DJ. Pressure effect on NO<sub>x</sub> and CO emissions in industrial gas turbines. *Turbo Expo Power Land, Sea, Air*, vol. 78552, American Society of Mechanical Engineers; 2000, p. V002T02A017.
- [8] Elkady AM, Herbon J, Kalitan DM, Leonard G, Akula R, Karim H, et al. Gas turbine emission characteristics in perfectly premixed combustion 2012.
- [9] Sinha AA, Choudhary T, Shukla AK, Ahmadi P. Thermo-economics, Emissions, and Sustainability Comparison of a Novel Hybrid Evaporative Cooled Solid Oxide Fuel Cell-Recuperated Gas Turbine with Conventional System. *Process Saf Environ Prot* 2024.
- [10] Montazerinejad H, Eicker U, Ahmadi P. Renewable fuel-powered micro-gas turbine and hydrogen fuel cell systems: Exploring scenarios of technology, control, and operation.

- Energy Convers Manag 2024;319:118944.
- [11] Montazerinejad H, Fakhimi E, Ghandehariun S, Ahmadi P. Advanced exergy analysis of a PEM fuel cell with hydrogen energy storage integrated with organic Rankine cycle for electricity generation. *Sustain Energy Technol Assessments* 2022;51:101885.
- [12] Zhao P, Wang J, Gao L, Dai Y. Parametric analysis of a hybrid power system using organic Rankine cycle to recover waste heat from proton exchange membrane fuel cell. *Int J Hydrogen Energy* 2012;37:3382–91.
- [13] Rist JF, Dias MF, Palman M, Zelazo D, Cukurel B. Economic dispatch of a single micro-gas turbine under CHP operation. *Appl Energy* 2017;200:1–18.
- [14] Choudhury A, Chandra H, Arora A. Application of solid oxide fuel cell technology for power generation—A review. *Renew Sustain Energy Rev* 2013;20:430–42.
- [15] Fubara TC, Cecelja F, Yang A. Modelling and selection of micro-CHP systems for domestic energy supply: The dimension of network-wide primary energy consumption. *Appl Energy* 2014;114:327–34.
- [16] Staffell I. Fuel cells for domestic heat and power: are they worth it? 2010.
- [17] Directive EC. Directive 2004/8/EC of the European Parliament and of the Council of 11 February 2004 on the promotion of cogeneration based on a useful heat demand in the internal energy market and amending Directive 92/42/EEC. *Off J Eur Union* 2004:50–60.
- [18] Caresana F, Pelagalli L, Comodi G, Renzi M. Microturbogas cogeneration systems for distributed generation: Effects of ambient temperature on global performance and components' behavior. *Appl Energy* 2014;124:17–27.
- [19] Desai NB, Bandyopadhyay S. Thermo-economic comparisons between solar steam Rankine and organic Rankine cycles. *Appl Therm Eng* 2016;105:862–75.
- [20] Martinez S, Michaux G, Salagnac P, Bouvier J-L. Micro-combined heat and power systems (micro-CHP) based on renewable energy sources. *Energy Convers Manag* 2017;154:262–

85.

- [21] Radenahmad N, Azad AT, Saghir M, Taweekun J, Bakar MSA, Reza MS, et al. A review on biomass derived syngas for SOFC based combined heat and power application. *Renew Sustain Energy Rev* 2020;119:109560.
- [22] Barbieri ES, Melino F, Morini M. Influence of the thermal energy storage on the profitability of micro-CHP systems for residential building applications. *Appl Energy* 2012;97:714–22.
- [23] Lai F, Wang S, Liu M, Yan J. Operation optimization on the large-scale CHP station composed of multiple CHP units and a thermocline heat storage tank. *Energy Convers Manag* 2020;211:112767.
- [24] Bianchi M, De Pascale A, Spina PR. Guidelines for residential micro-CHP systems design. *Appl Energy* 2012;97:673–85.
- [25] Darrow K, Tidball R, Wang J, Hampson A. Catalog of CHP technologies. US Environ Prot Agency, Washington, DC 2015:5–6.
- [26] Modi A, Bühler F, Andreasen JG, Haglind F. A review of solar energy based heat and power generation systems. *Renew Sustain Energy Rev* 2017;67:1047–64.
- [27] Vélez F, Segovia JJ, Martín MC, Antolín G, Chejne F, Quijano A. A technical, economical and market review of organic Rankine cycles for the conversion of low-grade heat for power generation. *Renew Sustain Energy Rev* 2012;16:4175–89.
- [28] Sharaf OZ, Orhan MF. An overview of fuel cell technology: Fundamentals and applications. *Renew Sustain Energy Rev* 2014;32:810–53.
- [29] Streimikiene D, Baležentis T. Multi-criteria assessment of small scale CHP technologies in buildings. *Renew Sustain Energy Rev* 2013;26:183–9.
- [30] Mikalsen R. Internal combustion and reciprocating engine systems for small and micro combined heat and power (CHP) applications. *Small Micro Comb. Heat Power Syst.*,

Elsevier; 2011, p. 125–46.

- [31] Sprouse III C, Depcik C. Review of organic Rankine cycles for internal combustion engine exhaust waste heat recovery. *Appl Therm Eng* 2013;51:711–22.
- [32] Aghaali H, Ångström H-E. A review of turbocompounding as a waste heat recovery system for internal combustion engines. *Renew Sustain Energy Rev* 2015;49:813–24.
- [33] Görgülü A, Yağlı H, Koç Y, Koç A. Comprehensive analysis of the effect of water injection on performance and emission parameters of the hydrogen fuelled recuperative and non-recuperative gas turbine system. *Int J Hydrogen Energy* 2020;45:34254–67.
- [34] Kenanoğlu R, Baltacıoğlu E. An experimental investigation on hydroxy (HHO) enriched ammonia as alternative fuel in gas turbine. *Int J Hydrogen Energy* 2020.
- [35] Quoilin S, Van Den Broek M, Declaye S, Dewallef P, Lemort V. Techno-economic survey of Organic Rankine Cycle (ORC) systems. *Renew Sustain Energy Rev* 2013;22:168–86.
- [36] Kaviri AG, Jaafar MNM, Lazim TM. Modeling and multi-objective exergy based optimization of a combined cycle power plant using a genetic algorithm. *Energy Convers Manag* 2012;58:94–103.
- [37] Hosseini SE, Barzegaravval H, Ganjehkaviri A, Wahid MA, Jaafar MNM. Modelling and exergoeconomic-environmental analysis of combined cycle power generation system using flameless burner for steam generation. *Energy Convers Manag* 2017;135:362–72.
- [38] Hosseini SE. Integrating a gas turbine system and a flameless boiler to make steam for hydrogen production in a solid oxide steam electrolyzer. *Appl Therm Eng* 2020;180:115890.
- [39] Backman JLH, Kaikko J. Microturbine systems for small combined heat and power (CHP) applications. *Small Micro Comb. Heat Power Syst.*, Elsevier; 2011, p. 147–78.
- [40] Lin P, Du X, Shi Y, Sun X-M. Modeling and controller design of a micro gas turbine for power generation. *ISA Trans* 2020.

- [41] Amidpour M, Man MHK. Cogeneration and Polygeneration Systems. Academic Press; 2020.
- [42] Gökalp I, Lebas E. Alternative fuels for industrial gas turbines (AFTUR). *Appl Therm Eng* 2004;24:1655–63.
- [43] Waitz IA, Gauba G, Tzeng Y-S. Combustors for micro-gas turbine engines 1998.
- [44] Arsalis A. Thermodynamic modeling and parametric study of a small-scale natural gas/hydrogen-fueled gas turbine system for decentralized applications. *Sustain Energy Technol Assessments* 2019;36:100560.
- [45] Valera Medina A, Morris S, Runyon J, Pugh DG, Marsh R, Beasley P, et al. Ammonia, methane and hydrogen for gas turbines. *Energy Procedia* 2015;75:118–23.
- [46] Petersen EL, Hall JM, Smith SD, de Vries J, Amadio AR, Crofton MW. Ignition of lean methane-based fuel blends at gas turbine pressures 2007.
- [47] Juste GL. Hydrogen injection as additional fuel in gas turbine combustor. Evaluation of effects. *Int J Hydrogen Energy* 2006;31:2112–21.
- [48] Kim HS, Arghode VK, Gupta AK. Flame characteristics of hydrogen-enriched methane–air premixed swirling flames. *Int J Hydrogen Energy* 2009;34:1063–73.
- [49] Schefer RW, Oefelein J. Reduced turbine emissions using hydrogen-enriched fuels. *Proc. 2002 US DOE Hydrog. Progr. Rev. NREL/CP-610-32405*, 2002, p. 1–16.
- [50] Schefer RW. Hydrogen enrichment for improved lean flame stability. *Int J Hydrogen Energy* 2003;28:1131–41.
- [51] Liu H, Cui Y, Chen B, Kyritsis DC, Tang Q, Feng L, et al. Effects of flame temperature on PAHs and soot evolution in partially premixed and diffusion flames of a diesel surrogate. *Energy & Fuels* 2019;33:11821–9.
- [52] Somehsaraei HN, Majoumerd MM, Breuhaus P, Assadi M. Performance analysis of a biogas-fueled micro gas turbine using a validated thermodynamic model. *Appl Therm Eng*

- 2014;66:181–90.
- [53] Al Moussawi H, Fardoun F, Louahlia H. Selection based on differences between cogeneration and trigeneration in various prime mover technologies. *Renew Sustain Energy Rev* 2017;74:491–511.
- [54] Isa NM, Tan CW, Yatim AHM. A comprehensive review of cogeneration system in a microgrid: A perspective from architecture and operating system. *Renew Sustain Energy Rev* 2018;81:2236–63.
- [55] Alanne K, Saari A. Sustainable small-scale CHP technologies for buildings: the basis for multi-perspective decision-making. *Renew Sustain Energy Rev* 2004;8:401–31.
- [56] Rocha DHD, Silva RJ. Exergoenvironmental analysis of a ultra-supercritical coal-fired power plant. *J Clean Prod* 2019;231:671–82.
- [57] Braimakis K, Magiri-Skouloudi D, Grimekis D, Karellas S. Energy-exergy analysis of ultra-supercritical biomass-fuelled steam power plants for industrial CHP, district heating and cooling. *Renew Energy* 2020.
- [58] Caglayan H, Caliskan H. Advanced exergy analyses and optimization of a cogeneration system for ceramic industry by considering endogenous, exogenous, avoidable and unavoidable exergies under different environmental conditions. *Renew Sustain Energy Rev* 2021;140:110730.
- [59] Patuzzi F, Prando D, Vakalis S, Rizzo AM, Chiaramonti D, Tirlor W, et al. Small-scale biomass gasification CHP systems: Comparative performance assessment and monitoring experiences in South Tyrol (Italy). *Energy* 2016;112:285–93.
- [60] Ahmadi G, Toghraie D, Akbari O. Energy, exergy and environmental (3E) analysis of the existing CHP system in a petrochemical plant. *Renew Sustain Energy Rev* 2019;99:234–42.
- [61] Santos M, André J, Costa E, Mendes R, Ribeiro J. Design strategy for component and working fluid selection in a domestic micro-CHP ORC boiler. *Appl Therm Eng*

2020;169:114945.

- [62] Dong L, Liu H, Riffat S. Development of small-scale and micro-scale biomass-fuelled CHP systems—A literature review. *Appl Therm Eng* 2009;29:2119–26.
- [63] Wang Y, Wehrle L, Banerjee A, Shi Y, Deutschmann O. Analysis of a biogas-fed SOFC CHP system based on multi-scale hierarchical modeling. *Renew Energy* n.d.;163:78–87.
- [64] González-Pino I, Pérez-Iribarren E, Campos-Celador A, Terés-Zubiaga J, Las-Heras-Casas J. Modelling and experimental characterization of a Stirling engine-based domestic micro-CHP device. *Energy Convers Manag* 2020;225:113429.
- [65] Cardozo E, Malmquist A. Performance comparison between the use of wood and sugarcane bagasse pellets in a Stirling engine micro-CHP system. *Appl Therm Eng* 2019;159:113945.
- [66] Thiers S, Aoun B, Peuportier B. Experimental characterization, modeling and simulation of a wood pellet micro-combined heat and power unit used as a heat source for a residential building. *Energy Build* 2010;42:896–903.
- [67] Elmer T, Worall M, Wu S, Riffat SB. Fuel cell technology for domestic built environment applications: State of-the-art review. *Renew Sustain Energy Rev* 2015;42:913–31.
- [68] Razmi AR, Janbaz M. Exergoeconomic assessment with reliability consideration of a green cogeneration system based on compressed air energy storage (CAES). *Energy Convers Manag* 2020;204:112320.
- [69] Jain M, Gupta S, Masand D, Agnihotri G, Jain S. Real-time implementation of islanded microgrid for remote areas. *J Control Sci Eng* 2016;2016.
- [70] Firouzmakan P, Hooshmand R-A, Bornapour M, Khodabakhshian A. A comprehensive stochastic energy management system of micro-CHP units, renewable energy sources and storage systems in microgrids considering demand response programs. *Renew Sustain Energy Rev* 2019;108:355–68.
- [71] International Energy Agency (IEA), *Global Energy & CO2 Status Report 2019: The latest*

- trends in energy and emissions in 2018 n.d.
- [72] IEA Net Zero 2050 Report, May 2021 n.d.
- [73] Sekar M, Alahmadi TA, Nithya S. Numerical simulation of industrial gas burners fueled with hydrogen-methane mixtures for enhanced combustion efficiency and reduced greenhouse gas emissions. *Fuel* 2024;370:131807.
- [74] Rosen MA, Koohi-Fayegh S. The prospects for hydrogen as an energy carrier: an overview of hydrogen energy and hydrogen energy systems. *Energy, Ecol Environ* 2016;1:10–29.
- [75] Mazloomi K, Gomes C. Hydrogen as an energy carrier: prospects and challenges. *Renew Sustain Energy Rev* 2012;16:3024–33.
- [76] El-Adawy M, Nemitallah MA, Abdelhafez A. Towards sustainable hydrogen and ammonia internal combustion engines: Challenges and opportunities. *Fuel* 2024;364:131090.
- [77] Dinesh MH, Kumar GN. Experimental investigation of variable compression ratio and ignition timing effects on performance, combustion, and Nox emission of an ammonia/hydrogen-fuelled Si engine. *Int J Hydrogen Energy* 2023;48:35139–52.
- [78] Manigandan S, Ponnusamy VK, Devi PB, Oke SA, Sohret Y, Venkatesh S, et al. Effect of nanoparticles and hydrogen on combustion performance and exhaust emission of corn blended biodiesel in compression ignition engine with advanced timing. *Int J Hydrogen Energy* 2020;45:3327–39.
- [79] Sun X, Jiang Y, Zhao P, Jing G, Ma T. Effect of ammonia/hydrogen blending and injection modes on combustion emission and performance of marine engine. *Fuel* 2024;371:131894.
- [80] Manigandan S, Praveenkumar TR, Ryu JI, Verma TN, Pugazhendhi A. Role of hydrogen on aviation sector: A review on hydrogen storage, fuel flexibility, flame stability, and emissions reduction on gas turbines engines. *Fuel* 2023;352:129064.
- [81] Hwang J, Maharjan K, Cho H. A review of hydrogen utilization in power generation and transportation sectors: Achievements and future challenges. *Int J Hydrogen Energy* 2023.

- [82] Razaghi M, Rahdar MH, Aghamohamadi N, Mohammadi M, Ahmadi P. Biofuel, solar-biofuel or geothermal energy; which resource can better contribute to an integrated energy system for residential energy demands. *Process Saf Environ Prot* 2024;181:103–30.
- [83] Lieuwen TC, Yang V. *Gas turbine emissions*. vol. 38. Cambridge university press; 2013.
- [84] Rao A, Liu Y, Ma F. Study of NO<sub>x</sub> emission for hydrogen enriched compressed natural along with exhaust gas recirculation in spark ignition engine by Zeldovich's mechanism, support vector machine and regression correlation. *Fuel* 2022;318:123577.
- [85] Zhao F, Sun B, Yuan S, Bao L, Wei H, Luo Q. Experimental and modeling investigations to improve the performance of the near-zero NO<sub>x</sub> emissions direct-injection hydrogen engine by injection optimization. *Int J Hydrogen Energy* 2024;49:713–24.
- [86] Lee J, Kim N II. Stabilization and soot/NO<sub>x</sub> emission of hydrogen-enriched methane flames in a turbulent jet with coaxial air under elevated pressures. *Int J Hydrogen Energy* 2023;48:37402–14.
- [87] Han L, Li J, Zhao D, Xi Y, Gu X, Wang N. Effect analysis on energy conversion enhancement and NO<sub>x</sub> emission reduction of ammonia/hydrogen fuelled wavy micro-combustor for micro-thermophotovoltaic application. *Fuel* 2021;289:119755.
- [88] Viteri JP, Viteri S, Alvarez-Vasco C, Henao F. A systematic review on green hydrogen for off-grid communities—technologies, advantages, and limitations. *Int J Hydrogen Energy* 2023.
- [89] Vance FH, de Goey LPH, van Oijen JA. Prediction of flashback limits for laminar premixed hydrogen-air flames using flamelet generated manifolds. *Int J Hydrogen Energy* 2023;48:27001–12.
- [90] Fruzza F, Lamioni R, Mariotti A, Salvetti MV, Galletti C. Flashback propensity due to hydrogen blending in natural gas: Sensitivity to operating and geometrical parameters. *Fuel* 2024;362:130838.
- [91] Chapman A, Itaoka K, Hirose K, Davidson FT, Nagasawa K, Lloyd AC, et al. A review of

- four case studies assessing the potential for hydrogen penetration of the future energy system. *Int J Hydrogen Energy* 2019;44:6371–82.
- [92] Muñoz P, Franceschini EA, Levitan D, Rodriguez CR, Humana T, Perelmuter GC. Comparative analysis of cost, emissions and fuel consumption of diesel, natural gas, electric and hydrogen urban buses. *Energy Convers Manag* 2022;257:115412.
- [93] Agostinho F, Silva ES, da Silva CC, Almeida CMVB, Giannetti BF. Environmental performance for hydrogen locally produced and used as an energy source in urban buses. *J Clean Prod* 2023;396:136435.
- [94] Baroutaji A, Wilberforce T, Ramadan M, Olabi AG. Comprehensive investigation on hydrogen and fuel cell technology in the aviation and aerospace sectors. *Renew Sustain Energy Rev* 2019;106:31–40.
- [95] Yang J, Wang H, Dong X, Gong M. Performances comparison of adsorption hydrogen storage tanks at a wide temperature and pressure zone. *Int J Hydrogen Energy* 2023.
- [96] Dincer I. Green methods for hydrogen production. *Int J Hydrogen Energy* 2012;37:1954–71.
- [97] Jia Y, Sun C, Shen S, Zou J, Mao SS, Yao X. Combination of nanosizing and interfacial effect: future perspective for designing Mg-based nanomaterials for hydrogen storage. *Renew Sustain Energy Rev* 2015;44:289–303.
- [98] Sadhasivam T, Kim H-T, Jung S, Roh S-H, Park J-H, Jung H-Y. Dimensional effects of nanostructured Mg/MgH<sub>2</sub> for hydrogen storage applications: a review. *Renew Sustain Energy Rev* 2017;72:523–34.
- [99] Hassan IA, Ramadan HS, Saleh MA, Hissel D. Hydrogen storage technologies for stationary and mobile applications: Review, analysis and perspectives. *Renew Sustain Energy Rev* 2021;149:111311.
- [100] Acar C, Dincer I. Review and evaluation of hydrogen production options for better environment. *J Clean Prod* 2019;218:835–49.

- [101] Inayat M, Sulaiman SA, Kurnia JC, Shahbaz M. Effect of various blended fuels on syngas quality and performance in catalytic co-gasification: A review. *Renew Sustain Energy Rev* 2019;105:252–67.
- [102] Rafiee A, Khalilpour KR, Prest J, Skryabin I. Biogas as an energy vector. *Biomass and Bioenergy* 2021;144:105935.
- [103] García R, Gil M V, Rubiera F, Chen D, Pevida C. Renewable hydrogen production from biogas by sorption enhanced steam reforming (SESR): A parametric study. *Energy* 2021;218:119491.
- [104] Stürmer B, Leiers D, Anspach V, Brüggling E, Scharfy D, Wissel T. Agricultural biogas production: A regional comparison of technical parameters. *Renew Energy* 2021;164:171–82.
- [105] Stürmer B, Theuretzbacher F, Saracevic E. Opportunities for the integration of existing biogas plants into the Austrian electricity market. *Renew Sustain Energy Rev* 2020:110548.
- [106] Krishnamoorthi M, Sreedhara S, Duvvuri PP. Experimental, numerical and exergy analyses of a dual fuel combustion engine fuelled with syngas and biodiesel/diesel blends. *Appl Energy* 2020;263:114643.
- [107] Zeng J, Xiao R, Yuan J. High-quality syngas production from biomass driven by chemical looping on a PY-GA coupled reactor. *Energy* 2021;214:118846.
- [108] Xie H, Li R, Yu Z, Wang Z, Yu Q, Qin Q. Combined steam/dry reforming of bio-oil for H<sub>2</sub>/CO syngas production with blast furnace slag as heat carrier. *Energy* 2020;200:117481.
- [109] Paulino RFS, Essiptchouk AM, Silveira JL. The use of syngas from biomedical waste plasma gasification systems for electricity production in internal combustion: Thermodynamic and economic issues. *Energy* 2020;199:117419.
- [110] Mei Z, Chen D, Zhang J, Yin L, Huang Z, Xin Q. Sewage sludge pyrolysis coupled with self-supplied steam reforming for high quality syngas production and the influence of initial moisture content. *Waste Manag* 2020;106:77–87.

- [111] Elkhailifa S, Al-Ansari T, Mackey HR, McKay G. Food waste to biochars through pyrolysis: A review. *Resour Conserv Recycl* 2019;144:310–20.
- [112] Fiore M, Magi V, Viggiano A. Internal combustion engines powered by syngas: A review. *Appl Energy* 2020;276:115415.
- [113] Kishore VR, Ravi M, Ray A. Effect of hydrogen content and dilution on laminar burning velocity and stability characteristics of producer gas-air mixtures. *Int J React Syst* 2008;310740.
- [114] Fossum M, Beyer R V, Bioenergy I. Co-combustion: Biomass fuel gas and natural gas. SINTEF Energy Res Trondheim 1998.
- [115] Thomson R, Kwong P, Ahmad E, Nigam KDP. Clean syngas from small commercial biomass gasifiers; a review of gasifier development, recent advances and performance evaluation. *Int J Hydrogen Energy* 2020.
- [116] Peng N, Gai C, Peng C. Enhancing hydrogen-rich syngas production and energy recovery efficiency by integrating hydrothermal carbonization pretreatment with steam gasification. *Energy* 2020;210:118655.
- [117] Benaissa S, Adouane B, Ali SM, Rashwan SS, Aouachria Z. Investigation on combustion characteristics and emissions of biogas/hydrogen blends in gas turbine combustors. *Therm Sci Eng Prog* 2022;27:101178.
- [118] Reale F, Sannino R. Water and steam injection in micro gas turbine supplied by hydrogen enriched fuels: Numerical investigation and performance analysis. *Int J Hydrogen Energy* 2021;46:24366–81.
- [119] Aalrebei OF, Al Assaf AH, Amhamed A, Swaminathan N, Hewlett S. Ammonia-hydrogen-air gas turbine cycle and control analyses. *Int J Hydrogen Energy* 2022.
- [120] Chen Y-Z, Zhao X-D, Xiang H-C, Tsoutsanis E. A sequential model-based approach for gas turbine performance diagnostics. *Energy* 2020:119657.

- [121] Pollet BG, Staffell I, Shang JL. Current status of hybrid, battery and fuel cell electric vehicles: From electrochemistry to market prospects. *Electrochim Acta* 2012;84:235–49.
- [122] Lü X, Wu Y, Lian J, Zhang Y, Chen C, Wang P, et al. Energy management of hybrid electric vehicles: A review of energy optimization of fuel cell hybrid power system based on genetic algorithm. *Energy Convers Manag* 2020;205:112474.
- [123] Barakat AA, Diab JH, Badawi NS, Nader WSB, Mansour CJ. Combined cycle gas turbine system optimization for extended range electric vehicles. *Energy Convers Manag* 2020;226:113538.
- [124] Rochelle D, Najafi H. A review of the effect of biodiesel on gas turbine emissions and performance. *Renew Sustain Energy Rev* 2019;105:129–37.
- [125] Włodarski W. Control of a vapour microturbine set in cogeneration applications. *ISA Trans* 2019;94:276–93.
- [126] Hashmi MB, Mansouri M, Assadi M. Dynamic Performance and Control Strategies of Micro Gas Turbines: State-of-the-Art Review, Methods, and Technologies. *Energy Convers Manag X* 2023:100376.
- [127] Balli O, Caliskan H. Various thermoeconomic assessments of a heat and power system with a micro gas turbine engine used for industry. *Energy Convers Manag* 2022;252:114984.
- [128] Konečná E, Teng SY, Máša V. New insights into the potential of the gas microturbine in microgrids and industrial applications. *Renew Sustain Energy Rev* 2020;134:110078.
- [129] Fershalov AY, Fershalov YY, Fershalov MY. Principles of designing gas microturbine stages. *Energy* 2020:119488.
- [130] Bazooyar B, Darabkhani HG. Design and numerical analysis of a 3 kWe flameless microturbine combustor for hydrogen fuel. *Int J Hydrogen Energy* 2019;44:11134–44.
- [131] Escamilla A, Sanchez D, Garcia-Rodriguez L. Assessment of power-to-power renewable energy storage based on the smart integration of hydrogen and micro gas turbine

- technologies. *Int J Hydrogen Energy* 2022;47:17505–25.
- [132] Hosseinimaab SM, Tousi AM. Optimizing the performance of a single-shaft micro gas turbine engine by modifying its centrifugal compressor design. *Energy Convers Manag* 2022;271:116245.
- [133] Ayaz SK, Altuntas O, Caliskan H. Enhanced life cycle modelling of a micro gas turbine fuelled with various fuels for sustainable electricity production. *Renew Sustain Energy Rev* 2021;149:111323.
- [134] Thu K, Saha BB, Chua KJ, Bui TD. Thermodynamic analysis on the part-load performance of a microturbine system for micro/mini-CHP applications. *Appl Energy* 2016;178:600–8.
- [135] Stathopoulos P, Paschereit CO. Retrofitting micro gas turbines for wet operation. A way to increase operational flexibility in distributed CHP plants. *Appl Energy* 2015;154:438–46.
- [136] Du Toit M, Engelbrecht N, Oelofse SP, Bessarabov D. Performance evaluation and emissions reduction of a micro gas turbine via the co-combustion of H<sub>2</sub>/CH<sub>4</sub>/CO<sub>2</sub> fuel blends. *Sustain Energy Technol Assessments* 2020;39:100718.
- [137] Lee JJ, Jeon MS, Kim TS. The influence of water and steam injection on the performance of a recuperated cycle microturbine for combined heat and power application. *Appl Energy* 2010;87:1307–16.
- [138] Gimelli A, Sannino R. Thermodynamic model validation of Capstone C30 micro gas turbine. *Energy Procedia* 2017;126:955–62.
- [139] Basrawi F, Ibrahim H, Yamada T. Optimal unit sizing of biogas-fuelled micro gas turbine cogeneration systems in a sewage treatment plant. *Energy Procedia* 2015;75:1052–8.
- [140] Sung T, Kim S, Kim KC. Thermo-economic analysis of a biogas-fueled micro-gas turbine with a bottoming organic Rankine cycle for a sewage sludge and food waste treatment plant in the Republic of Korea. *Appl Therm Eng* 2017;127:963–74.
- [141] Cagnano A, De Tuglie E. On-line identification of simplified dynamic models: Simulations

- and experimental tests on the Capstone C30 microturbine. *Electr Power Syst Res* 2018;157:145–56.
- [142] Henao NC, Lora EES, Maya DMY, Venturini OJ, Franco EHM. Technical feasibility study of 200 kW gas microturbine coupled to a dual fluidized bed gasifier. *Biomass and Bioenergy* 2019;130:105369.
- [143] Rasul MG, Ault C, Sajjad M. Bio-gas mixed fuel micro gas turbine co-generation for meeting power demand in Australian remote areas. *Energy Procedia* 2015;75:1065–71.
- [144] Stadler M, Cardoso G, Mashayekh S, Forget T, DeForest N, Agarwal A, et al. Value streams in microgrids: A literature review. *Appl Energy* 2016;162:980–9.
- [145] Jamshidiha M, Kamal MM, Cafiero M, Coussement A, Parente A. Experimental and numerical characterization of hydrogen combustion in a reverse-flow micro gas turbine combustor. *Int J Hydrogen Energy* 2024;55:1299–311.
- [146] Cong L, Zhijun S, Yimin L, Zhongning Z, Lina M. Experimental study on the performance of micro gas turbines under different intake environments. *Case Stud Therm Eng* 2024;58:104415.
- [147] Hu Z, Zhang X. Study on laminar combustion characteristic of low calorific value gas blended with hydrogen in a constant volume combustion bomb. *Int J Hydrogen Energy* 2019;44:487–93.
- [148] Gong C, Li Z, Li D, Liu J, Si X, Yu J, et al. Numerical investigation of hydrogen addition effects on methanol-air mixtures combustion in premixed laminar flames under lean burn conditions. *Renew Energy* 2018;127:56–63.
- [149] Yan Y, Gao W, Guo H, Yan H, Shen K, Zhang L, et al. Catalytic combustion characteristics of CH<sub>4</sub> in the micro cavity-combustor under different types of air inlet distribution. *Int J Energy Res* 2021;45:3870–82.
- [150] Choi J, Ahn M, Kwak S, Lee JG, Yoon Y. Flame structure and NO<sub>x</sub> emission characteristics in a single hydrogen combustor. *Int J Hydrogen Energy* 2022;47:29542–53.

- [151] Fu Z, Gao H, Zeng Z, Liu J, Zhu Q. Generation characteristics of thermal NO<sub>x</sub> in a double-swirler annular combustor under various inlet conditions. *Energy* 2020;200:117487.
- [152] Nada Y, Kidoguchi Y, Matsumoto M, Sugiyama K, Oono T, Fujii Y, et al. Effects of spacing between fuel and oxidizer nozzles on NO<sub>x</sub> emission from spray combustion furnace operating under various oxidizer temperatures. *Fuel* 2024;366:131398.
- [153] Banihabib R, Lingstädt T, Wersland M, Kutne P, Assadi M. Development and testing of a 100 kW fuel-flexible micro gas turbine running on 100% hydrogen. *Int J Hydrogen Energy* 2024;49:92–111.
- [154] Xing C, Liu L, Qiu P, Zhang L, Yu X, Chen X, et al. Research on combustion performance of a micro-mixing combustor for methane-fueled gas turbine. *J Energy Inst* 2022;103:72–83.
- [155] Bohn D, Lepers J. Effects of biogas combustion on the operation characteristics and pollutant emissions of a micro gas turbine. *Turbo Expo Power Land, Sea, Air*, vol. 36843, 2003, p. 247–57.
- [156] Wang Y, Liu J, Wang L, Fu Z, Weng P. Non-premixed combustion and NO<sub>x</sub> emission characteristics in a micro gas turbine swirl combustor fueled by methane and ammonia at various heat loads. *Heliyon* 2023;9:e14521.
- [157] Zong C, Ji C, Cheng J, Zhu T, Guo D, Li C, et al. Toward off-design loads: Investigations on combustion and emissions characteristics of a micro gas turbine combustor by external combustion-air adjustments. *Energy* 2022;253:124194.
- [158] Koç Y, Yağlı H, Goerguelue A, Koc A. Analysing the performance, fuel cost and emission parameters of the 50 MW simple and recuperative gas turbine cycles using natural gas and hydrogen as fuel. *Int J Hydrogen Energy* 2020;45:22138–47.
- [159] Adamou A, Turner J, Costall A, Jones A, Copeland C. Design, simulation, and validation of additively manufactured high-temperature combustion chambers for micro gas turbines. *Energy Convers Manag* 2021;248:114805.

- [160] Boretta A. Transitioning from low-emission dry micro-mix hydrogen-air combustion to zero-emission wet micro-mix hydrogen-oxygen combustion in hydrogen energy storage systems. *Int J Hydrogen Energy* 2024.
- [161] Savarese M, Cuoci A, De Paepe W, Parente A. Machine learning clustering algorithms for the automatic generation of chemical reactor networks from CFD simulations. *Fuel* 2023;343:127945.
- [162] Li Y, Li H, Guo H, Wang H, Yao M. A numerical study on the chemical kinetics process during auto-ignition of n-heptane in a direct injection compression ignition engine. *Appl Energy* 2018;212:909–18.
- [163] Mashruk S, Kovaleva M, Alnasif A, Chong CT, Hayakawa A, Okafor EC, et al. Nitrogen oxide emissions analyses in ammonia/hydrogen/air premixed swirling flames. *Energy* 2022;260:125183.
- [164] Heidenreich S, Foscolo PU. New concepts in biomass gasification. *Prog Energy Combust Sci* 2015;46:72–95.
- [165] Rovas D, Zabaniotou A. Exergy analysis of a small gasification-ICE integrated system for CHP production fueled with Mediterranean agro-food processing wastes: The SMART-CHP. *Renew Energy* 2015;83:510–7.
- [166] Huang Y, Surawski NC, Zhuang Y, Zhou JL, Hong G. Dual injection: An effective and efficient technology to use renewable fuels in spark ignition engines. *Renew Sustain Energy Rev* 2021;143:110921.
- [167] Escobar-Jiménez RF, Cervantes-Bobadilla M, García-Morales J, Aguilar JFG, Pérez JAH, Alvarez-Gallegos A. The effects of not controlling the hydrogen supplied to an internal combustion engine. *Int J Hydrogen Energy* 2020.
- [168] Ardebili SMS, Solmaz H, İpci D, Calam A, Mostafaei M. A review on higher alcohol of fusel oil as a renewable fuel for internal combustion engines: Applications, challenges, and global potential. *Fuel* 2020;279:118516.

- [169] Yildiz I, Caliskan H, Mori K. Energy, exergy and environmental assessments of biodiesel and diesel fuels for an internal combustion engine using silicon carbide particulate filter. *J Therm Anal Calorim* 2020;1–12.
- [170] Sheykhi M, Chahartaghi M, Pirooz AAS, Flay RGJ. Investigation of the effects of operating parameters of an internal combustion engine on the performance and fuel consumption of a CCHP system. *Energy* 2020;211:119041.
- [171] Capaldi P. A high efficiency 20 kWe microcogeneration unit based on a turbocharged automotive gas engine. *Appl Therm Eng* 2016;109:803–8.
- [172] Towoju OA, Ishola FA. A case for the internal combustion engine powered vehicle. *Energy Reports* 2020;6:315–21.
- [173] Wenzhi G, Junmeng Z, Guanghua L, Qiang B, Liming F. Performance evaluation and experiment system for waste heat recovery of diesel engine. *Energy* 2013;55:226–35.
- [174] Muccillo M, Gimelli A. Experimental development, 1D CFD simulation and energetic analysis of a 15 kW micro-CHP unit based on reciprocating internal combustion engine. *Appl Therm Eng* 2014;71:760–70.
- [175] Baskov V, Ignatov A, Polotnyanshikov V. Assessing the influence of operating factors on the properties of engine oil and the environmental safety of internal combustion engine. *Transp Res Procedia* 2020;50:37–43.
- [176] Leach F, Kalghatgi G, Stone R, Miles P. The scope for improving the efficiency and environmental impact of internal combustion engines. *Transp Eng* 2020:100005.
- [177] Ram NK, Singh NR, Raman P, Kumar A, Kaushal P. Experimental study on performance analysis of an internal combustion engine operated on hydrogen-enriched producer gas from the air–steam gasification. *Energy* 2020:118029.
- [178] Sheykhi M, Chahartaghi M, Balakheli MM, Hashemian SM, Miri SM, Rafiee N. Performance investigation of a combined heat and power system with internal and external combustion engines. *Energy Convers Manag* 2019;185:291–303.

- [179] Salam S, Choudhary T, Pugazhendhi A, Verma TN, Sharma A. A review on recent progress in computational and empirical studies of compression ignition internal combustion engine. *Fuel* 2020;279:118469.
- [180] Zheng CY, Wu JY, Zhai XQ, Yang G, Wang RZ. Experimental and modeling investigation of an ICE (internal combustion engine) based micro-cogeneration device considering overheat protection controls. *Energy* 2016;101:447–61.
- [181] Arbabi P, Abbassi A, Mansoori Z, Seyfi M. Joint numerical-technical analysis and economical evaluation of applying small internal combustion engines in combined heat and power (CHP). *Appl Therm Eng* 2017;113:694–704.
- [182] Lourenço AB, Carvalho M. Exergoeconomic and exergoenvironmental analyses of an off-grid reverse osmosis system with internal combustion engine and waste heat recovery. *Chem Eng J Adv* 2020;4:100056.
- [183] Zhu H, Zhang Y, Liu F, Wei W. Effect of excess hydrogen on hydrogen fueled internal combustion engine under full load. *Int J Hydrogen Energy* 2020.
- [184] Choi W, Kim J, Kim Y, Song HH. Solid oxide fuel cell operation in a solid oxide fuel cell–internal combustion engine hybrid system and the design point performance of the hybrid system. *Appl Energy* 2019;254:113681.
- [185] Yang Y, Zhang H, Yan P, Jermittiparsert K. Multi-objective optimization for efficient modeling and improvement of the high temperature PEM fuel cell based Micro-CHP system. *Int J Hydrogen Energy* 2020;45:6970–81.
- [186] Mehr AS, Lanzini A, Santarelli M, Rosen MA. Polygeneration systems based on high temperature fuel cell (MCFC and SOFC) technology: System design, fuel types, modeling and analysis approaches. *Energy* 2021:120613.
- [187] Meshksar M, Afshariani F, Rahimpour MR. Solar reformers coupled with PEMFCs for residential cogeneration and trigeneration applications. *Curr. Trends Futur. Dev. Membr., Elsevier*; 2020, p. 241–58.

- [188] Crespi E, Guandalini G, Gößling S, Campanari S. Modelling and optimization of a flexible hydrogen-fueled pressurized PEMFC power plant for grid balancing purposes. *Int J Hydrogen Energy* 2021;46:13190–205.
- [189] Chen X, Xu J, Yang C, Fang Y, Li W, Zhang Y, et al. Thermodynamic and economic study of PEMFC stack considering degradation characteristic. *Energy Convers Manag* 2021;235:114016.
- [190] Chen Z, Zuo W, Zhou K, Li Q, Huang Y, Jiaqiang E. Multi-objective optimization of proton exchange membrane fuel cells by RSM and NSGA-II. *Energy Convers Manag* 2023;277:116691.
- [191] Chen Z, Zuo W, Zhou K, Li Q, Huang Y, Jiaqiang E. Multi-factor impact mechanism on the performance of high temperature proton exchange membrane fuel cell. *Energy* 2023;278:127982.
- [192] Chen Z, Zuo W, Zhou K, Li Q, Yi Z, Huang Y. Numerical investigation on the performance enhancement of PEMFC with gradient sinusoidal-wave fins in cathode channel. *Energy* 2024;288:129894.
- [193] Özgür T, Yakaryılmaz AC. A review: Exergy analysis of PEM and PEM fuel cell based CHP systems. *Int J Hydrogen Energy* 2018;43:17993–8000.
- [194] Al-Nimr MA, Bukhari M, Mansour M. A combined CPV/T and ORC solar power generation system integrated with geothermal cooling and electrolyser/fuel cell storage unit. *Energy* 2017;133:513–24.
- [195] Liu G, Qin Y, Wang J, Liu C, Yin Y, Zhao J, et al. Thermodynamic modeling and analysis of a novel PEMFC-ORC combined power system. *Energy Convers Manag* 2020;217:112998.
- [196] Taner T. Energy and exergy analyze of PEM fuel cell: A case study of modeling and simulations. *Energy* 2018;143:284–94.
- [197] Verhaert I, Mulder G, De Paepe M. Evaluation of an alkaline fuel cell system as a micro-

- CHP. *Energy Convers Manag* 2016;126:434–45.
- [198] Salehi A, Mousavi SM, Fasihfar A, Ravanbakhsh M. Energy, exergy, and environmental (3E) assessments of an integrated molten carbonate fuel cell (MCFC), Stirling engine and organic Rankine cycle (ORC) cogeneration system fed by a biomass-fueled gasifier. *Int J Hydrogen Energy* 2019;44:31488–505.
- [199] Mamaghani AH, Najafi B, Shirazi A, Rinaldi F. 4E analysis and multi-objective optimization of an integrated MCFC (molten carbonate fuel cell) and ORC (organic Rankine cycle) system. *Energy* 2015;82:650–63.
- [200] Emadi MA, Chitgar N, Oyewunmi OA, Markides CN. Working-fluid selection and thermoeconomic optimisation of a combined cycle cogeneration dual-loop organic Rankine cycle (ORC) system for solid oxide fuel cell (SOFC) waste-heat recovery. *Appl Energy* 2020;261:114384.
- [201] Zeng H, Wang Y, Shi Y, Cai N. Biogas-fueled flame fuel cell for micro-combined heat and power system. *Energy Convers Manag* 2017;148:701–7.
- [202] Antonucci V, Brunaccini G, De Pascale A, Ferraro M, Melino F, Orlandini V, et al. Integration of  $\mu$ -SOFC generator and ZEBRA batteries for domestic application and comparison with other  $\mu$ -CHP technologies. *Energy Procedia* 2015;75:999–1004.
- [203] Kupecki J, Skrzypkiewicz M, Wierzbicki M, Stepień M. Experimental and numerical analysis of a serial connection of two SOFC stacks in a micro-CHP system fed by biogas. *Int J Hydrogen Energy* 2017;42:3487–97.
- [204] Ghorbani S, Khoshgoftar-Manesh MH, Nourpour M, Blanco-Marigorta AM. Exergoeconomic and exergoenvironmental analyses of an integrated SOFC-GT-ORC hybrid system. *Energy* 2020;206:118151.
- [205] Mojaver P, Abbasalizadeh M, Khalilarya S, Chitsaz A. Co-generation of electricity and heating using a SOFC-ScCO<sub>2</sub> Brayton cycle-ORC integrated plant: Investigation and multi-objective optimization. *Int J Hydrogen Energy* 2020;45:27713–29.

- [206] Soleymani E, Gargari SG, Ghaebi H. Thermodynamic and thermoeconomic analysis of a novel power and hydrogen cogeneration cycle based on solid. *Renew Energy* 2021.
- [207] Longo S, Cellura M, Guarino F, Brunaccini G, Ferraro M. Life cycle energy and environmental impacts of a solid oxide fuel cell micro-CHP system for residential application. *Sci Total Environ* 2019;685:59–73.
- [208] Bai R, Jernsittiparsert K. Optimal design of a micro combined CHP system applying PEM fuel cell as initial mover with utilization of Developed Pathfinder Optimizer. *Energy Reports* 2020;6:3377–89.
- [209] Wang F, Deng S, Zhang H, Wang J, Zhao J, Miao H, et al. A comprehensive review on high-temperature fuel cells with carbon capture. *Appl Energy* 2020;275:115342.
- [210] Bao J, Zhao L. A review of working fluid and expander selections for organic Rankine cycle. *Renew Sustain Energy Rev* 2013;24:325–42.
- [211] Dincer I, Demir ME. *4.8 Steam and Organic Rankine Cycles* 2018.
- [212] Boyaghchi FA, Montazerinejad H. Multi-objective optimisation of a novel combined cooling, heating and power system integrated with flat plate solar collectors using water/CuO nanofluid. *Int J Exergy* 2016;21:202–38.
- [213] Tchanche BF, Lambrinos G, Frangoudakis A, Papadakis G. Low-grade heat conversion into power using organic Rankine cycles—A review of various applications. *Renew Sustain Energy Rev* 2011;15:3963–79.
- [214] Lecompte S, Huisseune H, Van Den Broek M, Vanslambrouck B, De Paepe M. Review of organic Rankine cycle (ORC) architectures for waste heat recovery. *Renew Sustain Energy Rev* 2015;47:448–61.
- [215] Jafary S, Khalilarya S, Shawabkeh A, Wae-hayee M, Hashemian M. A complete energetic and exergetic analysis of a solar powered trigeneration system with two novel organic Rankine cycle (ORC) configurations. *J Clean Prod* 2020:124552.

- [216] Pereira JS, Ribeiro JB, Mendes R, Vaz GC, André JC. ORC based micro-cogeneration systems for residential application—A state of the art review and current challenges. *Renew Sustain Energy Rev* 2018;92:728–43.
- [217] Köse Ö, Koç Y, Yağlı H. Performance improvement of the bottoming steam Rankine cycle (SRC) and organic Rankine cycle (ORC) systems for a triple combined system using gas turbine (GT) as topping cycle. *Energy Convers Manag* 2020;211:112745.
- [218] Liu X, Nguyen MQ, Chu J, Lan T, He M. A novel waste heat recovery system combining steam Rankine cycle and organic Rankine cycle for marine engine. *J Clean Prod* 2020:121502.
- [219] Nazari N, Porkhial S. Multi-objective optimization and exergo-economic assessment of a solar-biomass multi-generation system based on externally-fired gas turbine, steam and organic Rankine cycle, absorption chiller and multi-effect desalination. *Appl Therm Eng* 2020;179:115521.
- [220] Moradi R, Marcantonio V, Cioccolanti L, Bocci E. Integrating biomass gasification with a steam-injected micro gas turbine and an Organic Rankine Cycle unit for combined heat and power production. *Energy Convers Manag* 2020;205:112464.
- [221] Arabkoohsar A, Andresen GB. Thermodynamics and economic performance comparison of three high-temperature hot rock cavern based energy storage concepts. *Energy* 2017;132:12–21.
- [222] Arabkoohsar A. Combined steam based high-temperature heat and power storage with an Organic Rankine Cycle, an efficient mechanical electricity storage technology. *J Clean Prod* 2020;247:119098.
- [223] Tchanche BF, Papadakis G, Lambrinos G, Frangoudakis A. Fluid selection for a low-temperature solar organic Rankine cycle. *Appl Therm Eng* 2009;29:2468–76.
- [224] Farrokhi M, Noie SH, Akbarzadeh AA. Preliminary experimental investigation of a natural gas-fired ORC-based micro-CHP system for residential buildings. *Appl Therm Eng* 2014;69:221–9.

- [225] Peris B, Navarro-Esbrí J, Molés F, Martí JP, Mota-Babiloni A. Experimental characterization of an Organic Rankine Cycle (ORC) for micro-scale CHP applications. *Appl Therm Eng* 2015;79:1–8.
- [226] Kaczmarczyk TZ, Żywica G, Ilnatowicz E. The impact of changes in the geometry of a radial microturbine stage on the efficiency of the micro CHP plant based on ORC. *Energy* 2017;137:530–43.
- [227] Yang S-C, Hung T-C, Feng Y-Q, Wu C-J, Wong K-W, Huang K-C. Experimental investigation on a 3 kW organic Rankine cycle for low-grade waste heat under different operation parameters. *Appl Therm Eng* 2017;113:756–64.
- [228] Algieri A. Comparative Investigation of the Performances of Subcritical and Transcritical Biomass-Fired ORC Systems for Micro-scale CHP Applications. *ANT/SEIT*, 2016, p. 855–62.
- [229] Liu H, Shao Y, Li J. A biomass-fired micro-scale CHP system with organic Rankine cycle (ORC)–Thermodynamic modelling studies. *Biomass and Bioenergy* 2011;35:3985–94.
- [230] Qiu G, Shao Y, Li J, Liu H, Riffat SB. Experimental investigation of a biomass-fired ORC-based micro-CHP for domestic applications. *Fuel* 2012;96:374–82.
- [231] Montazerinejad H, Ahmadi P, Montazerinejad Z. Advanced exergy, exergo-economic and exergo-environmental analyses of a solar based trigeneration energy system. *Appl Therm Eng* 2019;152:666–85.
- [232] Ferreira AC, Silva J, Teixeira S, Teixeira JC, Nebra SA. Assessment of the Stirling engine performance comparing two renewable energy sources: Solar energy and biomass. *Renew Energy* 2020.
- [233] Zare S, Tavakolpour-saleh AR, Aghahosseini A, Sangdani MH, Mirshekari R. Design and optimization of Stirling engines using soft computing methods: A review. *Appl Energy* 2020:116258.
- [234] Kaldehi BJ, Keshavarz A, Pirooz AAS, Batooei A, Ebrahimi M. Designing a micro Stirling

- engine for cleaner production of combined cooling heating and power in residential sector of different climates. *J Clean Prod* 2017;154:502–16.
- [235] Hosseinpour J, Sadeghi M, Chitsaz A, Ranjbar F, Rosen MA. Exergy assessment and optimization of a cogeneration system based on a solid oxide fuel cell integrated with a Stirling engine. *Energy Convers Manag* 2017;143:448–58.
- [236] Li T, Tang D, Li Z, Du J, Zhou T, Jia Y. Development and test of a Stirling engine driven by waste gases for the micro-CHP system. *Appl Therm Eng* 2012;33:119–23.
- [237] González-Pino I, Pérez-Iribarren E, Campos-Celador A, Las-Heras-Casas J, Sala JM. Influence of the regulation framework on the feasibility of a Stirling engine-based residential micro-CHP installation. *Energy* 2015;84:575–88.
- [238] Schneider T, Müller D, Karl J. A review of thermochemical biomass conversion combined with Stirling engines for the small-scale cogeneration of heat and power. *Renew Sustain Energy Rev* 2020;134:110288.
- [239] Bidhendi MV, Abbassi Y. Exploring dynamic operation of a solar dish-stirling engine: Validation and implementation of a novel TRNSYS type. *Sustain Energy Technol Assessments* 2020;40:100765.
- [240] Chen J, Li X, Dai Y, Wang C-H. Energetic, economic, and environmental assessment of a Stirling engine based gasification CCHP system. *Appl Energy* 2021;281:116067.
- [241] Udeh GT, Michailos S, Ingham D, Hughes KJ, Ma L, Pourkashanian M. A techno-environmental assessment of a biomass fuelled micro-CCHP driven by a hybrid Stirling and ORC engine. *Energy Convers Manag* 2021;227:113601.
- [242] Damirchi H, Najafi G, Alizadehnia S, Mamat R, Azwadi CSN, Azmi WH, et al. Micro combined heat and power to provide heat and electrical power using biomass and Gamma-type Stirling engine. *Appl Therm Eng* 2016;103:1460–9.
- [243] Najafi G, Hoseini SS, De Goey LPH, Yusaf T. Optimization of combustion in micro combined heat and power (mCHP) system with the biomass-Stirling engine using SiO<sub>2</sub> and

- Al<sub>2</sub>O<sub>3</sub> nanofluids. *Appl Therm Eng* 2020;169:114936.
- [244] Arashnia I, Najafi G, Ghobadian B, Yusaf T, Mamat R, Kettner M. Development of micro-scale biomass-fuelled CHP system using Stirling Engine. *Energy Procedia* 2015;75:1108–13.
- [245] Cardozo E, Erlich C, Malmquist A, Alejo L. Integration of a wood pellet burner and a Stirling engine to produce residential heat and power. *Appl Therm Eng* 2014;73:671–80.
- [246] Auñón-Hidalgo JA, Sidrach-de-Cardona M, Auñón-Rodríguez F. Performance and CO<sub>2</sub> emissions assessment of a novel combined solar photovoltaic and thermal, with a Stirling engine micro-CHP system for domestic environments. *Energy Convers Manag* 2021;230:113793.
- [247] Babaelahi M, Jafari H. Analytical design and optimization of a new hybrid solar-driven micro gas turbine/stirling engine, based on exergo-enviro-economic concept. *Sustain Energy Technol Assessments* 2020;42:100845.
- [248] Moghadam RS, Sayyaadi H, Hosseinzade H. Sizing a solar dish Stirling micro-CHP system for residential application in diverse climatic conditions based on 3E analysis. *Energy Convers Manag* 2013;75:348–65.
- [249] Cengel YA, Boles MA. *Thermodynamics: An Engineering Approach* 6th Edition (SI Units). The McGraw-Hill Companies, Inc., New York; 2007.
- [250] Van Wylen GJ, Sonntag RE, Borgnakke C. *Fundamentals of classical thermodynamics*. Wiley New York; 1976.
- [251] Dincer I, Rosen MA, Ahmadi P. *Optimization of energy systems*. John Wiley & Sons; 2017.
- [252] Bejan A, Tsatsaronis G, Moran MJ. *Thermal design and optimization*. John Wiley & Sons; 1995.
- [253] Hosseini SE. Design and analysis of renewable hydrogen production from biogas by integrating a gas turbine system and a solid oxide steam electrolyzer. *Energy Convers*

Manag 2020;211:112760.

- [254] Turns SR. Introduction to combustion. vol. 287. McGraw-Hill Companies New York, NY, USA; 1996.
- [255] Lefebvre AH, Ballal DR. Gas turbine combustion: alternative fuels and emissions. CRC press; 2010.
- [256] Rizk N, Mongia HC. Semianalytical correlations for NO<sub>x</sub>, CO, and UHC emissions 1993.
- [257] Mishra SK, Dahiya RP. Adiabatic flame temperature of hydrogen in combination with gaseous fuels. Int J Hydrogen Energy 1989;14:839–44.
- [258] Jing Y, Song X, Wu R, Wei J, Gong Y, Bao W, et al. Investigation on the improved lifted flame stabilization of methane/hydrogen mixtures with oxygen co-flow based on OH\* chemiluminescence. Int J Hydrogen Energy 2024;60:556–65.
- [259] Patel V, Shah R. Effect of hydrogen enrichment on combustion characteristics of methane swirling and non-swirling inverse diffusion flame. Int J Hydrogen Energy 2019;44:28316–29.
- [260] Gülder OL. Flame temperature estimation of conventional and future jet fuels 1986.
- [261] Novosselov I V, Malte PC, Yuan S, Srinivasan R, Lee JCY. Chemical reactor network application to emissions prediction for industrial gas turbine. Turbo Expo Power Land, Sea, Air, vol. 42363, 2006, p. 221–35.
- [262] Du Y, Cheng H, Li S, Chen X, Li Y, Ren W, et al. Core-shell equivalent reactor network model to bridging CFD and process simulations of a fluidized bed reactor. Chem Eng Sci 2024;287:119772.
- [263] Lamioni R, Mariotti A, Salvetti MV, Galletti C. Chemical Reactor Network modeling of ammonia–hydrogen combustion in a gas turbine: Stochastic sensitivity analysis. Appl Therm Eng 2024:122734.
- [264] Liu G, Wang J, Zheng L, Pan R, Lu C, Wang Y, et al. Effect of hydrogen addition on

- explosion characteristics of premixed methane/air mixture under different equivalence ratio distributions. *Energy* 2023;276:127607.
- [265] Wei ZL, Leung CW, Cheung CS, Huang ZH. Effects of equivalence ratio, H<sub>2</sub> and CO<sub>2</sub> addition on the heat release characteristics of premixed laminar biogas-hydrogen flame. *Int J Hydrogen Energy* 2016;41:6567–80.
- [266] Alabaş B, Tunç G, Taştan M, Yılmaz İ. Effect of oxygen enrichment of Biogas-Hydrogen mixtures in a premixed combustor on the combustion instability and emissions. *Fuel* 2023;340:127498.
- [267] Li G, Lu Y, Glarborg P. Development of a detailed kinetic model for hydrogen oxidation in supercritical H<sub>2</sub>O/CO<sub>2</sub> mixtures. *Energy & Fuels* 2020;34:15379–88.
- [268] G.P. Smith D.M. Golden MFNWMBEMG, C.T. Bowman R.K. Hanson SSWCGJG, [http://www.me.berkeley.edu/gri\\_mech/](http://www.me.berkeley.edu/gri_mech/) Research Inst. Chicago IL 2000. GRI-Mech 3.0 n.d.
- [269] CERFACS Chemistry n.d.:<https://chemistry.cerfacs.fr/en/chemical-database/>.
- [270] Kim G, Lee YD, Sohn CH, Choi KW, Kim HS. Experimental investigation on combustion and emission characteristics of a premixed flame in a gas-turbine combustor with a vortex generator. *Appl Therm Eng* 2015;77:57–64.
- [271] Li J, Li Y. Micro gas turbine: Developments, applications, and key technologies on components. *Propuls Power Res* 2023.